1 June 1978
Continental Drilling Workshop
Background Paper- E.3

DEPARTMENT OF DEFENSE

INTERESTS IN

CONTINENTAL DRILLING

BY

BOB ANDREWS

AND

JACK HEACOCK

OFFICE OF NAVAL RESEARCH
EARTH PHYSICS PROGRAM
CODE 463
ARLINGTON, VA. 22217

1 JUNE 1978

CONTENTS

DEPARTMENT OF DEFENSE

INTERESTS IN CONTINENTAL DRILLING

INTRODUCTION

It is necessary for the Department of Defense to understand the physical properties and structure of the earth's crust for a number of operationally important reasons. As a corollary, it is important, in order to develop efficient, cost-effective techniques for evaluating crustal properties from geophysical data observed at the surface, that methods be developed to infer the deep physical properties of the crustal rocks from the characteristics of the surface-recorded geophysical data. To develop such techniques requires actual samples of the deep crust in order to determine the lithology, porosity, fluid content, and other physical properties of the deep crust. Such data, combined with laboratory studies of the physical behavior and characteristics of rocks at crustal pressures and temperatures, constitute the fundamental building blocks upon which such a system for remotely sensing otherwise unmeasurable crustal properties can be developed.

In order to get a good idea of drilling conducted for or by DoD, we wrote to a number of military organizations and industrial concerns known to have requirements for drill hole data. A list of the responding sources of information is given in Appendix A of this report, and it is probably not comprehensive. It is apparent that some drilling done for DoD has a specific goal in mind, and upon completion of a given project, cores

and samples (if taken) and bore hole logs (if recorded) are not centrally archived and are often dispersed and/or lost. Some DoD drilling is for sensitive projects that are classified for periods of tens of years, and the geological information may never become available. It became apparent during our survey that it will require a considerable effort to ferret out all of the drill hole data available to the various organizations within DoD. The need for such a survey should be addressed during the Workshop on Continental Drilling for Scientific Purposes. We have included in Appendix B a brief listing of bore holes that were provided by the survey conducted for the preparation of this report. Also in this report (Appendix C) are recommendations for future crustal research from the participants in the Symposium on the Nature and Physical Properties of the Earth's Crust held in 1976 at Vail, Colorado, and published in the American Geophysical Union Geophysical Monograph 20.

GENERAL APPLICATIONS

The applications for DoD for a knowledge of crustal properties are numerous. In order to discharge its responsibilities for the defense of the nation, DoD is obligated to develop facilities and techniques which can ensure its continued ability to function in the case of attack by foreign powers. Not only must it establish invulnerable headquarters from which to function, but missile silos, which provide a strategic deterrent, must be invulnerable both to enemy attack and to natural disruption caused by earthquakes or by tectonic creep which can cause unpredictable deflections

in the local gravitational vertical.

The concept of invulnerable underground facilities protected from enemy action has a certain appeal for defense purposes. However, an understanding of earth properties immediately becomes essential for evaluating techniques of communication, power supply, environmental control, strength to withstand bombing overpressures, and vulnerability of surface access links (i.e., for personnel, power, water, ventilation, communication, and waste disposal). Civil work projects such as those of the Army Corps of Engineers call for engineering evaluations of the structural integrity of rock walls and footings, usually involving drilling to obtain rock samples.

SPECIFIC APPLICATIONS

Geothermal Energy for Remote DoD Bases

The operation of military bases requires energy. Remote island bases are especially vulnerable to a severance of energy supply links. In certain cases, as with our Pacific bases (e.g., at Pearl Harbor, Hickam Field, and Schofield Barracks on Oahu; the naval base on Adak, Alaska; and the military bases on Guam), there is the potential of supplying base energy needs from geothermal sources. The development of improved geophysical methods to evaluate subsurface temperatures, porosities, and fluid content is highly desirable for creating a cost-effective geophysical method for evaluating the viability of potential geothermal resources for operating such DoD bases.

Earthquake Risk Reduction at Military Bases

The need for deep drill holes for developing methods to evaluate stress buildup in seismically active areas has been discussed elsewhere. The Air Force is concerned with the impact of earthquakes on missile silos and their destabilizing effects on guidance systems. The possible destruction of DoD bases by earthquakes is a matter of valid concern. Navy has a clear responsibility to protect its shore bases against damage from any source, including natural hazards. The threat from earthquake damage is especially critical for naval bases since they are often located in coastal areas on unstable marine soils and filled land. Buildings in such an area are subject to distortion or collapse, either of which renders a building operationally useless. Because this can affect hospitals, power stations, communication stations, command headquarters, harbor ingress and egress, and the support of the Fleet by naval bases in general, this knowledge is critical to the Navy and vital to the security of the nation.

Direct Military Projects

The VELA UNIFORM PROJECT surveyed a number of available dry bore holes for studies of the change in seismic signal and noise characteristics as a function of depth. Descriptions and logs of the holes in this study, relevant to monitoring of underground nuclear explosions, have been presented in technical reports available through the Defense Documentation Center. Hundreds of holes have been drilled at the Nevada Test Site for geological studies in conjunction with domestic

underground nuclear testing. In addition, drill holes into crystalline basement from around the United States have been studied for missile silo site analysis.

Military/Civil Projects

Many holes have been drilled into crystalline basement at military installations for logistical support, including water supply wells, waste disposal wells, foundation investigations, and other civil work projects. The Army Corps of Engineers in particular conducts drilling and other geological operations in conjunction with flood control projects associated with reservoirs, hurricane protection, and river channel and levee improvements.

FUNDAMENTAL STUDIES

A broad range of fundamental physical properties of the earth's crust either directly affect DoD or have a potential impact, some of which should be developed to become operationally useful. These include the porosity, fluid content, stress concentration, strength, electromagnetic and seismic propagation characteristics, and the distribution of surface conductivity which affects VLF propagation signal patterns. Such information is applicable to an evaluation of: the volume, temperature, and fluid content of geothermal reservoirs; stress concentrations in seismically active areas (earthquake risk evaluation); the strength of subsurface layers; the distribution of surface conductivity patterns (which cause the refraction of electromagnetic navigation signals); and the possibility for electromagnetic or seismic crustal communication through the earth.

CONCLUSIONS

Currently, we are unable to determine deep physical properties of the continental crust with any certainty by geophysical observations at the earth's surface, although DoD research organizations are currently supporting studies aimed toward achieving this goal. A deep continental drilling program is needed to provide ground truth to test the geophysical techniques being developed. This is critically important to the achievement of this goal. Such an objective will have direct scientific and industrial benefits in addition to its criticality for achieving DoD objectives.

For the reasons outlined above, DoD has a vital interest directly involved with national security to ensure the progress and implementation of a continental drilling program. We wish to emphasize the importance of such a program and to lend the weight of our responsibilities and needs to the argument that such a program should be funded in the national interest.

APPENDIX A

Sources of Information

1. Nevada Test Site, Nevada

    a. Joseph W. LaComb
    Chief, test Construction Division
    FCTC
    DoD/DNA
    P. O. Box 208
    Mercury, Nevada 89023

    b. W. S. Twenhofel
    Chief, Special Projects Branch
    U.S. Geological Survey
    Box 25046
    Denver Federal Center
    Denver, Colorado 80225

    c. Grant Bruesch
    Fenix & Scisson, Inc.
    Mercury, Nevada 89023

2. Department of the Army

    a. Lloyd B. Underwood
    Chief, Geology Section
    Geotechnical Branch
    Engineering Division
    Directorate of Civil Works
    Office of the Chief of Engineers (DAEN-CWE-SG)
    Department of the Army
    Washington, D.C. 20314

    b. H. B. Willis
    Chief, Engineering Division
    Office of the Chief of Engineers (DAEN-CWE)
    Department of the Army
    Washington, D.C. 20314

3. Department of the Navy

    a. Nancy Bogart
    Naval Construction Battalion Center
    Port Hueneme, California 93043

b. E. H. Moser, Jr.
Naval Construction Battalion Center
Port Hueneme, California 93043

c. Stan Wahl
Public Works Department
Naval Construction Battalion Center
Port Hueneme, California 93043

d. Carl Austin
Code 266
Geothermal Utilization
Naval Weapons Center
China Lake, California

4. Defense Advanced Research Projects Agency

a. Wayne Helterbran
Acting Chief
VELA Seismological Center
312 Montgomery Street
Alexandria, Virginia 22314

5. Department of the Air Force

a. LCOL George Riddle
SAMSO/MNND
Norton Air Force Base, California 92409

6. Industry

a. R. D. Wolfe
Senior Project Engineer
Teledyne - Geotech
P. O. Box 28277
Dallas, Texas 75228

b. Sidney J. Green
Terra Tek
University Research Park
420 Wakara Way
Salt Lake City, Utah 84108

APPENDIX B

NON-COMPREHENSIVE LISTING OF COMPLETED DRILL HOLES OF INTEREST TO DOD

COMPLETED DRILL HOLES

Identification: About 18 drill holes at Nevada Test Site

Date Drilled:

Location: Rainier Mesa, Nevada Test Site, Nev.

Depth: Range from 429 m to 793 m

General Geology: Tertiary volcanic tuffs ov erlying Paleozoic, Cambrian, and Precambrian sedimentary rocks

Samples: All holes totally cored

Logs: Electric, density, velocity, radiation, caliper (some holes)

Source of Data: J. W. LaComb, Defense Nuclear Agency, Mercury, Nev.

Identification: About 16 holes at Nevada Test Site

Date Drilled:

Location: Nevada Test Site, Nev.

Depth: 1,524 m or deeper

General Geology:

Samples:

Logs:

Source of Data: J. W. LaComb, Defense Nuclear Agency, Mercury, Nev.

COMPLETED DRILL HOLES

Identification: Humble Oil No. 1 Government

Date Drilled: 20 Jun 60 to 5 Aug 60

Location: SE/4 Sec 8, Twp 13N, Rge 88W, Carbon County, Wyo.

Depth: 8,163 ft

General Geology: Tertiary to Cambrian sedimentary rocks with Precambrian quartzite at bottom

Samples:

Logs: Electric, microlog, sonic

Source of Data: W. Helterbran, VELA Seismological Center, Alexandria, Va. and R. D. Wolfe, Teledyne-Geotech, Dallas, Tex.

Identification: The Geotechnical Corp. Tabernacle Butte No. 1

Date Drilled: 18 Dec 63

Location: C NE/4 SW/4 Sec 25, Twp 29N, Rge 107W, Sublette County, Wyo.

Depth: 11,008 ft

General Geology: Tertiary to Cretaceous sedimentary rocks (at bottom)

Samples:

Logs: Electric, temperature, sonic-velocity, caliper, density

Source of Data: W. Helterbran, VELA Seismological Center, Alexandria, Va. and R. D. Wolfe, Teledyne-Geotech, Dallas, Tex.

COMPLETED DRILL HOLES

Identification: United Fuel Gas Co. No. 1 Sponaugle

Date Drilled: 1 Mar 60 to 18 July 60

Location: Circleville District, 7 miles S of Cherry Grove, Pendleton County, West Virginia

Depth: 13,001 ft

General Geology: Ordovician and Cambrian sedimentary rocks

Samples: Available

Logs: Microlog, velocity, caliper

Source of Data: W. Helterbran, VELA Seismological Center, Alexandria, Va. and R. D. Wolfe, Teledyne-Geotech, Dallas, Tex.

Identification: Stanolind Oil & Gas No. 1 Pinedale Unit

Date Drilled: 31 Mar 49

Location: Sec 17, Twp 33N, Rge 109W, Sublette County, Wyo.

Depth: 7,794 ft

General Geology: Tertiary sandy shales (at bottom)

Samples: None

Logs: Electric, sonic-velocity (from well 20 miles to SE)

Source of Data: W. Helterbran, VELA Seismological Center, Alexandria, Va. and R. D. Wolfe, Teledyne-Geotech, Dallas, Tex.

COMPLETED DRILL HOLES

Identification: Superior Oil Co. Kanab Creek Unit 32-16

Date Drilled: Dec 62

Location: C SW NE Sec 16, Twp 42S, Rge 7W, Kane County, Utah

Depth: 9,119 ft

General Geology: Mississippian to Cambrian sedimentary rocks (at bottom)

Samples: Available

Logs: Electric, sonic, caliper

Source of Data: W. Helterbran, VELA Seismological Center, Alexandria, Va. and R. D. Wolfe, Teledyne-Geotech, Dallas, Tex.

- -

Identification: Standard Oil Co. of Ca. Rattlesnake Hills No. 1

Date Drilled: 2 Jul 57 to 6 Apr 58

Location: 330 ft N and 330 ft W of SE corner Sec 15, Twp 11N, Rge 24E, Benton County, Washington

Depth: 10,655 ft

General Geology: Tertiary basalt (at bottom)

Samples: Available

Logs: Electric

Source of Data: W. Helterbran, VELA Seismological Center, Alexandria, Va. and R. D. Wolfe, Teledyne-Geotech, Dallas, Tex.

COMPLETED DRILL HOLES

Identification: J. Ray McDermott No. 1 State

Date Drilled: 18 Jul 59 to 1 Feb 60

Location: C SW SW Sec 2, Twp 43S, Rge 8W, Kane County, Utah

Depth: 10,503 ft

General Geology: Jurassic to Cambrian sedimentary rocks with Precambrian quartzite at bottom

Samples: Available

Logs: Electric, microlog, sonic

Source of Data: W. Helterbran, VELA Seismological Center, Alexandria, Va. and R. D. Wolfe, Teledyne-Geotech, Dallas, Tex.

Identification: Carter Oil Co. No. 1 USA (Carter(Humble) Vernal No. 6)

Date Drilled: Feb 52 to June 52

Location: 660 ft N and 660 ft E of SW corner of Sec 9, Twp 6S, Rge 21E, Uintah County, Utah

Depth: 9,002 ft

General Geology: Sequence of Tertiary sedimentary rocks (at bottom)

Samples: Available

Logs: Electric, sonic (approximately 4 miles away)

Source of Data: W. Helterbran, VELA Seismological Center, Alexandria, Va. and R. D. Wolfe, Teledyne-Geotech, Dallas, Tex.

COMPLETED DRILL HOLES

Identification: Phillips Petroleum Co. No. 1 "EE" University

Date Drilled: 4 Feb 59

Location: Sec 7, Block 24, University Lands 12 miles NE of Ft. Stockton, Pecos County, Texas

Depth: 25, 340 ft

General Geology: Permian to Ordovician sedimentary rocks (at bottom)

Samples:

Logs: Electric, temperature, microlog, velocity

Source of Data: W. Helterbran, VELA Seismological Center, Alexandria, Va. and R. D. Wolfe, Teledyne-Geotech, Dallas, Tex.

- -

Identification: The Geotechnical Corp. No. 1, Trigg

Date Drilled: 5 May 62

Location: T. W. Causey Survey 6 miles SE of Grapeville, Dallas County, Texas

Depth: 10, 231 ft

General Geology: Cretaceous to Cambrian sedimentary rocks with Precambrain igneous rocks at a depth of about 13,900 ft postulated on seismic exploratory work.

Samples: Available

Logs: Electric, temperature, velocity, caliper

Source of Data: W. Helterbran, VELA Seismological Center, Alexandria, Va. and R. D. Wolfe, Teledyne-Geotech, Dallas, Tex.

COMPLETED DRILL HOLES

Identification: U. S. Government Eniwetok E-1

Date Drilled: 1952

Location: Parry Island, Eniwetok Atoll, Marshall Islands (approx. 11°24' N Lat., 162°24' E Long.)

Depth: 4,222 ft

General Geology: Quaternary and Tertiary Limestones bottoming in olivine basalt

Samples: Available

Logs: Temperature, velocity

Source of Data: W. Helterbran, VELA Seismological Center, Alexandria, Va. and R. D. Wolfe, Teledyne-Geotech, Dallas, Tex.

Identification: Humble Oil & Refining Co. No. 3 Wendlandt

Date Drilled: Apr 61 to Sept 61

Location: Brooks Salt Dome, Jose M. Acosta League, Smith County, Texas

Depth: 12, 621 ft

General Geology: Tertiary to Cretaceous sedimentary rocks (at bottom)

Samples: Available

Logs: Electric, temperature, sonic, caliper

Source of Data: W. Helterbran, VELA Seismological Center, Alexandria, Va. and R. D. Wolfe, Teledyne-Geotech, Dallas, Tex.

COMPLETED DRILL HOLES

Identification: Amerada Petroleum No. 1 Marie Selle

Date Drilled: 15 Nov 61 to 5 Feb 62

Location: NE/4 NE/4 660 ft FNL, 660.5 ft FEL Sec 27, Twp 143N, Rge 92W, Dunn County, North Dakota

Depth: 12,168 ft

General Geology: Sequence of Tertiary to Ordovician sedimentary rocks (at bottom)

Samples: None

Logs: Sonic, caliper

Source of Data: W. Helterbran, VELA Seismological Center, Alexandria, Va. and R. D. Wolfe, Teledyne-Geotech, Dallas, Tex.

Identification: Pan American No. 1 Perdasofpy

Date Drilled: Nov 53 to Apr 54

Location: SE/4 NW/4 SW/4 Sec 11, Twp 4N, Rge 12W, Comanche County, Oklahoma

Depth: 9,674 ft

General Geology: Sequence of Ordovician to Cambrian sedimentary rocks with Precambrian granite from about 5,500 ft to bottom

Samples: At Pan American

Logs: Electric, velocity, density (seismic reflection profile over hole)

Source of Data: W. Helterbran, VELA Seismological Center, Alexandria, Va. and R. D. Wolfe, Teledyne-Geotech, Dallas, Tex.

COMPLETED DRILL HOLES

Identification: Continental Oil Co. Meridian Unit No. 1

Date Drilled: 28 May 50 to 17 Jul 51

Location: SW NE SE, Sec 31, Twp 16N, Rge 56E, White Pine County, Nev.

Depth: 10,312 ft

General Geology: Sequence of Mississippian to Ordovician sedimentary rocks (At bott

Samples: At Continental Oil Co.

Logs: Electric, sonic, and density

Source of Data: W. Helterbran, VELA Seismological Center, Alexandria, Va. and R. D. Wolfe, Teledyne-Geotech, Dallas, Tex.

Identification: Shell Oil Co. Diamond Valley No. 1

Date Drilled: 1956

Location: NE NW 660 ft N line and 1,877 ft W line Sec 30, Twp 23N, Rge 54E, Eureka County, Nev.

Depth: 8,042 ft

General Geology: Sequence of Tertiary to Devonian sedimentary rocks (at bottom)

Samples: None

Logs: Electric

Source of Data: W. Helterbran, VELA Seismological Center, Alexandria, Va. and R. D. Wolfe, Teledyne-Geotech, Dallas, Tex.

COMPLETED DRILL HOLES

Identification: Indiana Farm Bureau No. 1 Luther Brown

Date Drilled: 15 Apr 59 to 23 June 59

Location: SE/4 SE/4 Sec 20, Twp 5N, Rge 2E, Lawrence County, Indiana

Depth: 6,806 ft

General Geology: Sequence of Mississippian to Cambrian sedimentary rocks bottoming in Precambrian basalt

Samples: At Indiana Farm Bureau

Logs: Electric, sonic

Source of Data: W. Helterbran, VELA Seismological Center, Alexandria, Va. and R. D. Wolfe, Teledyne-Geotech, Dallas, Tex.

Identification: Gulf Oil Corp. East Glacier Blackfeet No. 1

Date Drilled: 11 Jan 61

Location: NW SW, Sec 3, Twp 30N, Rge 12W, Glacier County, Mont.

Depth: 10,700 ft

General Geology: Sequence of Cretaceous to Mississippian sedimentary rocks (at bottom

Samples: None

Logs: Microlog, sonic, caliper

Source of Data: W. Helterbran, VELA Seismological Center, Alexandria, Va. and R. D. Wolfe, Teledyne-Geotech, Dallas, Tex.

COMPLETED DRILL HOLES

Identification: Humble Oil & Refining Co. No. 1 Crosho Lake - Govt

Date Drilled: Jume 62 to Nov 62

Location: SE/4 SE/4 Sec 13, Twp 2N, Rge 87W, Rio Blanco County, Colo.

Depth: 9,106 ft

General Geology: Sequence of Cretaceous to Cambrian sedimentary rocks bottoming in Precambrian granite

Samples: At Humble Oil & Refining Co.

Logs: Electric, microlog, sonic, caliper

Source of Data: W. Helterbran, VELA Seismological Center, Alexandria, Va. and R. D. Wolfe, Teledyne-Geotech, Dallas, Tex.

- -

Identification: Warren Petroleum Corp. No. 1 Terry

Date Drilled: 25 Jul 55 to 13 Sept 55

Location: C SW/4 SE/4 Sec 21, Twp 23S, Rge 31E, Orange County, Fla.

Depth: 6,586 ft

General Geology: Sequence of Tertiary to Lower Cretaceous sedimentary rocks bottoming in Precambrian igneous rocks

Samples: None

Logs: Induction electric, sonic from 3,256 to bottom, density from 3,256 ft to botton

Source of Data: W. Helterbran, VELA Seismological Center, Alexandria, Va. and R. D. Wolfe, Teledyne-Geotech, Dallas, Tex.

COMPLETED DRILL HOLES

Identification: Disposal Well

Date Drilled:

Location: Rocky Mountain Arsenal, Colo.

Depth: 12,500 ft

General Geology:

Samples: ?

Logs:

Source of Data: L. B. Underwood, Army Corps of Engineers, Wash., D.C.

Identification: Dome Petroleum, et al., Winter Harbour No. 1

Date Drilled: 10 Sept 61 to 7 Apr 62

Location: Melville Island, Northwest Territory, Canada

Depth: 12,543 ft

General Geology: About 9,700 ft of Devonian sedimentary rocks overlying Silurian and Ordo-Silurian sedimentary rocks to total depth

Samples: At Dome Petroleum, et al.

Logs:

Source of Data: W. Helterbran, VELA Seismological Center, Alexandria, Va. and R. D. Wolfe, Teledyne-Geotech, Dallas, Tex.

COMPLETED DRILL HOLES

Identification: Kewanee Interamerican Oil Co. No. 1 Commonwealth of Puerto Rico

Date Drilled: 17 Nov 59 to 3 Apr 60

Location: Santa Isabel, Puerto Rico (17°58'12" N Lat., 66°25'04" W Long.)

Depth: 2,280 m

General Geology: Tertiary sedimentary rocks underlain by Upper Cretaceous volcanics (at bottom)

Samples: Available

Logs: Electric, caliper

Source of Data: R. D. Wolfe, Teledyne-Geotech, Dallas, Tex.

- -

Identification: The Geotechnical Corp. No. 5-A Guantanamo

Date Drilled: 9Sept 63 to 28 Sept 63

Location: Oriente Province, Cuba (19°58'01" N Lat., 75°05'14" W. Long.)

Depth: 1,981 m

General Geology: Tertiary shales (at bottom)

Samples:

Logs:

Source of Data: R. D. Wolfe, Teledyne-Geotech, Dallas, Tex.

COMPLETED DRILL HOLES

Identification: Seismological Station

Date Drilled:

Location: Pinedale, Wy.

Depth: Approximately 10,000 ft

General Geology:

Samples: ?

Logs:

Source of Data: L. B. Underwood, Army Corps of Engineers, Wash., D.C.

- -

Identification: NORAD

Date Drilled:

Location: Colorado Springs, Colo.

Depth: Several holes ranging from 500 ft to 2,400 ft

General Geology:

Samples: ?

Logs:

Source of Data: L. B. Underwood, Army Corps of Engineers, Wash., D.C.

COMPLETED DRILL HOLES

Identification: "Piledriver" Blast Resistant Openings

Date Drilled:

Location: Nevada Test Site

Depth: Several holes ranging from 1,200 ft to 1,500 ft

General Geology:

Samples: ?

Logs:

Source of Data: L. B. Underwood, Army Corps of Engineers, Wash., D.C.

- -

Identification: "Hardhat" Blast Resistant Openings

Date Drilled:

Location: Nevada Test Site

Depth: Several holes ranging from 500 ft to 800 ft

General Geology:

Samples: ?

Logs:

Source of Data: L. B. Underwood, Army Corps of Engineers, Wash., D.C.

COMPLETED DRILL HOLES

Identification: Over 500 drill holes at Nevada Test Site

Date Drilled:

Location: Nevada Test Site, Yucca Flat

Depth: Range from about 150 m to about 1,280 m

General Geology: Alluvium over tuff rocks over Paleozoic rocks

Samples: Cuttings at 3-m intervals; sidewall and conventional cores from many selected holes.

Logs:

Source of Data: W. S. Twenhofel, USGS, Denver, Colo.

Identification: Approximately 35 drill holes at Nevada Test Site

Date Drilled:

Location: Frenchman Flat, Nevada Test Site

Depth: Range from about 150 m to about 800 m

General Geology: Alluvium over tuff rock over Paleozoic rocks

Samples: Cuttings and selected cores

Logs:

Source of Data: W. S. Twenhofel, USGS, Denver, Colo.

COMPLETED DRILL HOLES

Identification: Over 50 drill holes at Nevada Test Site

Date Drilled:

Location: Pahute Flat, Nevada Test Site

Depth: Range of less than 100 m to about 4,250 m

General Geology: Volcanic rock sequence, granitic stock

Samples: Cuttings and selected cores

Logs:

Source of Data: W. S. Twenhofel, USGS, Denver, Colo.

Identification: Pot. #1, Pot. #2, Pot. #3, Pot. #4, Pot. # 5, Pot. #6, Pot. #7, and Non Pot. #3 (8 drill holes)

Date Drilled:

Location: Naval Air Station, Lemoore, Ca.

Depth: 1,323 ft for Pot. #1; all others 1,000 ft

General Geology:

Samples:

Logs:

Source of Data: E. H. Moser, Naval Construction Battalion Center, Port Hueneme, Ca.

COMPLETED DRILL HOLES

Identification: New Pot. #22 and Pot. #21 (2 drill holes)

Date Drilled:

Location: Naval Construction Battalion Center, Port Hueneme, Ca.

Depth: 1,100 ft for New Pot. #22; 1,000 ft for Pot. #21

General Geology: Sediments

Samples: Segments of New Pot. #22

Logs: Electric

Source of Data: E. H. Moser, Naval Construction Battalion Center, Port Hueneme, Ca.

Identification:

Date Drilled:

Location: Naval Air Station, Fallon, Nev.

Depth: 2,000 ft

General Geology:

Samples:

Logs:

Source of Data: E. H . Moser, Naval Construction Battalion Center, Port. Hueneme, Ca.

COMPLETED DRILL HOLES

Identification:

Date Drilled:

Location: Naval Weapons Center, China Lake, Ca. (White Hills)

Depth: 1,500 - 2,000 ft

General Geology:

Samples:

Logs:

Source of Data: E. H. Moser, Naval Construction Battalion Center, Port Hueneme, Ca.

- -

Identification:

Date Drilled:

Location: Naval Weapons Center, China Lake, Ca.

Depth: 1,300 ft

General Geology:

Samples: Cores at Univ. of Utah

Logs: MS Thesis, Univ. of Utah (Joy Hyde)

Source of Data: E. H. Moser, Naval Construction Battalion Center, Port Hueneme, Ca.

COMPLETED DRILL HOLES

Identification: Department of Energy Geothermal Drill Hole

Date Drilled:

Location: Naval Weapons Center, China Lake, Ca.

Depth: 4,824 ft

General Geology: Granitic

Samples: Cores at Univ. of Utah

Logs: Available at Naval Weapons Center, China Lake, Ca. (Dr. Carl Austin)

Source of Data: E. H. Moser, Naval Construction Battalion Center, Port Hueneme, Ca.

- -

Identification:

Date Drilled:

Location: San Clemente, Ca.

Depth: 1,000 ft

General Geology: Volcanics

Samples: Cores at Naval Weapons Center, China Lake, Ca.

Logs: Published in Naval Weapons Center Tech. Paper

Source of Data: E. H. Moser, Naval Construction Battalion Center, Port Hueneme, Ca.

COMPLETED DRILL HOLES

Identification: 2 drill holes

Date Drilled:

Location: Adak, Alaska

Depth: 1,000 ft and 2,067 ft

General Geology: Poorly consolidated volcanics

Samples: Cores at Naval Weapons Center, China Lake, Ca. (Dr. Carl Austin)

Logs: Available at Naval Weapons Center, China Lake, Ca. (Dr. Carl Austin)

Source of Data: E. H. Moser, Naval Construction Battalion Center, Port Hueneme, Ca.

Identification: Petroleum test wells

Date Drilled:

Location: Chocolate Mountains Naval Gunnery Range, Ca. (Further information available from Dr. Carl Austin, Naval Weapons Center, China Lake, Ca.)

Depth:

General Geology:

Samples:

Logs:

Source of Data: E. H. Moser, Naval Construction Battalion Center, Port Hueneme, Ca.

APPENDIX C

RECOMMENDATIONS FOR

FUTURE CRUSTAL RESEARCH

(From: Heacock, J. G. (ed.) 1977. The Earth's Crust - Its Nature and Physical Properties. Amer. Geophys. Union Geophys. Monogr. 20, p. 737-750).

APPENDIX. Recommendations for Future Crustal Research

There were 54 participants in the symposium on the Nature and Physical Properties of the Earth's Crust. Papers were presented to the entire group, which on the final day outlined the following General Research Considerations. Subsequently, smaller groups were formed which wrote Research Recommendations for specific areas. This was done while details of the presentations of the week were still fresh in the minds of the participants.

General Research Considerations

1. How does physical or chemical stratigraphy relate to geological stratigraphy? What processes affect these relationships?
2. In what ways does the crust relate to the mantle? In what ways does the lithosphere relate to the asthenosphere?
3. How do scaling effects influence our interpretations? What is the relationship between laboratory and field data?
4. What is the spectrum of crustal inhomogeneities?
5. To what extent and in what sense are different physical properties continuous in the crust? How are these properties affected by tectonic activity? How do they relate to each other?
6. What is typical of 'typical' crustal models? Data should be integrated into models. Broad-scale commonalities should be recognized (despite local inhomogeneities).
7. What are the definitive properties of various geologic provinces? To what degree do shields represent the lower (pre-Cambrian) crust? How can we best identify specific environments and associate physical and geological properties with them? Geologic province types should be studied on a multidisciplinary basis.
8. What are the artifacts of our measurement techniques?
9. What is the dynamic nature of the crust? Such evidence is needed to deduce evolutionary processes.
10. Where can we best establish common areas for conducting multidisciplinary studies? There is a need to agree on test range(s). Since different geophysical techniques respond to different parameters, it will be necessary to resolve differences between the models which result. For example, studies should include (a) seismic reflection, wide-angle reflection, and refraction, (b) deep drilling, and (c) electrical, thermal, geological, gravitational, and magnetic probing, etc., as they are appropriate.

Entire Assembly

Research Recommendations for Geology

The central problem in crustal studies is simply to describe the crust, the Moho, and the relation of the crust to the upper mantle. Until we know what the crust is like from top to base and how the crust varies laterally, hypotheses on crustal genesis and the role of plate tectonics in the development of ancient crust must remain rather speculative.

Studies should begin with the definition of major crustal provinces; that is, we must know what the different kinds of crust are that need to be described. Then the problem is to determine what vertical sections through the various types of crust are like. Vertical crustal sections may be determined in a number of ways with highly varying degrees of detail, certainty, and effort. One of the most satisfactory approaches is to recognize areas where vertical sections or deep portions of the crust are exposed by unusual tectonic activity, for example, the Ivrea zone in the Alps or possibly the Jotunheimen area in Norway. Unfortunately, the number of such occurrences is probably small and biased. Another approach is to investigate inclusions from diatremes which represent a natural boring through the crust and offer a relatively cheap opportunity to study samples of deep crustal material with the restriction that the samples are mixed up. Structural studies in shields across domes and major faults will give some idea of the vertical distribution of rock types. Laboratory petrologic studies may furnish geobarometers and geothermometers that allow us to place exposed rocks at their proper depth. More isotope studies are needed to determine the derivation of crustal material and fractionation patterns. Seismic reflection studies offer a more detailed picture of the crust than has hitherto been possible, especially when they are combined with other information. All these studies should eventually lead to deep drilling, the ultimate approach.

The problem of vertical movements and material transfer in the consolidated crust is still a major question. Vertical movements are commonly recorded in sedimentary rocks which require further study in order to define the problem properly. A mechanism must be found that explains vertical oscillations measured in kilometers and that still maintains isostatic equilibrium. What is the nature of the Moho? Does it move? Or are vertical movements largely accommodated in the upper mantle? What does it mean when deep crustal rocks such as granulites are exposed at the surface with 30 to 40 km of crust beneath them? What causes the formation of deep basins? How does the Moho vary within a tectonic province and from one province to another? All of these questions are fundamental to understanding the nature of the crust and crustal dynamics.

Geologic studies should be conducted with modern tectonic hypotheses in mind so that data collected can be used to attack these problems. However, facts and hypotheses must be kept separate. Complex problems should be studied in areas where exposures are adequate enough to allow their solution.

Many of these problems are so vast and complicated that their solutions may require central planning of coordinated studies. A general attempt must be made to explain conflicting views and conflicting observations and not necessarily to arrive at one interpretation but at least to understand why there is disagreement. Geological and geophysical interpretations need to be reconciled. Data integration workshops to coordinate various individual studies are needed for this purpose.

Scott B. Smithson
Chairman
A. R. Green
M. Holdaway
J. Eichelberger
S. Kaufman
Elaine Padovani

Research Recommendations for Internal Friction Measurements

Results of laboratory internal friction (Q^{-1}) measurements lead to several conclusions: (1) The removal of H_2O from open fractures raises Q, and Q > 2000 has been achieved in olivine basalts after outgassing. (2) Trace amounts of H_2O absorbed into thoroughly outgassed fractures lower the Q dramatically and Q = 10^2 is typical for rock containing fractures exposed to laboratory atmosphere, while Q = 10 is typical for 'moist' rocks. (3) The effects described in the first and second conclusions are reversible and have been observed over a frequency range from ~25 kHz to 50 Hz, at low confining pressures, and for longitudinal, flexural, and torsional waves. Therefore the effects are thought to be active for seismic waves. (4) The details of the mechanisms for the effects are presently not understood. Detailed application of the effects to the interpretation of seismic Q data requires an understanding of the mechanisms. It is recommended that the sources of the mechanisms be explored. The associated experiments should include confining pressure, pore pressure, temperature, frequency, and crack porosity as parameters. The measurement samples should be well characterized, particularly with regard to the nature and density of fractures. New improved techniques of characterizing fractures developed by the Massachusetts Institute of Technology should be incorporated into the characterization procedure. The selection of samples should also reflect current knowledge of crustal material.

B. R. Tittmann
Gene Simmons

Research Recommendations for the Evaluation of Physical and Mechanical Properties

A knowledge of the physical and mechanical properties of rocks has great practical importance. For example, the exploration, assessment, and development of mineral, oil, and geothermal areas depend upon the availability of laboratory data to predict in situ properties and to interpret geophysical field studies. Relationships among the seismic, electrical, thermal, and pressure sensitive properties of rocks and such quantities as their lithology, density, porosity, fluid content, and strength should be established in the laboratory in order to provide the background upon which to base such interpretations. We recognize several problem areas in the study of physical properties.

Scaling is a fundamental difficulty, and we must resolve the following questions. (1) Are short-term experiments in the laboratory applicable to longer-term behavior in the field? (2) Do microcracks control the physical response of rocks in the field to the same degree as they do in the laboratory? (3) How do joints and large fractures affect physical and mechanical properties? (4) Is there a relationship between microcracks and joints? (5) What are the effects of wavelength versus frequency? Do different seismic or electrical frequencies sample different wavelength effects?

Experiments which will help resolve these questions include (1) laboratory and field measurement of the physical and mechanical properties of a suite of granite samples of various dimensions from the same quarry and comparison of these laboratory measurements with measurements in the quarry, (2) examination of the effects of heterogeneity to determine whether samples which are homogeneous on one scale are homogeneous on a larger scale, and (3) examination of the effects of joints and fractures by carefully mapping them and performing quarry scale experiments.

Other studies central to the understanding of physical and mechanical properties of rocks include the following.

1. Pore pressure. All pressure sensitive properties (e.g., compressibility, seismic velocity, and electrical resistivity) are affected by pore pressure. Yet pore pressure is rarely measured in situ, and we have very little insight concerning effective stress states at depth in the crust. Field measurements of pore pressure should be included when velocity, resistivity, etc., logs are obtained, and these field data should be compared with laboratory results made under controlled conditions of pore and confining pressure.

2. Temperature effects. The effects of temperature on the physical properties of earth materials in situ should be documented in the laboratory. Special emphasis should be placed on the response of fluids and minerals to temperature and the relationships between laboratory and field behavior. These studies would be especially applicable to geothermal energy development.

3. Cycling effects. Stress cycling and temperature cycling to various maximum values and the response of rocks to repeated cycles of fluid injection and drainage should be studied to determine the behavior of rocks as a function of cycling history. Understanding cycling effects is important to such problems as the understanding of

tectonically active zones, secondary oil recovery, the development of geothermal energy in hot dry rocks, and the underground storage of waste material.

4. Interrelationships among physical and mechanical properties. By developing relationships between various mechanical and physical properties (e.g., electrical resistivity versus velocity or velocity versus crack porosity) we will be able to predict the behavior of rocks in situ and to interpret field observations given only one or two measured properties.

Understanding the stress-strain response of rocks is important for the development of earthquake prediction control capabilities and for the exploration of natural resources in tectonically active zones. The following aspects of stress-strain behavior should be examined. (1) The analysis of paleostress and paleotectonics by using structural geology, microcrack history, fluid inclusions, mineralogy, and petrology should be investigated. (2) The determination of present in situ stress by using direct methods of overcoring and hydrofracturing and indirect methods of seismic, electrical and geodetic surveys is important. Temporal effects of stress can be measured by using the in situ indirect methods stated above. (3) Laboratory studies that include the analysis of rock behavior under simulated conditions of stress, confining pressure, pore pressure, and temperature are also important. Limits to in situ stress can be determined from laboratory measurements of the strength of rock under simulated field conditions.

M. Feves
Chairman
M. Batzle
B. Brace
R. Corwin
S. Jones
D. Norton
H. Pratt
D. Turcotte
H. Wang
N. Warren

General Research Recommendations for Seismology

The techniques of seismology provide the most direct probe available to the earth scientist in his study of the earth. Recent advances in field and interpretation techniques have improved the ability to study the physical properties of the earth's crust and thereby to contribute significantly to the study of its nature and tectonic history. In addition to their general scientific importance, such studies are essential to an improved understanding of energy and natural resource exploration and of natural geological hazards and their mitigation.

Problem Areas

Some of the specific characteristics of and questions concerning the earth's crust which seismologists should investigate are the following.

1. Are discontinuities in the earth's crust sharp or transitional? What is their geological and petrological interpretation?
2. Are discontinuities, layers, or zones of similar physical properties continuous or semicontinuous across geological province boundaries?
3. What is the geographical distribution of crustal features such as low velocity, high Poisson's ratio, low Q, and high conductivity zones? Is there a common physical or chemical explanation for these observed properties?
4. What physical and chemical conditions can be inferred from field observations of compressional and shear wave velocities and seismic wave attenuation in the crust?
5. How do crustal structure and the distribution of physical properties of the crust relate to the dynamics of crustal evolution and tectonics?
6. Can we use our knowledge of the history and properties of the oceanic crust to aid in the interpretation of the more complicated continental crust and the study of the relationship and differences between the two?
7. What is the relationship of the crust to the underlying lower lithosphere and asthenosphere? For example, What is the nature of the coupling of the lithospheric plates to the asthenosphere? And how does it influence the crust?

Recommendations

The seismology group recognizes that various geophysical methods provide complementary as well as redundant information on physical properties; thus optimum mapping of the nature of the crust requires a multidisciplinary attack. The following are suggestions for the initial phase of a detailed seismological investigation of the earth's crust.

1. A geophysical study should be undertaken in a single area so that several seismic and other appropriate geophysical techniques can be employed in order to compare results and interpretations of the various methods and to allow an integrated interpretation. A

by COCORP (Committee for Continental Reflection Profiling) has been or will be employed. specific problem to investigate by using a multimethod approach is the nature of discontinuities in the crust and at the crust mantle boundary. It is suggested that this study might most efficiently be accomplished at a location where deep seismic reflection profiling

2. With the experience gained in the multidisciplinary study described above, geophysicists will be in the position to address many of the important contemporary geological problems. For example, a tectonically active area should be studied with special emphasis on the relationships among earthquake distribution and focal mechanisms (state of stress) and the physical properties of the crust determined by various seismological and other field investigations.

3. Future seismological field measurements (both in oceanic and on continental areas) should include compressional and shear wave velocity analysis and amplitude studies to aid in the interpretation of fine structure and in the determination of anelasticity (Q^{-1}) where possible.

4. We recommend that laboratory studies of compressional and shear wave velocities and Q of a broad suite of rocks, especially metamorphic rocks, be accomplished under a wide range of conditions appropriate to the earth's crust, including variations in confining pressure, temperature, saturation, and pore pressure. Such studies will allow comparison and inference from the laboratory and field investigations.

At present, a study of continental interiors forms one phase of the U.S. Geodynamics Program. The efforts of the Geodynamics Committee have largely been directed toward understanding the structure and evolution of sedimentary basins. The goals cited in this report differ from those of that committee in that we seek information pertaining to a broader range of crustal models and properties. However, the knowledge obtained by the two groups should be complementary and should lead to an enhanced knowledge of the structure and evolution of the crust.

G. Sutton
Cochairman
L. Braile
Cochairman
C. Prodehl
S. Mueller
M. Berry
A. Sanford
S. Kaufman
B. Mitchell
J. Orcutt
R. Buffler
D. Jurdy
S. Jones

Research Recommendations for Electrical Surveys

Although electrical surveying techniques have been used by geophysicists to study earth structures since early in this century, the methods are not as technically advanced as they are in some other geophysical disciplines, such as seismology, gravity, or geomagnetism. However, in the past decade there has been a rapid development of the capabilities of electrical surveying methods. Increased interest stems from the application of electrical methods for prospecting for oil and gas and, more recently, for prospecting for geothermal systems. In addition, electrical methods are beginning to find some application in the study of crustal structure. Three techniques in particular are being used; they are known as the direct current resistivity, the magnetotelluric, and the electromagnetic sounding methods. Each method appears to have its own special advantages and disadvantages, and so the methods are not strictly competitive for a specific problem.

Resolving Power

The electrical methods do not yet compete with the seismic method in terms of resolution or reliability. In part this shortcoming is a consequence of a lack of experience, but in part it is also the result of limitations inherent in the physics of electrical methods. The limitations to the precision with which earth structure can be determined are of two types.

One limitation is a lack of sensitivity of electromagnetic fields to earth structures smaller than a given size. For example, commonly, the strength of an electric or an electromagnetic field is measured with an accuracy of a few percent. If an earth structure being studied causes a change in the behavior of the field by less than this amount, it is unlikely that the earth structure can be detected. The solution to this problem is perhaps straightforward: the accuracy with which measurements are made can be increased, so that the effect of the structure being studied becomes larger than the error of measurement.

The other limitation is nonuniqueness, which is a different type of limitation. For example, it should be possible to detect a bed 1 ft (30 cm) thick at a depth of 1000 ft (300 m) if the resistivity of that bed is a thousandfold lower than the resistivity of the overlying rocks. However, precisely the same thing can be said about a bed 2 ft (60 cm) thick with a resistivity 500-fold lower than the resistivity of the overlying beds or a bed 5 ft (1.5 m) thick with a resistivity 200-fold lower, both at a depth of 1000 ft (300 m). In all three cases the effect on the electric or electromagnetic field will be substantially the same, so that the three cases cannot be distinguished. An increase in the precision of measurement does not provide a solution for this problem because the nature of the effect caused by the bed at depth does not change as the accuracy is increased. Auxilliary information must be provided before any distinction can be made between the cases.

Accuracy of Measurement

The accuracy with which electrical field surveys are carried out does not strain the current state of the art in instrumentation. It is common practice to measure direct current resistivity values in the field with an accuracy of ±5%. Certainly, equipment for more precise measurements is easily available, but the argument is made that usually errors introduced by small local changes in resistivity contribute a greater scatter to the data than is caused by errors in measurement. In order to detect a structure in the earth, it is probably necessary to have a change in resistivity that amounts to about 20% with present field standards. For a layered medium this means that a bed can be detected in which the contrast in either transverse resistance or longitudinal conductance amounts to about 50% of that in the overlying bed. In order to increase accuracy in such field surveys, it will be necessary to improve the measurement accuracy and to reduce the scatter of data caused by local inhomogeneities in resistivity. The first can be accomplished by routine improvements in field procedure and measurement practice, but the second requires careful thought. It may be that the scatter of field data can be reduced by making highly redundant measurements and performing some sort of averaging process, or it may be that certain configurations of electrodes will have minimal sensitivity to local changes in resistivity.

Magnetotelluric Method

With the magnetotelluric method the following considerations apply. The accuracy with which resistivity can be determined at a given frequency depends on the statistical behavior of the natural electromagnetic noise of the earth. Long observation times provide one with a better opportunity to get reliable estimates of earth resistivity but significantly increase the cost of magnetotelluric surveys. A question to be raised is whether it is more desirable to have a larger number of locations occupied with a lower accuracy so that the effects of lateral changes in resistivity can be evaluated or whether it is better to observe for a long period of time at a single station so that apparent resistivities can be determined with less uncertainty. It may well be that the use of a controlled source to provide frequencies that are not abundant in the natural electromagnetic specyrum will be a desirable adjunct to magnetotelluric sounding. Research should be directed to the question of how effectively the results of a magnetotelluric sounding can be improved by using an artificial source for at least part of the spectrum.

Data Reduction and Interpretation

Interpretive techniques for electrical surveying methods have advanced rapidly in recent years. The behavior of the electric or electromagnetic field in the presence of a layered structure, structures with simple geometric shapes, or structures with arbitrary shapes has been solved. Perhaps the most significant advance of recent years has been the application of mathematical inversion techniques to find earth

models which closely simulate the results observed in field surveys. The best success has been obtained with inversion in those cases when the earth can be modeled by a one-dimensional medium, that is, by a sequence of layers in which the resistivity varies only with depth. Here a number of inversion techniques have been developed in which it is possible to simulate a set of field data with an average error of less than 1% by using very limited computer time. Only in this case do the capabilities of the interpretation method exceed the quality of the field data which are provided. For two-dimensional and three-dimensional problems, while the mathematical solutions are available, the numerical techniques are not yet advanced enough to permit inversions to be done with a practical amount of work. It is probable that further research both on numerical techniques for determining the electric and electromagnetic fields about bodies of arbitrary shapes and on numerical methods for doing inversions will be productive areas of research. It is quite important in this research that the door be left open for new approaches. The art of modeling and inversion is still at too early a stage of development for the best lines of attack or the ultimate limitations to be recognized.

Multidisciplinary Approach

The product of further development of techniques for measuring and interpreting electrical structures should be a capability for defining electrical structures with resolutions comparable to or better than those now obtained in gravity and density modeling. An important factor in reaching this goal will probably be our ability to incorporate diverse geophysical data into the interpretation of electrical data. For example, the seismic technique is capable of measuring earth structures with considerable accuracy. Often seismic velocities and electrical resistivities vary together. In porous rocks, both acoustic wave speed and resistivity are determined by the porosity. Within a given rock unit, resistivity and wave speed will correlate with a reasonably high degree of reliability. Therefore if a problem in nonuniqueness arises in the interpretation of electrical data, the earth's structure can be determined from seismic data, while the earth resistivity would be determined with an electrical method. Less work has been done on the interrelation of resistivity and wave speed in nonporous rocks, but it is likely that for restricted ranges of conditions, resistivity and wave speed will correlate in crystalline rocks. Much more research needs to be done on this topic before we can determine to what degree seismic results will assist us in evaluating electrical survey data.

Summary

In summary, while electrical surveying methods are undergoing rapid development at the present time, they must be considered to be relatively far behind the other geophysical methods in their present state of development. When electrical methods are improved to the point that they include the current level of sophistication of modern digital recording and data processing techniques, they should provide

us with an increasingly valuable tool for studying earth structures, including those associated with the accumulation of natural resources and those that may give rise to natural hazards. Even today, electrical methods are quite useful for prospecting for oil and gas, minerals, and geothermal energy. In addition, the use of resistivity measurements to assist in earthquake prediction and volcanic hazard prediction offers considerable promise.

G. Keller
Cochairman
J. van Zijl
Cochairman
C. Clay
B. Sternberg
N. Harthill
D. Strangway
F. Dowling
C. Skokan
B. Lienert
R. Corwin

Research Recommendations For The Thermal State Of The Crust

It is the objective of research on the thermal state of the crust to define the thermal regime (steady state distribution of temperature and fluid pressure) and the thermal evolutionary processes which affect changes in the regime active in the crust.

Measurements of surface heat flow provide the best direct evidence for this evolution. The role of crustal radioactivity is known to be important; and the study of it requires that heat flow measurements and near-surface concentrations of radioactivity be determined simultaneously. The role of deep crustal heat production versus the mantle contribution is poorly understood (and needs to be studied).

Parametric Data

In order to quantify the thermal history of crustal rocks, it is necessary to obtain certain parametric data as defined by transport theory. These include thermal conductivity, heat capacities, coefficients of thermal expansion, compressibilities (of fluids in a water-salt system) and of rocks over temperatures from ambient to 1000°C and for pressures from 1 bar to 10 kbar, permeabilities of rocks over a scale of fracture distributions, and viscosity of salt-water systems.

The study of magmas requires a knowledge of all the above parameters except permeability. It also requires data in the viscoelastic and the plastic-brittle transition regions. Such data would then permit the analysis of hypothetical thermal regimes in the crust by a numerical simulation of transport processes. Improvements are required in the simulation of systems which exist for $10^4 - 10^6$ years and incorporate hundreds of cubic kilometers of crust.

Theory

The theory of heat transport must provide for an efficient and effective simulation of thermal energy transport processes operative in the crust and for the transport properties of various phases. Improvements needed in numerical simulation include more efficient solutions to the partial differential equations. Theoretical developments must be applied to real crustal environments.

Field Surveys

Heat flux from the crust provides a boundary condition required to interpret subsurface conditions. Surveys directed toward this object objective should measure thermal gradients, conductive and convective fluxes, in situ thermal conductivity, permeability (bulk rock and fracture controlled), and fluid compositions.

Hydrothermal Systems

The role of hydrothermal systems is particularly relevant to current problems in the use of geothermal energy, and therefore we suggest the following studies: (1) in situ measurements of temperature,

two-phase flow, permeability, fluid composition, host rock composition, mineral content, and characteristics of fluid inclusions, (2) surface measurements of heat flow, gravity, water fluxes and geochemical and electrical properties, (3) laboratory measurements of transport properties of fluids and rocks, (4) modeling that includes numerical simulation and scale models, and (5) measurements of the origin of heat from magma chambers, natural geothermal gradients, and radiogenic sources.

D. L. Turcotte
D. Norton

List of Participants

The following people participated in the symposium: J. K. Applegate, Boise State University; P. C. Badgley, Office of Naval Research; M. Batzle, Massachusetts Institute of Technology; M. Berry, Energy, Mines and Resources, Ottawa; H. Bezdek, Office of Naval Research; W. F. Brace, Massachusetts Institute of Technology; L. W. Braile, Purdue University; R. Buffler, University of Texas at Galveston; J. L. Carter, University of Texas at Dallas; P. Cheng, University of Hawaii; C. S. Clay, University of Wisconsin at Madison; R. Corwin, University of California at Berkeley; F. Dowling, Office of Naval Research; J. Eichelberger, Los Alamos Scientific Laboratory; M. Feves, Massachusetts Institute of Technology; and A. R. Green, Exxon Production Research Company.

Other participants were B. C. Haimson, University of Wisconsin at Madison; M. Harthill, Group Seven, Inc.; J. G. Heacock, Office of Naval Research; M. Holdaway, Southern Methodist University; R. M. Housley, Rockwell International Science Center; S. Jones, Chevron Oil Field Research Company; D. Jurdy, Princeton University; S. Kaufman, Cornell University; G. V. Keller, Colorado School of Mines; A. H. Lachenbruch, U. S. Geological Survey; M. Landisman, University of Texas at Dallas; B. Lienert, University of Texas at Dallas; M. Manghnani, University of Hawaii; B. J. Mitchell, Saint Louis University; W. Muehlberger, University of Texas at Austin; S. Mueller, Institut für Geophysik, Zurich; D. Norton, University of Arizona; J. Oliver, Cornell University; and J. Orcutt, Scripps Institution of Oceanography.

Completing the list of participants are E. Padovani, University of Texas at Dallas; R. Phinney, Princeton University; H. R. Pratt, Terra Tek; C. Prodehl, University of Karlsruhe, Karlsruhe; D. A. Richter, Massachusetts Institute of Technology; A. R. Sanford, New Mexico Tech; C. Skokan, Colorado School of Mines; J. Skokan, Gulf Minerals Resources Company; G. Simmons, Massachusetts Institute of Technology; S. B. Smithson, University of Wyoming; B. K. Sternberg, University of Wisconsin at Madison; D. Strangway, University of Toronto; G. Sutton, University of Hawaii; B. R. Tittmann, Rockwell International Science Center; D. L. Turcotte, Cornell University; J. S. van Zijl, National Physical Research Laboratory, Pretoria; H. Wang, University of Wisconsin at Madison; N. Warren, University of California at Los Angeles; and K. Westhusing, Energy Research and Development Administration.

SUBJ
GPHYS
IP
RFAI

**UNIVERSITY OF UTAH
RESEARCH INSTITUTE
EARTH SCIENCE LAB.**

Presented at
86th Northwest Mining Assoc.
Conv. – Dec 6 1980
Spokane, WA

RECENT AND FUTURE ADVANCES IN THE INDUCED POLARIZATION METHOD

BY

Philip G. Hallof, Ph.D., and William H. Pelton, Ph.D.

INTRODUCTION

The induced polarization (IP) method was introduced into Canadian exploration practice in the period from 1955 to 1960. Two measurement techniques were widely used, the pulse-transient method (time domain) and the variable frequency method (frequency domain). In the fifteen years following 1960, striking improvements were made in both frequency domain and time domain IP equipment, but only limited progress was made in a better understanding of the IP phenomenon, its source, and how to use it.

However, in the five year period since 1975, considerable progress has been made in our understanding of the IP method. Beginning with an understanding of the exact equivalence of the IP measurements in the phase-domain, the frequency-domain and the time-domain (see Figure 1), we have progressed to the study of the IP effect over the entire frequency range of interest. These studies have led to a greatly advanced understanding of the IP method in at least three important areas:-

i) Our understanding of the IP phenomenon itself has been vastly increased. A greater knowledge of the source of the IP effect and its detailed behavior has suggested additional uses for the method, beyond the simple detection of anomalies.

ii) A better idea of what we wanted to measure, and modern solid-state electronics, have resulted in greatly improved measurement techniques and instrumentation.

iii) The advent of smaller, less expensive digital computers has greatly helped with the interpretation of IP field data. Rapid forward problem solutions and the possibility of direct inversion of IP field data have made it possible for the geophysicists to give the exploration geologist a much better picture of just what the source of a particular IP anomaly might be.

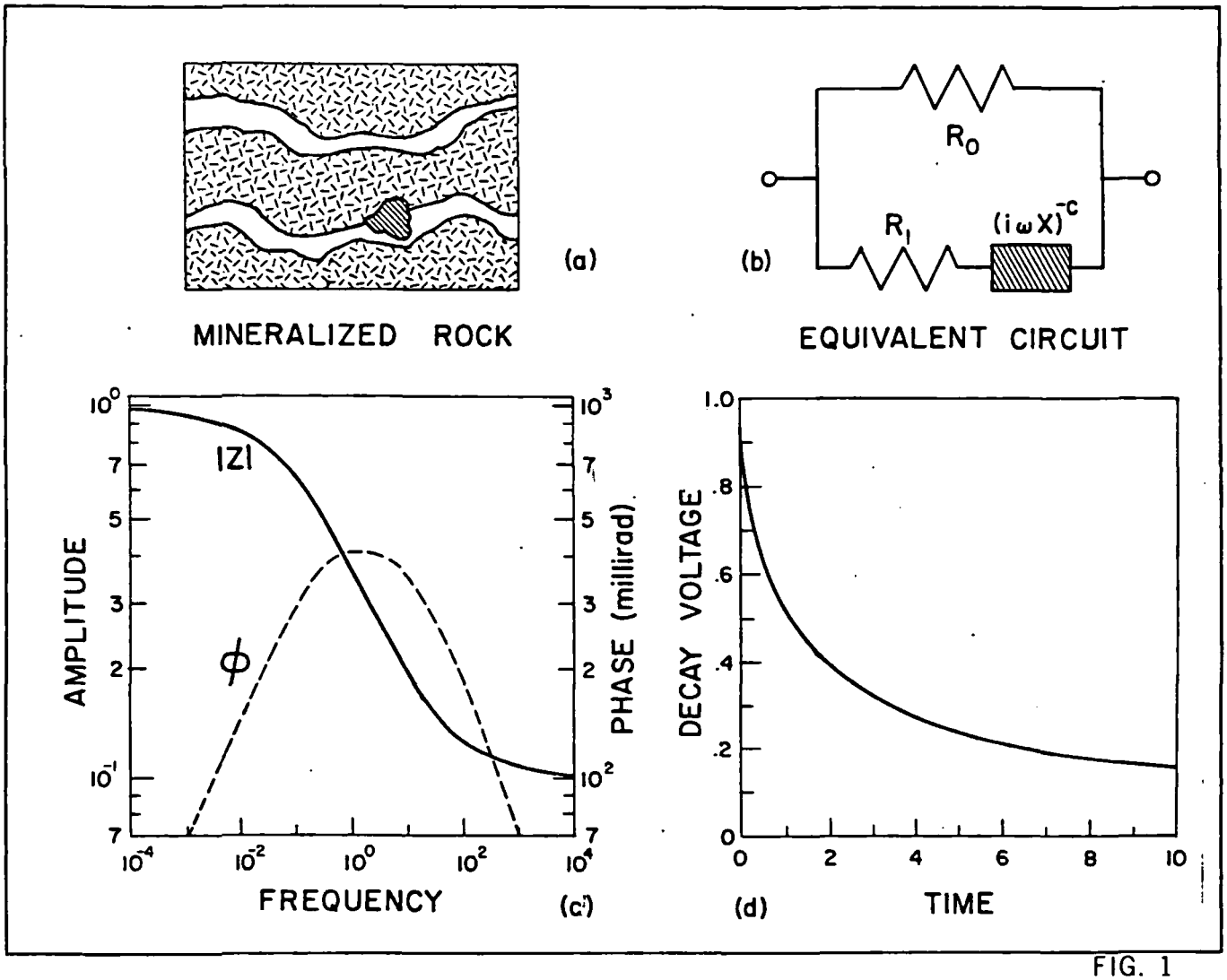

FIG. 1

WHAT IS THE NATURE OF THE IP EFFECT

Spectral induced polarization measurements (the measurement of the phase shifts over a wide frequency range) in open-pit mines, gave the first information concerning the detailed nature of the IP phenomenon. It became clear that four parameters, not just two (resistivity and IP

effect) were necessary to completely describe the IP effect.

The equation shown on Figure 2 and Figure 3 is formally known as the Cole-Cole Dispersion Equation; the four electrical parameters are:

Ro - the dc resistivity value

m - the IP effect (in non-dimensional form)

τ - the time constant of the IP effect

c - the exponent of the frequency (ω)

Since the very beginning of our experience with spectral IP measurements, we have found that these four parameters, and the Cole-Cole equation will adequately describe any IP effect that has been measured. The first measurements were made using one meter electrode intervals, within open-pit mines. The circles on Figure 4 and Figure 5 show the data points measured over massive graphite and massive sulphides at the Anvil Mine. As the solid line curves on the drawings show, the measured data points can be almost exactly replaced using a Cole-Cole Dispersion.

The four parameters obtained by the computer inversion of the graphite data are typical of those that have been measured over all graphite deposits. The IP effect is very large and the time constant (τ) is much greater than 1.0 seconds.

Large IP effects are also measured over massive sulphide sources. However, invariably the time constant value for (τ) is less than 1.0 seconds. The measurements shown on Figure 6 are for a massive sulphide source at the Kidd Creek Mine; again there is a large IP effect, and a small time constant.

The critical frequency (Fc) for a Cole-Cole Dispersion is defined as that frequency for which the maximum phase-shift is measured. An examination of the equation and curves in Figure 2 shows that as the time-constant (τ) is increased by a factor of ten, the critical frequency (Fc) will decrease by a factor of ten. Therefore, we can expect that for the spectral IP response of polarizable sources (Fc) will be inversely proportional to (τ).

An understanding of the physical parameters that affect the time-constant (τ) of a spectral IP response has come from two areas of research. One is the study of the spectral IP response from artificial rocks; these samples are prepared using metallic particles of known material and size (see Figure 8 for example). The second line of attack has been to formulate the mathematical expressions that might describe the macro-characteristics of conduction in a mineralized rock, with certain simplifying assumptions. Initially spherical particles were assumed for this work and an example of the predicted spectral results is shown on Figure 7.

We have shown these two different sets of data, because they are very similar in character. Further, they show the same result that all of

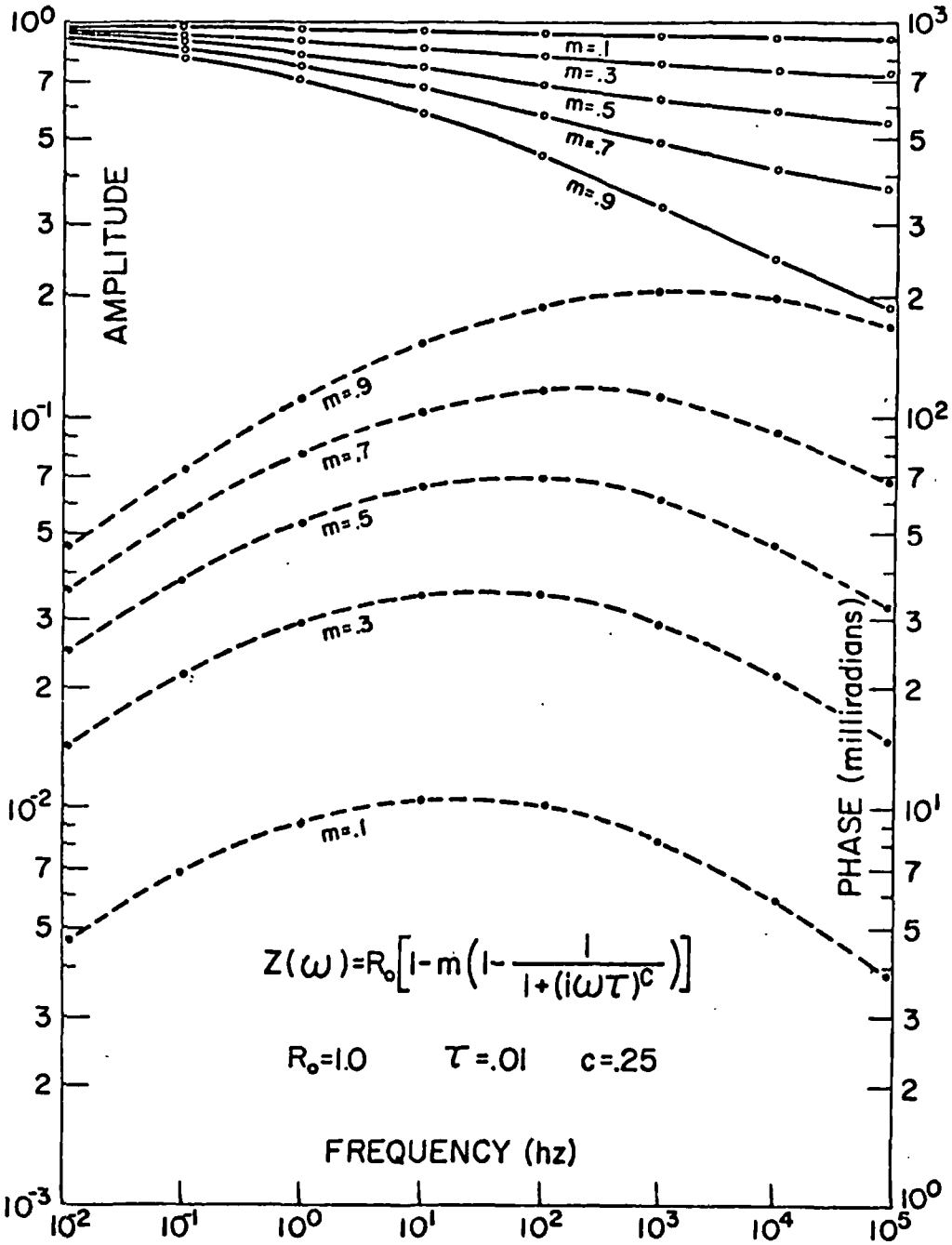
AMPLITUDE
PHASE (milliradians)
m=.1
m=.3
m=.5
m=.7
m=.9
m=.9
m=.7
m=.5
m=.3
m=.1
$Z(\omega)=R_o\left[1-m\left(1-\frac{1}{1+(i\omega\tau)^c}\right)\right]$
R_o=1.0 τ=.01 c=.25
FREQUENCY (hz)

FIG. 2

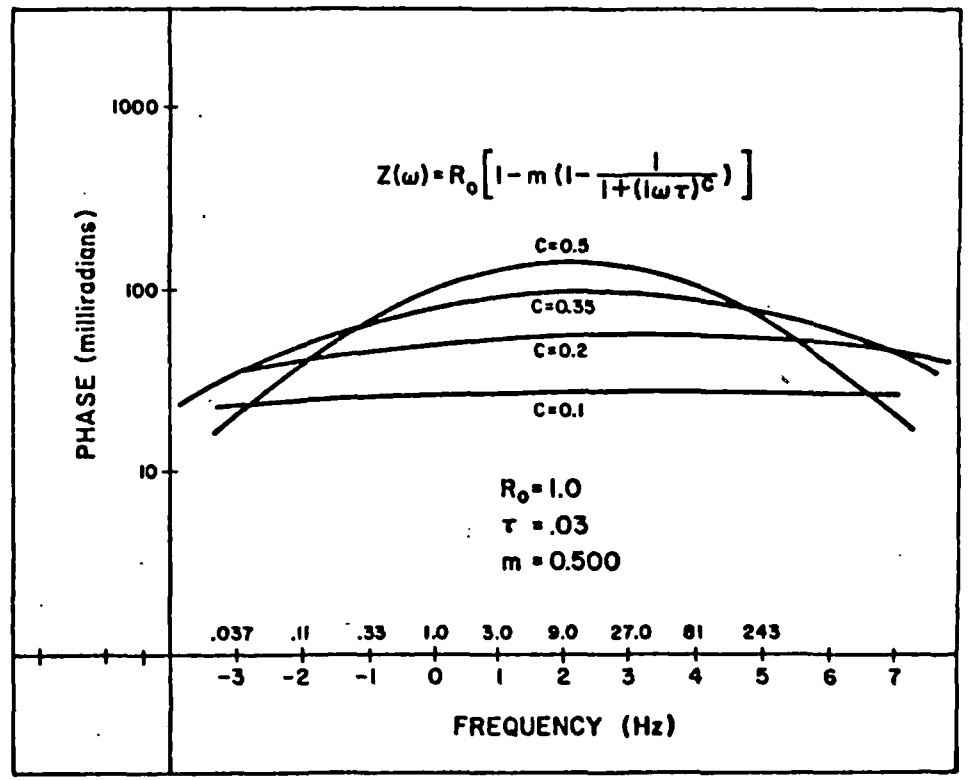
PHASE (milliradians)
$Z(\omega)=R_o\left[1-m\left(1-\frac{1}{1+(i\omega\tau)^c}\right)\right]$
C=0.5
C=0.35
C=0.2
C=0.1
R_o=1.0
τ=.03
m=0.500
.037 .11 .33 1.0 3.0 9.0 27.0 81 243
FREQUENCY (Hz)

FIG. 3

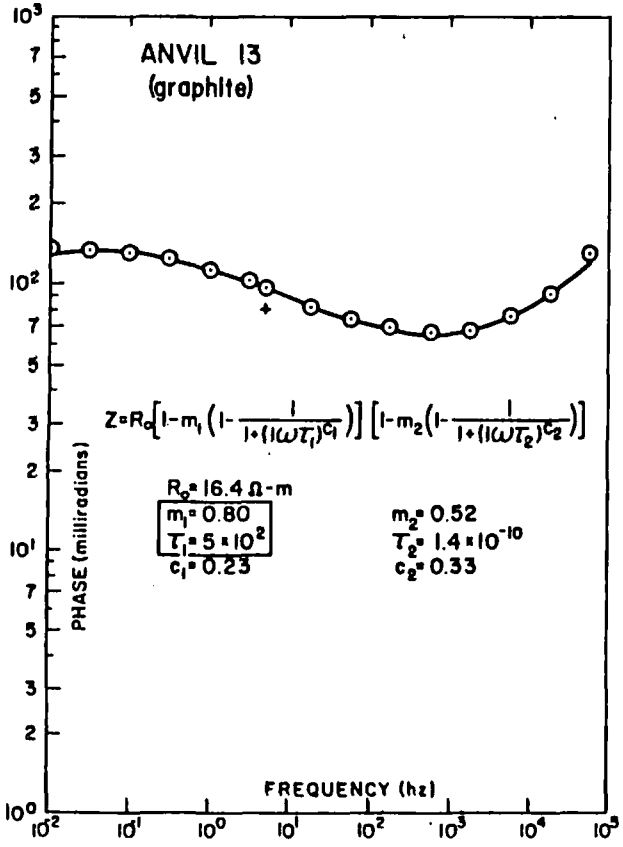

FIG. 4

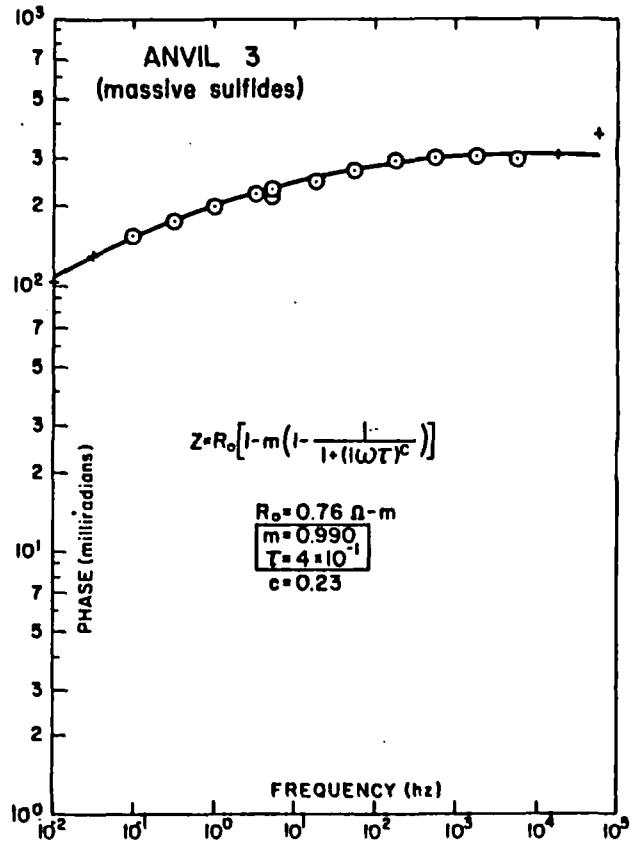

FIG. 5

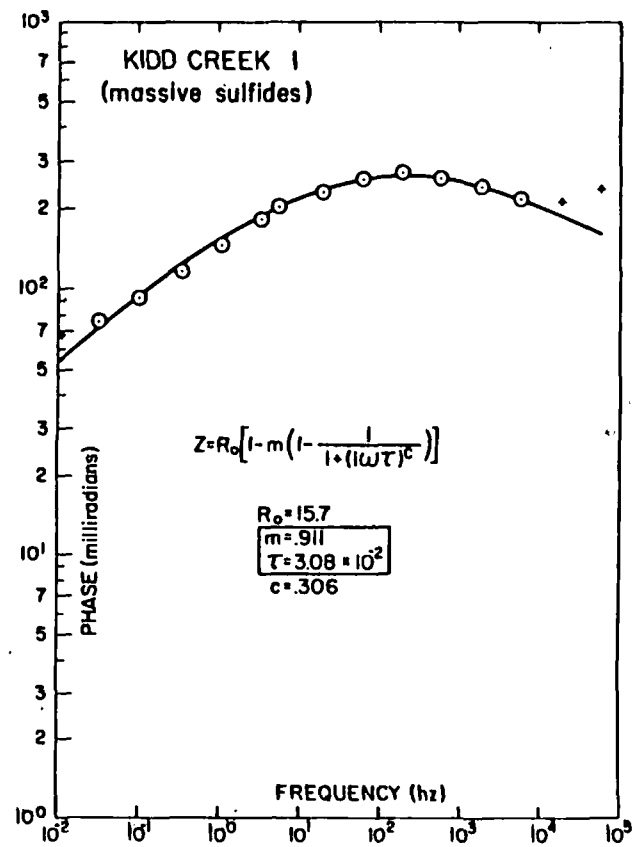

FIG. 6

THEORETICAL RESULTS FOR VARIATION IN GRAIN SIZE OF POLARIZABLE PARTICLE

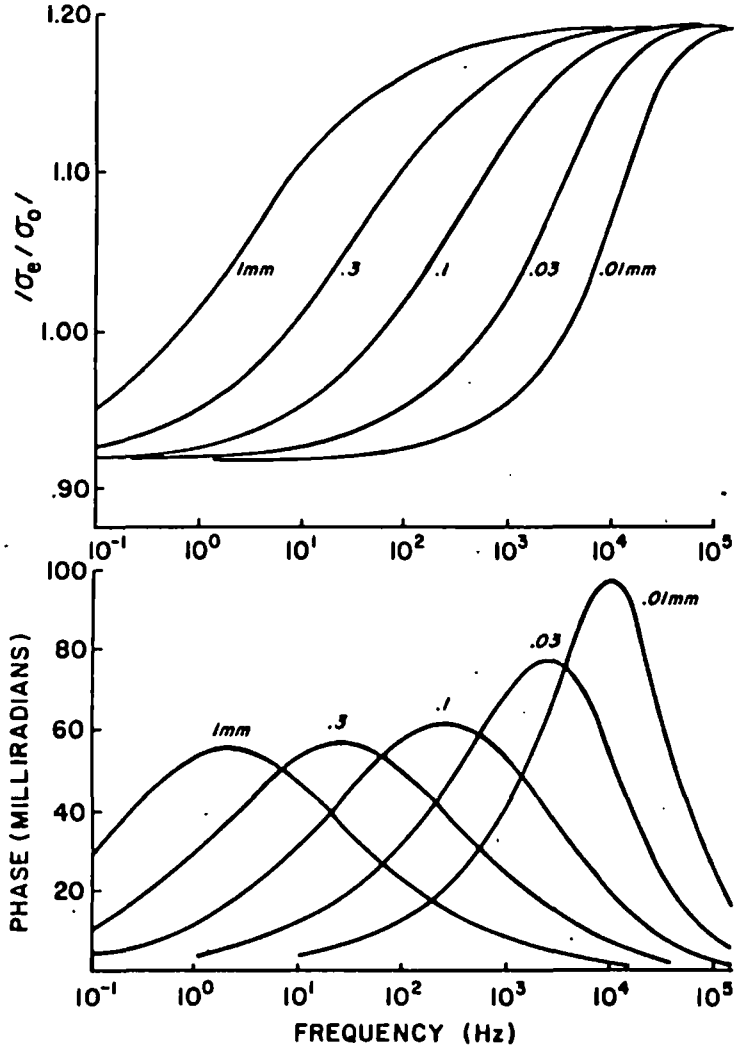

from Wong

FIG. 7

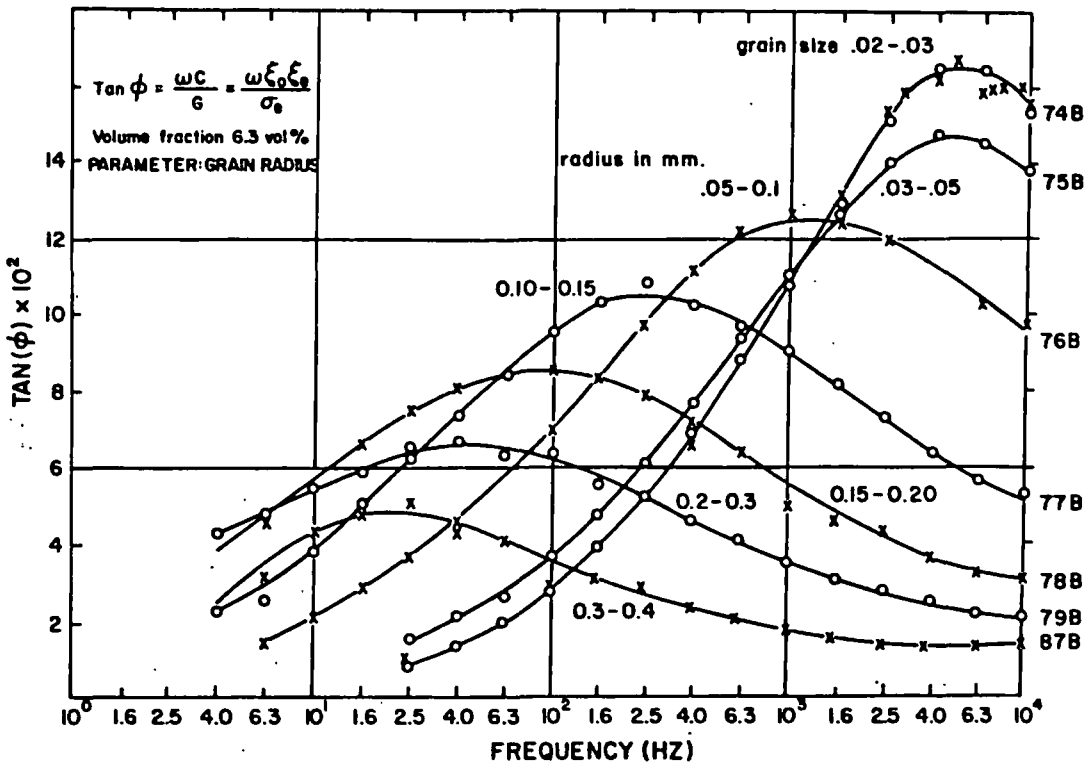

from Wong
data by Grissemann

FIG. 8

our research has shown. The time-constant (τ) of a spectral IP dispersion curve is directly related to the physical size of the metallic particles that are the source of the IP effect. The critical (Fc) is therefore inversely related to the grain-size. Thus, for all of the massive sulphide deposits for which we have spectral measurements, the effective grain-size of the polarizable particles is appreciably smaller than that for graphite sources.

There is one additional test we have devised to confirm the validity of the electrochemical model we have developed to describe the detailed nature of the IP phenomenon. The spectral IP results for a single mineral electrode (pyrite, chalcopyrite, bornite, galena, etc.) immersed in distilled water can be measured, and then inverted using the computer. This inversion determines the various electrical parameters that describe the electrical transfer function for that particular mineral. These electrical parameters, and the analytically determined concentrations of the metal cation in the solution after steady-state current flow has been achieved, can be used to calculate the reaction valence (total number of electrons involved) of the chemical reaction at the interface. This measured value of the reaction valence can be compared to the various values that would be possible from various chemical reactions.

In past research, these measured numbers have not agreed within an order of magnitude with those predicted by the commonly accepted dissolution reaction equations for the various sulphide minerals. The results we have achieved for galena (Figure 10) and chalcopyrite (Figure 9) are typical of the work that has been done recently. The measured values of the reaction valence give much closer agreement to the predicted valence than was previously the case. For chalcopyrite, the predicted reaction varies with the copper ion concentration, and the agreement is still quite acceptable.

With the success of the above described research, has come the implication that we may now understand the IP phenomenon well enough to use some of our knowledge in a predictive way. The resistivity and phase-shift data plotted in the pseudo-section format on Figure 11 are from the Kennedy Property near Winnemucca, Nevada. The results suggest a broad, weak IP anomaly that might be due to a "porphyry copper" type source containing a small concentration of metallic mineralization. However, one notices immediately that the phase-shifts measured at 9.0 Hz are the same magnitude as those measured at 0.11 Hz (a factor of 3^{-4} lower in frequency). This is the same Spectral IP characteristic that was previously measured at the Brenda Mine in British Columbia.

This unusual circumstance is confirmed by the spectral plots for two typical dipole pairs, shown in Figure 12 and Figure 13. With the inductive coupling effects removed by computer inversion, the phase-shift vs. frequency curve is very flat over a frequency range of 3^{8}Hz. This requires a very low (c_1) value of 0.125 (see Figure 3); more importantly, a value of IP effect (m) in excess of 0.500 is necessary. Therefore, although the measured phase-shifts are low in magnitude, the true IP effect within the source material must be large. This should not be considered to be a weak anomaly.

CHALCOPYRITE

$[CuSO_4]$ 0	10^{-5}	10^{-4}	10^{-3}	Reaction Valence
4.6				
3.5	1.5	.95	.53	Measured
3.6				
4.0	1.33	1.33		Actual

$$CuFeS_2 \longleftrightarrow Cu^{2+} + Fe^{2+} + 2S + 4e^-$$

$$\frac{2}{3}\,CuFeS_2 + Cu^{2+} + \frac{4}{3}e^- \longleftrightarrow \frac{1}{3}\,Cu_5FeS_4 + \frac{1}{3}\,Fe^{2+}$$

(Wadsworth, 1980)

FIG. 9

GALENA

[NaCl] 0.10	Reaction Valence
1.6	Measured
1.6	
2.0	Actual

$$PbS \longleftrightarrow Pb^{2+} + S^0 + 2e^-$$

(Sato, 1960)

FIG. 10

W A BOWES KENNEDY AREA WINNEMUCCA NEVADA X=200 JUNE 197

Apparent Resistivity(ohm-m)

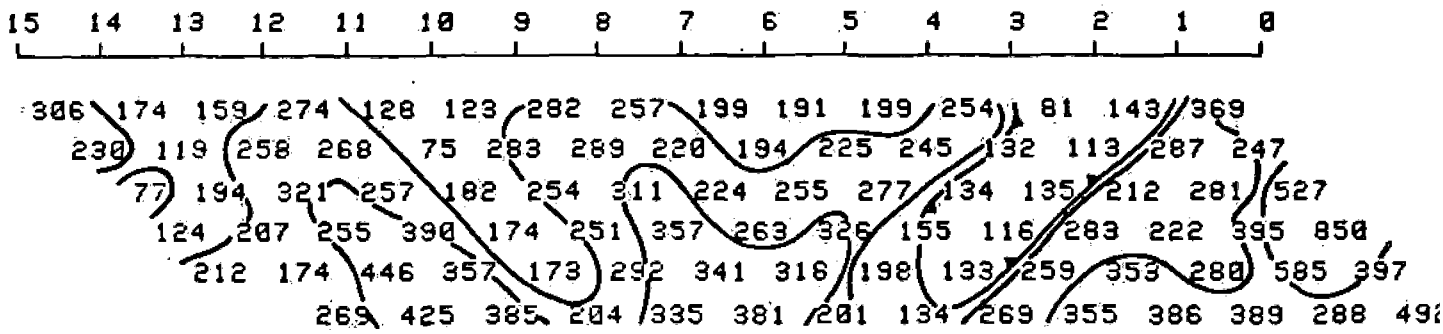

Decoupled Phase(mrad) 9 Hz

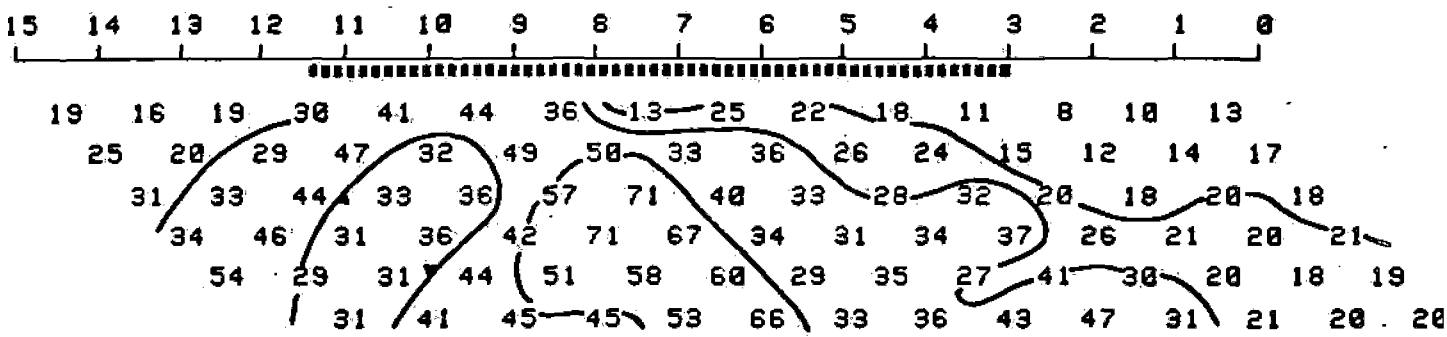

Decoupled Phase(mrad) .1111 Hz

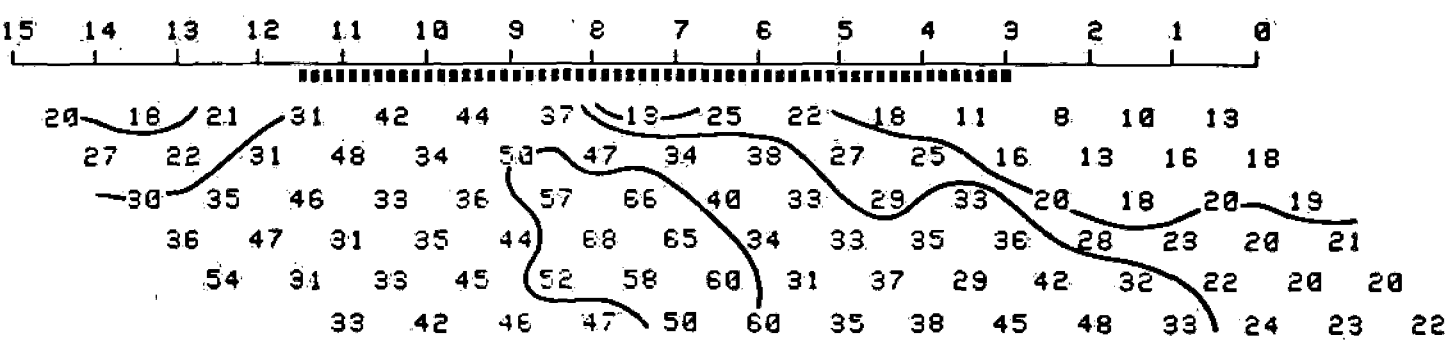

FIG. 11

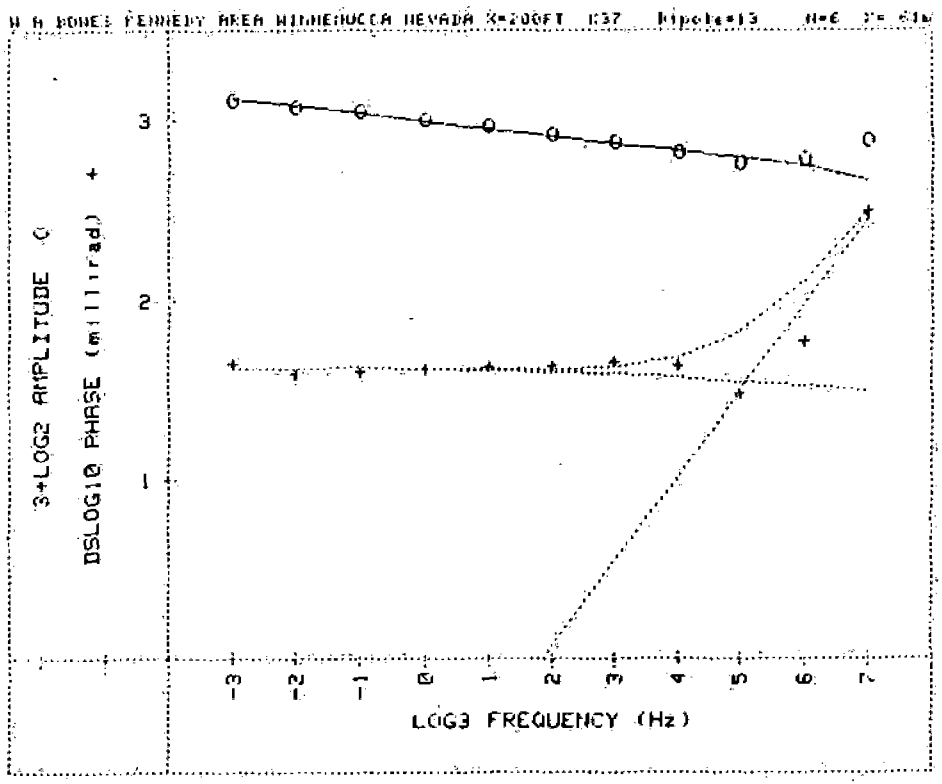

Iter	Lambda	Rchsq	R0	M1	T1	C1	M2	T2	C2
0	1.E-02	.00068	1.599	.587	2.0E+01	.125	1.000	2.0E-05	.992
1	1.E-01	.00064	1.599	.586	2.0E+01	.125	1.000	2.1E-05	1.000
2	1.E+00	.00063	1.596	.584	2.0E+01	.125	1.000	2.1E-05	1.000
3	1.E+00	.00063	1.595	.583	2.0E+01	.125	1.000	2.1E-05	1.000

Pct Std Deviations 5.4 1.6 499.4 0.0 0.0 10.5 9.8

Correlation Matrix

1.0000							
.5235	1.0000						
.9782	.3667	1.0000					
0.0000	0.0000	0.0000	0.0000				
0.0000	0.0000	0.0000	0.0000	0.0000			
-.3604	.0864	-.3990	0.0000	0.0000	1.0000		
-.6447	.0924	-.7125	0.0000	0.0000	.7305	1.0000	

Apparent Resistivity Measured at 1 Hz is 425

Apparent Resistivity Calculated from Inductive Coupling is 2117

FIG. 12

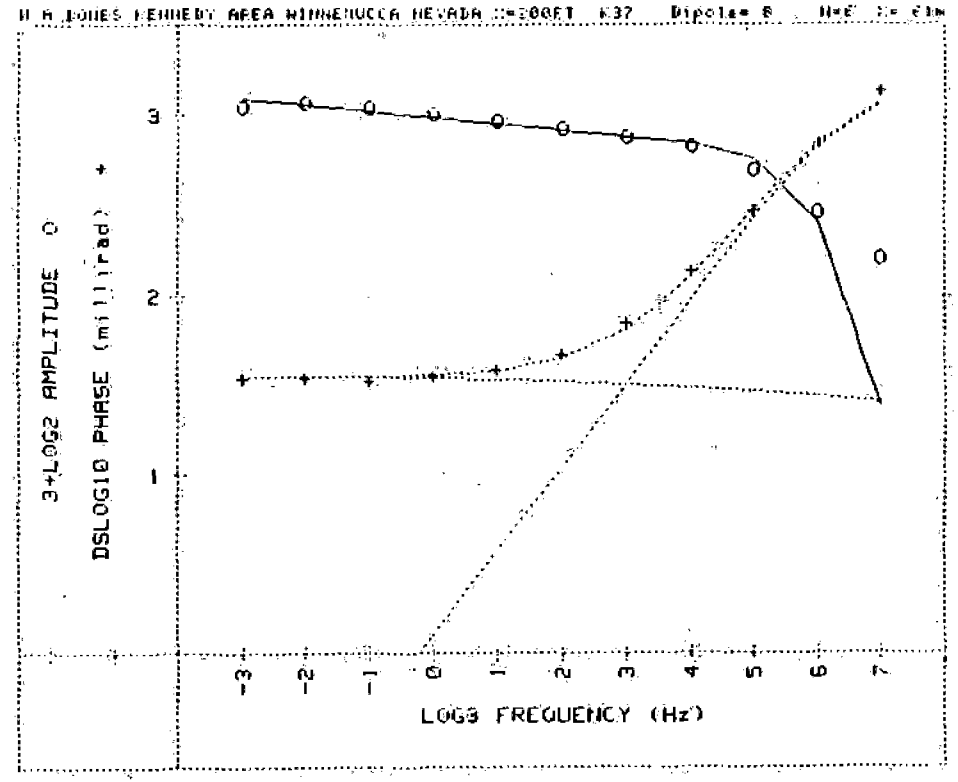

Iter	Lambda	Rchsq	R0	M1	T1	C1	M2	T2	C2
0	1.E-02	.00182	1.482	.517	2.0E+01	.125	1.000	1.8E-04	.977
1	1.E-02	.00182	1.481	.518	1.9E+01	.125	1.000	1.8E-04	.978

Pct Std Deviations 6.7 2.6 1243.0 0.0 0.0 5.4 2.8

Correlation Matrix

1.0000						
.6234	1.0000					
.9780	.4657	1.0000				
0.0000	0.0000	0.0000	0.0000			
0.0000	0.0000	0.0000	0.0000	0.0000		
.1969	.0726	.2067	0.0000	0.0000	1.0000	
-.4224	.0470	-.4586	0.0000	0.0000	.4189	1.0000

Apparent Resistivity Measured at 1 Hz is 201

Apparent Resistivity Calculated from Inductive Coupling is 235

FIG. 13

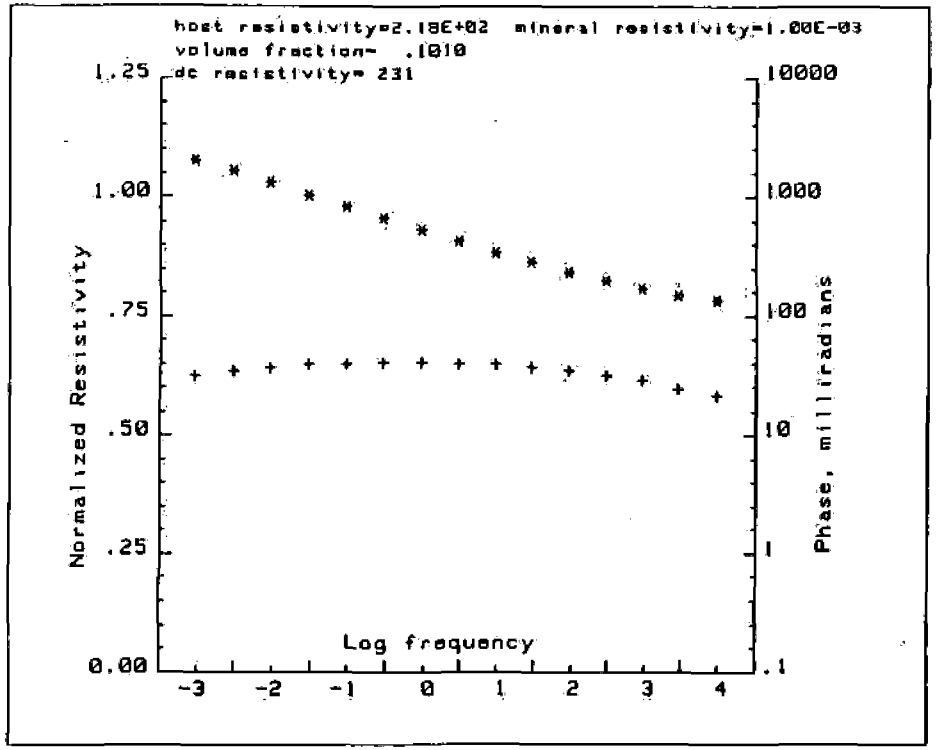
host resistivity=2.18E+02 mineral resistivity=1.00E-03
volume fraction= .1010
dc resistivity= 231
Normalized Resistivity
Phase, milliradians
Log frequency
1.25
1.00
.75
.50
.25
0.00
10000
1000
100
10
1
.1
-3
-2
-1
0
1
2
3
4

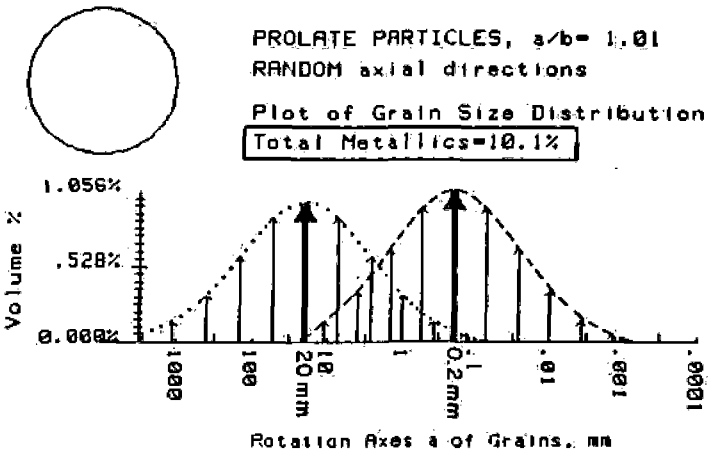
PROLATE PARTICLES, a/b= 1.01
RANDOM axial directions
Plot of Grain Size Distribution
Total Metallics=10.1%
Volume %
1.056%
.528%
0.000%
1000
100
20mm
10
1
0.2mm
.1
.01
.001
.0001
Rotation Axes a of Grains, mm

FIG. 14

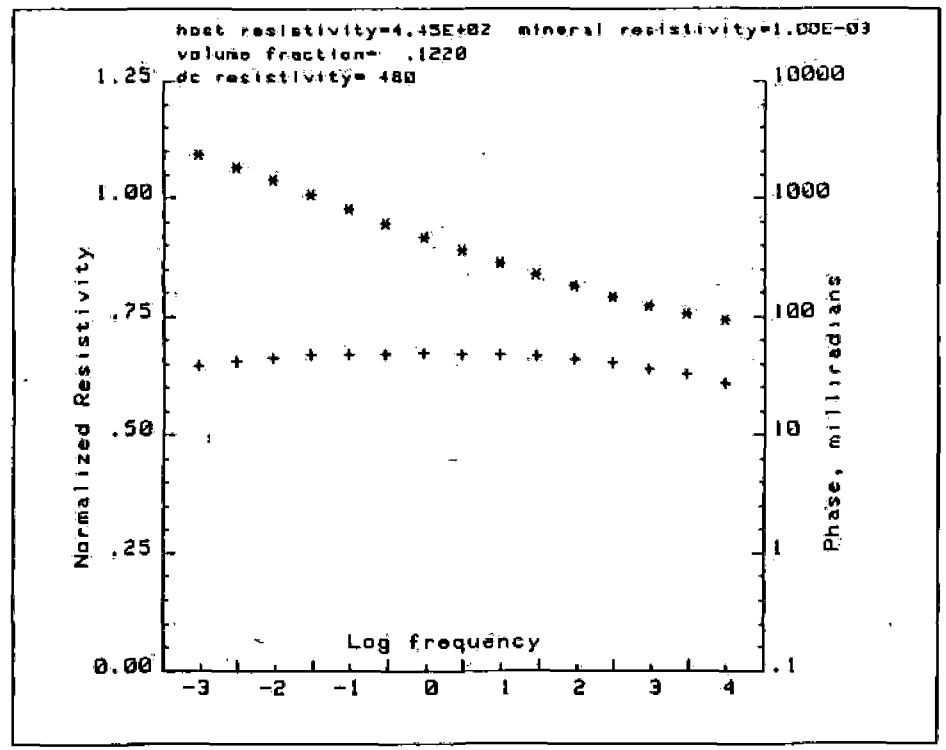
host resistivity=4.45E+02 mineral resistivity=1.00E-03
volume fraction= .1220
dc resistivity= 480
Normalized Resistivity
Phase, milliradians
Log frequency
1.25
1.00
.75
.50
.25
0.00
10000
1000
100
10
1
.1
-3
-2
-1
0
1
2
3
4

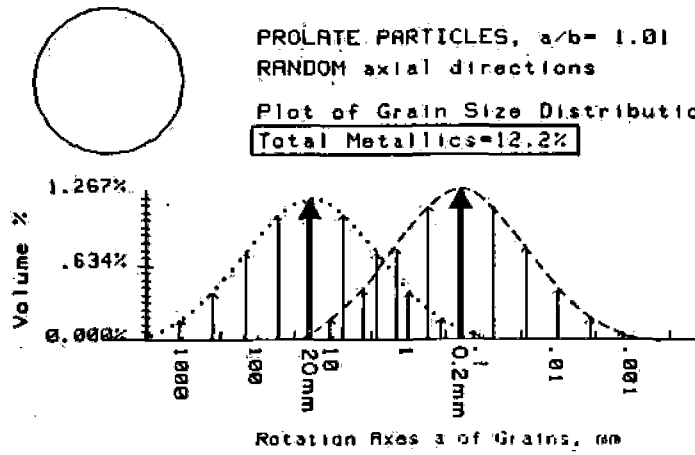
PROLATE PARTICLES, a/b= 1.01
RANDOM axial directions
Plot of Grain Size Distribution
Total Metallics=12.2%
Volume %
1.267%
.634%
0.000%
1000
100
20mm
10
1
0.2mm
.1
.01
.001
.0001
Rotation Axes a of Grains, mm

FIG. 15

We used these results in our first attempt to predict the nature of the mineralization that is the source of the "weak" anomaly shown in Figure 11. The mathematical formula used to predict the spectra shown in Figure 7 has been expanded to include prolate and oblate spheroids, as well as spheres, of metallic material. By a trial and error process, the spectra shown in Figure 14 and Figure 15 were generated as being a "good fit" to the measured data.

The chosen parameters for the sources are probably not unique; however, some valid points can be drawn from the calculation presented.

i) the flat-spectrum (small c value) cannot be obtained from a single grain-size (time-constant) population. There must be at least two different grain-size populations present.

ii) Although the two grain-size distributions, with mean values of 20mm and 0.2mm, are probably not exactly correct, a difference of at least two orders of magnitude is necessary to produce the value c = 0.125.

iii) Despite the low magnitude for the IP field anomaly, the true IP effect within the source is large ($m_1 > 0.500$) and this results in a fairly high concentration of metallic mineralization predicted for the source (10 - 12% total metallic mineralization).

The first drill hole at the Kennedy Project is now nearing completion; it was collared at approximately station No. 5 along the line of data shown in Figure 11. There was metallic mineralization throughout the drill hole, with an increase below about 75-80 meters of depth.

Throughout the entire length of the drill hole (in excess of 250 meters), there were two different types of mineralization present. There were veinlets (large grain-size) that might, or might not, contain quartz. All of the veinlets contained chalcopyrite or molybdenite or chalcopyrite with molybdenite; some pyrite was also present. There was also fine-grained disseminated metallic magnetite throughout the hole (the small grain-sized source). The magnetite contains appreciable gold value; there is enough gold present to give detectable assays throughout the length of the hole.

We do not have enough information to determine if the total-concentration of metallic mineralization approaches 10 to 12 percent. However, in other respects the source of the IP anomaly does seem to approximate that predicted by the spectral IP analysis.

IMPROVED MEASUREMENT TECHNIQUES AND INSTRUMENTATION

The much publicized "explosion" in solid-state, semi-conductor

electronic components has produced as many changes in the geophysical instrumentation industry as it has in other phases of modern life. Beginning with diodes and transistors and now including complex microprocessor chips, there has been a bewildering number of improvements in this industry. They have resulted in a major reduction in the size of, and the power requirements of (smaller battery packs), geophysical field instruments; at the same time the reliability, digital data storage capability and analysis capability have been almost infinitely increased.

The Phoenix IPV-2, Prospecting Phase IP system is an example of one of the least complicated units that can be engineered with modern electronics. The types of features that can now be made available are:

i) Microprocessor-controlled signal stacking of each measurement to give almost infinite noise rejection through coherent detection.

ii) Matched, heated crystal clocks give phase stability between current source and voltmeter without connecting cable.

iii) Dual-channel electronics permits two separate voltages to be measured simultaneously.

iv) Digital readout of magnitude and phase-shift of measured voltage at either channel.

v) Five frequency capability (0.11, 0.33, 1.0, 3.0, 9.0 Hz) permits limited analysis of spectral character of any anomaly.

vi) Appreciable increase in survey speed over either frequency-domain or time-domain IP systems.

By completing a reconnaissance survey with a single frequency (typically 0.33 Hz or 1.0 Hz) it is possible to achieve the lowest cost possible for IP field surveys. However, once an anomaly is detected, the IPV-2 can be used to make detailed measurements that give some feeling for the character of the spectral response of the source.

If detailed measurements are made at only two frequencies, it is possible to make some statement about the critical frequency (Fc) of the IP spectrum from the source. On Figure 17 and Figure 18 are shown the detailed phase-IP measurements made using X = 100' and 0.33 Hz over two anomalies previously located by a reconnaissance IP survey using larger electrode intervals. On both Line 18E and Line 15E the anomalous pattern indicates a relatively narrow source, with some depth to the top.

During the detailed survey with X = 100', several of the anomalous values in each anomalous pattern were measured at both 0.33 Hz and 3.0 Hz.

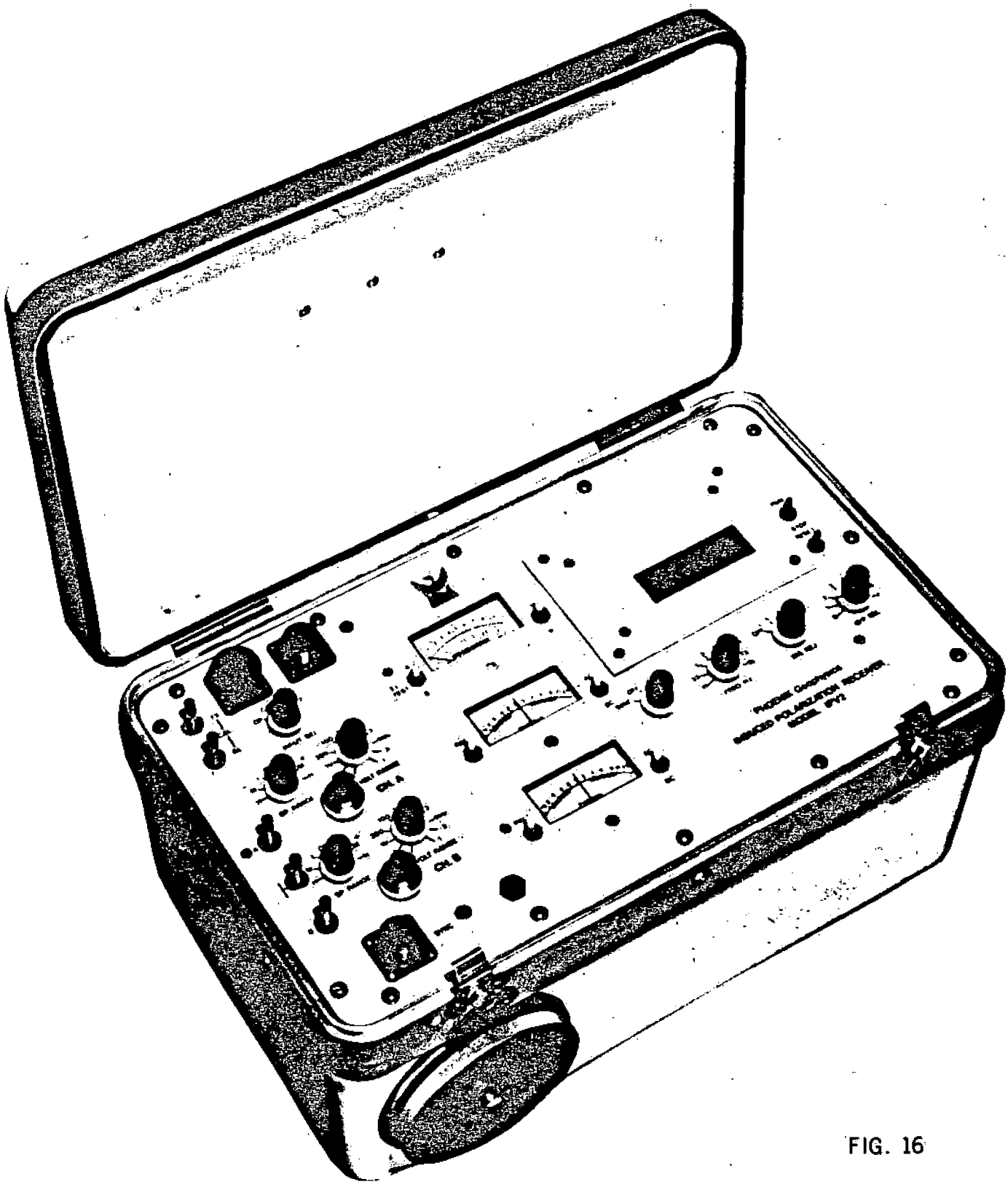

FIG. 16

PRICE COMPANY BLOCK NO.8 PROPERTY
IPV-2 PHASE IP TEST

LINE-18E

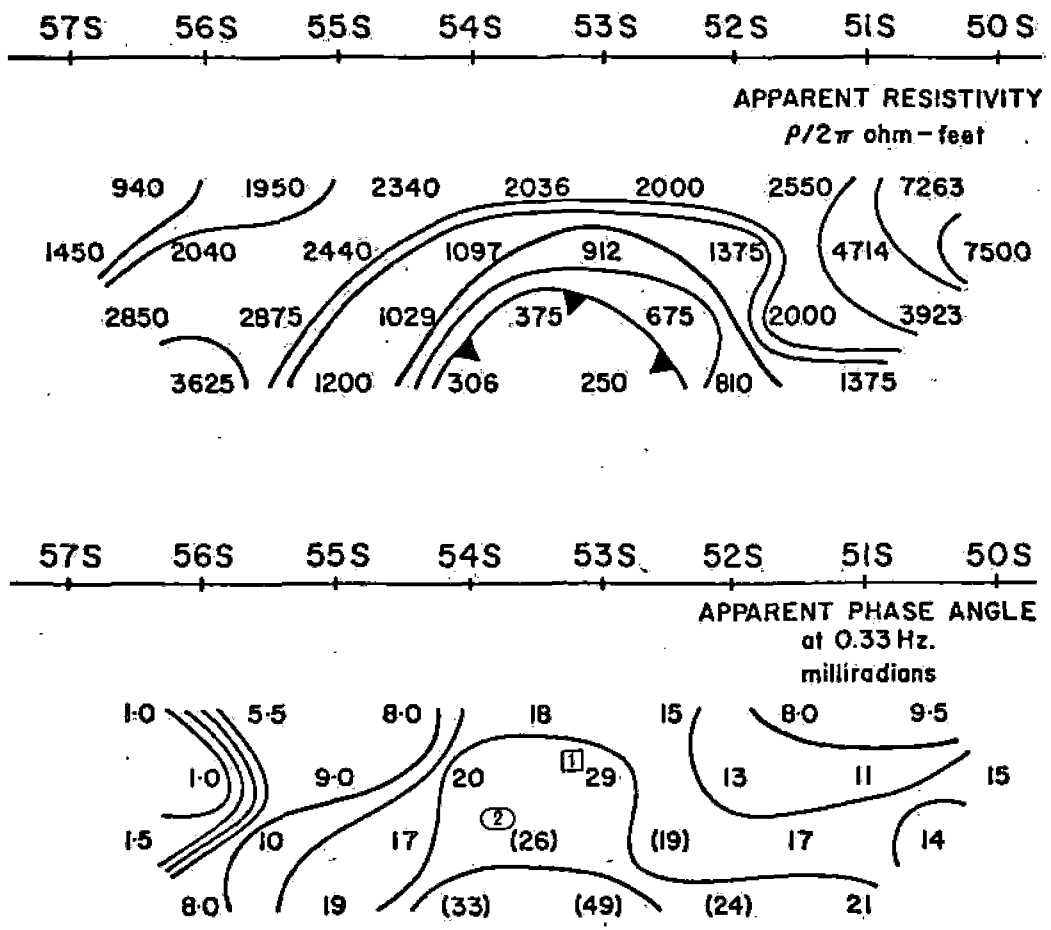

FIG. 17

PRICE COMPANY BLOCK NO.8 PROPERTY
IPV-2 PHASE IP TEST

LINE-15E

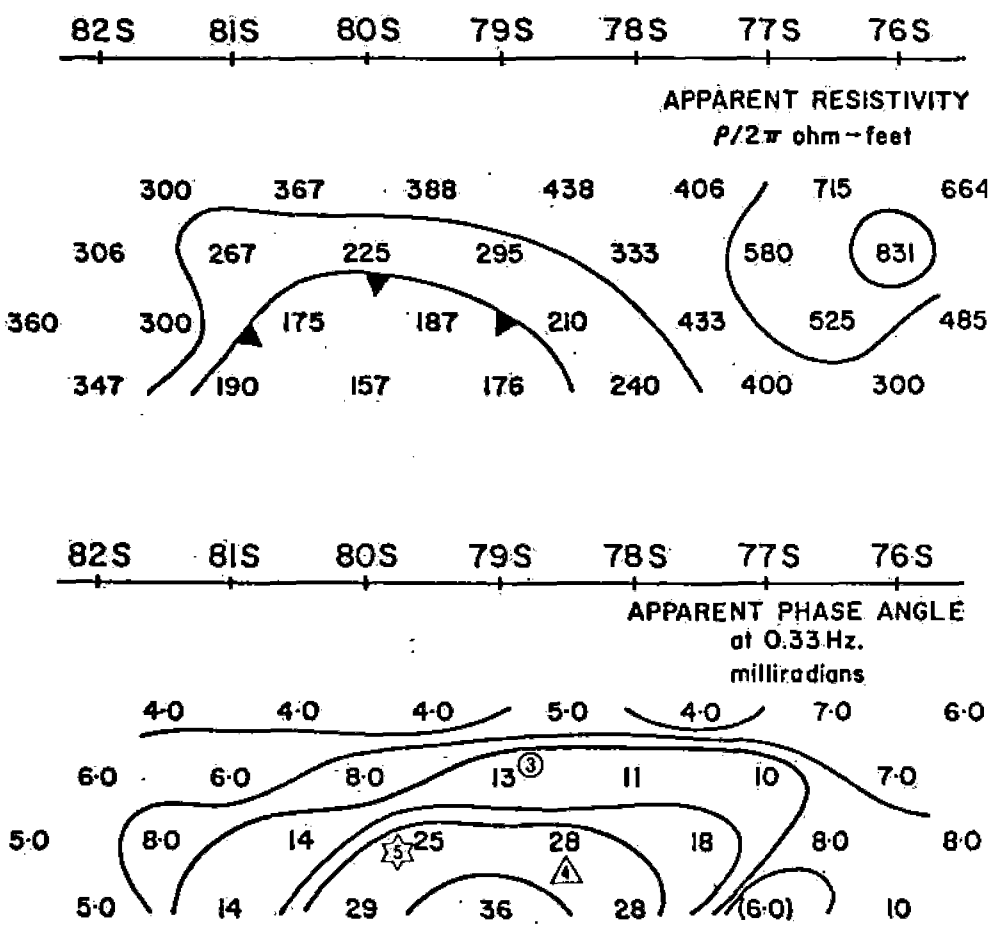

FIG. 18

The results are shown on Figure 19 and Figure 20. On Line 18E, the apparent phase values measured increase with frequency, indicating a value for Fc above 3.0 Hz. On Line 15E the apparent phase values were decreasing with frequency, indicating a value for Fc that is below 0.33 Hz.

The relationship we have established between the critical frequency (Fc) - the time constant (τ) - and the grain-size of the polarizable particles, coupled with our experience over known zones suggests that the grain-size of the source of the anomaly on Line 18E is appreciably smaller than the grain-size of the source of the anomaly on Line 15E.

Our expectation that the large grain-size source is more likely to be graphite is confirmed by the drilling of the two anomalies. The anomaly on Line 18E was found to be due to massive sulphide mineralization; the source of the anomaly located on Line 15E was a graphitic tuff zone, with small concentrations of pyrite.

If field time is taken to make measurements at all five frequencies, it is possible to make a more formal presentation of the spectral characteristics of two anomalies. On Figure 21, is shown a computer-plotted pseudo-section of a single line of phase IP data. The plot shows the apparent resistivity value and the apparent phase value (1.0 Hz) measured for each dipole pair. At the lower part of the data plot is shown the short (five frequency) spectrum (normalized to the value at 1.0 Hz) for each dipole pair.

In this case, the two anomalous zones had a considerable strike length, in an area where the surface was largely covered. The electrical parameters of the two sources were much the same; however, as shown on Figure 21, the source of Zone I is clearly different from the source of Zone II. From drilling, it is known that Zone I is due to a broad, irregular zone of pyrite and sphalerite (with appreciable silver) in a tuffaceous rock unit. The source of Zone II is pyrrhotite in an adjoining andesite rock unit.

Another example of a difference in spectral character is shown in Figure 22. In this location, the source of Zone A had been traced for a considerable distance along strike. Zone B was detected only on two adjacent lines. The difference in spectral character strongly suggests that Zone B is not merely a greater width to the mineralized zone that is the source of Zone A.

The Phoenix IPV-3, Spectral IP Receiver is the most advanced induced polarization receiver ever put into field operation (Figure 23). It completely replaces a truck-mounted system that was assembled largely from off-the-shelf computers, voltmeters, oscilloscopes, etc. The entire system is controlled by the Phoenix CP-1, geophysical computer, that was designed especially for this function. Through an FM-modulated link, the CP-1 also controls the spectral IP current source. Some of the more important features of the IPV-3 are:

i) Six simultaneous voltage channels plus current monitor.

LINE-18E $R\Phi_{0.3-3.0}$ TEST

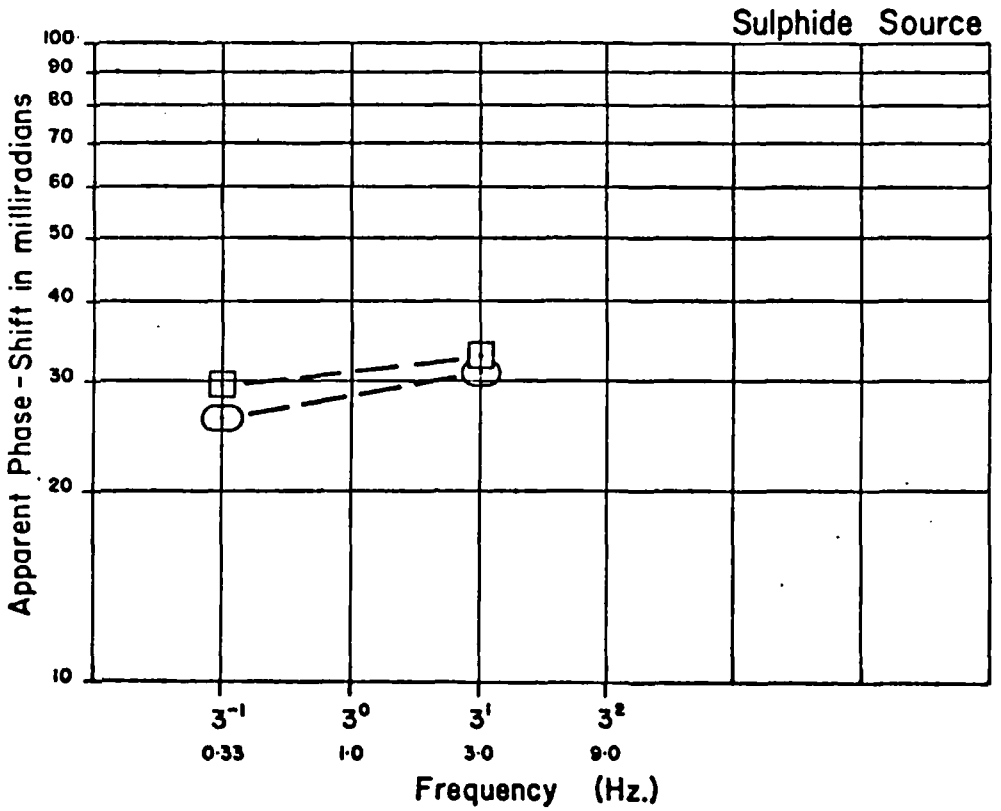

FIG. 19

LINE-15E $R\Phi_{0.3-3.0}$ TEST

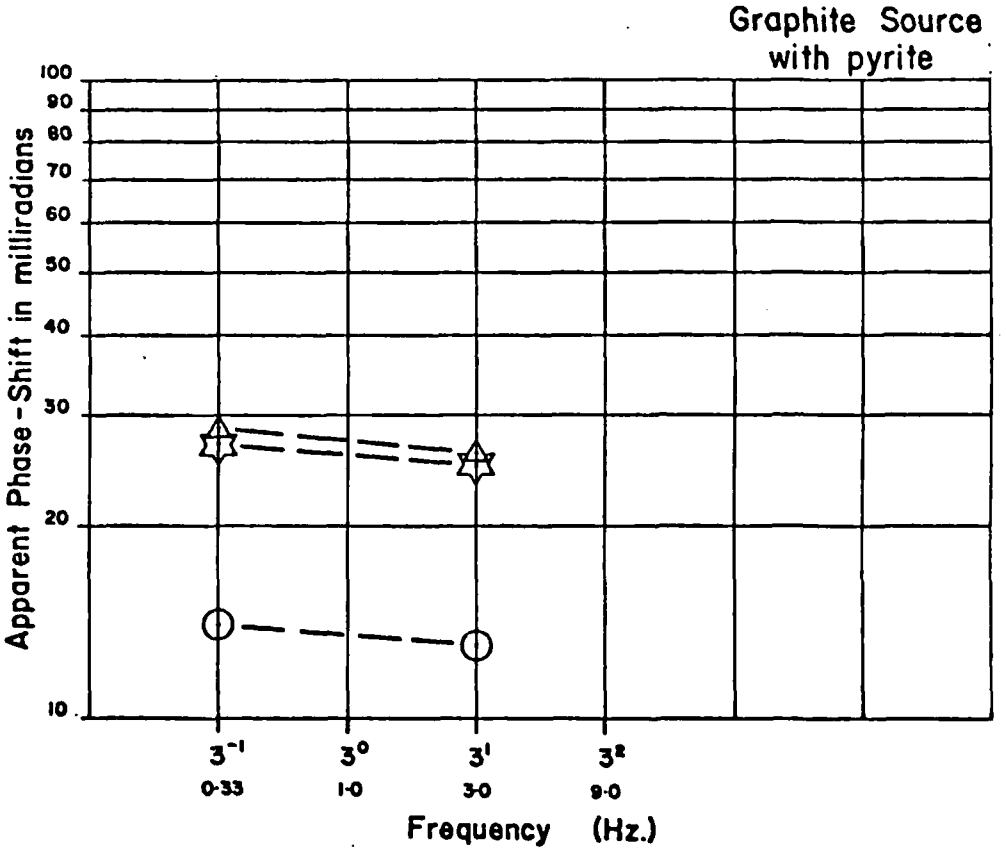

FIG. 20

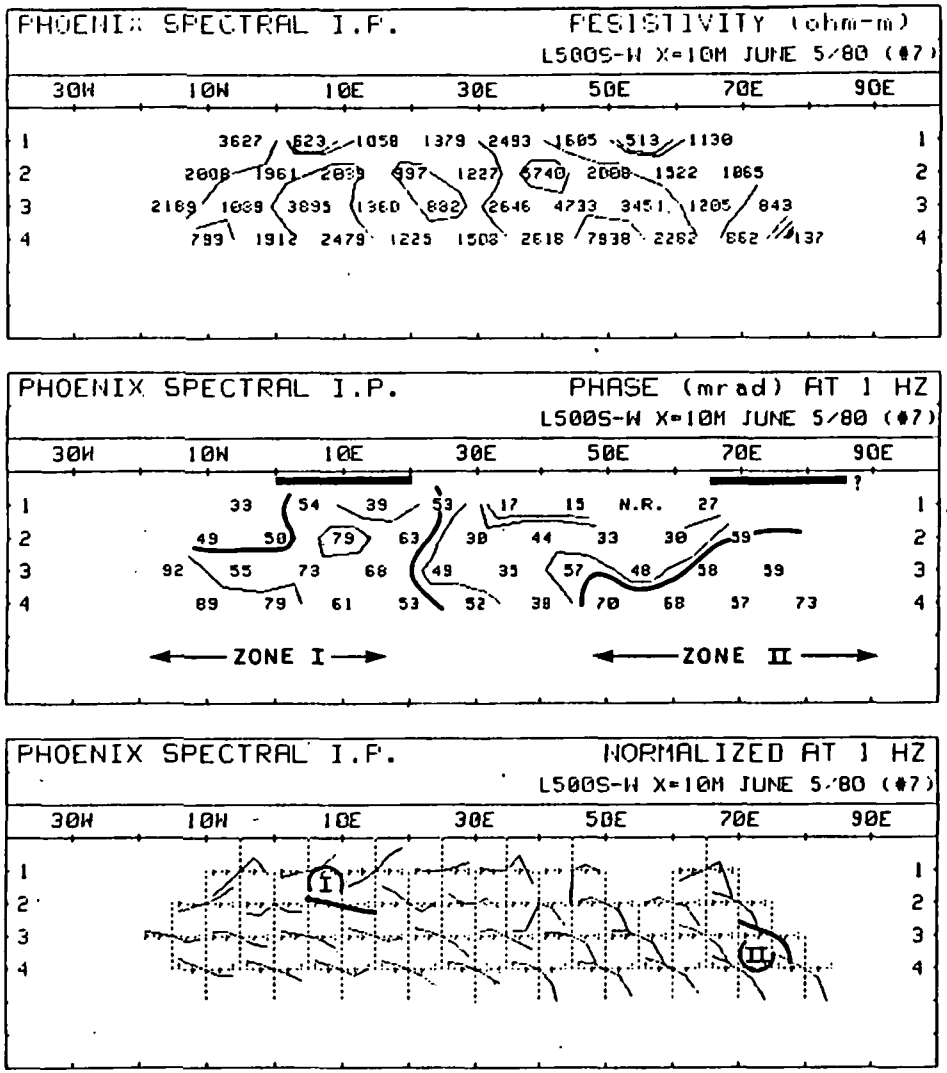
PHOENIX SPECTRAL I.P.
RESISTIVITY (ohm-m)
L500S-W X=10M JUNE 5/80 (#7)
30W 10W 10E 30E 50E 70E 90E
PHOENIX SPECTRAL I.P.
PHASE (mrad) AT 1 HZ
L500S-W X=10M JUNE 5/80 (#7)
30W 10W 10E 30E 50E 70E 90E
ZONE I
ZONE II
PHOENIX SPECTRAL I.P.
NORMALIZED AT 1 HZ
L500S-W X=10M JUNE 5/80 (#7)
30W 10W 10E 30E 50E 70E 90E
I
II

FIG. 21

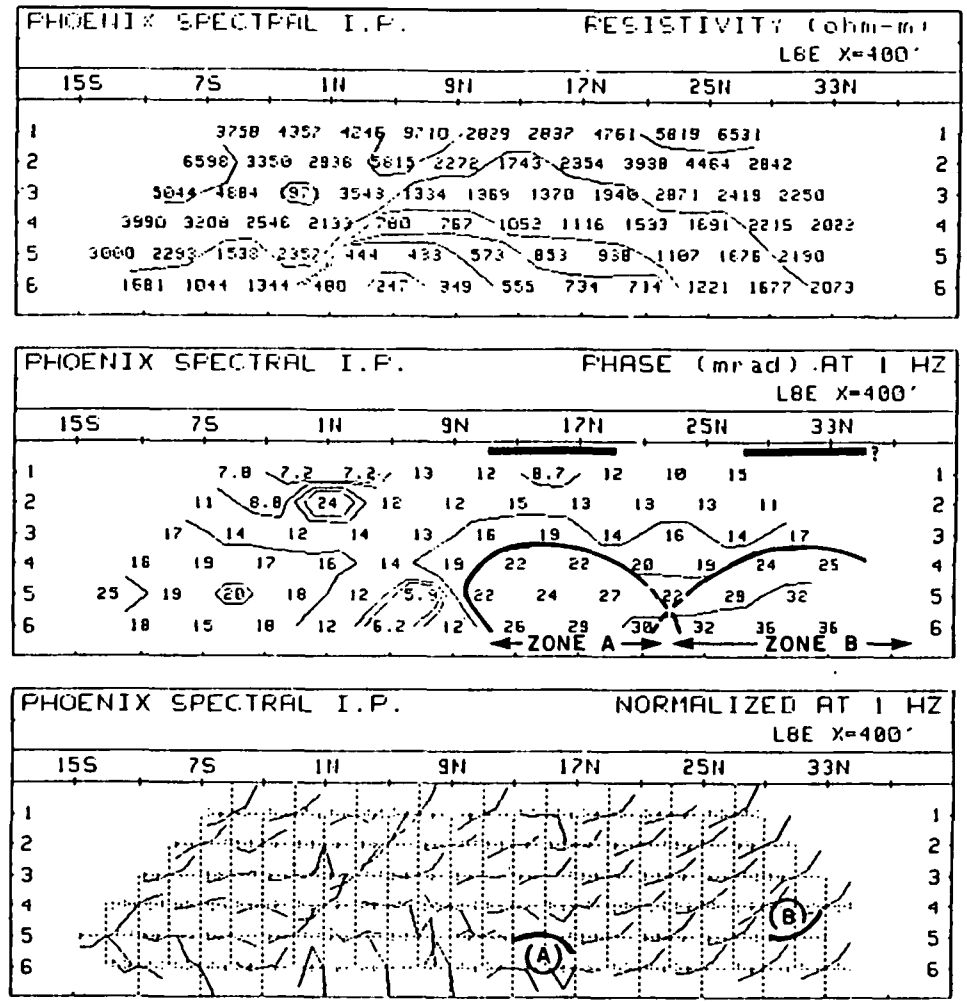
PHOENIX SPECTRAL I.P.
RESISTIVITY (ohm-m)
L8E X=400'
15S 7S 1N 9N 17N 25N 33N
PHOENIX SPECTRAL I.P.
PHASE (mrad) AT 1 HZ
L8E X=400'
15S 7S 1N 9N 17N 25N 33N
ZONE A
ZONE B
PHOENIX SPECTRAL I.P.
NORMALIZED AT 1 HZ
L8E X=400'
15S 7S 1N 9N 17N 25N 33N
A
B

FIG. 22

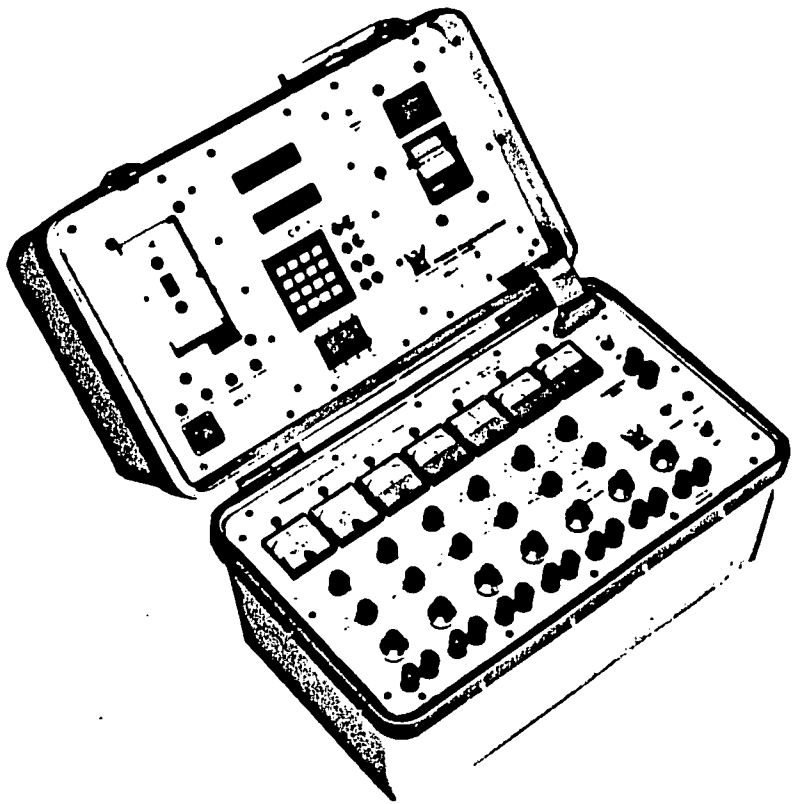

FIG. 23

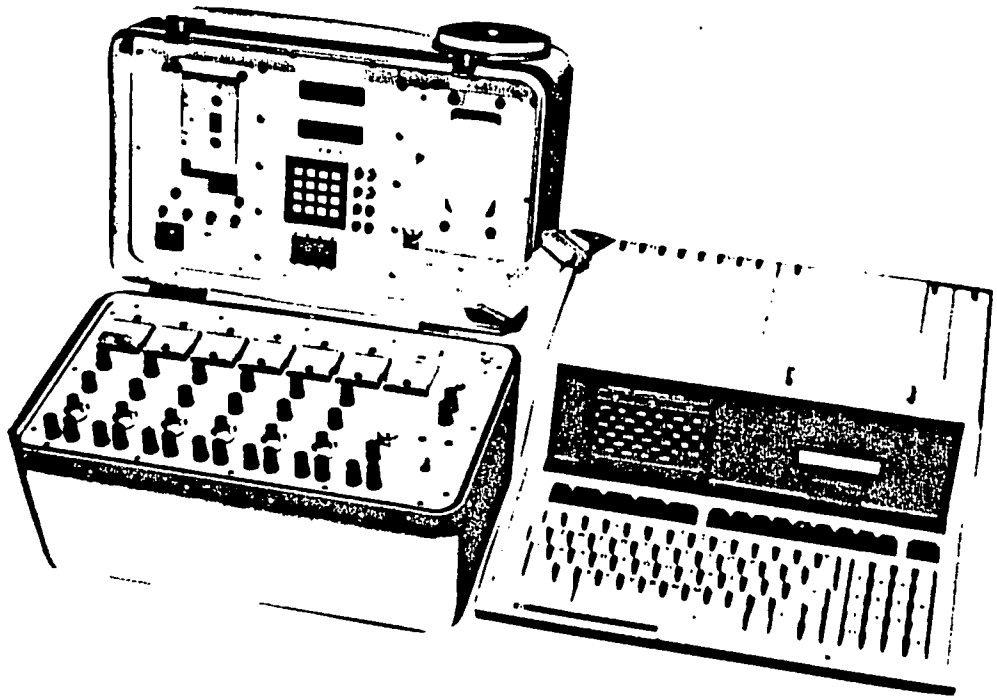

FIG. 24

ii) Frequency range from 2^{-14} Hz (0.00006 Hz) to 2^{+16} Hz (65,536 Hz) with automatic scanning programmable through CP-1.

iii) Real time de-convolution and coherent filtering via use of CP-1.

iv) Field Data available through digital read-out and recorded on paper tape and tape cassette.

v) Field results directly transferrable from tape cassette through CP-1 and interface to computer for analysis and interpretation. (Figure 24).

By using the IPV-3 and the HP=85 computer in the field, the geophysicist has at his disposal all of the interpretational power of the spectral IP method. As shown on Figure 25 it is possible to remove the inductive coupling effects from the broad-band spectral IP results. When this information is removed, it is possible to invert the remaining, decoupled IP spectra and determine the apparent values of Ro, m, τ, c for that particular dipole-pair measurement.

For the spectra shown in Figure 25, the values are m = 0.172; c = 0.376; τ = 0.044 sec.; these parameters suggest a small grain-size, and in fact the source is a massive sulphide zone in New Brunswick. The parameter values obtained by inverting the spectral curve from all of the anomalous dipole pairs were essentially the same; we have found this to be universally true if the anomaly is due to a single, more-or-less uniform source.

For the spectral curve shown in Figure 26, the parameter values of the source are m = 0.509; c = 0.180; τ = 540 seconds. The large time-constant confirms the large grain-size for the graphite zone that is the source of the anomaly.

For IP measurements with large electrode intervals in areas of low resistivity (high conductivity) inductive coupling effects will completely distort IP field data. This can happen even for low frequency measurements (in the variable frequency method) or long time delay measurements (in the time domain technique). When the inductive coupling effects are removed from the spectral curve for each dipole pair (as in Figure 12 and Figure 25) the pseudo-section can be reconstructed using the decoupled data.

The data pseudo-section shown in Figure 27 is from the Elura Deposit near Cobar, New South Wales. The resistivity results show a deep, variable high conductivity surface layer. The phase IP measurements at 3.0 Hz with X = 100 meters are completely dominated by inductive coupling effects that essentially depend only upon the electrode separation (n). However, when the inductive effects are removed from the data for each dipole pair, the pseudo-section clearly shows the presence of the massive sulphide zone, at depth, at approximately station 2500E.

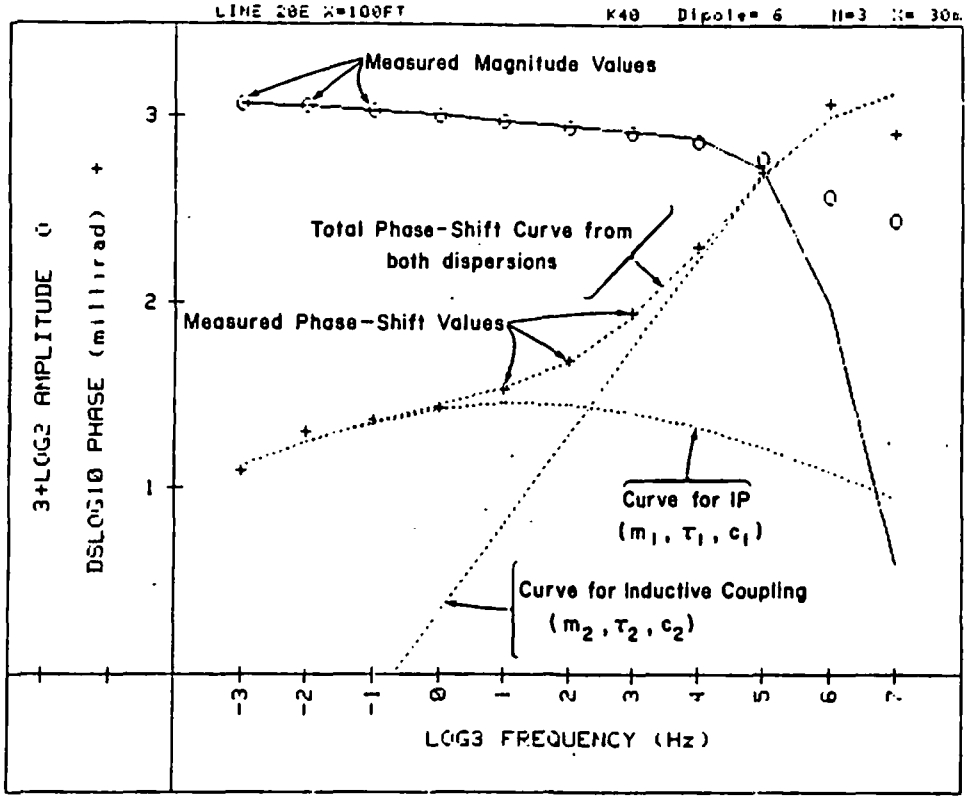

				IP EFFECT			INDUCTIVE COUPLING EFFECT		
Iter	Lambda	Rchsq	R0	M1	T1	C1	M2	T2	C2
0	1.E-02	.05405	1.089	.221	4.0E-02	.329	1.000	1.1E-04	1.000
1	1.E-02	.00168	1.063	.196	2.5E-02	.373	1.000	3.6E-04	1.000
2	1.E-03	.00058	1.072	.186	3.1E-02	.355	1.000	3.3E-04	1.000
3	1.E-04	.00067	1.071	.174	4.3E-02	.373	1.000	3.4E-04	1.000
4	1.E-05	.00066	1.071	.172	4.4E-02	.376	1.000	3.4E-04	1.000
Pct Std Deviations			.8	16.4	84.2	13.5	0.0	5.5	0.0

Correlation Matrix

1.0000							
.5173	1.0000						
-.4239	-.9715	1.0000					
-.5302	-.9438	.8971	1.0000				
0.0000	0.0000	0.0000	0.0000	0.0000			
-.2093	-.6596	.6657	.5348	0.0000	1.0000		
0.0000	0.0000	0.0000	0.0000	0.0000	0.0000	0.0000	

Apparent Resistivity Measured at 1 Hz is 78

Apparent Resistivity Calculated from Inductive Coupling is 10

FIG. 25

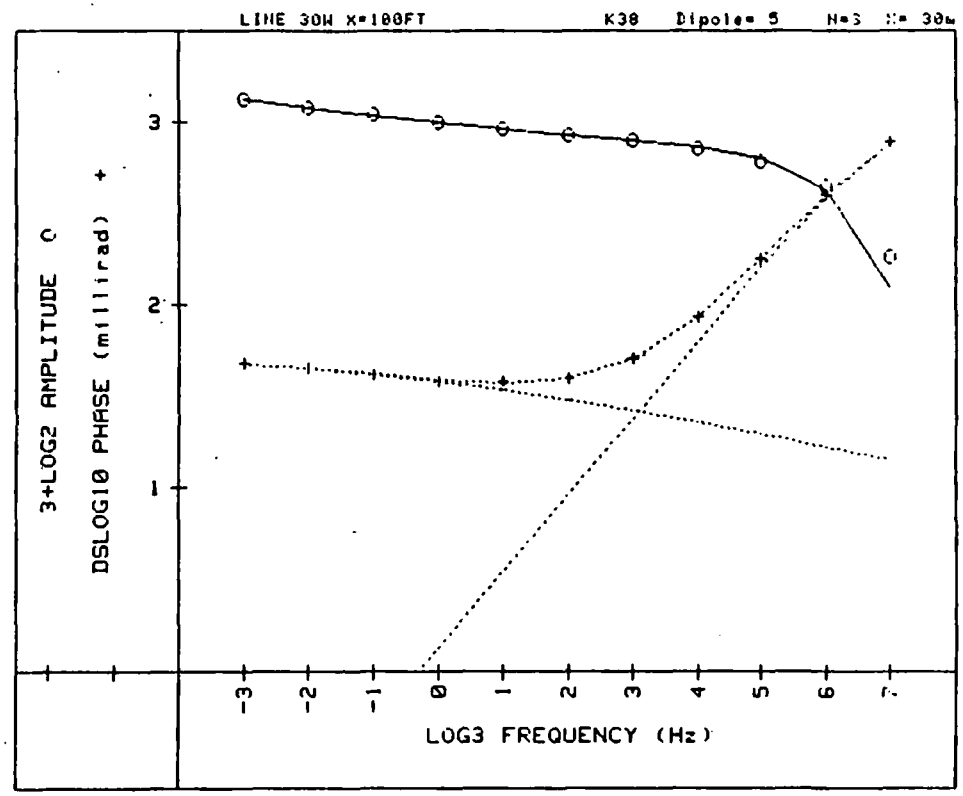

Iter	Lambda	Rchsq	R0	M1	T1	C1	M2	T2	C2
0	1.E-02	.01496	1.776	.571	1.2E+02	.180	1.000	1.5E-04	.978
1	1.E-02	.00083	1.569	.483	1.3E+02	.180	1.000	9.3E-05	.893
2	1.E-03	.00008	1.616	.487	1.9E+02	.180	1.000	8.6E-05	.891
3	1.E-04	.00006	1.677	.502	4.0E+02	.180	1.000	8.7E-05	.882
4	1.E-05	.00005	1.704	.508	5.3E+02	.180	1.000	8.7E-05	.879
5	1.E-06	.00005	1.707	.509	5.4E+02	.180	1.000	8.7E-05	.879
Pct Std Deviations			2.4	2.0	53.1	0.0	0.0	2.0	1.0

Correlation Matrix

1.0000						
.9916	1.0000					
.9885	.9710	1.0000				
0.0000	0.0000	0.0000	0.0000			
0.0000	0.0000	0.0000	0.0000	0.0000		
-.1166	-.0889	-.1282	0.0000	0.0000	1.0000	
-.4909	-.4268	-.5273	0.0000	0.0000	.7128	1.0000

Apparent Resistivity Measured at 1 Hz is 231

Apparent Resistivity Calculated from Inductive Coupling is 26

FIG. 26

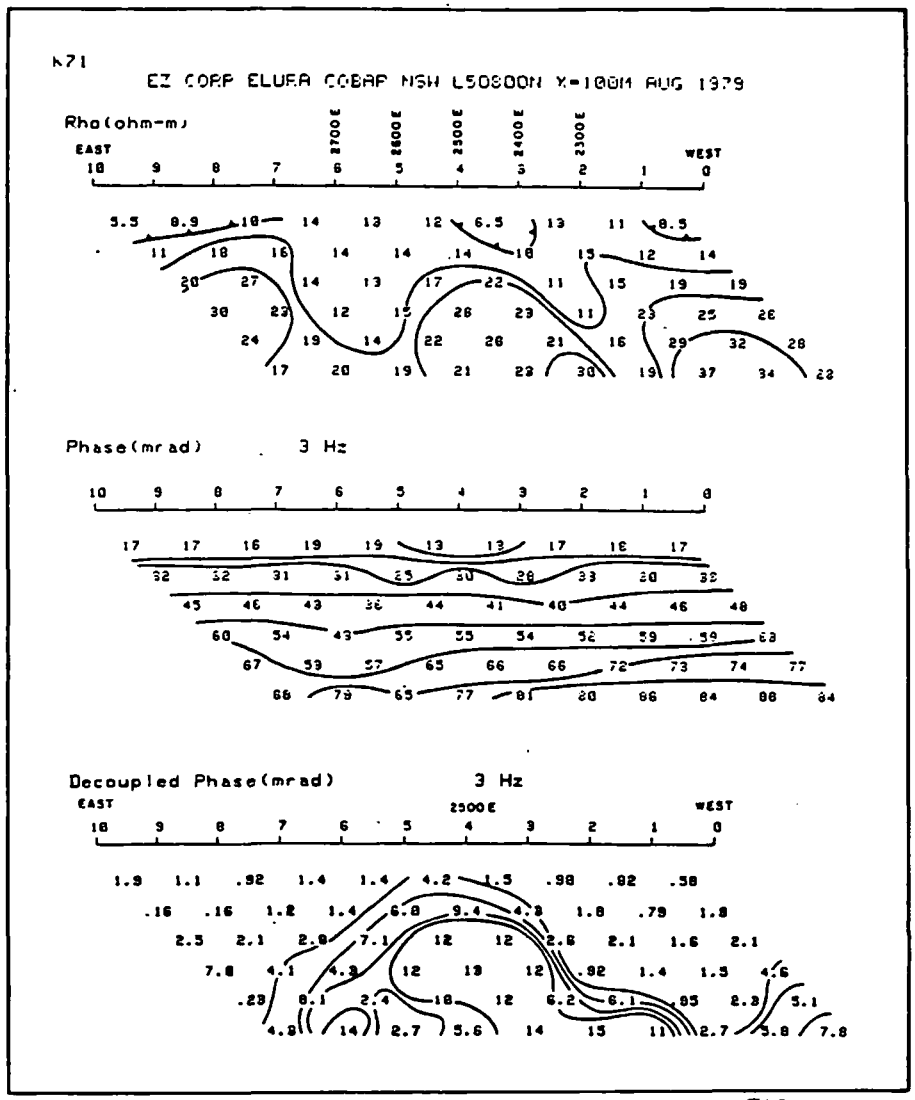

FIG. 27

COMPUTER ASSISTED INTERPRETATION OF IP DATA

The increased size, storage capability and speed of the modern digital computer has been a big boon to the exploration geophysicist. Forward problem solutions for potential methods (gravity, magnetics, etc.) have been available for some time. Recently, numerical modelling methods and large, very fast computers have made similar forward problem solutions available for applied field geophysics such as resistivity and induced polarization.

The forward problem solution shown in Figure 28 is for a fairly normal, dipping source. (The geometry is Two-Dimensional). The patterns of the induced polarization and resistivity pseudo-sections are similar to those we have previously seen from field data over dipping sources.

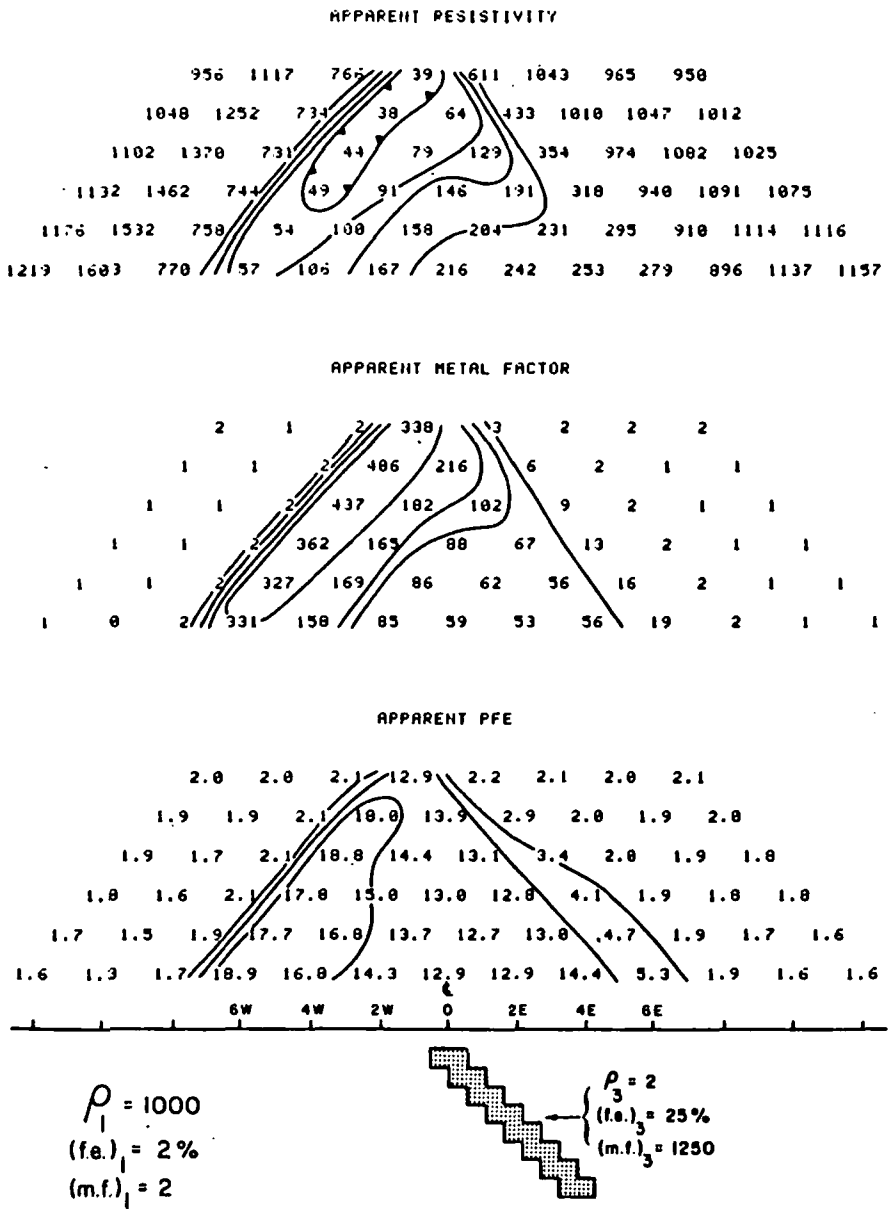
APPARENT RESISTIVITY
956 1117 766 39 611 1043 965 950
1048 1252 734 38 64 433 1010 1047 1012
1102 1370 731 44 79 129 354 974 1082 1025
1132 1462 744 49 91 146 191 318 940 1091 1075
1176 1532 758 54 100 158 204 231 295 910 1114 1116
1219 1683 770 57 106 167 216 242 253 279 896 1137 1157
APPARENT METAL FACTOR
2 1 2 338 3 2 2 2
1 1 2 486 216 6 2 1 1
1 1 2 437 182 102 9 2 1 1
1 1 2 362 165 88 67 13 2 1 1
1 1 2 327 169 86 62 56 16 2 1 1
1 0 2 331 158 85 59 53 56 19 2 1 1
APPARENT PFE
2.0 2.0 2.1 12.9 2.2 2.1 2.0 2.1
1.9 1.9 2.1 18.0 13.9 2.9 2.0 1.9 2.0
1.9 1.7 2.1 18.8 14.4 13.1 3.4 2.0 1.9 1.8
1.8 1.6 2.1 17.8 15.0 13.0 12.8 4.1 1.9 1.8 1.8
1.7 1.5 1.9 17.7 16.8 13.7 12.7 13.8 4.7 1.9 1.7 1.6
1.6 1.3 1.7 18.9 16.8 14.3 12.9 12.9 14.4 5.3 1.9 1.6 1.6
6W 4W 2W 0 2E 4E 6E
ρ1 = 1000
(f.e.)1 = 2%
(m.f.)1 = 2
ρ3 = 2
(f.e.)3 = 25%
(m.f.)3 = 1250

FIG. 28

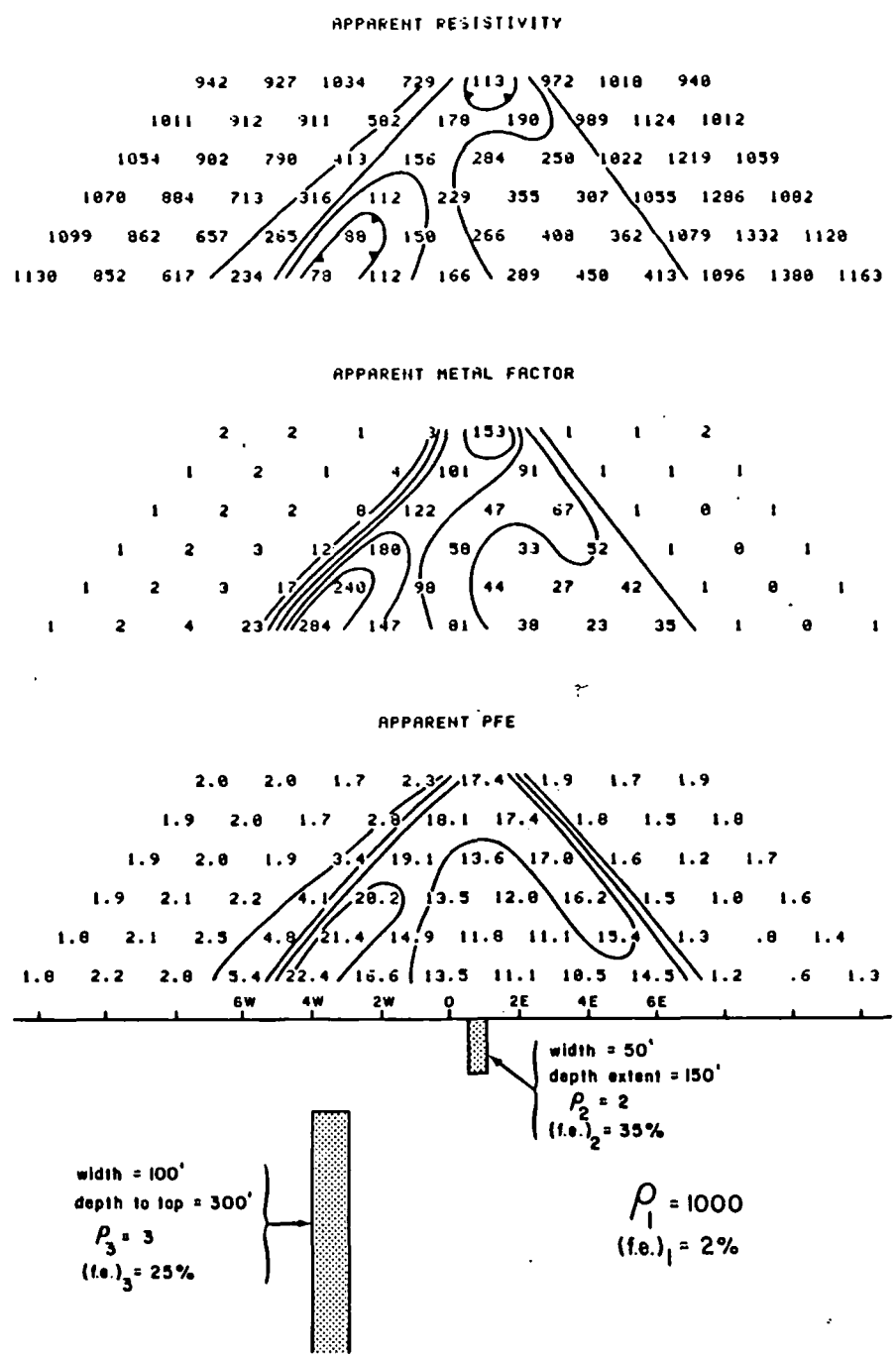
APPARENT RESISTIVITY
942 927 1034 729 113 972 1018 940
1011 912 911 582 178 190 989 1124 1012
1054 902 790 413 156 284 250 1022 1219 1059
1070 884 713 316 112 229 355 307 1055 1286 1082
1099 862 657 265 88 150 266 408 362 1079 1332 1120
1130 852 617 234 78 112 166 289 450 413 1096 1380 1163
APPARENT METAL FACTOR
2 2 1 3 153 1 1 2
1 2 1 4 101 91 1 1 1
1 2 2 8 122 47 67 1 0 1
1 2 3 12 180 58 33 52 1 0 1
1 2 3 17 240 98 44 27 42 1 0 1
1 2 4 23 284 147 81 38 23 35 1 0 1
APPARENT PFE
2.0 2.0 1.7 2.3 17.4 1.9 1.7 1.9
1.9 2.0 1.7 2.8 18.1 17.4 1.8 1.5 1.8
1.9 2.0 1.9 3.4 19.1 13.6 17.0 1.6 1.2 1.7
1.9 2.1 2.2 4.1 20.2 13.5 12.0 16.2 1.5 1.0 1.6
1.8 2.1 2.5 4.8 21.4 14.9 11.8 11.1 15.4 1.3 .8 1.4
1.8 2.2 2.8 5.4 22.4 16.6 13.5 11.1 10.5 14.5 1.2 .6 1.3
6W 4W 2W 0 2E 4E 6E
width = 50'
depth extent = 150'
ρ2 = 2
(f.e.)2 = 35%
width = 100'
depth to top = 300'
ρ3 = 3
(f.e.)3 = 25%
ρ1 = 1000
(f.e.)1 = 2%

FIG. 29

Recently however, we had occasion to try to interpret a field anomaly that was very similar to that shown in Figure 29. The presence of the shallow, limited depth extent source was known from previous drilling. By the trial and error method, we were able to show that the pattern (which is very similar to that in Figure 28) need not have originated from a dipping source.

By limiting the solutions somewhat, it is possible to create computer programs to do the inverse problem. That is, the computer accepts the field data as input and as output gives the vertical, tabular source that gives the best "least square fit" to that data. For comparison, the computer also outputs the pseudo-section data that would be measured for the source it has chosen.

The simplest problem is for resistivity data alone. The results shown in Figure 30 are from a geothermal exploration program in which the resistivity survey was completed using X = 250 meters. The large, deep resistivity low was measured on the side of an extinct volcano, under recent lava flows. The computer inversion gives a major, poorly determined, conductor (with a high conductivity times width product) at a depth of 350 to 400 meters. This data was used to show the geologist that the source of the resistivity anomaly could be a good geothermal target.

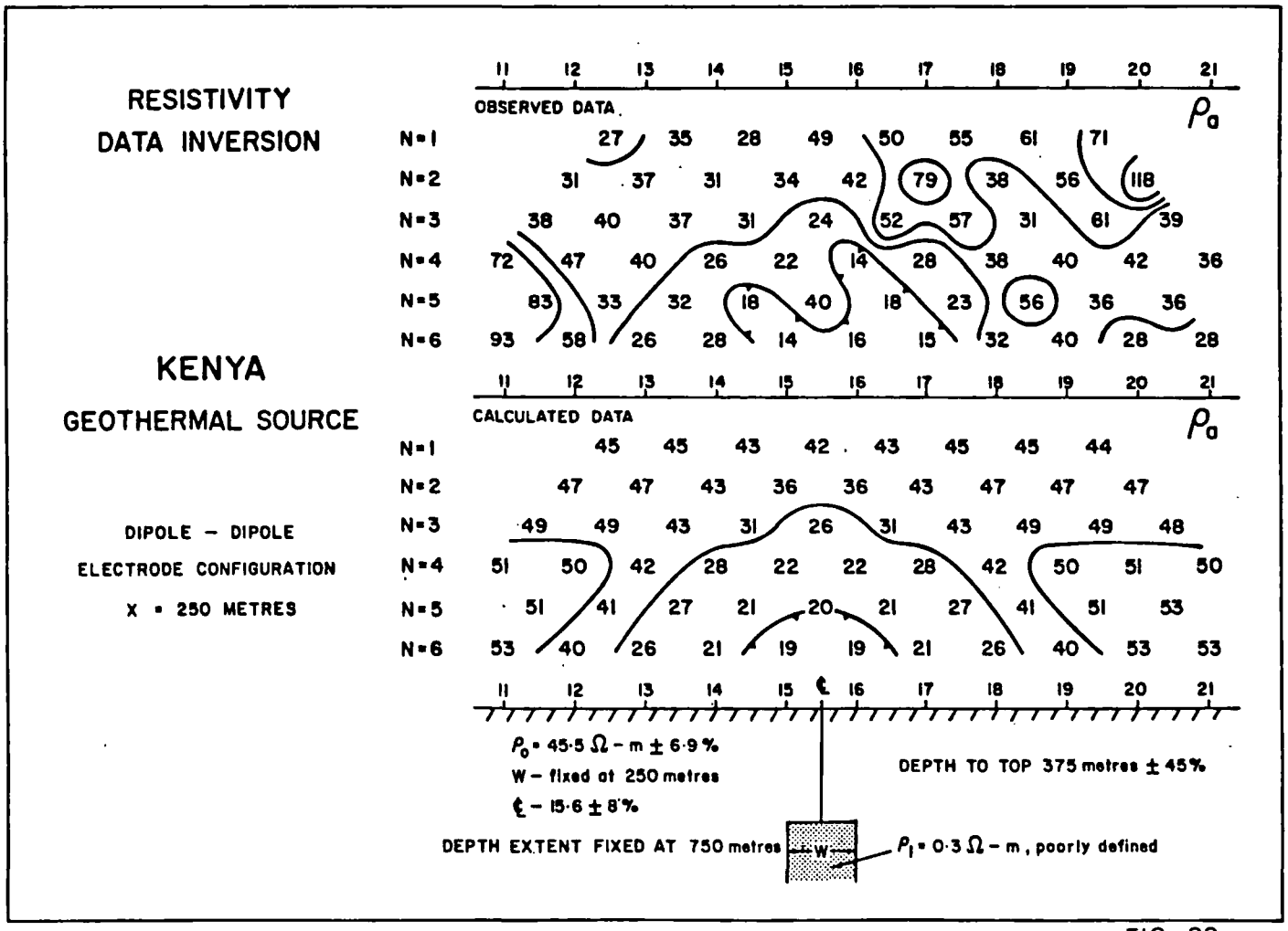

FIG. 30

The example shown in Figure 31 and Figure 32 is from the Pine Point Area. The computer inversion shows that in this case the source has a poor resistivity contrast with the surrounding limestones. However, the IP effect is quite anomalous.

If there is conductive overburden present, and the source itself is conductive, the inversions will be more complex. The data shown on Figure 33 and Figure 34 were measured with X = 100 feet, in an area where the depth of overburden was determined to be about fifty feet. The calculated results give a "good fit" to the measured data, and the source described by this inversion is a typical Canadian Shield, massive sulphide deposit.

The inversion program can also be used to show that two dissimilar anomalies can in fact be due to the same type of source. The inversions of the IP data shown in Figure 35 and Figure 36 are those for the field data previously shown in Figure 17 and Figure 18. The background resistivities are very different, and the depths to the top of the sources are different by a factor of three. However, the indicated source parameters are much the same. As we saw previously, the spectral characteristics of the IP anomaly from the two sources are quite different.

The use of the computer inversion techniques make it possible to obtain an estimate of the source parameters, even in situations in which an unusual geologic environment would make it difficult to interpret the data. The field results shown in Figure 37 are from a deeply buried source in a highly conductive environment. The rocks in which the survey was completed were porous, and filled with saline water. However, the inversion output on Figure 38 shows the source is not unlike that determined in Figure 34.

WHAT OF THE FUTURE?

There seems to be almost no limit to the future development of the induced polarization method. As the orebodies for which we search become deeper, and more difficult to detect, we will need all of the help we can get.

A simple extension of what we are now doing should lead to the following examples in the next twelve to twenty-four months.

a) The computer can be used to store parameters obtained by the computer inversions of spectral IP data. Therefore, it will be possible to correlate the electrical parameters (m, τ, c) of all sources known in a given geographical area or a certain geologic environment. For a new, unknown source, the computer could be asked to output the probability that the unknown source will be due to metallic mineralization of a certain type.

The data shown in Figure 39 was a first attempt at such a correlation. On the plot are shown the IP effect vs. Time-Constant (m, vs.τ) coordinates for a few massive sulphide

PINE POINT, N-38A, X=200FT

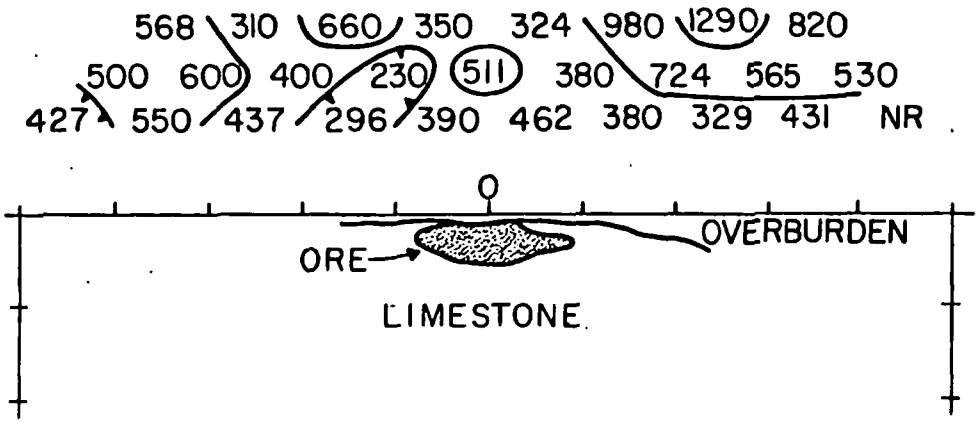

RESISTIVITY MODEL

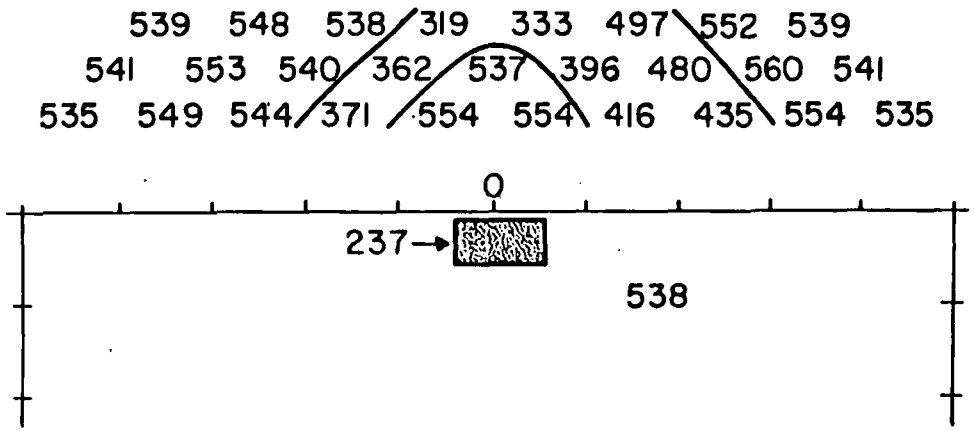

FIG. 31

PINE POINT, N-38A, X=200 FT

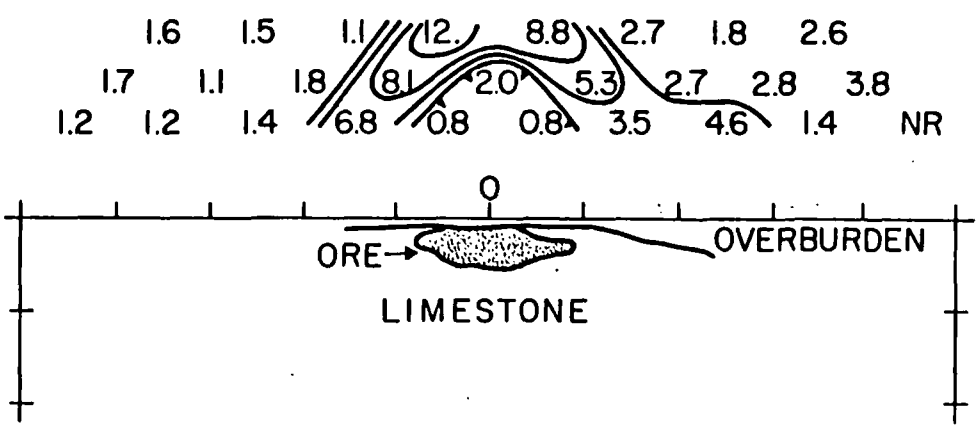

IP MODEL

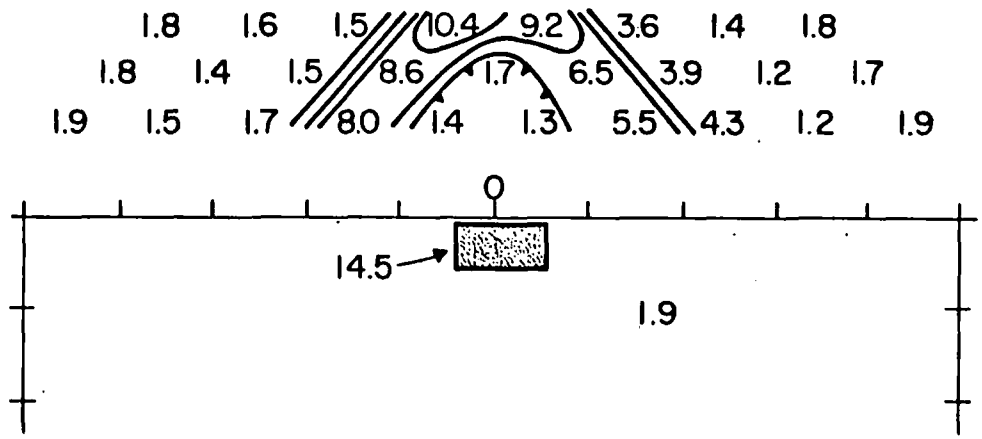

FIG. 32

COMPUTER INTERPRETATION

OF GEOPHYSICAL DATA

INDUCED POLARIZATION AND RESISTIVITY

CANADIAN SHIELD MASSIVE SULPHIDE DEPOSIT, OVERLAIN BY CONDUCTIVE OVERBURDEN
ISO - COPPERFIELDS LINE 0+00

DETERMINE: HORIZONTAL POSITION
DEPTH TO TOP
WIDTH
RES OF SOURCE
RES OF OVERBURDEN
IP OF SOURCE

DIPOLE-DIPOLE ARRAY X = 100 FEET 100FT

RESISTIVITY DATA - OBSERVED (OHM-METERS)

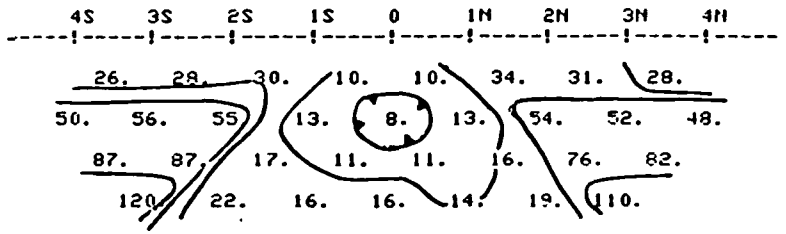

INDUCED POLARIZATION DATA - OBSERVED (PFE)

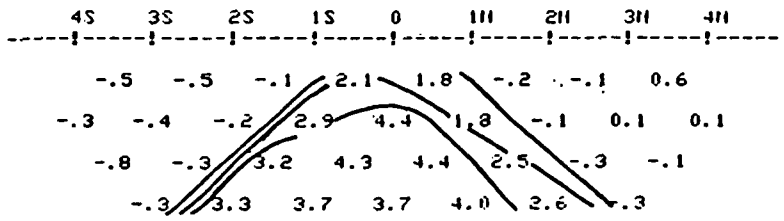

FIG. 33

RESISTIVITY DATA - CALCULATED (OHM-METERS)

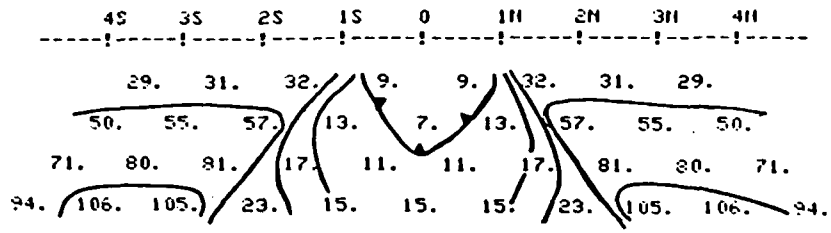

INDUCED POLARIZATION DATA - CALCULATED (PFE)

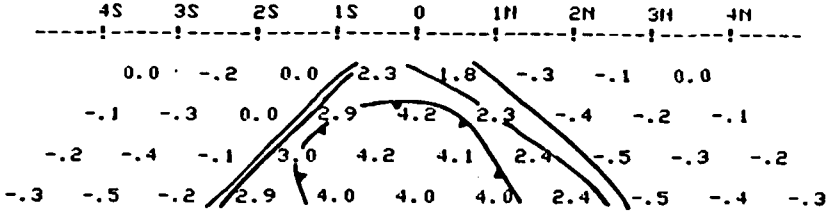

PARAMETERS OF THE CALCULATED SOURCE

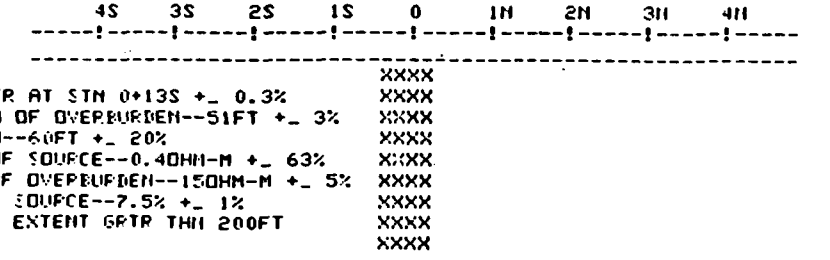

	XXXX
CENTER AT STN 0+13S +_ 0.3%	XXXX
DEPTH OF OVERBURDEN--51FT +_ 3%	XXXX
WIDTH--60FT +_ 20%	XXXX
RES OF SOURCE--0.4OHM-M +_ 63%	XXXX
RES OF OVERBURDEN--150HM-M +_ 5%	XXXX
IP OF SOURCE--7.5% +_ 1%	XXXX
DEPTH EXTENT GRTR THN 200FT	XXXX
	XXXX

FIG. 34

LINE-18E

FINAL MODEL FOR DATA SET 1

OBSERVED DATA

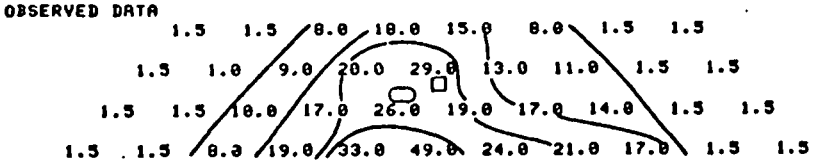

100*DIAGONAL OF INFORMATION DENSITY MATRIX

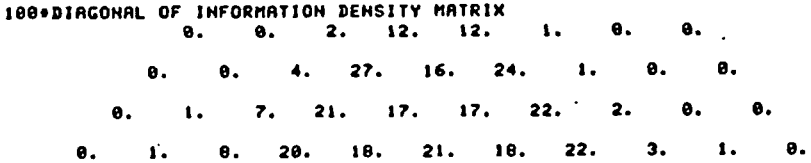

CALCULATED DATA

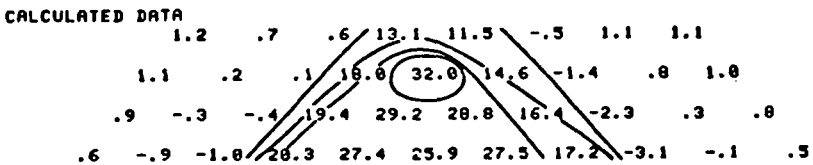

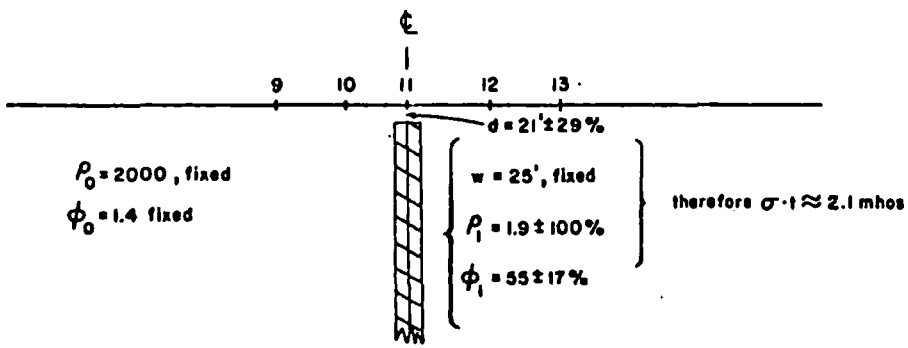

FIG. 35

LINE-15E

graphite source, with some pyrite

LINE-15E

phase at 0.3 Hz.

FINAL MODEL FOR DATA SET 1

OBSERVED DATA

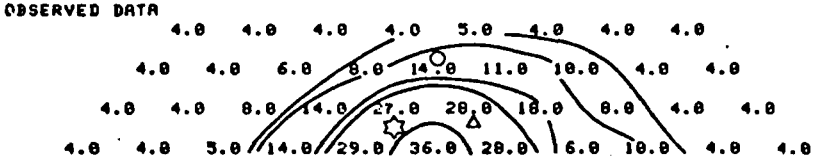

100*DIAGONAL OF INFORMATION DENSITY MATRIX

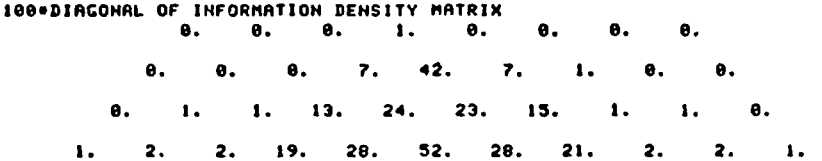

CALCULATED DATA

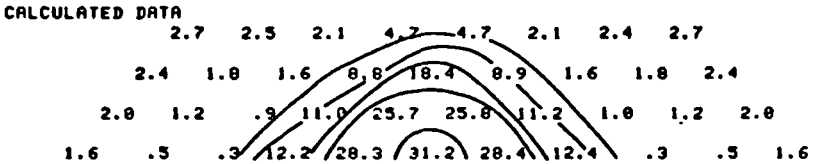

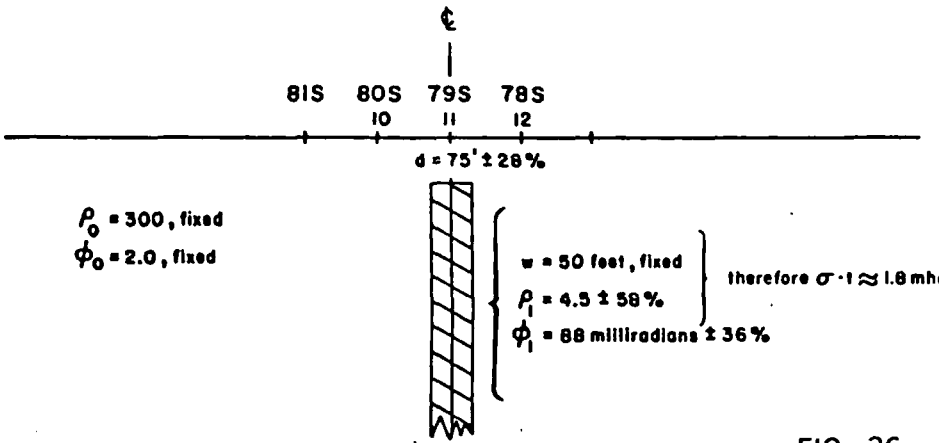

FIG. 36

COMPUTER INTERPRETATION

OF GEOPHYSICAL DATA

INDUCED POLARIZATION AND RESISTIVITY

DEEPLY BURIED SOURCE IN VERY CONDUCTIVE ENVIRONMENT - DETERMINE POSITION, DEPTH, AND PHYSICAL PROPERTIES OF SOURCE

DIPOLE-DIPOLE ARRAY X = 25 METERS 25M

RESISTIVITY DATA - OBSERVED (OHM-METERS)

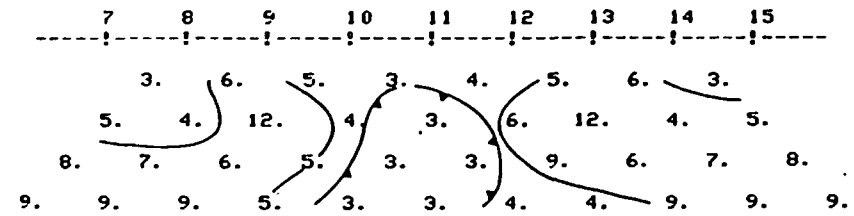

INDUCED POLARIZATION DATA - OBSERVED (PFE)

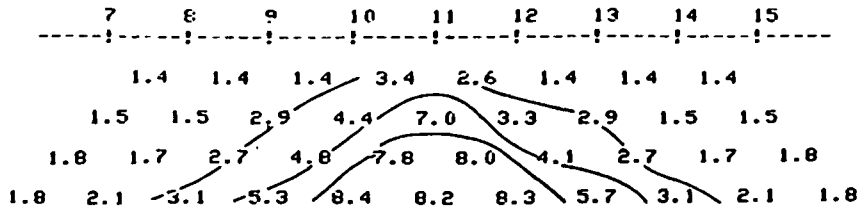

FIG. 37

RESISTIVITY DATA - CALCULATED (OHM-METERS)

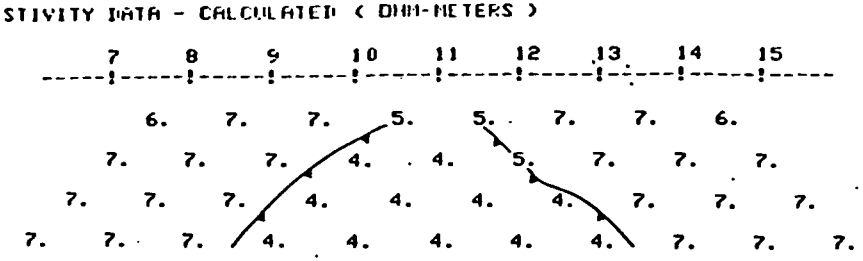

INDUCED POLARIZATION DATA - CALCULATED (PFE)

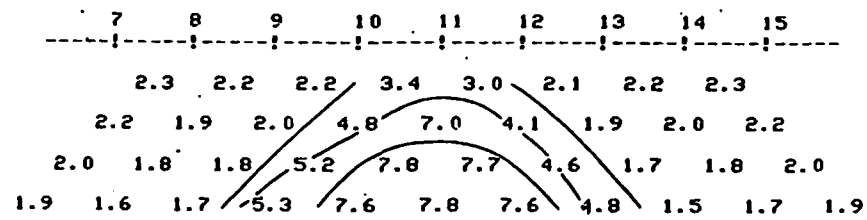

PARAMETERS OF THE CALCULATED SOURCE

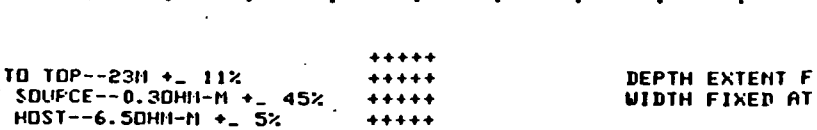

DEPTH TO TOP--23M +_ 11%
RES OF SOURCE--0.30HM-M +_ 45%
RES OF HOST--6.50HM-M +_ 5%
IP OF SOURCE--23 +_ 16%
IP OF HOST--2.3 +_ 11%
CENTER AT STN 10+90 +_ 1%

+++++
+++++
+++++
+++++
+++++
+++++
+++++

DEPTH EXTENT FIXED AT >50M
WIDTH FIXED AT 25M

FIG. 38

sources and massive graphite sources in Canada. More recent determinations have not been added to the plot, although additional field work in North America and Australia has shown the same grouping.

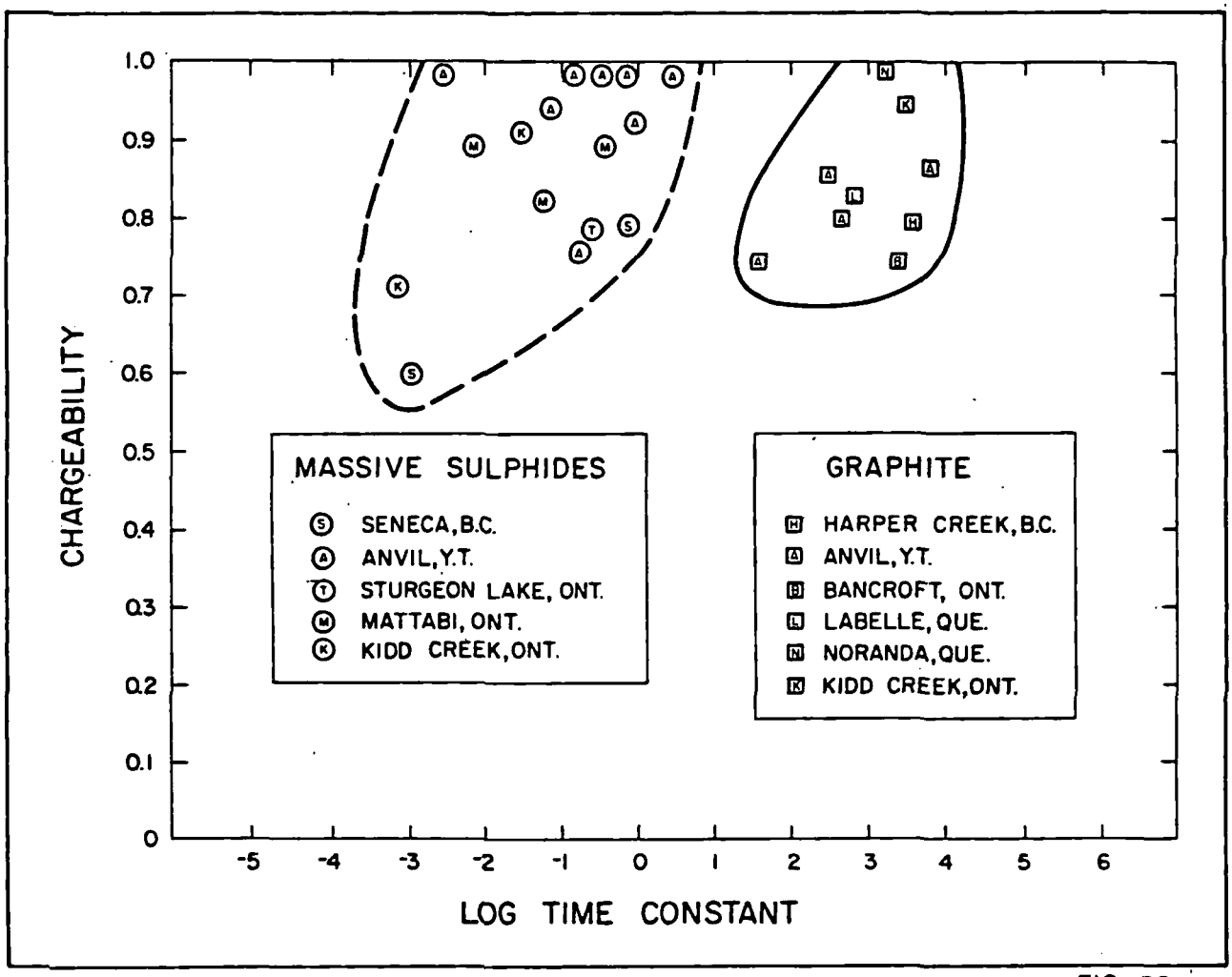

FIG. 39

b) The frequency range of spectral IP measurements with the IPV-3 System extends well up into the range that is normally used for electromagnetic prospecting. Indeed, as we have shown previously, the inductive coupling (EM) effects must be removed from the spectral IP plot before the electrical parameters of the source can be determined. In the near future, it should be possible to use this electromagnetic coupling information to gain further insight about the source.

The induced polarization and resistivity results in Figure 40 are from an area in South Australia. There is a known

pyrrhotite zone at Station 4 to Station 3, and a narrow Pb-Zn-Ag zone at about Station 0. The resistivity data shows a low over the conductive pyrrhotite zone. The raw phase data at 9.0 Hz and 0.11 Hz shows that IP effects are present, but the measurements (particularly at 9.0 Hz) are distorted by inductive coupling (EM) effects. When the inductive effects are removed, there is a definite IP anomaly from the pyrrhotite zone and a weak IP anomaly from the Pb-Zn-Ag zone. (see Figure 41).

The pseudo-sections shown in Figure 42 are a first attempt to use the inductive effects that have been removed from the dipole-dipole IP data. The M3 parameter is the electromagnetic component that has been removed from the measurement with each dipole pair.

The source centered at Station 4 to Station 3 gives a resistivity low, an IP high, and also a very large electromagnetic component. The source centered at Station 0 gives a weak, but definite IP anomaly. This source is not large enough to give a resistivity low using X = 25 meters. However, the electromagnetic coupling between the IP survey wires and the source is different from the resistive coupling between the electrodes and the source. There definitely is an electromagnetic component due to the Pb-Zn-Ag source.

c) With small desk-top computers, the calculation of a single forward IP problem can require five to ten hours. However, recent advances in small computers and new, interaction interfaces between CRT Displays and light-stylus hardware, will soon give the exploration geophysicist almost instantaneous interpretation capability.

For instance, the geometry shown on Figure 43 could be the first guess at the source of an IP anomaly. The geometry would be drawn upon the CRT Display by the geophysicist using an active light-stylus. At the push of a key, the computer would almost instantly display the pseudo-section shown. The computer would then print a "hard copy" of the field data, the calculated data and the geometry and parameters of the source.

The geophysicist could then use the light-stylus to alter the geometry to that shown in Figure 44. A push of the "operate" key would produce the pseudo-section shown in Figure 44. The pattern is only slightly different, but if it has greater similarity to the field data pattern, the geophysicist knows that he is on the right track.

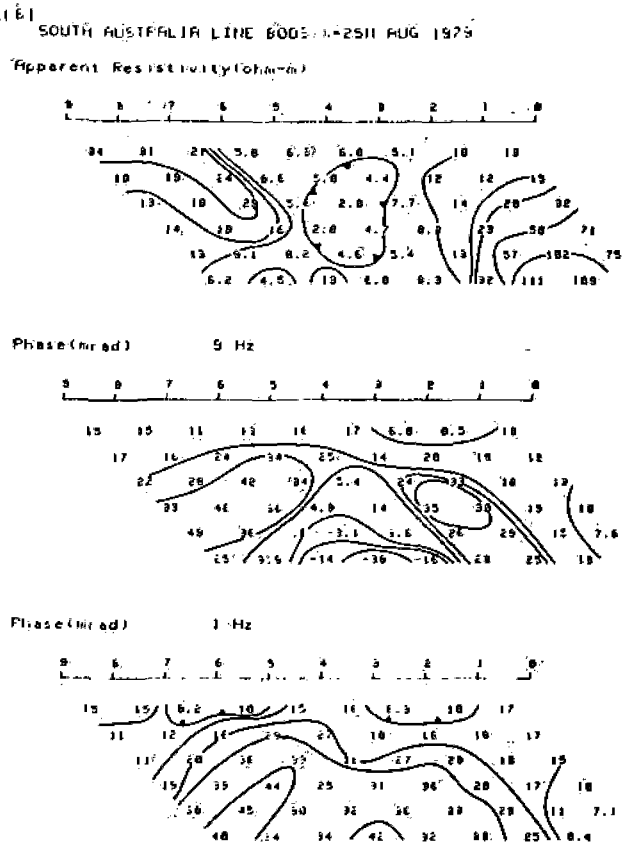

FIG. 40

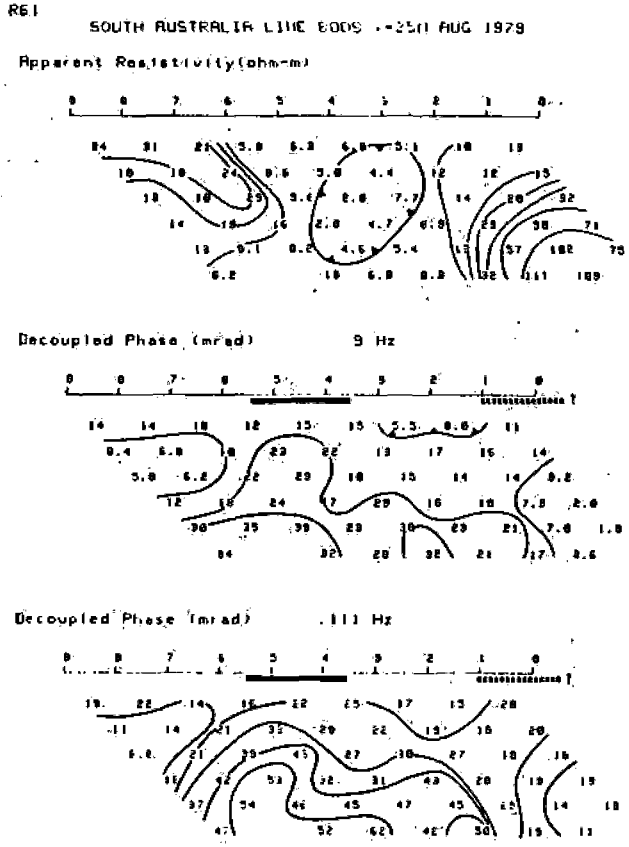

FIG. 41

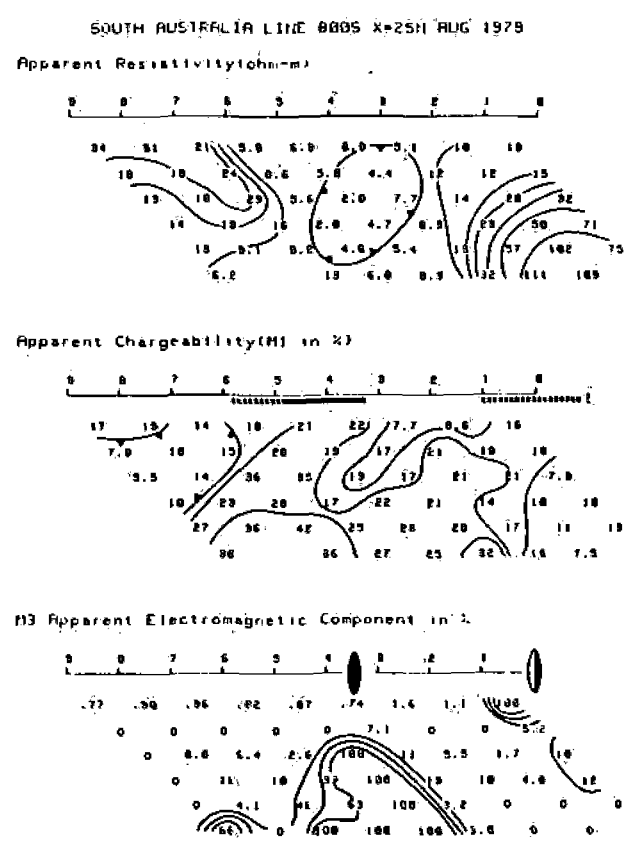

FIG. 42

APPARENT RESISTIVITY

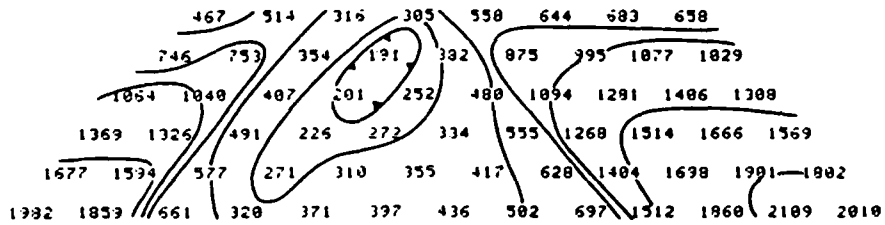

APPARENT RESISTIVITY

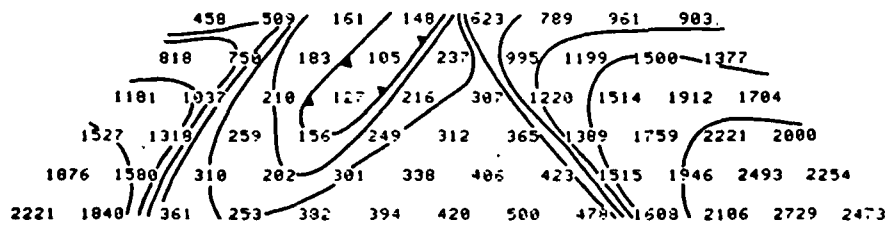

APPARENT METAL FACTOR

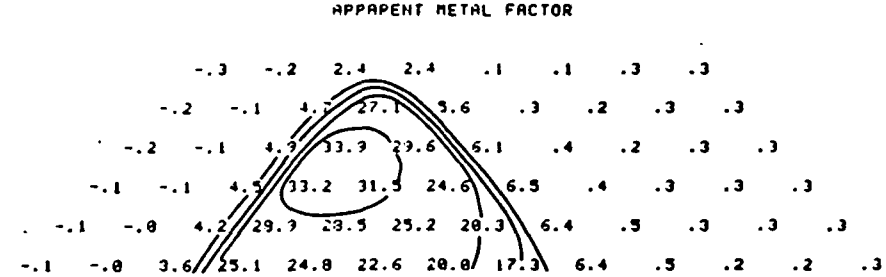

APPARENT METAL FACTOR

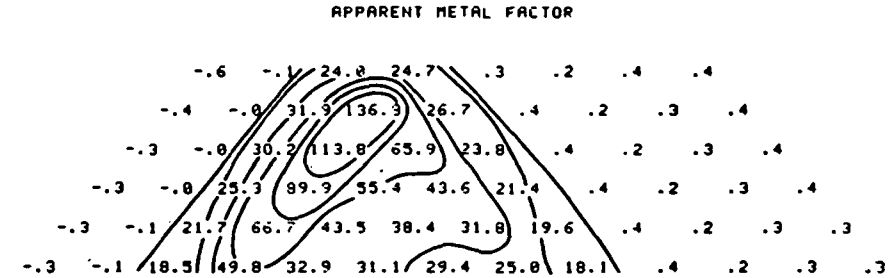

APPARENT PFE

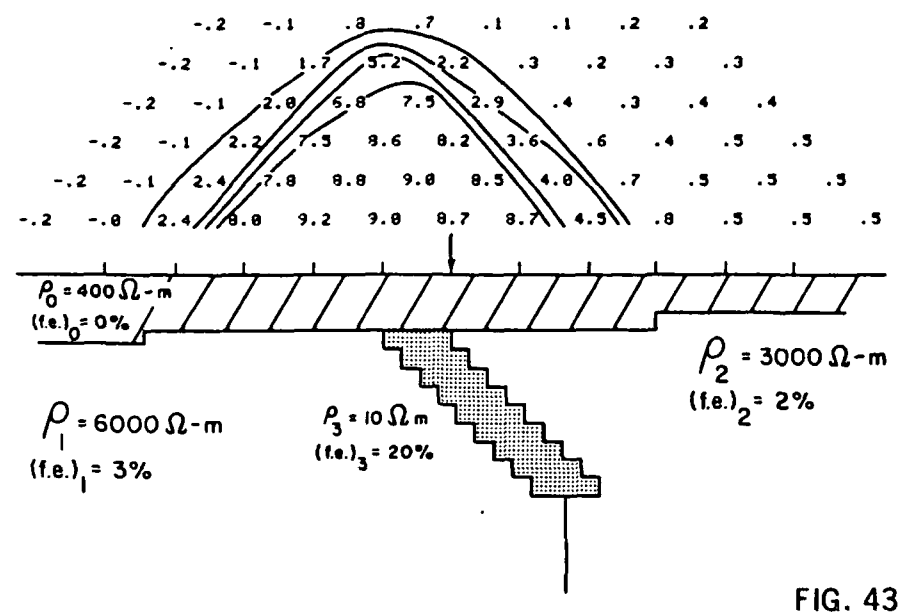

FIG. 43

APPARENT PFE

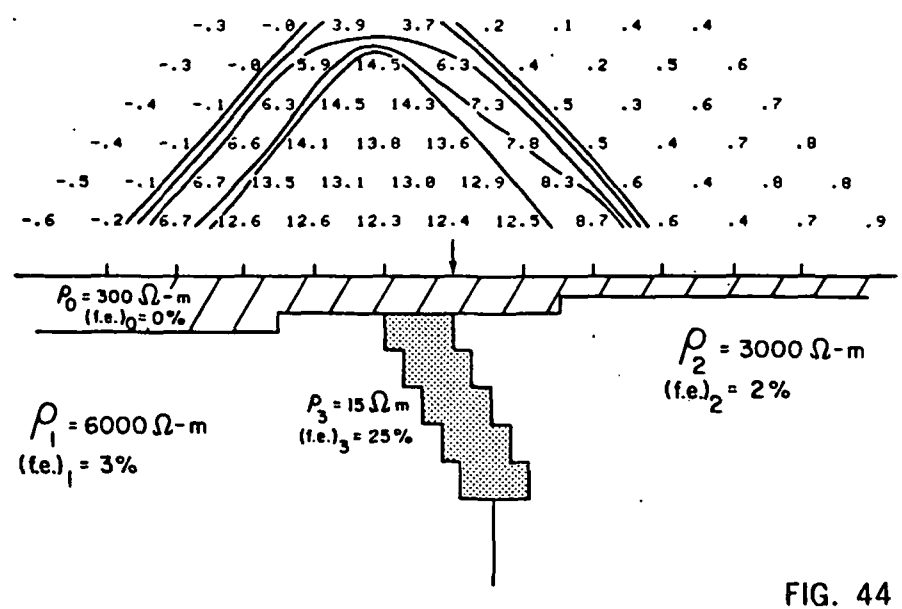

FIG. 44

Toronto Office: 200 Yorkland Blvd., Willowdale, Ont. M2J 1R5
Vancouver Office: 214 - 744 West Hastings St., British Columbia, V6C 1A6
Denver Office: 4690 Ironton St., Colorado, 80239, U.S.A.

DOWNHOLE FISSION TRACK - $^{40}K/^{40}Ar$ AGE DETERMINATIONS AND THE MEASUREMENT OF PERTURBATIONS IN THE GEOTHERMAL GRADIENT

Progress Report

R. B. Forbes, D. L. Turner, C. W. Naeser and D. B. Hawkins

Geophysical Institute
University of Alaska
Fairbanks, Alaska 99701

June 1975-December 1976

Date Published - March 1977

PREPARED FOR THE U.S. ENERGY RESEARCH AND DEVELOPMENT ADMINISTRATION
UNDER CONTRACT NO. E(45-1)-2229, TASK AGREEMENT NO. 11

ABSTRACT

Fission track and $^{40}K/^{40}Ar$ mineral age determinations of cores taken from the GT-1 and 2 (los Alamos) and Eielson (Alaska) drill holes have documented a downhole decrease in apparent radiogenic ages.

The measured geothermal gradient in GT-2 ranges between 50° and 60°C/km. Although an apatite fission track age of 242 (± 48) m.y. was obtained for amphibolites in outcrop, apatite fission track ages of 54.3 (± 10.8) and 68.6 (± 7) m.y. were determined for quartz monzonite underlying the erosional unconformity cut by GT-1 and GT-2, respectively. Apparent apatite ages show a systematic downhole decrease to zero at a depth of 6154' (1.88 km) where the measured temperature is 135°C.

Neither biotite or hornblende appear to have suffered argon loss above 8000' from the most recent thermal perturbation, but the slight decrease in apparent biotite $^{40}K/^{40}Ar$ age (1.26 m.y.) near the bottom of the hole is significant.

The Eielson drill hole penetrates schists of the Yukon-Tanana Complex, and the measured geothermal gradient ranges from 34 to 41°C. Biotite and apatite show a consistent downhole decrease in apparent radiogenic age. Biotite age/depth relations approach a linear function as determined by a best fit regression line with a correlation coefficient of .9666. This line has a zero age intercept of 5.94 km, where the extrapolated temperature is 215°C; a geologically determined argon blocking temperature for biotite in metamorphic rocks.

Apatite fission track ages show a consistent decrease with increasing depth in the hole. A best fit regression line through the apatite plots gives a zero age intercept of 3.43 km where the projected temperature ranges from 117°-141°C; a finding which reinforces the importance

Ar/ Ar dating is to be initiated in spring 1974, following the installation of the new RF generator-incremental temperature control system.

commenced work on core from the second (GT-2) drill hole (Figure 1). Figures 2 and 3 illustrate the section and geothermal gradient intersected by GT-2.

In cooperation with LASL investigators, including William Laughlin (LASL) and Doug Brookins, University of New Mexico, representative GT-2 core samples were selected for mineral separation and analysis. Biotite, hornblende, apatite, zircon, and sphene were separated from crushed core samples in the Geophysical Institute laboratories. Biotite and hornblende $^{40}K/^{40}Ar$ dating was done at the Geophysical Institute geochronology laboratory, and apatite, sphene and zircon fission track dating was accomplished by Charles Naeser, U.S.G.S., Denver. Splits of the biotite and hornblende separates were also sent to Doug Brookins for Rb/Sr dating.

A total of 14 separate Precambrian samples were analyzed. These included an outcrop sample of biotite amphibolite from Guadalupe Box, about 21 km southwest of GT-1; 2 core samples from GT-1; and 11 core samples from GT-2. Five samples contained datable biotite-amphibole pairs, and muscovite was dated from the 5487 foot interval of GT-2. Each K/Ar analysis was done in duplicate, and a total of 43 $^{40}K/^{40}Ar$ ages were determined (see Figure 4; Table 1; and Appendix A).

Interpretation of mica age data:

Biotite and muscovite K/Ar ages are easily perturbed by relatively low temperature thermal events, with temperatures of approximately 200-300°C being sufficient to cause significant argon loss. Such a "resetting of the clock" is shown by all of the analyzed mica samples, based on a 1.66 ± 0.5 b.y. whole rock Rb/Sr isochron defined by Brookins (Figure 5),

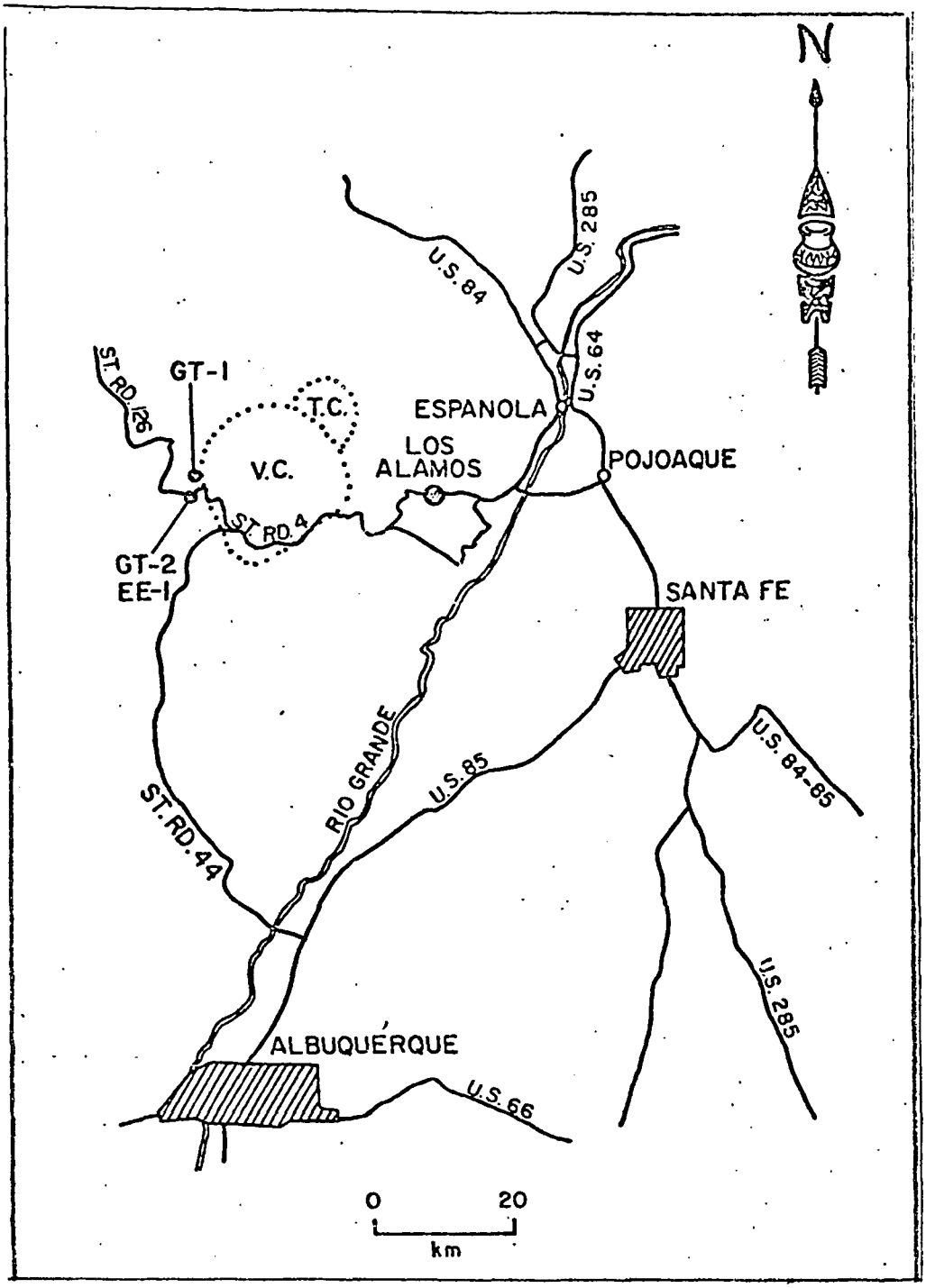

Figure 1. Sketch map showing the location of test holes GT-1 and GT-2. (Courtesy of W. Laughlin, LASL)

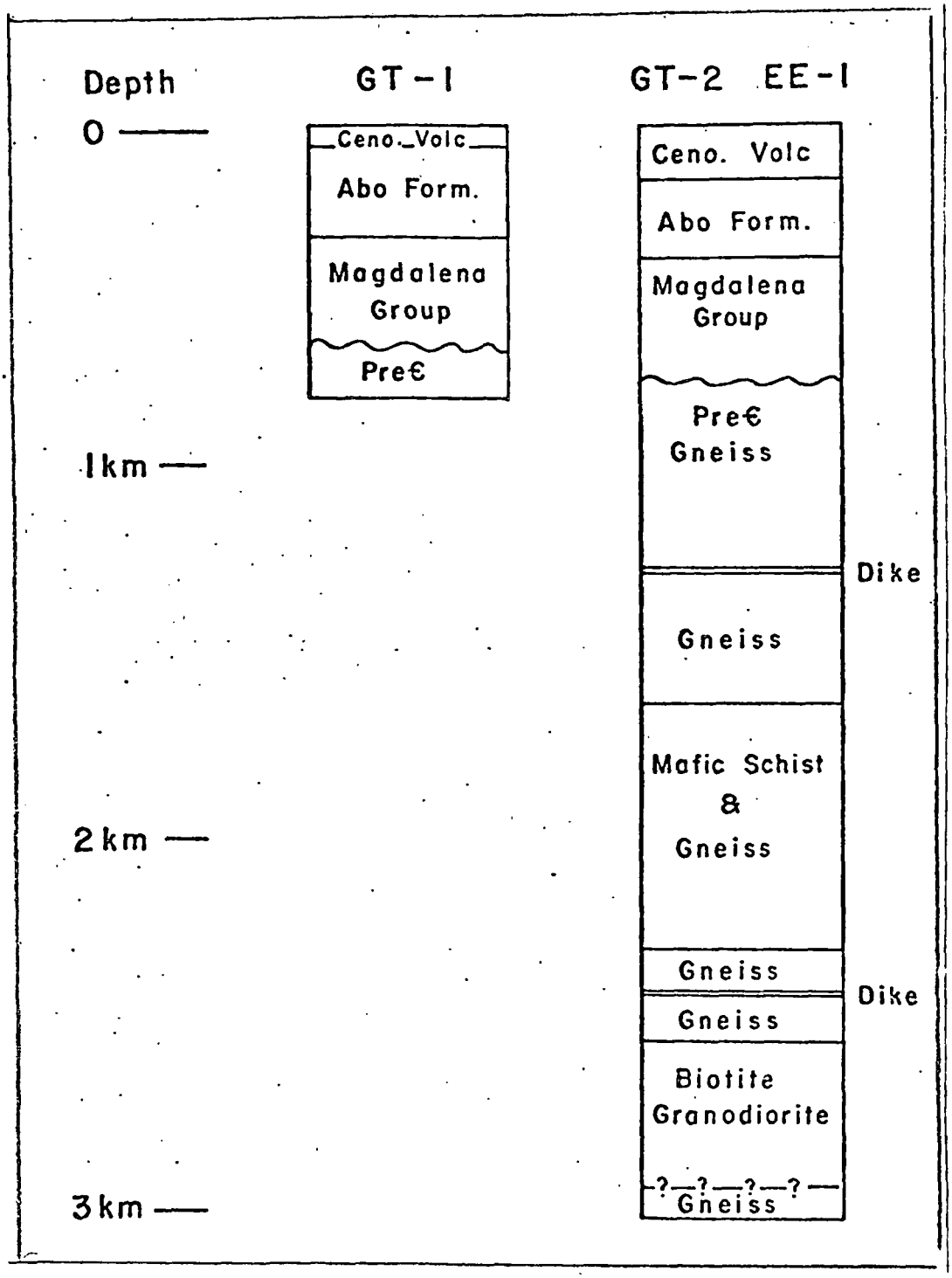

Figure 2. Geologic sections penetrated by test holes GT-1 and GT-2. (Courtesy of LASL)

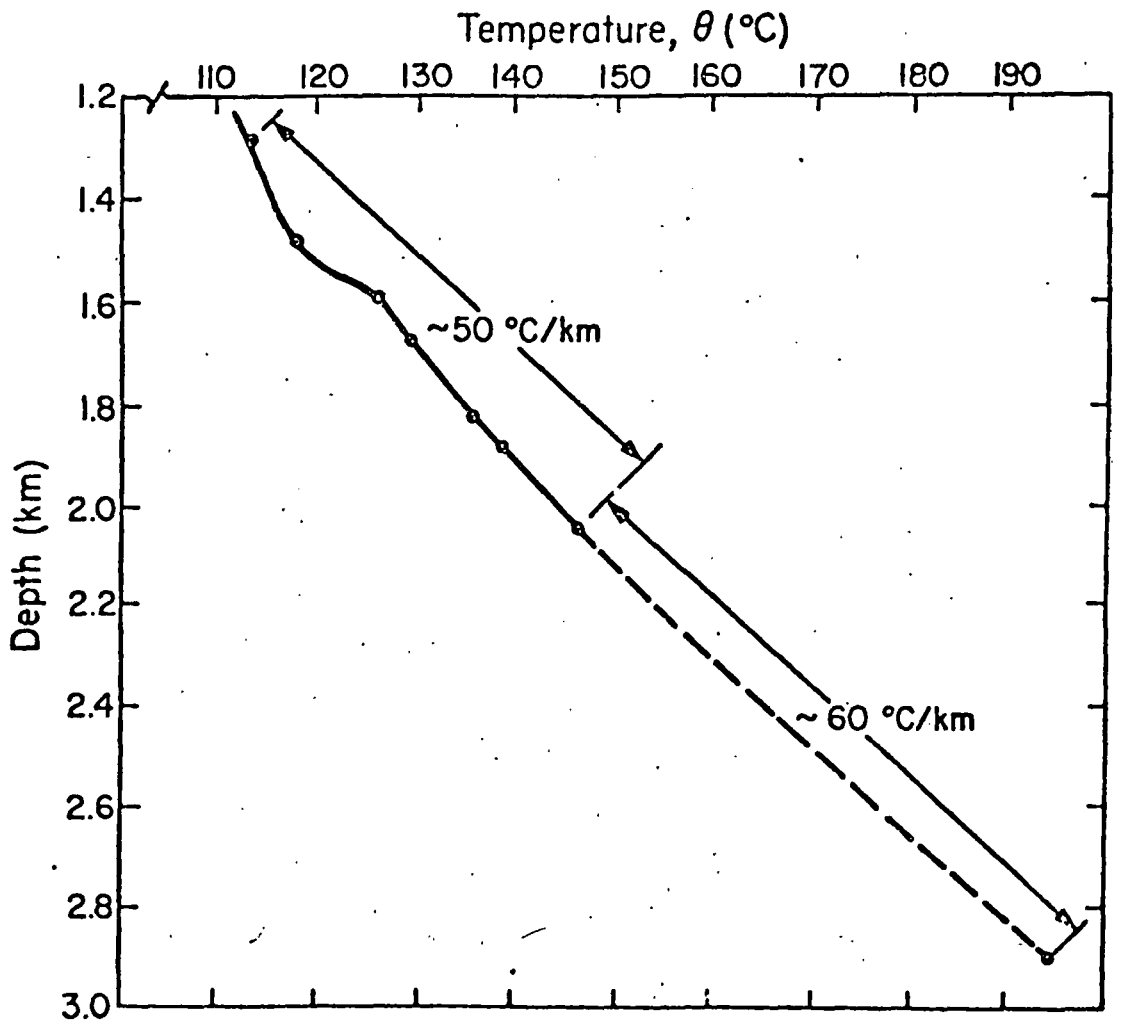

Figure 3. Measured geothermal gradient in GT-2. (Courtesy of LASL)

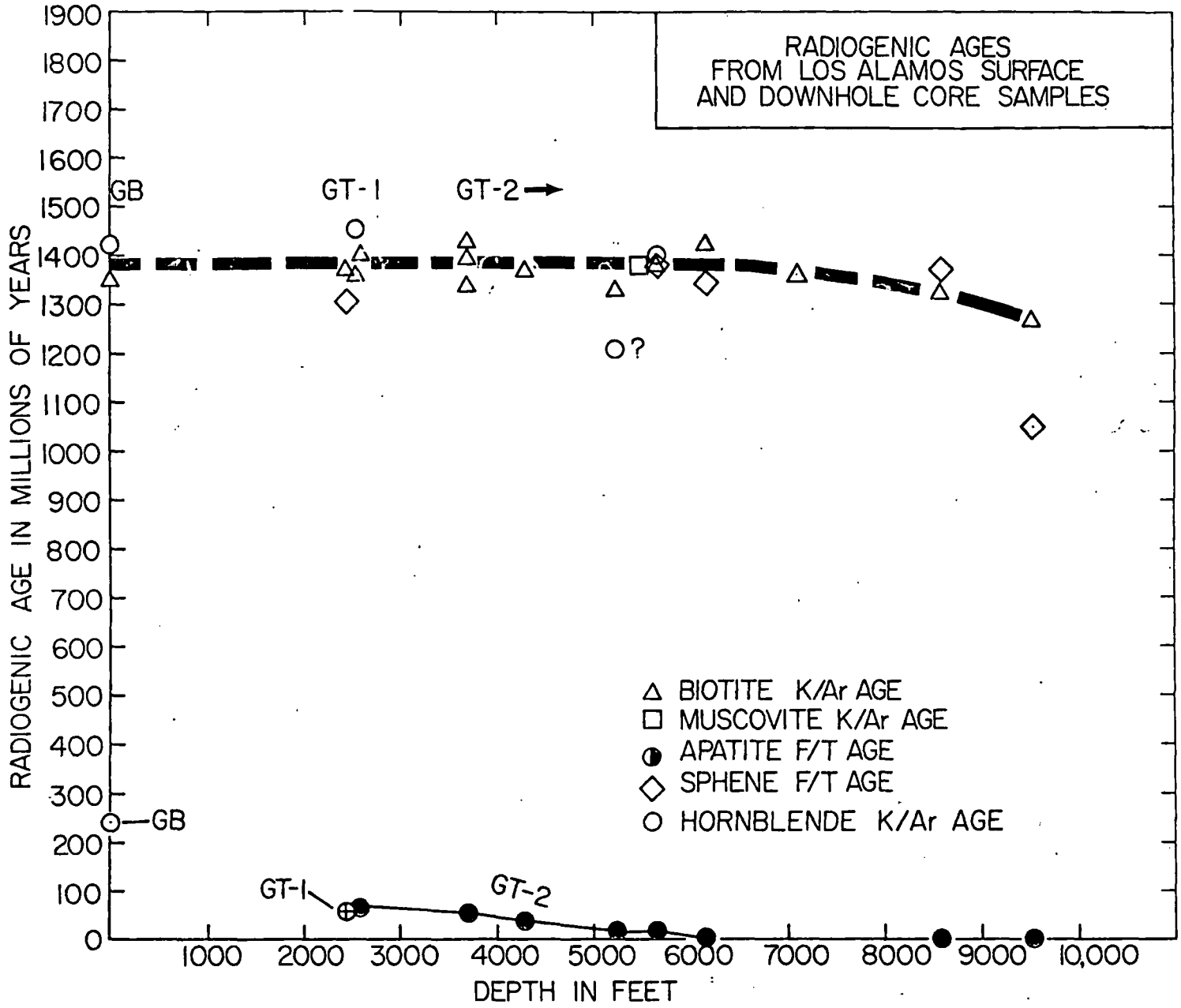

HOLE
ATURE °C

Figure 4. Radiogenic ages from Los Alamos surface and downhole core samples.

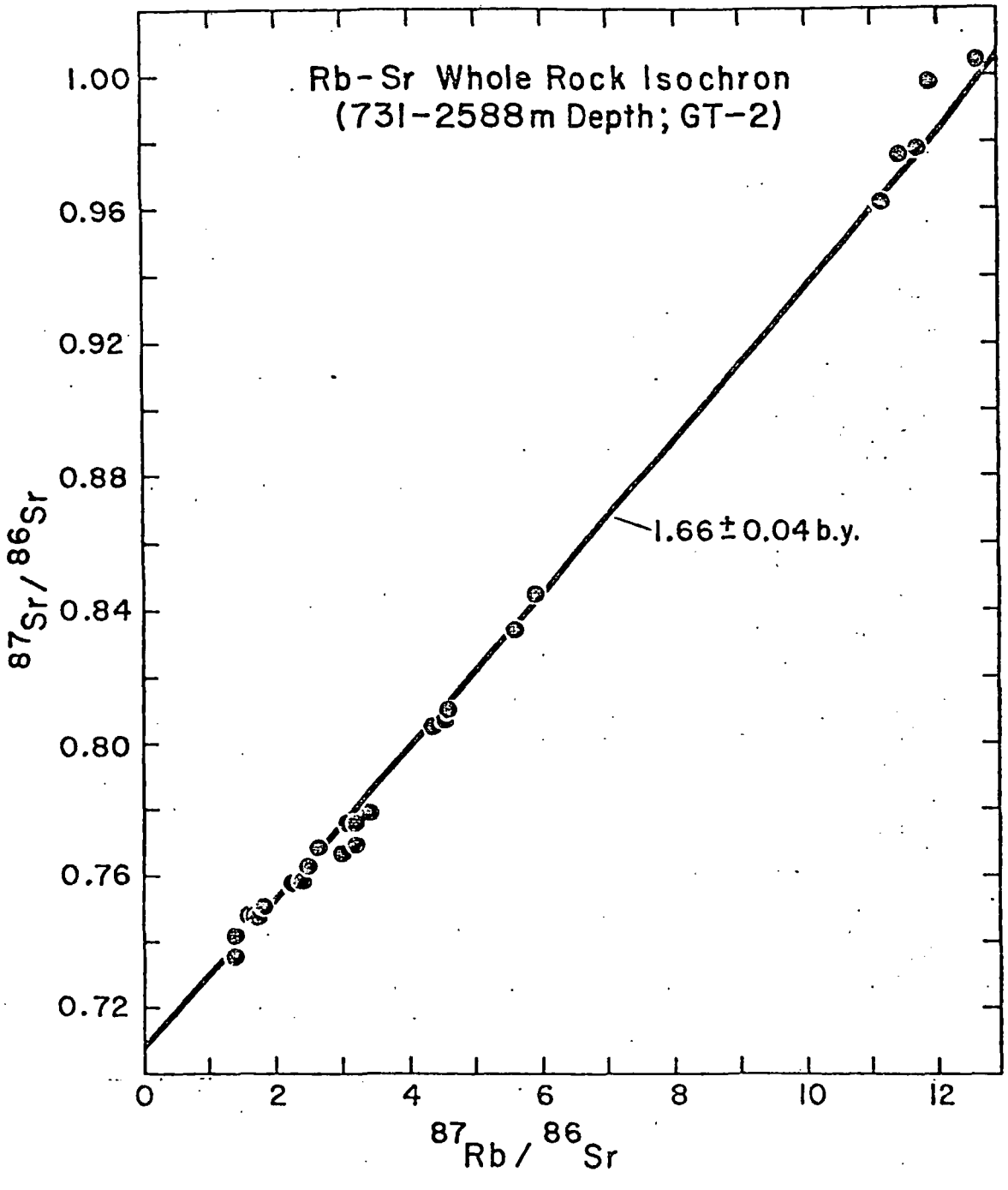

Figure 5. Rb-Sr whole rock isochron determined for GT-2 cores taken from 731-2588 meters, by Brookins (report in preparation).

which represents the time when Sr isotopes were last equilibrated in the whole rock system.

Mica ages from the amphibolite outcrop, all GT-1 samples, and GT-2 samples down to 7103 feet average 1.37 $\pm$ 0.03 (1σ) b.y. This average age is shown by the dashed line in Figure 4, and it is concordant with Brookins' whole rock Rb/Sr isochron age of 1.4 $\pm$ 0.2 b.y. for the leucocratic monzogranite dike, which cuts the gneisses in the interval between 1295 and 1311 meters in GT-2; which leads us to conclude that the intrusion of the dikes was accompanied by a thermal event of sufficiently high temperature to reset the K-Ar mica ages.

The 135°C temperature measured at a depth of 1.88 km, rather than the 50-60°C temperatures encountered at similar depths in areas with "normal" geothermal gradients is presumed to be related to Valles Caldera volcanism. However, these temperatures were not sufficiently high to partially reset the 1.37 b.y. ages. At depths of 2.67 and 2.90 km, however, temperatures were high enough at some time in the geologic past to cause additional argon loss, reducing the 1.37 b.y. age to 1.32 and 1.26 b.y., respectively. This effect is shown graphically in Figure 4.

Interpretation of amphibole age data:

Amphiboles are considered to be more resistant to thermal resetting by argon loss, than biotite or muscovite. This observation is reinforced by the 1.41 b.y. hornblende versus 1.35 b.y. biotite age from outcrops at Guadalupe Box, and the 1.44 b.y. hornblende versus 1.35 b.y. biotite age from the 2540 foot interval of GT-1. In GT-2, hornblende and biotite ages are essentially concordant at the 5654 foot and 7103 foot intervals.

The amphibole-biotite pair from the 5234 foot interval of GT-2, however, gives a rather surprising result. The hornblende age is anomalously low at 1.21 b.y. (2 replicate analyses), while the biotite gives the expected age of 1.33 b.y. A significant kink was measured in the GT-2 geothermal gradient at this depth (Figure 3), which may indicate recent hydrothermal encroachment.

In this regard, Kulp and Basset (1961) have shown that $^{40}K/^{40}Ar$ ages are unaffected by the removal of up to 50% of the potassium in biotites by base exchange in laboratory experiments. However, comparable experiments have not been conducted on amphiboles. The discordance may be due to hydrothermal resetting of the hornblende age, with no accompanying effect on the biotite. This speculation is supported by the fact that the fission track apatite age is also partially reset at this depth, as discussed in a following section.

Interpretation of fission track age data:

Based on the 1.66 b.y. Rb/Sr whole rock isochron determined by Brookins for the basement rocks, and the relatively small area of the geothermal anomaly, we had hoped that comparative radiogenic (FT, K/Ar, Rb/Sr) dating of basement rock (amphibolite and gneiss) samples from the cores versus those taken from outcrops 13 to 16 miles southeast of the GT-1 drill site, would reveal whether or not the thermal perturbation associated with high heat flow was related to Valles volcanism or an earlier thermal event.

We first determined the comparative apatite fission track ages of apatite from amphibolites taken from an outcrop in Guadalupe Box (ca. 16 miles southeast of the GT-1 drill site) and core from the 2439' level in

GT-1. As shown in Table 2, the results were very encouraging, as the apatite from a depth of 2439' level in GT-1 where the temperature was approximately 100°C gave a FT age of 54.3 ($\pm$ 10.8) m.y. versus 242 ($\pm$ 48) for apatite taken from the Guadalupe Box outcrop sample, where a $^{40}K/^{40}Ar$ age of 1.3 b.y. had also been determined for coexisting biotite.

The 242 m.y. rather than Precambrian apatite FT age is most probably related to the rise and retreat of crustal isotherms caused by the accumulation of Pennsylvanian, Permian, and Mesozoic rocks, and the subsequent uplift and erosion of part of the sedimentary cover.

FT/K-Ar studies of core from GT-2 have shown a systematic downhole decrease in the apparent FT age of apatite which approaches a linear depth-temperature function (Figure 6 and Table 2). The 68.6 ($\pm$ 7) m.y. apatite FT age of the quartz monzonite which underlies the erosional unconformity penetrated by GT-2, is similar to that determined for quartz monzonite at a similar depth in GT-1 (54.3 [$\pm$ 10.8] m.y.). The 54-68 m.y. apatite FT age of basement rocks at an average depth of 2500' in the two holes, indicates that the apatite fission track age has been reset (partially annealed) by the same thermal perturbation. As shown in Figure 6 and Table 2, the apparent apatite fission track age decreases to 0 at 6154', where the downhole temperature is 135°C. Apatites from core sampled at the 8581' and 9525' intervals also give zero ages.

Figure 7 is a downhole temperature-apatite fission track age diagram which contains three curves plotted for the following: (1) measured fission track age/downhole temperature data for GT-2; (2) calculated fission track age/downhole temperature data based on an initial 242 m.y. apatite fission track age, and annealing curve data for 10^7 years; (3) same as (2) above, as calculated for 10^6 years.

Table 2

Table of Data for Apatite
Fission Track Ages of Rocks from GT-2 Core

Feet	Depth	Kilometers	Rock Type	Fission Track Age in Millions of Years	Downhole Temperature
Surface	Outcrop	0.00	amphibolite	242.0 (± 48) m.y.	Ambient
2439'	GT-1	.74	quartz monzonite	54.3 (± 10.8) m.y.	100°C
2580'	GT-2	.79	quartz monzonite	68.6 (± 7) m.y.	100°C
3697'	GT-2	1.13	quartz monzonite	55.1 (± 6) m.y.	110°C
4279'	GT-2	1.3	quartz monzonite	38.2 (± 4) m.y.	113°C
5234'	GT-2	1.6	granodiorite gneiss	13.2 (± 1.3) m.y.	125°C
5654'	GT-2	1.72	hornblende-biotite-plagioclase schist	17.4 (± 1.7) m.y.	128°C
6154'	GT-2	1.88	granodiorite	0.0 m.y.	135°C
7103'	GT-2	2.17	granodiorite	0.0 m.y.	---
8581'	GT-2	2.61	granodiorite	0.0 m.y.	177°C
9525'	GT-2	2.90	granodiorite	0.0 m.y.	197°C

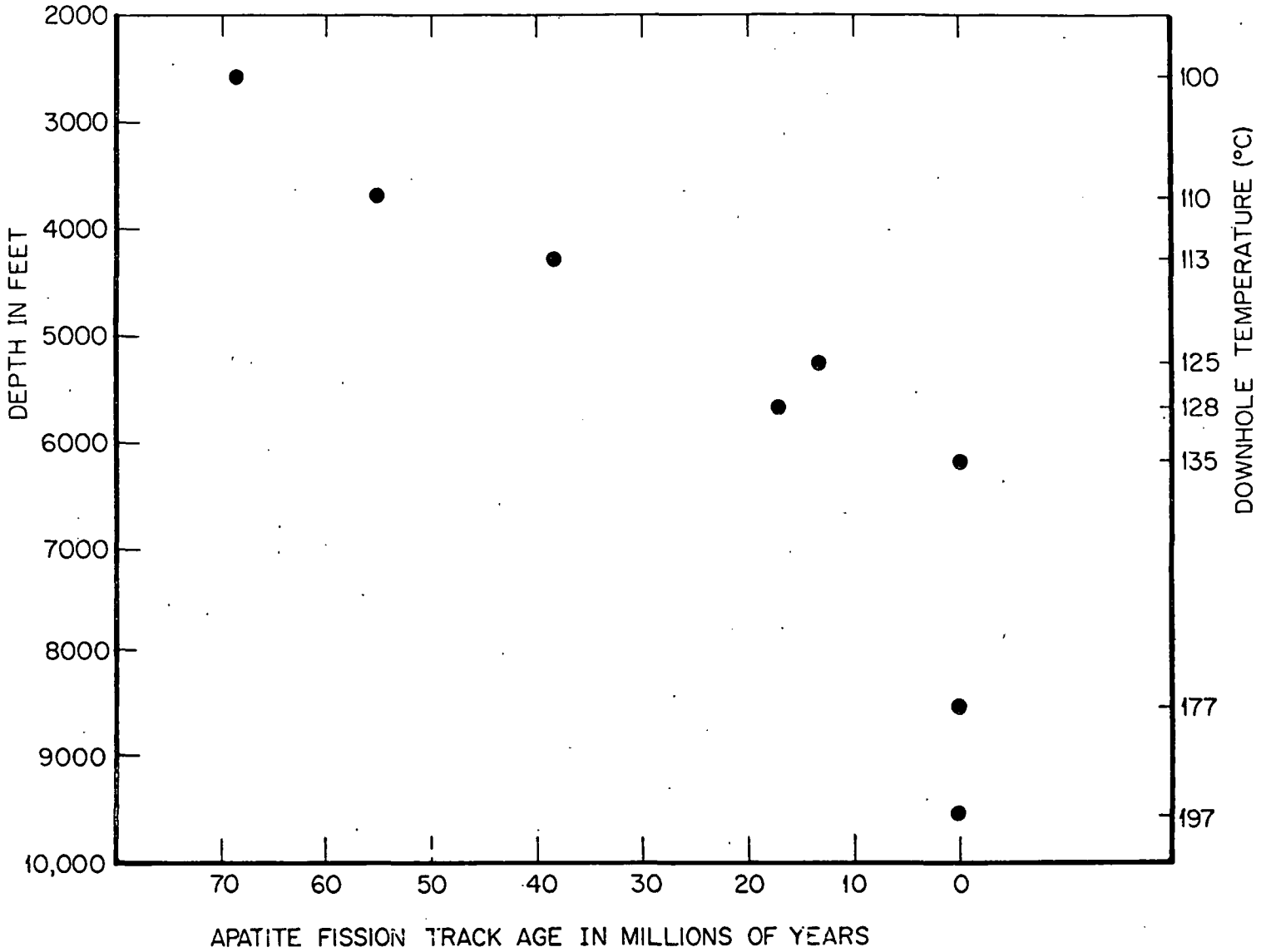

Figure 6. Depth/apparent fission track age diagram for apatite taken from GT-2 core.

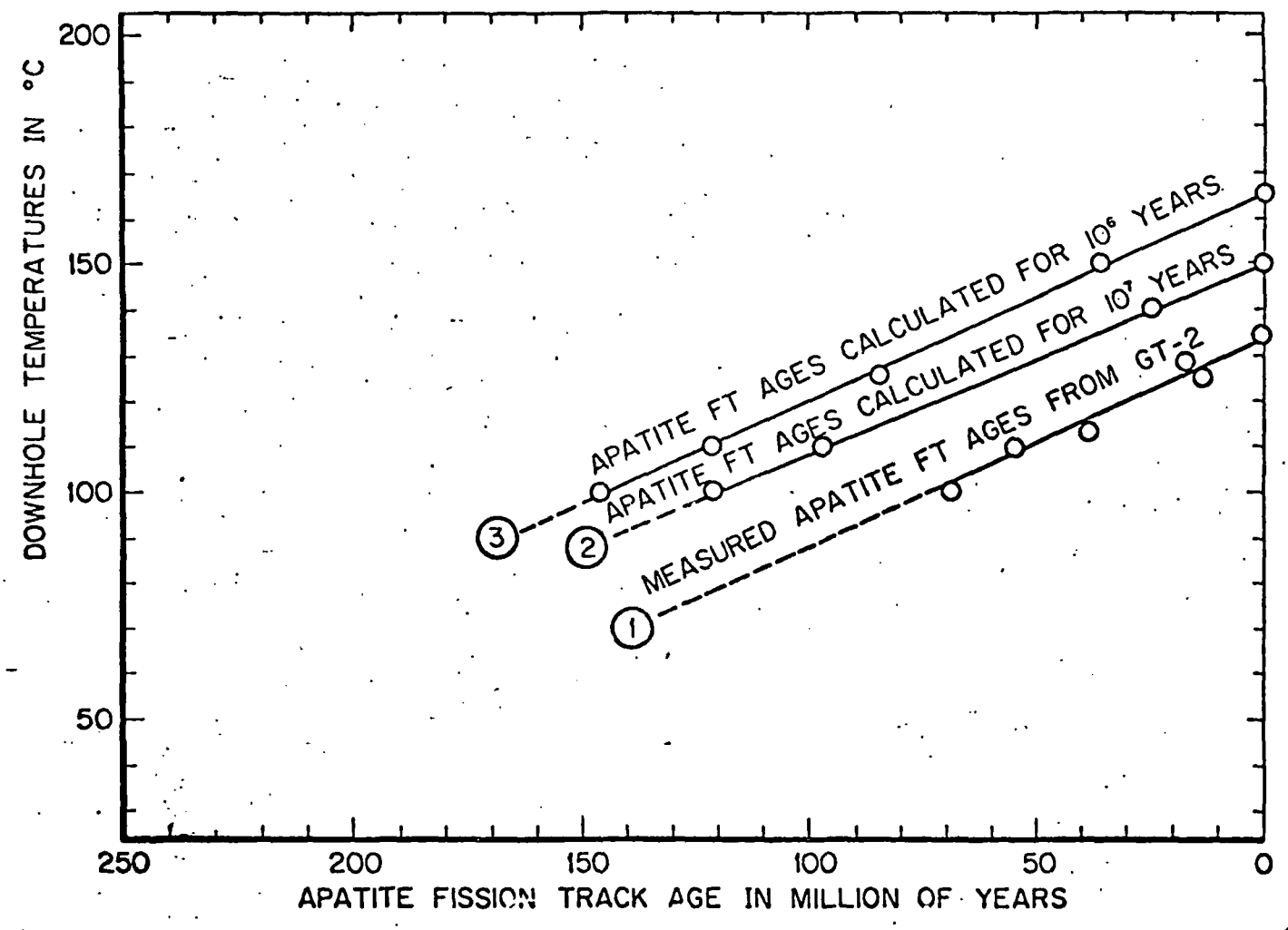

Figure 7. Apatite fission track age/downhole temperature diagram.

Line #1, Figure 3, reinforces the premise that the decreasing downhole apatite fission track ages are the result of progressive annealing of apatite with an ititial fission track age similar to that determined for apatite from the Guadalupe Box outcrops (242 m.y.). Curves #2 and #3, as plotted from data on the annealing curves, show that measured downhole temperatures are somewhat low to achieve 100% annealing of apatite fission tracks at 6154' in 10^6 or 10^7 years, and that a temperature of 150°C would be required to completely anneal the apatite at 6154' in 10^7 years. However, a 20°C discordance for 100% annealing in 10^6 years is very small, considering the fact that the annealing data were extrapolated to 10^9 years from experimental runs of 2-3 weeks. Most importantly, a zero age at a downhole temperature of 135°C indicates a relatively recent geothermal perturbation (10^7 years).

Maximum temperatures associated with the perturbation can be estimated from the data displayed on Figure 4. The plots indicate that neither biotite nor hornblende have experienced argon loss (as indicated by a decrease in apparent age) above 8000' in the drill hole, with the exception of the amphibole from a depth of 5234', which appears to have been hydrothermally altered.

The onset of argon outgassing in biotite is believed to occur between 200 and 250°C, and the negative deflection in the curve on Figure 4, appears to be valid, based on the 1260 m.y. biotite age at the bottom of the hole. The lowered sphene fission track age (1050 m.y.) also suggests the previous onset of track annealing. According to previously determined sphene track annealing curves (Naeser and Faul,

1969) (Calk and Naeser, 1973), bottom hole temperatures should have exceeded 300°C to have produced about 20% partial track annealing in 10^7 years. This estimated temperature appears to be excessive, however, based on our understanding of argon blocking temperatures in biotite. Previously perturbed bottom hole temperatures of 300 to 350°C, declining to the present temperature of 197°C should have produced much younger apparent biotite ages; an enigma which leads us to question the validity of the sphene fission track age of core from the bottom of the drill hole.

Apatite Fission Track Annealing Experiments

The discordance between the measured and calculated downhole apatite fission track ages, as illustrated in Figure 7, suggested to us that the apatite track annealing curves (Figure 8), which have been extrapolated from laboratory experiments, may have been displaced toward higher temperatures than those which apply to natural systems. We were specifically concerned that the discordance might be due to the fact that the track annealing curves had been derived from dry incremental heating experiments at 1 atmosphere, while track annealing phenomena in natural systems could be affected by confining and water partial pressure. We therefore conducted a series of laboratory experiments on the comparative annealing behavior of apatite under pressures up to 1.5 kilobars, in the presence of water, at temperatures of 270°C (as compared to dry experimental runs at 1 atmosphere).

The experiments were performed in our Temptes HRB-4 hydrothermal unit, in test tube bombs, by Dr. Daniel Hawkins, and fission track analysis were done by C. Naeser at the U.S.G.S. Denver Federal Center.

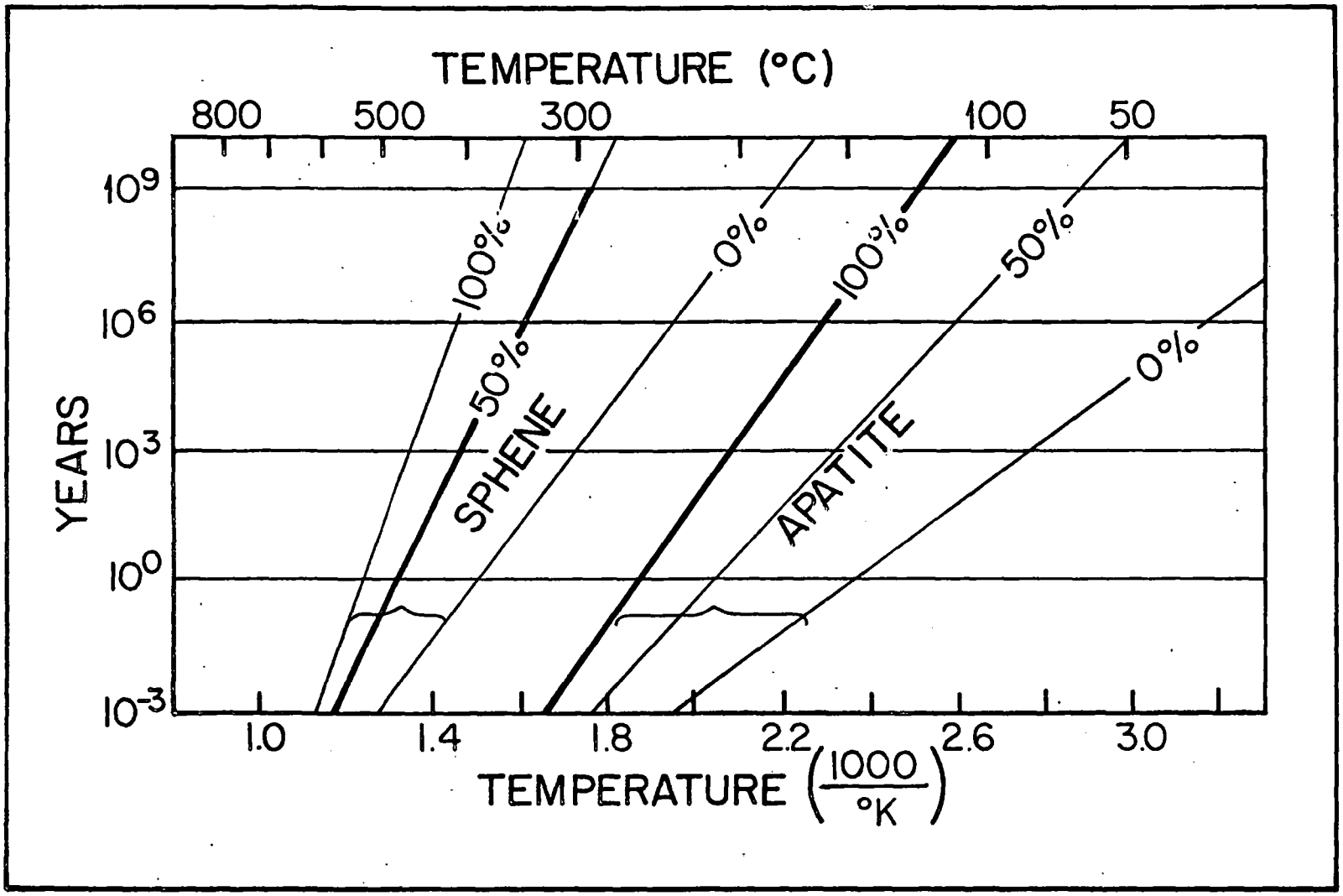

Figure 8. Experimentally determined track-loss curves for sphene and apatite. (Calk and Naeser, 1973)

The first experiment included 98-hour runs on wet and dry charges, at 271-273°C and pressure increments of 1 atmosphere and 500, 1140 and 1673 bars. The results of the first experiment are summarized in Table 3.

Based on the above data, there does not seem to be any significant difference in the amount of track annealing in the wet or dry runs with increasing pressure.

We have also conducted a second experiment, to investigate apatite annealing behavior over 8 rather than 4 days, in the presence of distilled water, 2 m Na_2CO_3 and 2 m NaF aqueous solutions. These two solutions were chosen because the carbonate solution is strongly basic and has both OH^- and CO_3^- ions which should substitute in the apatite structure; and the NaF solution was selected to see if F^- diffusion could affect fission track annealing in apatite. The design of the experiment is outlined below:

Table 4

Sample	Temp.	Pressure (bars)	Condition	Time
1	276	1	Dry	8 days
2	272	513	Dist. H_2O	"
3	272	513	2mNa_2CO_3	"
4	272	513	2m NaF	"
5	270	1066	Dist. H_2O	"
6	270	1066	2mNa_2CO_3	"
7	270	1066	2mNaF	"
8	273	1550	Dist. H_2O	"
9	273	1550	2mNa_2CO_3	"
10	273	1550	2mNaF	"

Table 3

Apatite Fission Track Annealing Data From Experiment #1

Run	Temperature °C	Pressure (bars)	Time (hrs)	No. Tracks Counted	Ps $t/cm^2 \pm \sigma$	* Track Loss (% annealing)
1 (dry)	273	500	98	607	$1.46 \times 10^5 \pm 0.06$	15.1
2 (wet)	273	500	98	675	$1.62 \times 10^5 \pm 0.06$	5.7
3 (dry)	272	1140	98	626	$1.50 \times 10^5 \pm 0.06$	12.6
4 (wet)	272	1140	98	610	$1.46 \times 10^5 \pm 0.06$	15.1
5 (dry)	271	1 atmosphere	98	624	$1.50 \times 10^5 \pm 0.06$	12.6
6 (dry)	272	1673	98	637	$1.53 \times 10^5 \pm 0.06$	11.1
7 (wet)	272	1673	98	626	$1.50 \times 10^5 \pm 0.06$	12.6

Average = 1.51×10^5 t/cm^2 Average = 12.1% annealing

$\sigma = \pm 0.054 \times 10^5$

$\sigma = \pm 0.02 \times 10^5$

* % loss calculated from 1.72×10^5 t/cm^2 of unheated apatite standard, derived from 9 counting experiments on replicate fractions, by C. Naeser.

The hydrothermal laboratory runs have been completed, and C. Naeser is currently supervising track counting of the apatite grains from the various runs. Track annealing data from the second experiment will be available in April or May 1977.

Possible differences in the track annealing characteristics of volcanic versus plutonic apatite:

According to the previously determined apatite annealing curves (Figure 8), 98 hours (5.9×10^3 minutes) at 275°C should produce 50% track annealing, rather than the 12% recorded in our first experiment.

We have repeatedly calibrated our thermocouples, and we are confident that temperatures within the bombs have been measured to within $\pm$ 1% at 260°C. Naeser is equally confident in the thermometry and experimental data which were used to define his annealing curves. The most probable explanation is a possible difference in the track annealing characteristics of apatites from differing petrologic settings (e.g. intrusive, extrusive and metamorphic). Differences in crystallization temperature and chemical composition could be expected to have resultant effects on lattice geometry....and perhaps track annealing characteristics as well. We are concerned that the apatite standard used in our experiments was separated from a welded tuff; whereas the annealing curves were originally determined from experiments with apatites from plutonic rocks.

At this stage in our work, we think it would be prudent to conduct additional track annealing studies on volcanic, intrusive and metamorphic apatites to determine whether or not there is a difference in annealing characteristics, and if so....the relative magnitude of the problem.

The Eielson Drill Hole Project

The Eielson drill hole is located 26 miles southeast of Fairbanks, Alaska, and cuts regionally metamorphosed crystalline schists of the Yukon-Tanana basement complex throughout its entire depth of 9774'. It is the deepest hole yet drilled in Alaskan basement rocks, and the bottom hole temperature is 94.7°C (Figure 9).

Metamorphic grade increases with depth from the upper greenschist to the lower amphibolite facies, including the transition from the garnet through the staurolite and kyanite isograds (Table 5). Petrologic studies indicate that the initial metamorphic recrystallization temperatures of the rocks exposed in the bottom of the hole were between 580°C and 620°C and that the present geothermal gradient is similar to the gradient which existed during metamorphism (Forbes and Weber, 1975).

Figure 10, a depth/temperature diagram, illustrates the measured geothermal gradient as determined by Lachenbruch and Sass (unpublished data). Careful inspection of the diagram shows that the gradient is not truly linear, and that the gradient is traced by a segmented curve which defines gradients of 34-41°C.

Figure 11 illustrates the relationship between $^{40}K/^{40}Ar$ and fission track mineral ages versus depth in seven core samples from the Eielson hole, and five cores from shallow depths (140' and 275') in adjacent test holes. Measured downhole temperatures are shown along the top of the diagram. The plots in Figure 11 show a decrease in apparent radiogenic age with increasing depth, as defined by the biotite, muscovite, and apatite curves. The hornblende ages show a reversal, which may (or may not) be reflected in the small deflections(?) which appear to be present

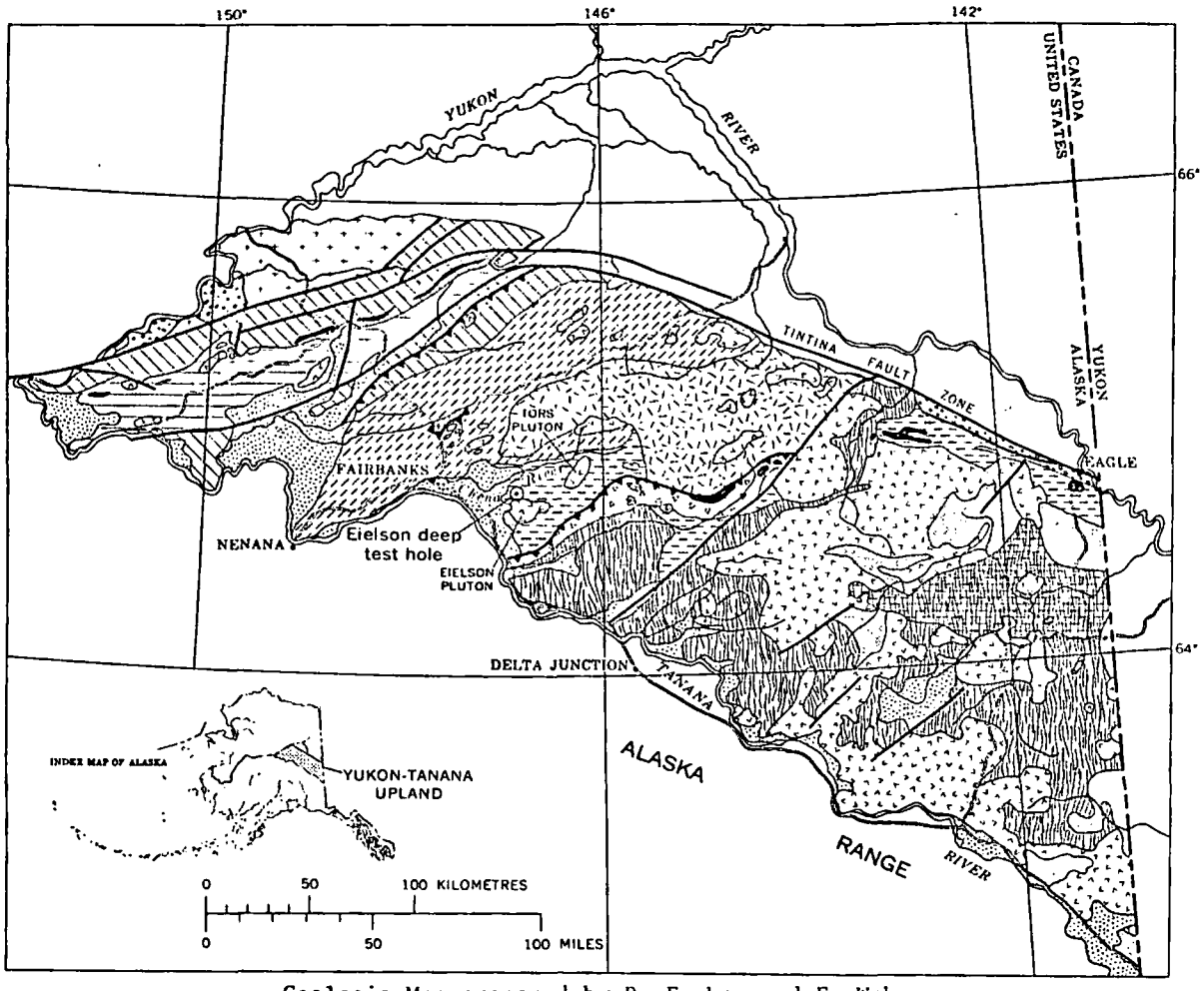

Geologic Map prepared by R. Forbes and F. Weber

EXPLANATION

SEDIMENTARY AND METAMORPHIC ROCKS

- Alluvium of Yukon-Tanana Upland and Tanana Valley — QUATERNARY
- Conglomerate, sandstone, shale, and tuff (nonmarin — CRETACEOUS AND (OR) TERTIARY
- Conglomerate, graywacke, quartzite, shale, and siltstone — JURASSIC AND (OR) CRETACEOUS
- Quartzite, phyllite, grit, slate, chert, limestone, greenstone, dolomite, conglomerate, siltstone, and graywacke — CAMBRIAN(?) TO DEVONIAN

METAMORPHIC ROCKS

- Undifferentiated metamorphic rocks
- Quartz-mica schist, quartzite, greenschist, amphibolite, and marble
- Greenschist-facies rocks
- Quartz-mica schist, quartzite, carbonaceous schist, chlorite, actinolite, and quartz schists, greenstone, and phyllite — PRECAMBRIAN AND (OR) PALEOZOIC
- Phyllite, calc-phyllite, slate, and quartzite; carbonaceous, quartz-mica, chlorite, calcareous, actinolite, and quartz schists; marble and greenstone
- Greenschist- to epidote-amphibolite-facies rocks (transitional)
  Includes mica schist and quartz-mica schist
- Amphibolite-facies rocks
- Quartz-mica gneiss and schist (much is garnetiferous), quartzite, amphibolite, and augen gneiss
  Orthogneiss where stippled
- Quartz-mica gneiss and schist (much is garnetiferous), quartzite, amphibolite, and marble
- Cataclastic rocks including augen gneiss
- Eclogitic rocks interlayered with calcium-magnesium schists — PRECAMBRIAN AND (OR) PALEOZOIC

IGNEOUS ROCKS

- Mostly granodiorite and quartz monzonite but includes other granitic rocks and mafic to felsic volcanic rocks — MESOZOIC AND CENOZOIC
- Diabase, diorite, gabbro, and basaltic volcanic rocks intruded into and interlayered with chert, shale, siltstone, graywacke, sandstone, and conglomerate (Rampart Group) — PERMIAN(?)
- Serpentinite, peridotite, diorite, gabbro and metabasalt — DEVONIAN(?) AND OTHER PALEOZOIC(?)

Geology not shown north of Tintina fault zone or south of Tanana River

Fault
Includes buried, approximate, and doubtful segments.

Thrust fault
Sawteeth on upper plate

Approximate contact

Figure 9. Geologic map of the Yukon-Tanana Basement Complex, showing the location of the Eielson Test Hole.

Table 5. Petrologic data for the Eielson Core Samples (Forbes and Weber, 1975)

Core	Depth (ft)	Rock type	Constituent minerals: Major (>10 percent)	Minor (2–10 percent)	Accessory (<2 percent)	Metamorphic facies or isograd
DDH1	40	Calc-mica schist	Carbonate, muscovite, quartz,	Sphene, plagioclase (albite), chlorite.	Phlogopite, opaques, zircon, apatite.	Greenschist.
DDH2	521	do	do	Chlorite, sphene, plagioclase (albite).	Phlogopite, apatite, opaques.	Do.
EDT1	1,032 1,034 1,035½	do	do	Chlorite	Opaques, plagioclase (albite), sphene, apatite, tourmaline.	Do.
EDT2	2,010	Calc-mica-phlogopite schist.	Carbonate, muscovite, quartz, phlogopite.	Chlorite, sphene	Tourmaline, plagioclase (albite), opaques, zircon(?), apatite.	Do.
EDT3	2,341	Phlogopite-clinozoisite schist.	Phlogopite, quartz, epidote (clinozoisite).	Plagioclase (albite), muscovite.	Sphene, apatite, opaques.	Do.
	2,343½	Calc-mica schist	Carbonate, muscovite, quartz, phlogopite.		Opaques, sphene	Do.
	2,345	Clinozoisite-carbonate-mica schist.	Carbonate, muscovite, quartz, phlogopite, epidote (clinozoisite).		Tourmaline, opaques, albite, sphene.	Do.
EDT4	3,193	Calc-greenschist	Amphibole (actinolite), biotite, carbonate, epidote (clinozoisite).	Chlorite, quartz	Plagioclase (albite), opaques sphene.	Do.
	3,195½	do	Chlorite, phlogopite, actinolite, carbonate.	Quartz	Sphene, plagioclase (albite), epidote.	Do.
EDT5	4,065	Garnet-bearing quartz-mica schist (hornfels?).	Quartz, muscovite, garnet.	Plagioclase, chlorite.	Tourmaline, carbonate.	Albite-epidote-hornfels(?).
	4,066	Garnet-tourmaline rocks (hornfels?).	Garnet, tourmaline, quartz, plagioclase (albite-oligoclase).	Chlorite, muscovite	Opaques	Do.
	4,067½	Garnet-mica schist (hornfels?).	Quartz, muscovite	Tourmaline, chlorite.	Opaques, plagioclase (albite-oligoclase).	Albite-epidote.
						Possible garnet isograd.
EDT6	5,011	Garnet-mica schist	Muscovite, plagioclase (oligoclase), garnet, quarts.	Biotite, plagioclase (oligoclase).	Opaques, chlorite	Albite-epidote.
	5,013	do				
EDT7	6,141	Biotite-bearing amphibolite.	Hornblende, biotite.	Plagioclase (oligoclase), quartz, opaques.	Apatite, sphene	Do.
	6,142	Garnet-mica schist	Biotite, muscovite, quartz.	Plagioclase (albite-oligoclase), garnet.	Epidote, opaques	Do.
	6,143	Biotite-amphibolite	Hornblende, biotite.	Plagioclase (oligoclase), quarts, sphene.	Apatite	Do.
EDT8	7,140	Epidote-bearing quarts-mica schist.	Biotite, muscovite, plagioclase (oligoclase), quarts.	Epidote (clinozoisite).	Opaques, apatite	Do.
EDT8—Con.	7,140½	Garnet-mica schist	Muscovite, biotite, garnet, quarts, plagioclase (albite-oligoclase).		Epidote, opaques, apatite.	Do.
	7,142½	Biotite-hornblende schist.	Hornblende, biotite.	Quarts	Sphene, opaques, plagioclase.	Do.
	7,144	do	Hornblende, biotite.	Sphene, plagioclase (oligoclase), quarts, garnet.	Opaques, epidote, chlorite.	Do.
						Kyanite and staurolite isograds.
EDT9	8,216	Kyanite-staurolite schist.	Muscovite, garnet, kyanite, quartz.	Staurolite, plagioclase (oligoclase), biotite.	Opaques, chlorite	Amphibolite facies.
	8,217	do	Biotite, muscovite, garnet, staurolite, quartz.	Plagioclase (albite-oligoclase), tourmaline, kyanite.	do	Do.
	8,218	do	Biotite, muscovite, garnet, plagioclase (oligoclase), quartz.	Tourmaline, kyanite, staurolite.	do	Do.
	8,218½	Andalusite-bearing kyanite-staurolite schist.	Biotite, muscovite, garnet, kyanite, quartz.	Staurolite andalusite, plagioclase (oligoclase).	do	Do.
EDT10	9,196	Biotite-epidote schist.	Biotite, epidote, quarts.	Sphene, plagioclase (oligoclase).	Opaques, apatite	Do.
	9,198	Quarts-mica schist	Muscovite, quartz	Chlorite, plagioclase (oligoclase), biotite.	Apatite, opaques, allanite.	Do.
EDT11	9,766	Diopside-bearing actinolite-carbonate-mica schist.	Carbonate, phlogopite, quartz, plagioclase (oligoclase).	Actinolite, K-feldspar, diopside.	Sphene, zoisite	First evidence of reaction tremolite +3 calcite +2 quartz +5 diopside +3 CO_2 +H_2O.
	9,767	do	Carbonate, phlogopite, actinolite, quarts, plagioclase (albite-oligoclase).	Muscovite	Sphene, opaques	Amphibolite facies.
	9,770	Actinolite-bearing calc-mica schist.	Phlogopite, muscovite, quarts, plagioclase (oligoclase).	Carbonate, actinolite.	Sphene, zoisite, opaques.	Do.

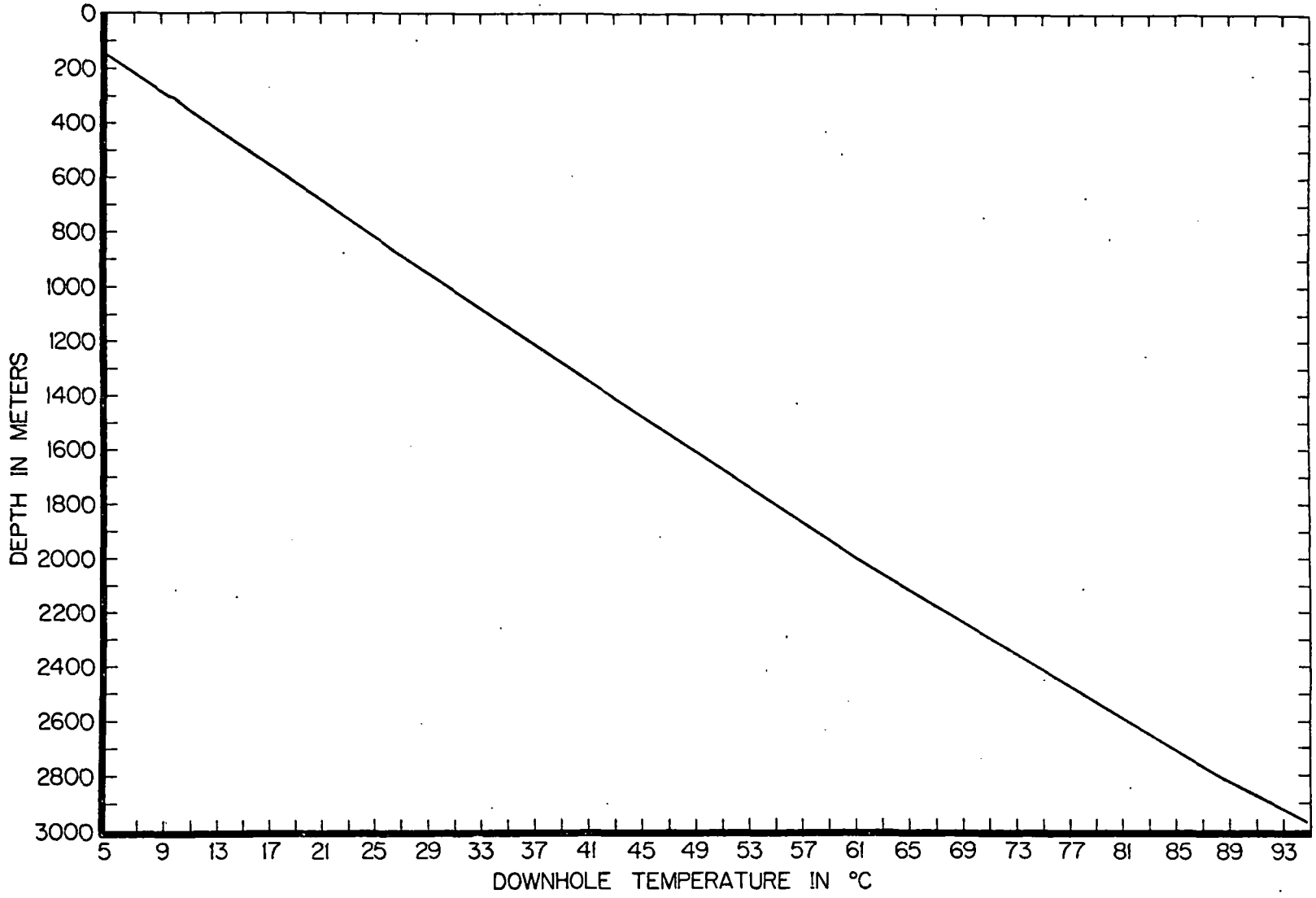

Figure 10. Measured downhole temperatures in the Eielson drill hole. (Lachenbruch and Sass, unpublished data)

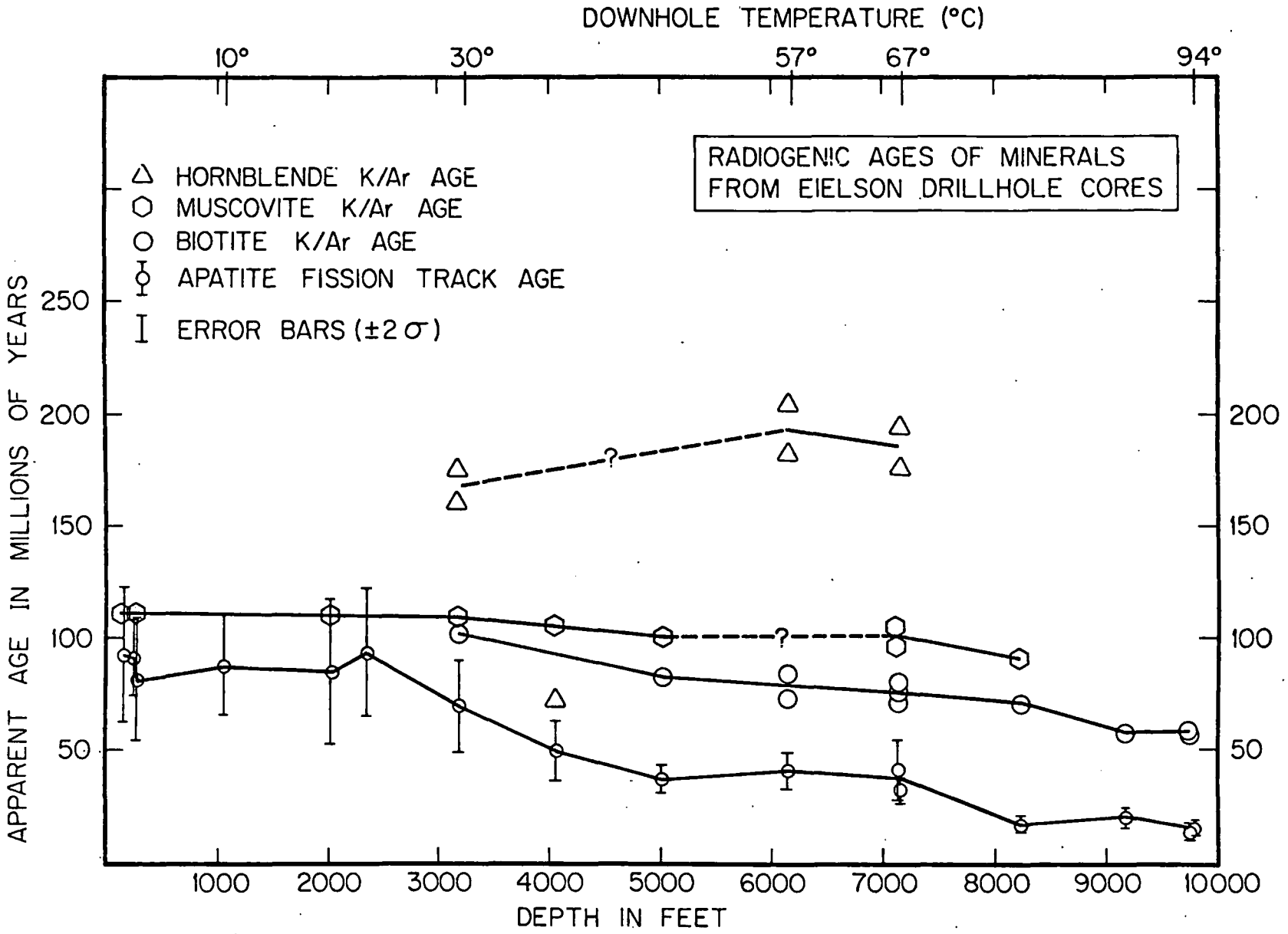

Figure 11. Apparent age/depth diagram for minerals from the Eielson drill hole cores.

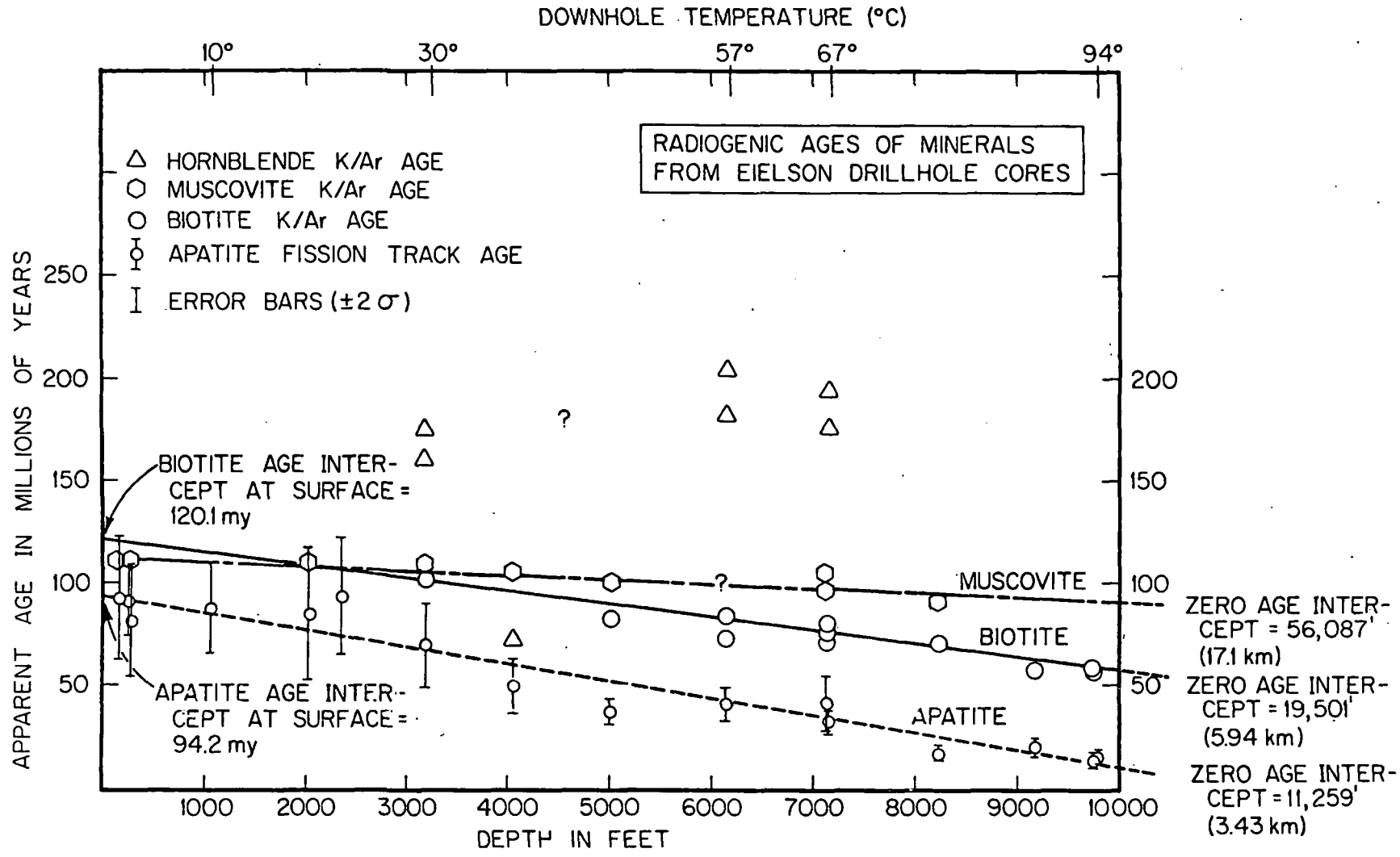

Figure 11A. Apparent age/depth diagram with best fit regression lines for muscovite, biotite and apatite plots.

between 5000' and 7000' in the mica and apatite curves. Figure 11A shows best fit lines for biotite, muscovite and apatite plots, as determined by linear regression analyses.

Depth/age relations of apatite:

Although there is considerable scatter and the probability of large analytical error in the apatite plots for the upper 5000' of the hole, apparent apatite fission track age shows a consistent decrease with increasing depth in the hole (Table 6). A best fit line through the apatite plots gives a zero age intercept of 11259' (3.43) km, where the extrapolated temperature is 141°C, using 41°C/km as the thermal gradient, as taken from the 2700'-3000' segment of the measured geothermal gradient curve in Figure 10. If a 34°C gradient is used, the temperature would be 117°C.

A comparison of the projected zero apatite age (3.43 km/113°C) from Eielson hole data to that from GT-2 (1.88 km/135°), provides contrasting examples of apparent apatite fission track age relations in perturbed versus more representative geothermal gradients; and reinforces the importance of the 100°C isotherm and apatite annealing in natural systems.

Depth/age relations of biotite and argon blocking temperatures:

The downhole decrease in apparent biotite $^{40}K/^{40}Ar$ age approaches a linear function as shown by the excellent fit of the regression line (correlation coefficient = .9666) in Figure 11. The zero biotite age intercept is calculated to be at 19,501' (5.94 km) with a temperature of 215°C, based on a projected thermal gradient of 41°C/km.

These data are important to geochronology, as they provide a geologically determined value for the argon blocking temperature of biotite in metamorphic rocks. These data suggest that the biotite

Table 6. Apatite fission track age data for the Eielson cores

Sample	Mineral	ρ_s x10^3 t/cm^2	ρ_i x10^3 t/cm^2	T x10^6 yr	±σ	U ppm
DDH-140 (DF-1283)	Apatite	5.28 (22)	3.60 (15)	93	31	0.10
DDH-238 (DF-1289)	Apatite	17.76 (74)	12.48 (52)	91	16	0.36
DDH-275 (DF-1284)	Apatite	4.56 (19)	3.60 (15)	81	28	0.10
EDT-1035 (DF-1270)	Apatite	8.64 (36)	6.24 (26)	88	23	0.18
EDT-2010 (DF-1271)	Apatite	3.84 (16)	2.88 (12)	85	32	0.08
EDT-2341 (DF-1272)	Apatite	6.00 (25)	4.08 (17)	94	29	0.12
EDT-3195 (DF-1273)	Apatite	5.52 (23)	5.04 (21)	70	21	0.15
EDT-4065 (DF-1274)	Apatite	5.28 (22)	6.72 (28)	50	14	0.20
EDT-5010 (DF-1275)	Apatite	12.70 (53)	21.60 (90)	38	6	0.63
EDT-6141 (DF-1276)	Apatite	9.84 (41)	14.88 (62)	42	8	0.43
EDT-7140 (DF-1277)	Apatite	3.60 (15)	5.52 (23)	42	14	0.16
EDT-7142 (DF-1278)	Apatite	15.60 (65)	30.50 (127)	33	5	0.89
EDT-8218 (DF-1279)	Apatite	20.40 (85)	81.80 (341)	16	2	2.40
EDT-9196 (DF-1280)	Apatite	4.80 (20)	15.36 (64)	20	5	0.45
EDT-9766 (DF-1281)	Apatite	7.92 (33)	34.56 (144)	15	3	1.0
EDT-9770 (DF-1282)	Apatite	11.28 (47)	45.12 (188)	16	3	1.3

Neutron dose = $1.045 \times 10^{15} n/cm^2$

$\lambda_F = 6.85 \times 10^{-17} yr^{-1}$

$^{40}K/^{40}Ar$ clock is started when declining temperatures approach 215°C. Using a geothermal gradient of 34°C/km, the projected blocking temperature would be 195°C.

Depth/age relations of muscovite:

The muscovite curve is somewhat surprising as the rate of decrease in apparent age is less than would be expected, based on relatively small increase in the argon blocking temperature of muscovite versus biotite. An attempt to calculate the zero age intercept for muscovite gives a depth of 56,087' (17.1 km) and a projected temperature of 581°C, which is much higher than the estimated argon blocking temperature for muscovite derived from experimental and natural systems by other workers.

At present, we are unable to explain why the apatite and biotite data should provide geologically reasonable results, while the muscovite data from the same rocks yield an Ar blocking temperature which is apparently anomalous.

Depth/age relations of amphiboles:

The amphibole data are seemingly discordant to the other curves, as the apparent ages are older at 6141'-6142' and 7142'-7147' than those at 3193' and 4065'. Furthermore, the hornblende age at 4065' is anomalously low, compared to the other hornblende ages from the core and from outcrop samples taken from other localities in the Yukon-Tanana Uplands.

The anomalously low hornblende age from the 4065' core is difficult to explain, but the very low potassium content of this particular amphibole (.089 wt. %) may be due to selective depletion by hydrothermal leaching. As previously discussed, this process may have also lowered the apparent age of hornblende from the 5234' interval in GT-2.

In summary, we do not really understand the apparent reversal in the depth/age relations of hornblendes separated from the Eielson cores. If real, however, the reversal could be explained by low angle faulting which juxtaposed rocks from greater depth over those nearer the present surface. This model requires thrusting to have occurred while the rocks were at temperatures below the argon blocking temperature of hornblende, but higher than the blocking temperature of biotite, as the age/depth curve for the latter appears to be linear and unbroken (Figure 12A).

It is clear that age data for amphiboles from other intervals in the Eielson hole are needed, if we are to solve the problem of the apparent downhole age reversal additionally, planned $^{39}Ar/^{40}Ar$ dating, including incremental heating studies, may lead to a better understanding of the apparent anomalies.

Rate of epeirogenic uplift and erosion of the Yukon-Tanana Uplands:

We were interested in the possibility of calculating the average rate of epeirogenic uplift and removal of overlying crust, from the biotite and apatite age data. If we assume that the biotite $^{40}K/^{40}Ar$ clock was started when it passed through the 215°C isotherm at 5.94 km, it has taken 120 million years for the biotite bearing schists to reach the surface, as outcrops. According to this model, the average rate of uplift can be derived from an equation, where:

$$\text{Average rate of uplift} = \frac{\text{present depth of biotite argon blocking isotherm}}{\text{Surface biotite age}}$$

The above expression is highly simplistic, as it assumes that:

(1) No major thermal perturbations have occurred other than the downward migration of isotherms related to the erosion of overlying crust, and....

(2) The linear extrapolations to the zero age intercepts on the depth/age plots are valid.

If the biotite data displayed in Figure 11A are used, we obtain .05 mm/year as an average rate of uplift and erosion. This is a very reasonable average rate, which is in good agreement with estimates derived by other workers using different methods. Our confidence in this figure is reinforced by remarkably convergent results obtained from the apatite data, which give an average rate of .04 mm/year.

Figure 12, a depth/apparent age plot, with geotherms positioned for a geothermal gradient of 33°C/km, illustrates hypothetical cooling age paths for apatite and biotite, as derived from the intercept data in Figure 11A. The diagram also illustrates the difference in the slope of paths representing average erosion rates of .04 and .05 mm/year, and hypothetical cooling age paths for amphiboles with argon blocking temperatures of 400°, 350° and 300°C, as a function of a .05 mm/year average erosion rate.

Figure 12 shows that rapid transit through the cooling isotherms reduces the discordance in the apparent surface ages of minerals with differing blocking temperatures; while transit through the cooling isotherms in a higher geothermal gradient increases the apparent age of the minerals with less effect on discordance in the ages of minerals from the same host rock.

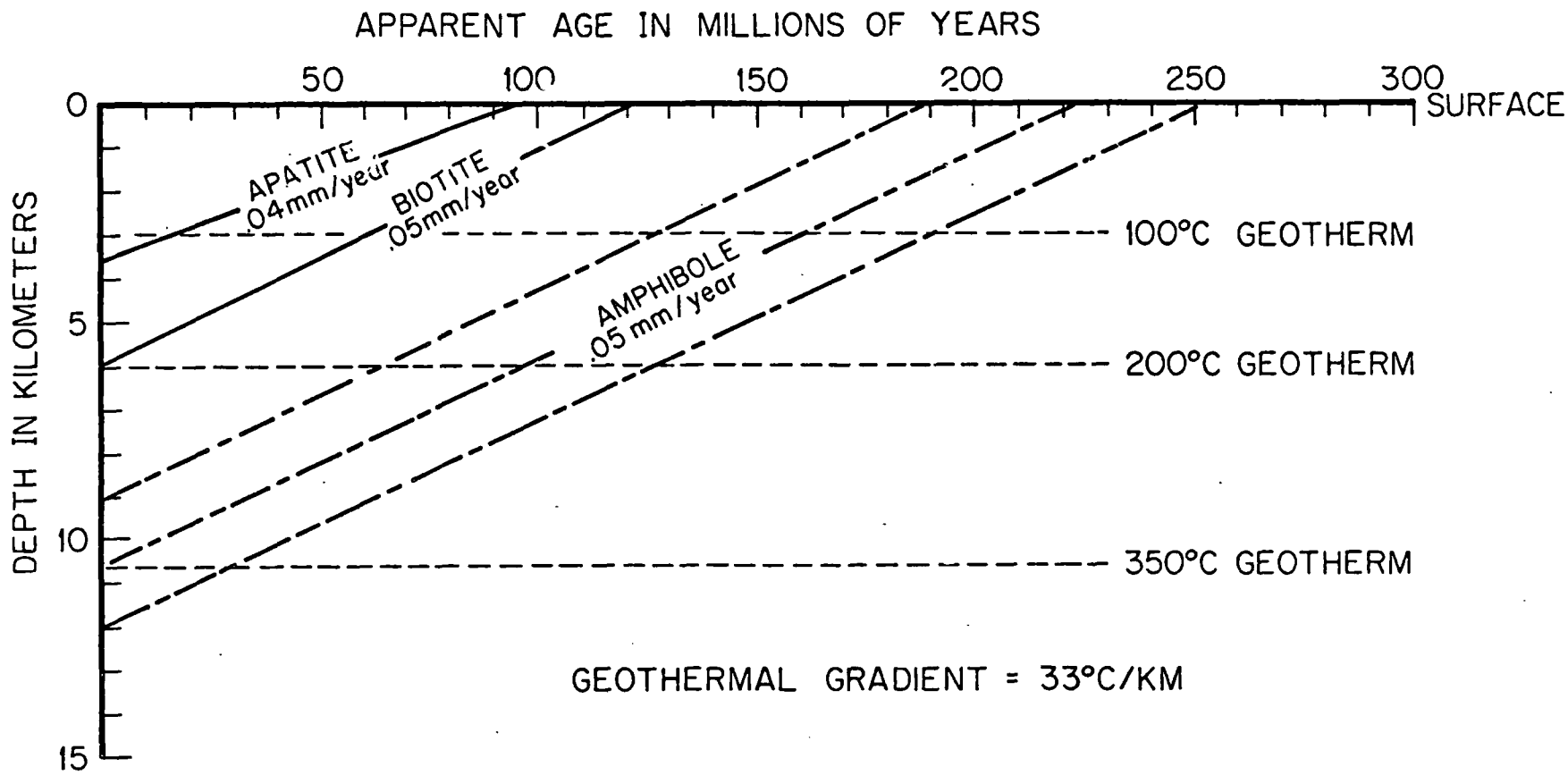

Figure 12. Depth/apparent age diagram illustrating hypothetical cooling age paths for apatite, biotite and amphibole. In fact, downhole amphibole ages do not follow this path; an anomaly which remains to be explained.

Mass Spectrometer Modifications and Improvements

One of the goals outlined in our proposal was the major upgrading of our argon mass spectrometer. We had the following objectives in mind:

1. We wished to obtain a significant reduction of the memory effect of previously-run samples on subsequent sample.

   The original source ran at an ion accelerating potential of 4000 volts, causing heavy ion bombardment of the source plates, with the result that gas from previous samples was driven into these plates, to be knocked out by ion bombardment during subsequent runs. This gas "memory" from previous runs was of different isotopic composition than that of the analyzed sample, so the measured isotopic composition of the sample would appear to vary with time during the analysis. This effect is typical in static rare gas analysis, and cannot be eliminated completely, but we wished to reduce the effect as much as possible in order to improve both the accuracy and the precision of our isotope measurements.

2. The instrument sensitivity must remain at or near the previous value.

   The sensitivity (signal output measured in volts versus size of argon sample introduced) of a mass spectrometer is a function of ion accelerating potential, as well as several other parameters. We wished to maintain our former instrument sensitivity, while running the ion source at a much lower ion accelerating potential (2000 vs. 4000 volts) in order to

reduce the memory effect discussed above. In order to do this, the ionization efficiency of the new ion source had to be several times greater than that of the old source.

3. Ionization stability must be as good or better than that of the previous ion source.
4. The electronics must be all solid state, so as to eliminate down time due to vacuum tube failures experienced with the previous ion source emission regulator.
5. Increased ionization filament life must be obtained.
6. The ion source must be self-aligning to facilitate mechanical assembly.

In order to meet these objectives, the following equipment was built and installed in October 1976.

1. Ionization source -- built by an outside contractor to specifications provided by the Isotope Geology Branch of the U.S. Geological Survey.
2. Emission regulator -- built by the electronics shop of the Geophysical Institute according to our modification of a U.S. Geological Survey solid-state design.
3. Source divider -- built by the electronics shop of the Geophysical Institute according to our modification of a U.S. Geological Survey design.

We have been extremely pleased with the results of these modifications, which have enabled us to realize every one of the objectives discussed above.

The new ion source, together with its supporting electronics, is being operated at 1800 volts ion accelerating potential versus 4000

volts for the original source, and is actually twice as sensitive as the original source. We have seen a significant decrease in the memory effect discussed above, and stability of ionization has been excellent during the three and a half months the spectrometer has been back in routine operation.

In addition, the higher sensitivity has resulted in an improved signal-to-noise ratio on ^{36}Ar peaks which has, in turn, resulted in a significant improvement in the precision of measurement.

Application of the $^{39}Ar/^{40}Ar$ Dating Method to Geothermal Studies

The approved research program included the addition of a new RF generator-incremental temperature control unit for our argon extraction system, which is essential to the planned $^{39}Ar/^{40}Ar$ studies. Currently, Dr. Turner is a visiting scientist at the U.S. Geological Survey geochronology laboratory in Menlo Park, California, where he is working with the new $^{39}Ar/^{40}Ar$ technique, in preparation for the installation of the new equipment in the Geophysical Institute geochronology laboratory.

Dr. Turner will return to the Geophysical Institute in March 1977 to install the new RF generator-incremental temperature control system and to initiate the new $^{39}Ar/^{40}Ar$ dating program.

REFERENCES

Calk, L. C. and Naeser, C. W. (1973). The thermal effect of a basalt intrusion on fission tracks in quartz monzonite: Jour. Geol., V. 81, p. 189-198.

Forbes, R. B. and Weber, F. R. (1975). Progressive metamorphism of schists recovered from a deep drill hole near Fairbanks, Alaska: Jour. Research, U.S. Geological Survey, V. 3, No. 6, Nov.-Dec. 1975, p. 647-657.

Kulp, J. L. and Basset, W. H. (1961). The base exchange effects on K-Ar and Rb-Sr isotopic ages: Ann. N.Y. Acad. Sci., V. 91, Art. 2, p. 225.

Naeser, C. W. and Faul, H. (1969). Fission track annealing in apatite ans sphene: Jour. Geophys. Res., V. 74, p. 705-710.

APPENDIX A

EIELSON HOLE (EDT)

Sample No.	Rock Type	Mineral Dated	K_2O (weight percent)	Sample Weight (grams)	$^{40}Ar_{rad}$ (moles/gm) $\times 10^{-11}$	$\frac{^{40}Ar_{rad}}{^{40}K} \times 10^{-3}$	$\frac{^{40}Ar_{rad}}{^{40}Ar_{total}}$	Age $\pm$ 1 σ (m.y.)
1035.5' (76234)		impure muscovite	9.283 9.303 $\bar{x}$ = 9.293	0.1941	154.835	6.596	0.910	109.5 $\pm$ 3.3
1035.5' (77001) replicate		impure muscovite	"	0.1247	261.199	11.130	0.888	181.2 $\pm$ 5.4 $\bar{x}$ = 145.3
2010' (76142)		muscovite	9.420 9.410 9.440 9.425 $\bar{x}$ = 9.424	0.2969	157.434	6.614	0.826	109.8 $\pm$ 3.3
2010 (76155) replicate		muscovite	"	0.3008	158.604	6.663	0.878	110.6 $\pm$ 3.3 $\bar{x}$ = 110.2
2341' (76237)		biotite	9.060 9.055 $\bar{x}$ = 9.058	0.1540	141.234	6.173	0.913	102.7 $\pm$ 3.1
2341' (76238) replicate		biotite	"	0.1440	142.032	6.208	0.907	103.2 $\pm$ 3.1 $\bar{x}$ = 102.9

EIELSON HOLE (EDT)

Sample No.	Rock Type	Mineral Dated	K_2O (weight percent)	Sample Weight (grams)	$^{40}Ar_{rad}$ (moles/gm) $\times 10^{-11}$	$\frac{^{40}Ar_{rad}}{^{40}K} \times 10^{-3}$	$\frac{^{40}Ar_{rad}}{^{40}Ar_{total}}$	Age $\pm$ 1 σ (m.y.)
3193 (74011)	Calc-greenschist	biotite	7.694 7.624 $\bar{x}$ = 7.659	0.2824	120.486	6.228	0.951	103.5 $\pm$ 3.1
3193 (73074)	Calc-greenschist	hornblende	0.320 0.320 0.320 0.320 $\bar{x}$ = 0.320	1.9888	8.814	20.900	0.672	177.7 $\pm$ 5.3
3193 (74116) replicate	"	"	0.310 0.320 $\bar{x}$ = 0.315	2.7933	8.629	10.850	0.764	176.8 $\pm$ 7.1 $\bar{x}$ = 177.2
3195.5' (76138)		biotite	8.380 8.350 8.380 8.390 $\bar{x}$ = 8.375	0.1771	130.739	6.180	0.721	102.8 $\pm$ 3.2
3195.5 (76140) replicate		biotite	"	0.2134	129.247	6.110	0.943	101.6 $\pm$ 3.0 $\bar{x}$ = 102.2
3195.5' (76151)		impure hornblende	0.149 0.151 0.147 0.149 $\bar{x}$ = 0.149	0.6512	3.724	9.844	0.600	161.2 $\pm$ 4.8
3195.5' (77003) replicate		impure hornblende	"	0.7990	3.649	9.647	0.191	158.1 $\pm$ 4.7 $\bar{x}$ = 159.6

Sample No.	Rock Type	Mineral Dated	K_2O (weight percent)	Sample Weight (grams)	$^{40}Ar_{rad}$ (moles/gm) $\times 10^{-11}$	$\frac{^{40}Ar_{rad}}{^{40}K} \times 10^{-3}$	$\frac{^{40}Ar_{rad}}{^{40}Ar_{total}}$	Age $\pm$ 1 σ (m.y.)
3195.5' (76148)		impure paragonite	0.190 0.190 0.190 0.190 $\bar{x}$ = 0.190	0.2294	2.427	5.058	0.110	84.5 $\pm$ 2.5
3195.5' (76231) Replicate		impure paragonite	"	0.2427	2.365	4.929	0.135	82.4 $\pm$ 2.5 $\bar{x}$ = 83.4
4065' (76147)		hornblende	0.090 0.092 0.086 0.086 $\bar{x}$ = 0.089	0.3305	0.978	4.376	0.139	73.4 $\pm$ 3.7
4065 (76174) Replicate		hornblende	"	0.3220	0.969	4.334	0.100	72.7 $\pm$ 4.4 $\bar{x}$ = 73.0
4065' (76177)		muscovite	9.687 9.672 $\bar{x}$ = 9.680	0.0912	156,505	6.401	0.841	106.4 $\pm$ 3.2
4065' (76208) Replicate		muscovite	"	0.2108	154.762	6.330	0.915	105.2 $\pm$ 3.2 $\bar{x}$ = 105.8
5010' (76141)		biotite	9.163 9.210 $\bar{x}$ = 9.187	0.1392	117.480	5.063	0.943	84.6 $\pm$ 2.5

EIELSON HOLE (EDT)

Sample No.	Rock Type	Mineral Dated	K_2O (weight percent)	Sample Weight (grams)	$^{40}Ar_{rad}$ (moles/gm) $\times 10^{-11}$	$\frac{^{40}Ar_{rad}}{^{40}K} \times 10^{-3}$	$\frac{^{40}Ar_{rad}}{^{40}Ar_{total}}$	Age $\pm$ 1 σ (m.y.)
5010' (76239) Replicate		biotite	"	0.1214	118.439	5.104	0.907	85.3 $\pm$ 2.6 $\bar{x}$ = 84.9
5010' (76150)		muscovite	10.580 10.573 10.540 10.580 $\bar{x}$ = 10.568	0.1197	162.771	6.097	0.845	101.4 $\pm$ 3.0
5010 (76154) Replicate		muscotite	"	0.1279	161.630	6.055	0.795	100.8 $\pm$ 3.0 $\bar{x}$ = 101.1
6141' (76248)		hornblende	0.360 0.360 0.360 0.360 $\bar{x}$ = 0.360	0.2931	11.034	12.130	0.463	196.8 $\pm$ 5.9
6141 (76252) Replicate		hornblende	"	0.4645	11.964	13.160	0.698	212.5 $\pm$ 6.4 $\bar{x}$ = 204.6
6141 (76176)		impure biotite	8.203 8.157 8.110 8.140 $\bar{x}$ = 8.153	0.2679	91.016	4.420	0.925	74.1 $\pm$ 2.2
6141 (76210)		impure biotite	"	0.1813	91.452	4.441	0.904	74.4 $\pm$ 2.2

Sample No.	Rock Type	Mineral Dated	K_2O (weight percent)	Sample Weight (grams)	$^{40}Ar_{rad}$ (moles/gm) $\times 10^{-11}$	$\frac{^{40}Ar_{rad}}{^{40}K} \times 10^{-3}$	$\frac{^{40}Ar_{rad}}{^{40}Ar_{total}}$	Age $\pm$ 1 σ (m.y.)
6141 (76210) Replicate	biotite amphibolite	biotite	9.466 9.468 $\bar{x}$ = 9.467	0.3021	121.495	5.081	0.934	84.9 $\pm$ 2.5
6142 (74115)	biotite amphibolite	hornblende	0.370 0.377 $\bar{x}$ = 0.373	2.6368	11.992	12.710	0.808	205.6 $\pm$ 6.2
6142 (73073)	"	hornblende	0.379 0.381 0.382 0.376 0.380 0.380 $\bar{x}$ = 0.380	1.7427	10.860	11.320	0.794	184.2 $\pm$ 5.5
7140' #1 (76096)		biotite	9.140 9.143 $\bar{x}$ = 9.142	0.1445	105.880	4.585	0.907	76.8 $\pm$ 2.3
7140' #1 (76230) Replicate		biotite	"	0.1564	105.250	4.558	0.826	76.3 $\pm$ 2.3 $\bar{x}$ = 76.6

Sample No.	Rock Type	Mineral Dated	K_2O (weight percent)	Sample Weight (grams)	$^{40}Ar_{rad}$ (moles/gm) $\times 10^{-11}$	$\frac{^{40}Ar_{rad}}{^{40}K} \times 10^{-3}$	$\frac{^{40}Ar_{rad}}{^{40}Ar_{total}}$	Age $\pm$ 1 σ (m.y.)
7140' #2 (76144)		biotite	9.023 9.027 9.043 9.083 $\bar{x}$ = 9.044	0.1015	107.932	4.725	0.866	79.1 $\pm$ 2.4
7140 #2 (76152) Replicate		biotite	"	0.1502	106.723	4.672	0.770	72.2 $\pm$ 2.3 $\bar{x}$ = 76.5
7140 (76136)		muscovite	10.447 10.410 $\bar{x}$ = 10.429	0.1822	157.056	5.962	0.778	99.3 $\pm$ 3.0
7140 (76153) Replicate		muscovite	"	0.1615	156.100	5.926	0.740	98.7 $\pm$ 3.0 $\bar{x}$ = 99.0
7140.5 (76029)		biotite	8.927 8.965 8.890 8.987 $\bar{x}$ = 8.942	0.1787	99.718	4.415	0.869	74.0 $\pm$ 2.2
7140.5 (76025) Replicate		biotite	"	0.1959	98.298	4.352	0.861	73.0 $\pm$ 2.2 $\bar{x}$ = 73.5
7140.5 (76008)		muscovite	9.956 9.860 $\bar{x}$ = 9.908	0.2042	160.727	6.422	0.798	106.7 $\pm$ 3.2
7140.5 (76004) Replicate		muscovite	"	0.2277	160.285	6.404	0.752	106.4 $\pm$ 3.2 $\bar{x}$ = 106.5

Sample No.	Rock Type	Mineral Dated	K_2O (weight percent)	Sample Weight (grams)	$^{40}Ar_{rad}$ (moles/gm) x 10^{-11}	$\frac{^{40}Ar_{rad}}{^{40}K}$ x 10^{-3}	$\frac{^{40}Ar_{rad}}{^{40}Ar_{total}}$	Age $\pm$ 1 σ (m.y.)
'142.5 (77004)		hornblende	0.562 0.560 0.562 0.562 $\bar{x}$ = 0.562	0.5060	15.823	11.160	0.718	181.6 $\pm$ 5.4
'142.5 (76247) lelicate		hornblende	"	0.2854	14.762	10.410	0.686	170.0 $\pm$ 5.1 $\bar{x}$ = 175.8
'142.5 (76233)		impure biotite	7.391 7.487 7.435 7.490 $\bar{x}$ = 7.451	0.0971	90.615	4.815	0.810	80.6 $\pm$ 2.4
'142.5 (76240) eplicate		impure biotite	"	0.1133	90.980	4.834	0.811	80.9 $\pm$ 2.4 $\bar{x}$ = 80.7
7147.5 (74144)	Biotite-Amphibolite	biotite	9.040 8.972 $\bar{x}$ = 9.006	0.1118	112.359	4.939	0.860	82.6 $\pm$ 2.5
7147.5 (74147) replicate		biotite	9.040 8.972 $\bar{x}$ = 9.006	0.1034	111.669	4.909	0.934	82.1 $\pm$ 2.5 $\bar{x}$ = 82.3
7147.5 (75013)		hornblende	0.600 0.590 $\bar{x}$ = 0.595	0.7723	16.334	10.870	0.784	177.2 $\pm$ 5.3
7147.5 (75026) replicate		hornblende	0.600 0.590 $\bar{x}$ = 0.595	1.9370	18.084	12.030	0.796	195.2 $\pm$ 5.9 $\bar{x}$ = 186.2

Sample No.	Rock Type	Mineral Dated	K_2O (weight percent)	Sample Weight (grams)	$^{40}Ar_{rad}$ (moles/gm) $\times 10^{-11}$	$\frac{^{40}Ar_{rad}}{^{40}K} \times 10^{-3}$	$\frac{^{40}Ar_{rad}}{^{40}Ar_{total}}$	Age $\pm$ 1 σ (m.y.)
8218 (76098)		impure biotite	7.350 7.270 7.330 7.260 $\bar{x}$ = 7.303	0.1893	78.837	4.274	0.885	71.7 $\pm$ 2.1
8218 (76099) Replicate		impure biotite	"	0.1776	78.051	4.231	0.932	70.9 $\pm$ 2.1 $\bar{x}$ = 71.3
8218 (76092)		muscovite	9.172 9.142 $\bar{x}$ = 9.157	0.1658	128.463	5.554	0.836	92.6 $\pm$ 2.8
8218 (76097) Replicate		muscovite	"	0.1550	128.494	5.555	0.842	92.6 $\pm$ 2.8 $\bar{x}$ = 92.6
9196 (76157)		biotite	9.420 9.437 $\bar{x}$ = 9.429	0.1173	83.067	3.488	0.803	58.7 $\pm$ 1.8
9196 (76228) Replicate		biotite	"	0.1581	82.712	3.473	0.819	58.4 $\pm$ 1.8
9196 (77005) Replicate		biotite	"	0.1516	83.181	3.493	0.354	58.8 $\pm$ 1.8 $\bar{x}$ = 58.6

EIELSON HOLE (EDT)

Sample No.	Rock Type	Mineral Dated	K_2O (weight percent)	Sample Weight (grams)	$^{40}Ar_{rad}$ (moles/gm) $\times 10^{-11}$	$\frac{^{40}Ar_{rad}}{^{40}K} \times 10^{-3}$	$\frac{^{40}Ar_{rad}}{^{40}Ar_{total}}$	Age $\pm$ 1 σ (m.y.)
9766 (76137)		biotite	9.174 9.170 9.124 9.174 $\bar{x}$ = 9.161	0.2218	82.240	3.554	0.905	59.8 $\pm$ 1.8
9766 (76207)		biotite	"	0.2555	80.354	3.473	0.923	58.4 $\pm$ 1.8
9767 (73066)	Calc-Tramolite-Phlogopite-Schist	phlogopite	9.639 9.704 $\bar{x}$ = 9.671	0.3910	94.945	3.886	0.850	65.3 $\pm$ 2.0
9770 (76102)		biotite	9.453 9.480 $\bar{x}$ = 9.467	0.1028	85.657	3.582	0.688	60.3 $\pm$ 1.8
9770 (76158) Replicate		biotite	"	0.1022	82.908	3.449	0.803	58.0 $\pm$ 1.7 $\bar{x}$ = 59.1

LOS ALAMOS DEEP DRILL HOLE

Sample No. Depth in feet Lab. Number	Rock Type	Mineral Dated	K_2O (weight percent)	Sample Weight (grams)	$^{40}Ar_{rad}$ (moles/gm) $\times 10^{-11}$	$\frac{^{40}Ar_{rad}}{^{40}K} \times 10^{-3}$	$\frac{^{40}Ar_{rad}}{^{40}Ar_{total}}$	Age $\pm$ 1 σ (b.y.)
Surface at Guadalupe Box (74172)	amphibolite	biotite	7.127 7.107 $\bar{x}$ = 7.117	0.1051	2068.600	115.100	0.992	1.34 $\pm$ .04
Surface at Guadalupe Box (74175) Replicate	amphibolite	biotite	"	0.1144	2100.220	116.800	0.996	1.36 $\pm$ .04 $\bar{x}$ = 1.35
Surface at Guadalupe Box (75030)	amphibolite	hornblende	0.141 0.143 0.144 0.143 $\bar{x}$ = 0.143	0.4943	44.808	124.300	0.824	1.42 $\pm$ .04
Surface at Guadalupe Box (75031) Replicate	amphibolite	hornblende	"	0.4573	44.500	123.400	0.675	1.41 $\pm$ .04 $\bar{x}$ = 1.41
2439.5-8 (GT-1) (74166)	monzogranitic gneiss	biotite	9.180 9.250 $\bar{x}$ = 9.215	0.1209	2467.600	106.000	0.993	1.27 $\pm$ .04
2439.5-8 (GT-1) (74168) Replicate	monzogranitic gneiss	biotite	"	0.1194	2740.300	117.700	0.990	1.37 $\pm$ .04 $\bar{x}$ = 1.32

Sample No. Depth in feet Lab Number	Rock Type	Mineral Dated	K_2O (weight percent)	Sample Weight (grams)	$^{40}Ar_{rad}$ (moles/gm) $\times 10^{-11}$	$\frac{^{40}Ar_{rad}}{^{40}K} \times 10^{-3}$	$\frac{^{40}Ar_{rad}}{^{40}Ar_{total}}$	Age $\pm$ 1 σ (b.y.)
2540-8 (GT-1) (75008)	amphibolite	amphibole	0.544 0.550 $\bar{x}$ = 0.547	0.7291	181.737	131.500	0.976	1.48 $\pm$ .04
2540-8 (GT-1) (75021) Replicate	amphibolite	amphibole	"	0.7363	170.176	123.200	0.980	1.41 $\pm$ .04 $\bar{x}$ = 1.44
2540-8 (GT-1) (74159)	amphibolite	biotite	8.767 8.770 $\bar{x}$ = 8.768	0.1177	2590.430	117.000	0.997	1.36 $\pm$ .04
2540-8 (GT-1) (74161) Replicate	amphibolite	biotite	"	0.1195	2547.660	115.000	0.996	1.35 $\pm$ .04 $\bar{x}$ = 1.35
2580 (GT-2) (74140)	monzogranitic gneiss	biotite	9.305 9.375 $\bar{x}$ = 9.340	0.1284	2816.400	119.400	0.988	1.38 $\pm$ .04
2580 (GT-2) (74141) Replicate	monzogranitic gneiss	biotite	"	0.1222	2901.120	123.000	0.995	1.41 $\pm$ .04 $\bar{x}$ = 1.39
3696-1 (GT-2) (74148)	monzogranitic gneiss	biotite	9.218 9.190 $\bar{x}$ = 9.204	0.1193	2780.990	119.600	0.996	1.38 $\pm$ .04
3696-1 (GT-2) (74149) Replicate	monzogranitic gneiss	biotite	"	0.1181	2804.170	120.600	0.993	1.39 $\pm$ .04

Sample No. Depth in feet Lab. Number	Rock Type	Mineral Dated	K_2O (weight percent)	Sample Weight (grams)	$^{40}Ar_{rad}$ (moles/gm) $\times 10^{-11}$	$\frac{^{40}Ar_{rad}}{^{40}K} \times 10^{-3}$	$\frac{^{40}Ar_{rad}}{^{40}Ar_{total}}$	Age $\pm$ 1 σ (b.y.)
3696-1 (GT-2) (74119)	monzogranitic gneiss	biotite	9.218	0.1813	2646.870	113.800	0.968	1.34 $\pm$ .04
Replicate			9.190					
			$\bar{x}$ = 9.204					$\bar{x}$ = 1.37
3697 (GT-2) (75122)	monzogranitic gneiss	biotite	8.747	0.1960	2498.180	113.200	0.992	1.33 $\pm$ .04
			8.728					
			$\bar{x}$ = 8.737					
3697 (GT-2) (74153)	monzogranitic gneiss	biotite	"	0.0957	2992.730	135.600	0.998	1.43 $\pm$ .04
Replicate								$\bar{x}$ = 1.38
4279 1-10 (GT-2) (74154)	monzo-granite	biotite	8.013	0.1010	2394.540	118.500	0.999	1.38 $\pm$ .04
			7.987					
			$\bar{x}$ = 8.002					
4279 1-10 (GT-2) (74156)	"	biotite	"	0.1254	2387.830	118.100	0.997	1.37 $\pm$ .04
Replicate								$\bar{x}$ = 1.37
5234 (GT-2) (74151)	granodioritic gneiss	biotite	8.956	0.1163	2548.570	112.400	0.994	1.32 $\pm$ .04
			9.000					
			$\bar{x}$ = 8.978					
5234 (GT-2) (74152)	"	biotite	"	0.0984	2587.940	114.100	0.998	1.34 $\pm$ .04
Replicate								$\bar{x}$ = 1.33

Sample No. Depth in feet Lab. Number	Rock Type	Mineral Dated	K_2O (weight percent)	Sample Weight (grams)	$^{40}Ar_{rad}$ (moles/gm) $\times 10^{-11}$	$\frac{^{40}Ar_{rad}}{^{40}K} \times 10^{-3}$	$\frac{^{40}Ar_{rad}}{^{40}Ar_{total}}$	Age $\pm$ 1 σ (b.v.)
5234 (GT-2) (75005)	granodioritic gneiss	hornblende	1.350 1.360 $\bar{x}$ = 1.355	0.7370	342.031	99.930	0.995	1.21 $\pm$ .04
5234 (GT-2) (75018) Replicate	"	hornblende	"	0.5812	338.615	98.930	0.994	1.21 $\pm$ .04 $\bar{x}$ = 1.21
5487 Slab (GT-2) (74155)	muscovite vein	muscovite	10.740 10.748 $\bar{x}$ = 10.744	0.0914	3267.710	120.400	0.993	1.39 $\pm$ .04
5487 Slab (GT-2) (74158) Replicate	"	muscovite	"	0.0781	3287.400	121.100	0.990	1.40 $\pm$ .04
5487 Slab (GT-2) (74158) Replicate	"	muscovite	"	0.0781	3286.090	121.100	0.991	1.40 $\pm$ .04 $\bar{x}$ = 1.40
5487 Core (GT-2) (74165)	"	muscovite	10.530 10.540 $\bar{x}$ = 10.535	0.1431	3103.170	116.600	0.995	1.36 $\pm$ .04
5487 Core (GT-2) (74167) Replicate	"	muscovite	"	0.1412	3120.270	117.300	0.995	1.37 $\pm$ .04 $\bar{x}$ = 1.36

Sample No. Depth in feet Lab. Number	Rock Type	Mineral Dated	K_2O (weight percent)	Sample Weight (grams)	$^{40}Ar_{rad}$ (moles/gm) $\times 10^{-11}$	$\frac{^{40}Ar_{rad}}{^{40}K} \times 10^{-3}$	$\frac{^{40}Ar_{rad}}{^{40}Ar_{total}}$	Age $\pm$ 1 σ (b.y.)
5654 (GT-2) (74142)	amphibole-biotite schist	biotite	8.636 8.632 $\bar{x}$ = 8.634	0.1225	2559.350	117.400	0.996	1.37 $\pm$ .04
5654 (GT-2) (74143) Replicate	"	biotite	"	0.1291	2607.490	119.600	0.996	1.38 $\pm$ .04 $\bar{x}$ = 1.37
5654 (GT-2) (74118)	amphibole-biotite schist	hornblende	1.270 1.260 $\bar{x}$ = 1.265	0.8279	383.326	120.000	0.993	1.39 $\pm$ .04
5654 (GT-2) (75015) Replicate	"	hornblende	"	0.5688	349.569	109.400	0.992	1.30 $\pm$ .04
5654 (GT-2) (75027) Replicate	"	hornblende	"	0.4668	340.198	106.000	0.990	1.27 $\pm$ .04 $\bar{x}$ = 1.32
6154 (GT-2) (74145)	biotite granodiorite	biotite	8.438 8.444 $\bar{x}$ = 8.441	0.1768	2635.150	123.600	0.999	1.42 $\pm$ .04
6154 (GT-2) (74146) Replicate	"	biotite	"	0.1313	2670.870	125.300	0.997	1.43 $\pm$ .04 $\bar{x}$ = 1.42

Sample No. Depth in feet Lab. Number	Rock Type	Mineral Dated	K_2O (weight percent)	Sample Weight (grams)	$^{40}Ar_{rad}$ (moles/gm) $\times 10^{-11}$	$\frac{^{40}Ar_{rad}}{^{40}K} \times 10^{-3}$	$\frac{^{40}Ar_{rad}}{^{40}Ar_{total}}$	Age $\pm$ 1 σ (b.y.)
7103 (GT-2) (76003)	granodiorite gneiss	biotite	9.052 8.872 $\bar{x}$ = 8.962	0.1262	262.423	115.900	0.993	1.35 $\pm$ .04
7103 (GT-2) (76068) Replicate	"	biotite	"	0.1483	2748.880	121.400	0.995	1.40 $\pm$ .04 $\bar{x}$ = 1.37
7103 (GT-2) (76039)	"	hornblende	1.330 1.320 $\bar{x}$ = 1.325	0.2898	400.407	119.600	0.955	1.38 $\pm$ .04
7103 (GT-2) (76039) Replicate	"	hornblende	"	0.2898	401.225	119.900	0.956	1.39 $\pm$ .04 $\bar{x}$ = 1.38
8581 (GT-2) (75070	biotite granodiorite	biotite	9.555 9.563 $\bar{x}$ = 9.559	0.1230	2650.320	109.800	0.992	1.30 $\pm$ .04
8581 (GT-2) (75075) Replicate	"	biotite	"	0.1290	2779.000	115.100	0.998	1.35 $\pm$ .04 $\bar{x}$ = 1.32
9529 (GT-2) (75076)	"	biotite	9.053 9.059 $\bar{x}$ = 9.056	0.2202	2464.140	107.700	0.994	1.28 $\pm$ .04

Sample No. Depth in feet Lab. Number	Rock Type	Mineral Dated	K_2O (weight percent)	Sample Weight (grams)	$^{40}Ar_{rad}$ (moles/gm) $\times 10^{-11}$	$\frac{^{40}Ar_{rad}}{^{40}K} \times 10^{-3}$	$\frac{^{40}Ar_{rad}}{^{40}Ar_{total}}$	Age $\pm$ 1 σ (b.y.)
9529 (GT-2) (75078) Replicate	"	biotite	9.053 9.059 $\bar{x}$ = 9.056	0.2310	2344.460	102.500	1.000	1.24 $\pm$ .04 $\bar{x}$ = 1.26

APPLICATION OF MODERN WELL LOGGING METHODS TO SALT SOLUTION CAVITIES

John W. Caldwell and J. M. Strabala
BIRDWELL, a Division of
Seismograph Service Corporation

Presented at the Third Symposium on Salt
April 21-24, 1969 Cleveland, Ohio

APPLICATION OF MODERN WELL LOGGING METHODS TO SALT SOLUTION CAVITIES

JOHN W. CALDWELL and J. M. STRABALA

INTRODUCTION

It has become increasingly important to know the physical dimensions and orientation of cavities produced by solution mining. The need to provide data for such engineering problems as maximum operating efficiency and profit, roof strength and safety factors, determination of property boundries, the feasability of underground storage, and others have led to the development of tools to provide this information.

Two acoustical tools, the "SEISCALIPER"[TM] and "SEISVIEWER"[TM], have been introduced to the field in recent months and can help provide much of this information. The tools are similar in principle, in that they are both acoustical transceiver devices, however, each was developed to investigate a specific area of interest and will be treated separately in this report. The operating principles, the manner in which the tools function, the data produced by each tool and its interpretation will be presented.

[TM] is a trademark of Seismograph Service Corporation

SEISCALIPER

A complete SEISCALIPER™ System, as depicted in Figure 1, consists of the surface display unit, the logging truck, with its associated multi-conductor wire line system and the downhole instrument. The surface panel, with the polar coordinate oscilloscope, functions as a signal monitor and visual readout in conjunction with power and tool information pulse control. Shown in the lower part of Figure 1 is the SEISCALIPER tool, an acoustic pulse sounding instrument for cavern size and shape determination.

The system is based on taking a measurement of the time required for an acoustic pulse, from a transducer, to travel through fluid, strike a reflective surface and return. Distance is determined from the time measured and the sound velocity of the fluid.

One of the most important features of a survey tool is the acoustic pulse. In order to conduct an accurate and detailed survey, it becomes necessary to provide the most narrow, practical beam width possible from the transducer thereby assuring a small target and greater definition of the reflecting surface. Since the maximum transducer diameter is limited by casing size, the only practical beam pattern control is frequency. The SEISCALIPER system operates at a frequency of 500 kilohertz and a focused beam width of 2 degrees or less. The maximum range in water or brine, assuming an average reflecting target, is approximately 500 feet. For good targets, such as a flat surface normal to and as large as the beam, the range

is increased by 20 percent, or more.

Included in the receiver electronics is a time varying gain (TVG) control circuit that reduces the gain of the amplifier to a minimum at the pulse generation and increases exponentially with time. Thus, the near targets and far targets are recorded at essentially the same signal level. The result, is to produce a clear, sharp signal such that the recording clearly defines the cavity contour and the receiver is not saturated with high level, near target arrivals which could obscure small signals from distant targets.

The downhole instrument pictured in Figure 2 is 6 ft. long, 4-3/4 inches in diameter. The electronics are in the upper section, the motor drive and magnetic north sensor are in the middle, and the rotating section, which incorporates the transducers, is near the bottom of the tool.

The three separate signal transducers are encapsulated in polyurethane and located in the dark "cut-out" portion of the rotating section. These are mechanically positioned, one each to "look up" and to "look down" at angles of 45°, and one directed horizontally. Any one of the transducers may be selected "on command" from the surface control panel. The operator choosing the best combination for existing cavern conditions.

Both the transducer speed of rotation and the transmitter firing rate are determined by the range or two-way travel time of

the signal to the cavern wall. The more distant the target, the slower the firing, which in turn controls the tool speed of rotation. The normal sequence of operation is, first, the command pulse to transmit, second, a variable delay for the signal return from the target, and third, rotate the transducer 2°. The cycle is repeated 180 times for one complete revolution.

The surface presentation, or scope display, is referenced to the rotating transducers by identical motors and is controlled by the same computer logic. This assures that the surface recording is synchronized and properly oriented with the transducer beam direction downhole.

Associated with the downhole instrumentation is a magnetic north sensor. It generates a series of easily recognizable, bright pulses displayed on the scope when the tool rotates through magnetic north.

In-situ calibration comes from a target at a known distance of 5 feet. Arranged on the downhole instrument is a spring-loaded target which is released on command. In its extended position it provides a known distance object for an exact calibration. The calibration is truly environmental in that it takes place downhole in the cavity media and under the same conditions that the survey is to be conducted. This automatically compensates for such variables as temperature, pressure and fluid densities. Surface panel controls can also be used to calibrate the tool if the varying conditions downhole are known.

Figure 3 depicts the SEISCALIPER in a solution-filled cavity where the tool has been lowered by a logging cable to the desired depth. A scanning transducer unit provides the focused acoustic signal which travels through the fluid striking the cavity boundry. This signal is reflected and subsequently detected by the receiving transducer. Having this signal, which is representative of the time interval, and the acoustic velocity of the fluid, the distance to the cavity wall is determined and recorded. The transducer section is set in rotation, scanning the cavity boundry through 360°, making a complete horizontal investigation of the cavity boundry at any given depth. This process is repeated at successive levels as often as desired, usually in 5 or 10 foot increments over the vertical extent of the cavity.

The signal is transmitted to the surface by the logging cable where a permanent record of the cavity boundry at the desired depth is recorded.

Figure 4 illustrates the display of a composited record, made at a given level, as it appears on the oscilloscope along with the associated surface control panel. The operation of the downhole tool, its calibration and choice of scale and transducer used are selected and regulated from this panel.

The recording is made by exposing the graticle of the oscilloscope to polaroid film where the film records the individual radial vectors, representative of distances, into a continuous permanent record, available for immediate viewing, as shown by Figure 5.

In the picture, distance is measured from the center of the reference rings radially out to the leading edge of the signal. The signal appears as the oval-shaped, segmented pattern near the second reference ring. Since the length of each vector, from the center to the intercept with the signal, is a cavity radius then the whole pattern is a scaled cross-sectional view of the cavern at the specified level. Reference rings provide this polar display with a scale of the radial distance. One of the five scales, 25, 50, 100, 250 and 500 ft., as measured from the center of the picture to the outermost reference ring, may be selected. The choice of scale is dependent on the resolution desired and physical limits of the cavity.

The picture is oriented by means of a north magnetic marker that is displayed by the white dashed line from the center of the picture to the outermost ring. This marker is the result of a pulse that is triggered and recorded each time the scanning section is rotated through magnetic North.

The outermost reference ring is graduated in degrees from 0° to 360°. The azimuth ring is fixed, and must be related to the north marker to provide directional reference to the cavity cross-section. In practice, a transparent protractor is used to orient the picture and the distance of the cavity radius, in feet, is scaled off for a desired magnetic bearing. This information is tabulated for later use in constructing cross-section profiles along magnetic bearings and for use in volumetric computations.

An accurate measurement, with any sounding device, must take

into account the physical properties of the fluid in the cavity. A measurement of distance is dependent on the fluid velocity, and the velocity in turn is dependent on the temperature, and specific gravity of the fluid. Figure 6 shows this relationship. On the two extremes are solutions at a temperature of 64°, specific gravity of 1, with a velocity of 4850 ft. per sec.; and at 140°, specific gravity of 1.2, with a velocity of 6150 ft. per sec. If this velocity contrast is not taken into account, distance errors will result. It is not unreasonable to approach these end points in solution mining, where fresh water is injected from surface and saturated brine produced at depth.

As described earlier, the use of a target at a fixed distance calibrates the system precisely and precludes any knowledge of these variables. As the tool descends in the hole, the system calibration can readily be checked by observation of the fixed distance target and recalibrating to compensate for gravity segregation, pressure, or temperature changes of the fluid.

One of the unique features of the SEISCALIPER tool is the use of multiple transducers to "look up" and "down". Figure 7 shows the extent of coverage afforded by this arrangement. The choice of transducers can be made from the surface to any of the three directions providing an investigation of the cavity wall as depicted by the tool in Position 2. As the tool descends over the vertical distance of the cavity, it can be seen that a complete and detailed inspection of the cavity walls, including the roof and floor can be made.

Figure 7 also illustrates that an insoluble section of the

roof has fallen and accumulated as debris on the floor of the cavity. Cavitation has produced an enlargement in the form of an "attic" that would escape detection by horizontal observations alone. The "attic" may be detected and mapped by "looking up" and varying the depth of the tool in and near Position 1. The extent and size of the debris can be likewise surveyed by "looking down", raising and lowering the tool from Position 3.

For purposes of constructing cross-sectional profiles and making volumetric calculations it becomes necessary to relate observed boundaries, made by angle shots, to their respective vertical and horizontal positions relative to the borehole. This can be illustrated in Figure 7 by the right triangle ABC, where A is a point on the cavity, and line AC is the observed or scaled distance from the oscillograph picture, and the angle ACB is fixed at 45 degrees. The vertical correction BC is obtained from the cosine and the corrected depth is point B. The horizontal displacement of point A is determined by the sine giving us the distance AB. These corrections are made for measurements taken from the oscillograph pictures along desired magnetic bearings and tabulated for the construction of cross-section profiles and use in volumetric computations.

An "up" shot, as viewed from tool Position 1, is shown by Figure 8. The recorded signal, with the exception of the southeast direction, exhibits a uniform radial distance from the tool. The southeast direction shows an abrupt shift in the signal, indicating the roof to be at a much greater distance and forming an "attic" to

the roof as depicted in Figure 7. The shift in the signal represents a vertical displacement of over 50 ft.

Data derived from the SEISCALIPER Survey is usually presented in three ways. First, the oscillograph pictures are labeled as to depth, scale and angle of observation. The horizontal recordings provide a cross-section, already to scale, of the cavity at specific depths. Next, a computed tabulation of the data is presented. The cavity radius in feet is listed for 12 magnetic bearings, the incremental and cumulative volumes in cubic feet and barrels, and salt in tons, is given for each level. This presentation is shown in Figure 9. The data is calculated separately for the roof, horizontal and floor surveys. The horizontal program is designed to compute the volume between two successive depths with the area of the cylinder determined by the cavity radius at the 12 magnetic bearings. The roof and floor observations are programmed to compute an envelope based on the near and far limits of the cavity as determined from cross-sectional profiles.

Finally, profiles of the cavity are plotted to scale from the tabulated data measured from the pictures. Six cross-sections are displayed showing the profile of the cavity at 12 magnetic bearings from the well bore. The profiles represent a compilation of horizontal, roof and floor observations to delineate the cavity boundries.

SEISVIEWER

The SEISVIEWER™ is a short ranged magnetically oriented investigative tool and was designed primarily to evaluate fractured reservoirs. This tool was originally designed by Mobil Research and Developement Field Research Laboratory as the BOREHOLE TELEVIEWER. The high resolution of the "borehole picture", produced in any type fluid, finds other applications and particularly as a casing inspection tool.

In the initial drilling phase of an intended solution mining operation, it would be beneficial to know such variables as fracturing and jointing cut by the borehole. These features, when detected, could affect the design and safety factors in the early stages of construction.

The data obtained from the SEISVIEWER is presented in continuous strip form showing the surveyed borehole scaled to depth and magnetically oriented.

The complete SEISVIEWER System, as shown in Figure 10, consists of a downhole scanning instrument, logging unit with its multi-conductor cable, and the surface panel. The borehole tool, with its major parts of motor-driven acoustic transducer and flux-gate magnetometer, scans the borehole wall and orients the resulting log, respectively. Rotating at 3 revolutions per second the 2 mega-

hertz acoustic transducer is pulsed at a rate of 2000 times per second. The focused acoustic beam directed on the wall, reflects as a function of the acoustic impedance and the wall rugosity. Therefore, since the amplitude of the return signal depends on the wall surface conditions and the associated physical properties, fracturing or highly disturbed zones are easily recognized by poor to no reflected signal.

The detected acoustic signals are amplified along with the magnetometer north marker pulse and transmitted to the surface through the multi-conductor cable.

The surface panel combines this downhole information to produce an oriented acoustic picture of the sidewall. An oscilloscope sweep is triggered from the north marker and its intensity is modulated by the detected signal. This system is comparable to a simplified, ordinary television presentation, with horizontal line spacing controlled by the logging speed, the intensity, by the amplitude of the reflected signal, and the orientation by the magnetic north sensor pulse. The completed picture is then a compilation of a multitude of transducer scans, which when photographed combine to make a "log picture" of the borehole wall. The log is displayed with this cylindrical picture of the borehole wall split vertically at magnetic north and laid out flat.

Figure 11 shows the complete tool with the acoustic transducer near the bottom, the flux-gate magnetometer in the center, and the electronics cartridge at the top. Centralizers, shown above and below the instrument, center the tool in the hole, where ideally the

borehole wall is normal to the scanning beam.

Several examples are presented which show the capabilities of the tool to furnish information that previously could only be surmised.

Figure 12 is a portion of log recorded in a mud-filled, rotary-drilled hole shortly after drilling was completed. The section is interpreted as being highly fractured, with the fractures exhibited as the dark sinusoidal features. The angle of dip varies greatly as shown by sharply dipping fractures in both the left and right strips of log display and relatively low angle dips exhibited by the middle strip.

Figure 13 is an isometric drawing of a low angle fracture or bedding plane intersecting the borehole and a corresponding steep dip intersection of the borehole along with the corresponding log display. At any angle, other than horizontal or vertical, a characteristic sine wave pattern will be created. The steeper the dip, the more elongated the sinusoidal pattern will be. The attitude of the fracture can be found from the log, by determining its strike and dip. The angle of dip is determined by

$$\text{Angle} = \tan^{-1} \frac{h}{d}$$

where d is the diameter of the hole, and h is the distance from crest to trough of the sinusoidal wave form as measured from the log. The trough of the wave form points in the direction of the angle of dip and can be read from the oriented log display. The strike being

perpendicular to the direction of dip, can be readily determined.

Figure 14 shows a set of 3 high-angle, nearly vertical fractures characterized by the sine wave pattern with the minimal points of the troughs at depths of 7050 and 7070. The third minimal point is out of view at the bottom of the picture. The direction of the angle of dip is south as shown by the orientation of the log.

Figure 15 shows a vertical fracture, extending for more than 100 feet, that is interpreted to be induced by drilling. This log was run at the same time as conventional logs, at the completion of drilling. The fracture plane extends in an east-west direction producing a mirror image as it bisects the hole. The vertical extent and orientation suggest the fracture could be the result of the relaxing of the consistent regional forces and perhaps further intensified by excessive pump pressures during the drilling operation. The lateral extent of this type fracture is unknown and could present problems during subsequent cementing or hydraulic fracturing operations of the well. In the case of solution mining, this type fracturing could introduce additional problems to controlled mining operations.

Two high-angle fractures are shown in Figure 16 that nearly intersect within the borehole. The attitudes of the fractures indicate that the two planes cross each other a short distance beyond the borehole. The two fractures shown are representative of the orientation and angle of dip of two sets of fractures that extend over 40' of hole.

The fracture indicated between 5561 and 5562 has a calculated dip of 58° and from the low point of the trough, the direction of dip is N 70 E as read from the log. The other fracture occurs between 5562 and 5564 and has a calculated dip of 74° and the direction of dip is N 45 W.

The SEISVIEWER can be used to inspect casing for splits, perforations and irregularities that might go undetected by other means of surveying. Orientation, however, cannot be determined inside steel casing. Figure 17 is a section of casing that has been perforated. The log strip on the left was run on a compressed vertical scale and the strip on the right was run on a 1 to 1 ratio showing the holes in their true proportion. This affords a positive check of density and placement of perforations. Figure 18 is an example of split casing. The log strip at the far right was run with a compressed scale and low gain setting to produce a picture highly sensitive to the slightest irregularity in the casing wall.

An area of interest is indicated by the dark section on the log. The picture second from the right was run at a higher gain setting delineating the major feature indicated by the triangular appearing black section. The third picture from the right, also run at high gain, but with the vertical and horizontal scale in a 1 to 1 ratio, can be compared with the actual photograph of the ruptured casing on the far left.

ACKNOWLEDGEMENTS

We wish to thank the Mobil Research and Developement Corporation Field Research Laboratory, and especially Dr. Joe Zemanek, for the kind cooperation and for the use of his slides and data from his paper "The Borehole Televiewer - A New Logging Concept for Fracture Location and Other Types of Borehole Inspection".

REFERENCES

EDO Western Corporation, Nov. 1967, "The Acoustic Propagation Characteristics of a Saturated Brine Solution".

Zemanek, Dr. Joe, Oct. 1968, "The Borehole Televiewer - A New Logging Concept for Fracture Location and Other Types of Borehole Inspection".

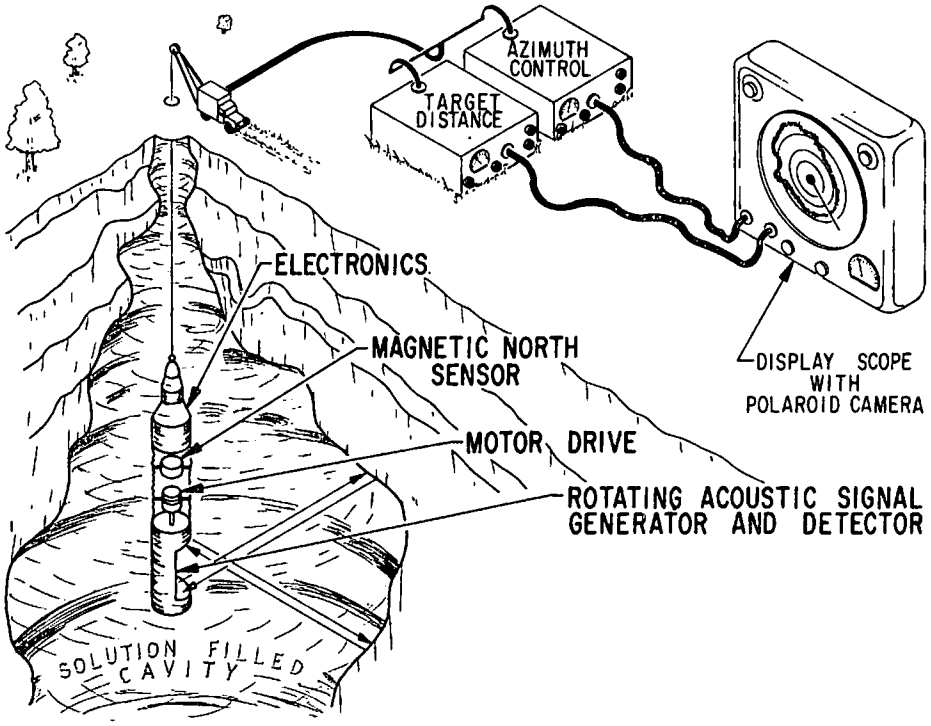

Figure 1 Seiscaliper System

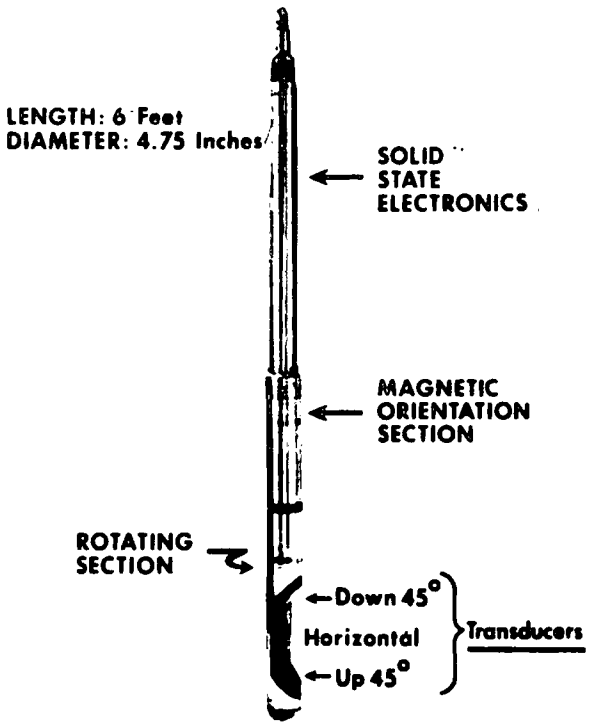

Figure 2 Seiscaliper Subsurface Tool

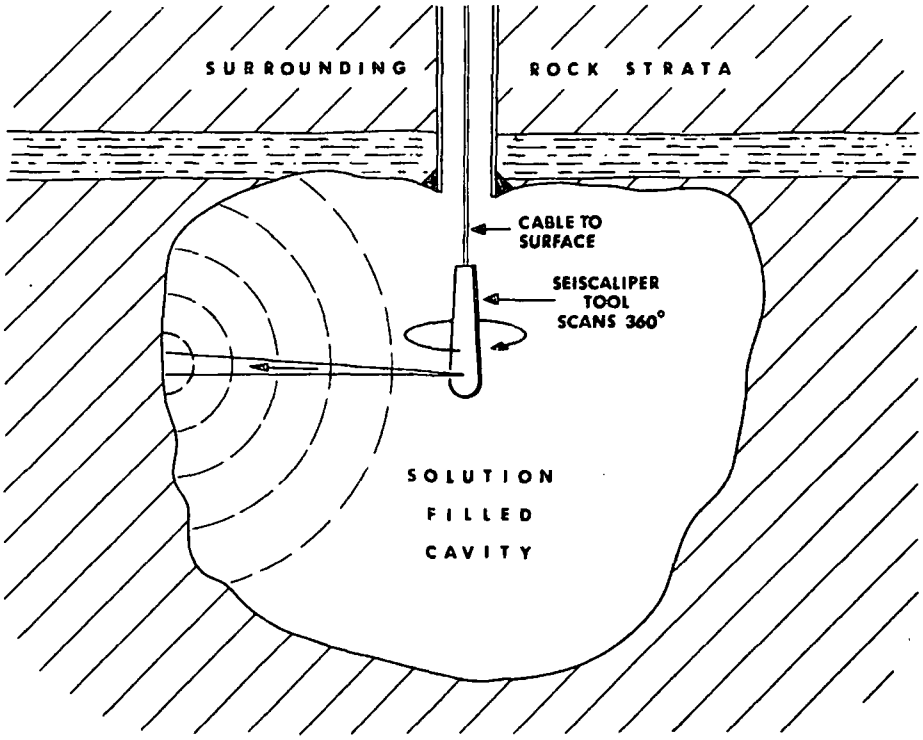

Figure 3 Seiscaliper Tool in a Solution Filled Cavity

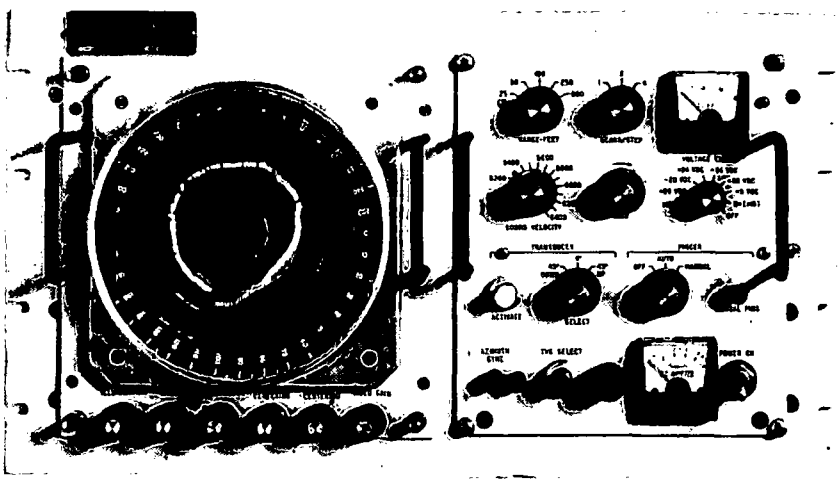

Figure 4 Seiscaliper Surface Control Panel

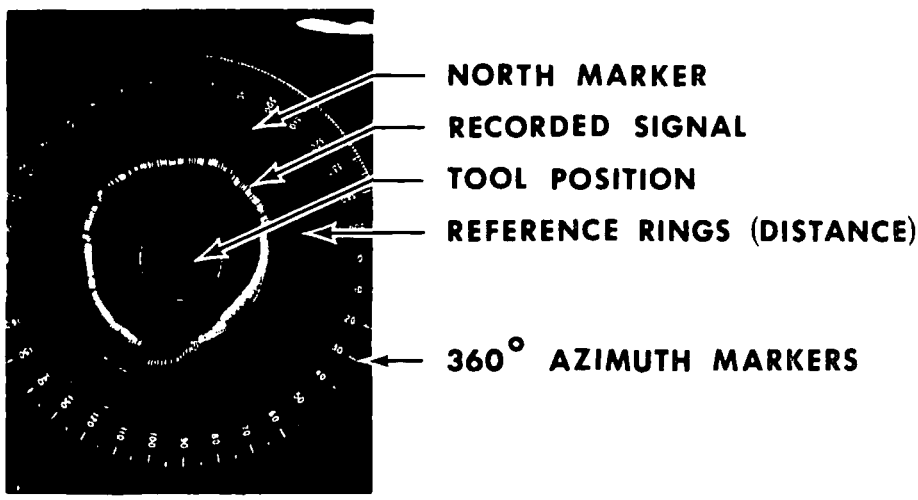

Figure 5 Seiscaliper Recording

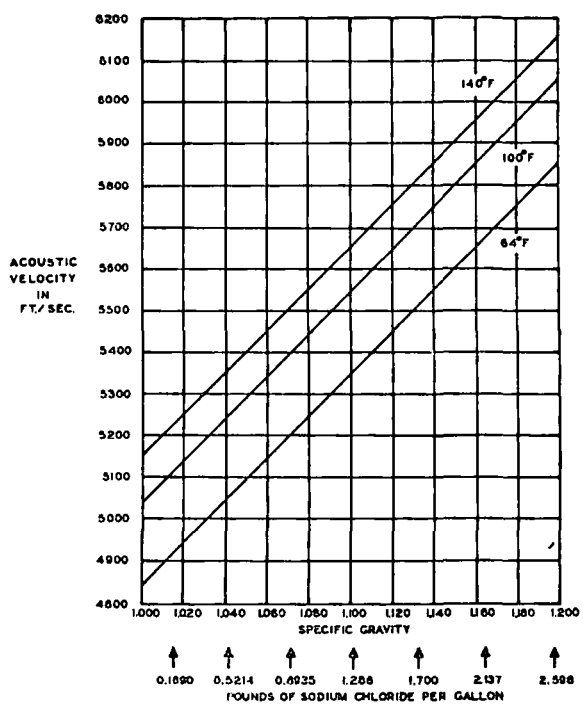

Figure 6 Velocity Versus Specific Gravity of Sodium Chloride Solutions (After EDO)

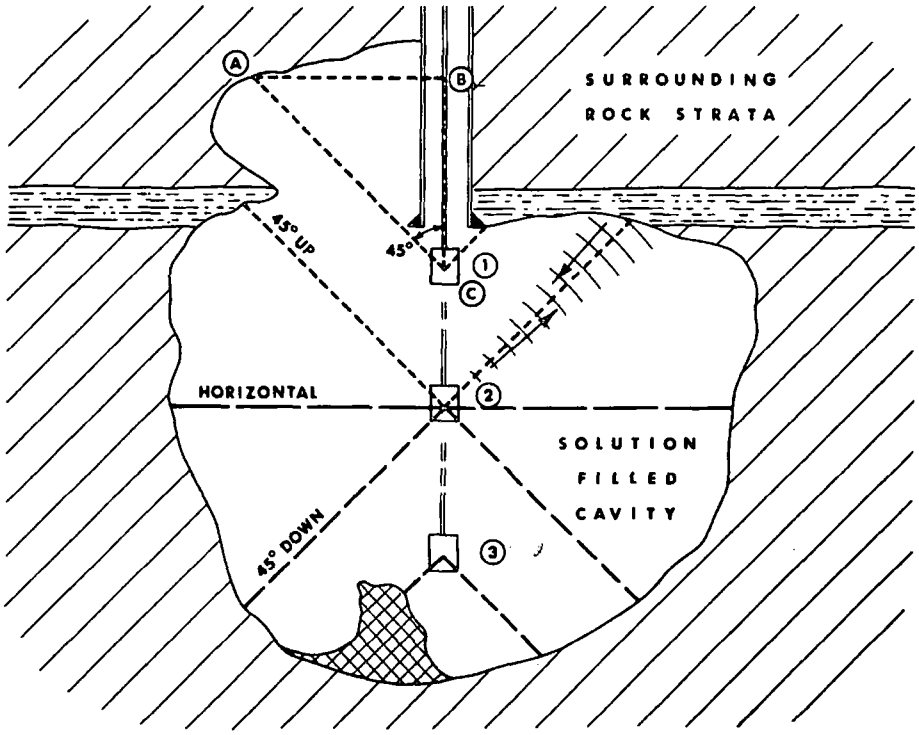

Figure 7 Investigative Capabilities of Seiscaliper Tool

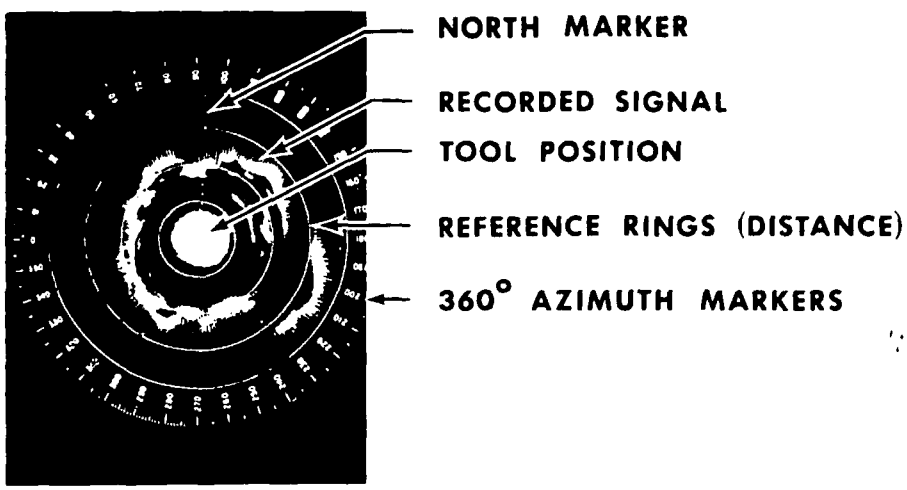

Figure 8 Seiscaliper Recording 45° Up

BIRDWELL SEISCALIPER SURVEY

COMPANY NAME & WELL
LOCATION
COMMENTS

HORIZONTAL OBSERVATIONS
DATE OF SURVEY

DEPTH FEET	CAVITY RADIUS IN FEET AT MAGNETIC BEARINGS 0	30	60	90	120	150	180	210	240	270	300	330	INCREMENTAL VOLUME CU. FT.	BARRELS	CUMULATIVE VOLUME CU. FT.	BARRELS	SALT IN TONS
2005	61	46	37	39	53	179	243	485	500	500	430	160	0.0	0.0	0.0	0.0	
2010	68	49	42	34	47	225	240	446	500	500	475	181	1401414.0	249566.2	1401414.0	249566.2	95206.1
2015	69	45	40	40	50	281	260	475	500	500	500	227	1479356.0	263446.3	2880770.0	513012.4	195692.2
2020	83	44	39	39	56	265	278	500	500	500	500	255	1578655.0	281129.6	4459425.0	794142.0	303240.6
2025	72	44	39	39	50	244	433	500	500	500	500	266	1665690.0	296628.4	6125115.0	1090770.0	416507.4
2030	78	56	50	50	78	327	500	500	500	500	500	250	1808874.0	322127.4	7933989.0	1412897.0	539510.6
2035	78	56	50	50	73	297	500	500	500	500	500	202	1856602.0	330626.9	9790591.0	1743523.0	665759.6
2040	67	50	39	39	73	347	500	500	500	500	500	235	1857178.0	330729.4	11647769.0	2074252.0	792047.6
2045	78	50	50	56	94	300	500	500	200	150	239	144	1340652.0	238745.6	12988421.0	2312997.0	883211.8
2050	101	50	50	50	95	347	500	500	168	112	207	213	997468.8	177630.9	13985889.0	2490627.0	951039.6
2055	90	56	35	34	45	106	403	168	112	78	78	168	618280.4	110104.4	14604169.0	2600731.0	993082.6
2060	90	56	35	39	45	123	290	157	123	78	78	135	289135.8	51489.8	14893304.0	2652220.0	1012743.8

Figure 9 Computed Tabulation of Cavern Data

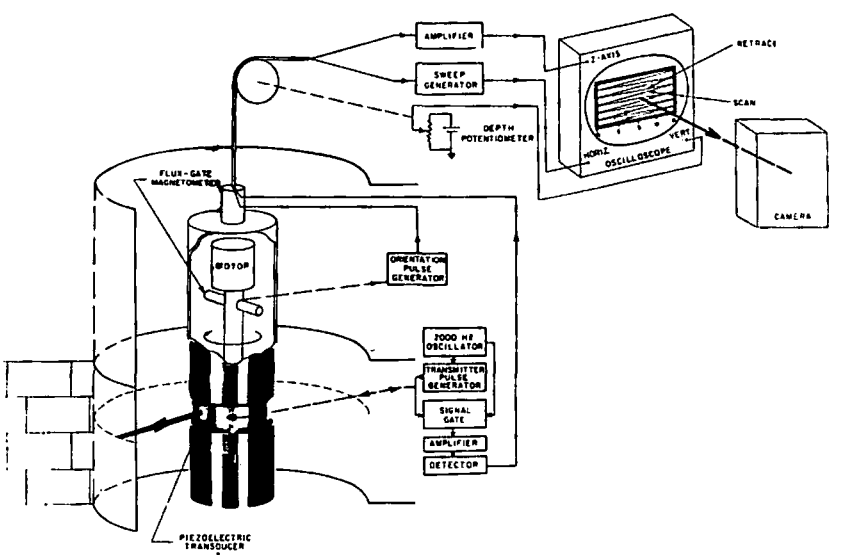

Figure 10 Block Diagram of the Seisviewer Logging System

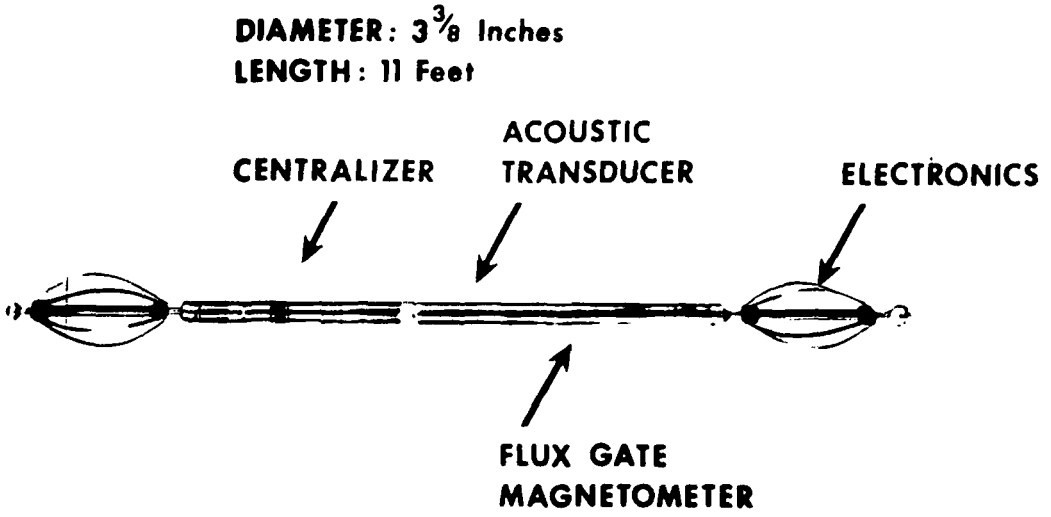

Figure 11 Borehole Seisviewer Logging Tool

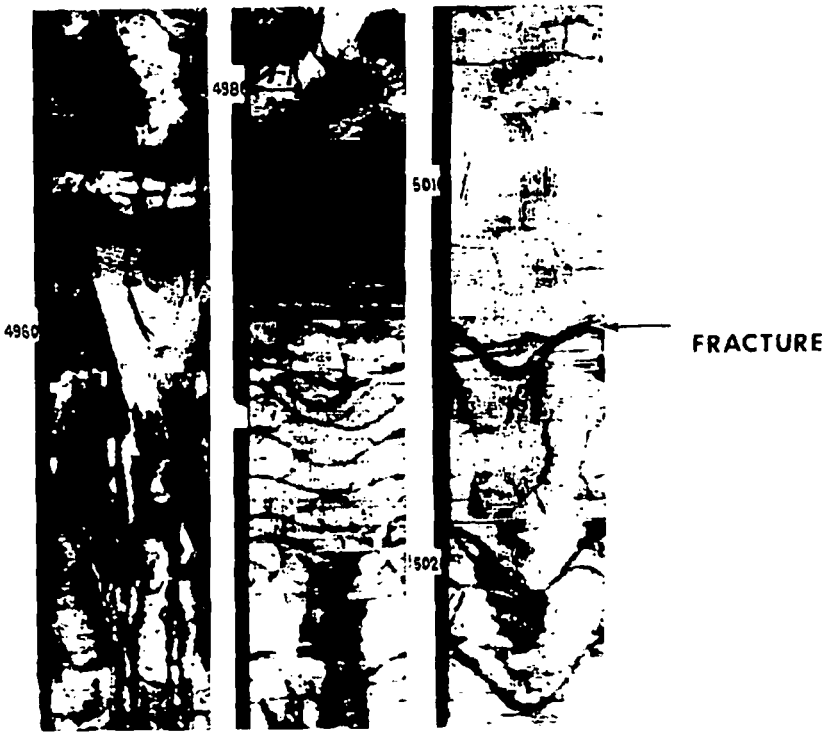

Figure 12 Highly Fractured Section

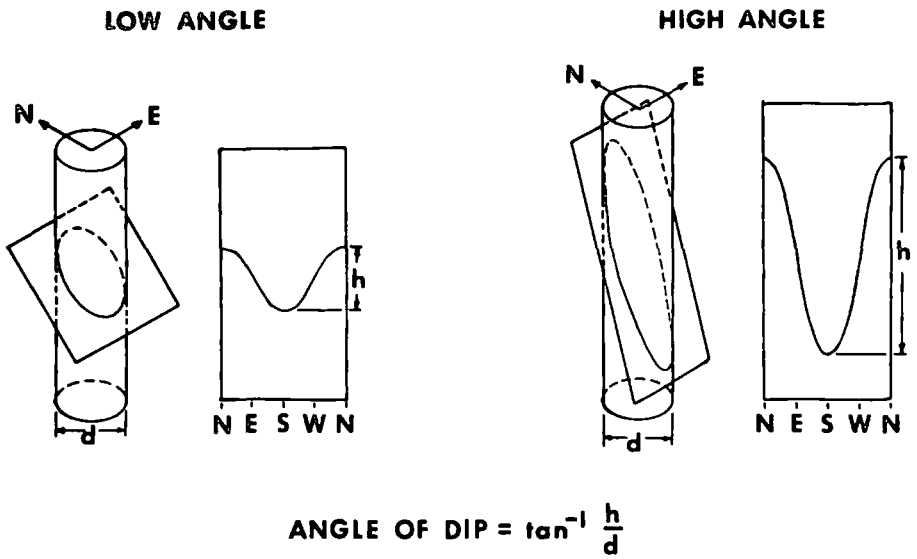

Figure 13 Isometric Drawings of Fracture Planes Intersecting the Borehole

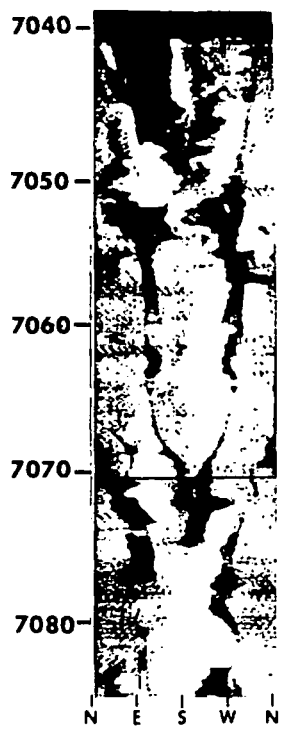

Figure 14 Near Vertical Fracture Pattern

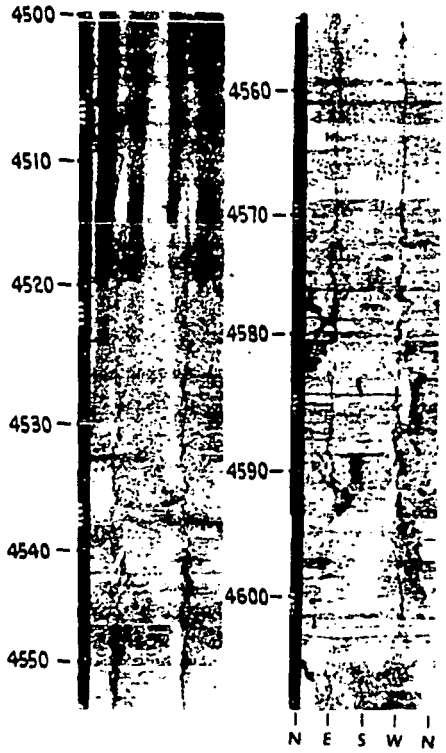

Figure 15 Drilling Induced Fractures

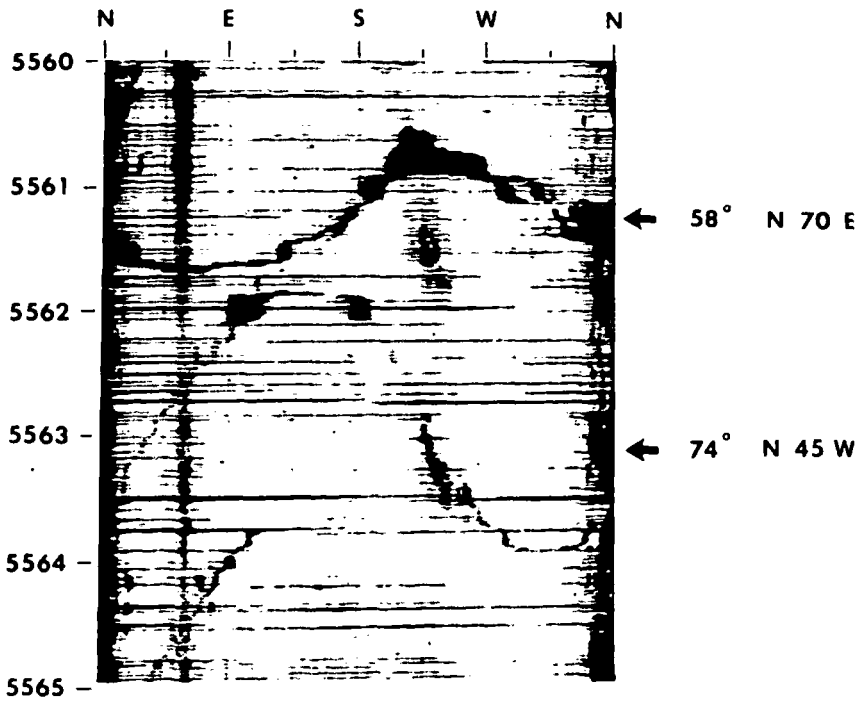

Figure 16 High Angle Fractures Intersecting Near Borehole

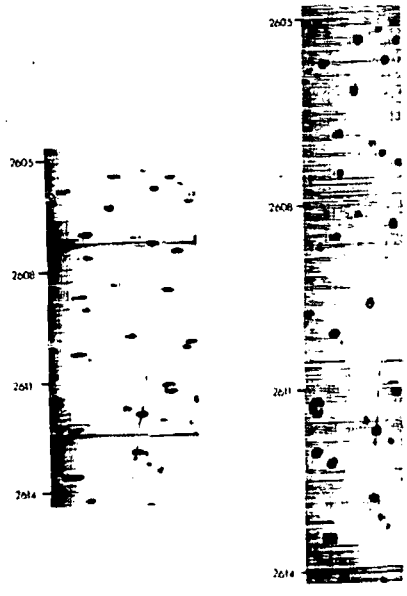

Figure 17 Casing Perforations

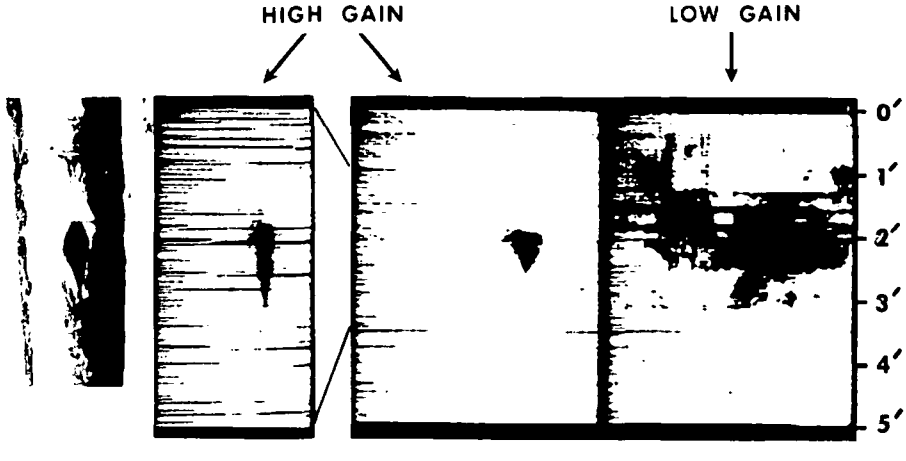

Figure 18 Casing Rupture

An Approach to Rock Mechanics Using Well Logging and Geophysical Techniques

By R. W. Baltosser and W. M. Sturdevant

Birdwell Division
Seismograph Service Corporation
A SUBSIDIARY OF RAYTHEON COMPANY
P.O. BOX 1590 • TULSA, OKLAHOMA 74102

Reprinted from NEW MEXICO PROFESSIONAL ENGINEER April 1971

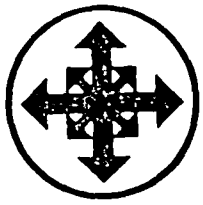

A Comparison of Various Directional Survey Models and an Approach To Model Error Analysis

J. E. Walstrom, SPE-AIME, Standard Oil Co. of California
R. P. Harvey, Standard Oil Co. of California
H. D. Eddy, Standard Oil Co. of California

Introduction

It is often desirable to know the position of specified points on the axis of a wellbore relative to the top-hole location. The current interest in directional survey calculations is related to the increased number of highly deviated holes drilled from offshore platforms and Arctic or urban drillsites. Positional accuracy is important in the following situations: (1) when two wellbores approach each other closely and it is important to avoid an intersection; (2) when a relief well is drilled to a wild well and it is important to achieve intersection, or near intersection, at some specified depth in the wild well; (3) when the bottom of a well, or perhaps some intermediate point, is close to a property boundary; and (4) when making equity participation calculations.

Suppose, as in the conventional manner, readings of inclination angle, I, with the vertical, and azimuthal angle, A, with the north, are taken at a number of specified depths in the wellbore. Each pair of measurements defines the direction of the tangent to the axis of the wellbore at the corresponding point or station. Suppose there are $n+1$ stations along the wellbore, including the top of the hole, so that there are n station intervals. Suppose such data are provided in triads of readings I_i, A_i and L_i, where I_i and A_i are in radians, L_i is the distance in feet along the axis of the wellbore from the top of the hole to station i, and where $i = 0, 1, 2, \ldots, n$, so that $L_0 = 0$. The distance between two stations measured along the axis of the wellbore is given by $S_i = L_i - L_{i-1}$, with $S_0 =$ zero.

The position of points along the axis of the wellbore is calculated with respect to a coordinate reference frame that has its origin at the top of the wellbore. The positive X direction is east, the positive Y direction is north, and Z is measured vertically downward. The computations used in all directional survey methods are based on the following three differential equations:

$$dX = \sin I \sin A \, dL,$$

$$dY = \sin I \cos A \, dL,$$

$$dZ = \cos I \, dL,$$

where L is the distance along the axis of the wellbore.

There is no calculational procedure that can be expected to determine the bottom-hole position relative to the top-hole position of a wellbore with complete certainty. Errors arise in two ways: (1) there are errors inherent in the calculational procedure used to determine the bottom-hole position, principally because the original data set is incomplete in terms of defining the hole; and (2) random errors occur in the readings of I, A, and L. In this paper we use the terms "model", "method", and "calculational procedure" interchangeably.

The present paper is confined mainly to a discussion of different calculational procedures and is, therefore, pertinent to the effect of errors of the first type. A statistical analysis is given in Ref. 2 that deals with consequences of errors of the second type.

The best known mathematical model for making

The classic terminal angle method of directional survey calculation is grossly susceptible to error, and the recommendation is that it be abandoned. There are too many alternatives that are better. One of them is the balanced tangential method, which has proved highly efficient in more than three years of use.

directional survey calculations is the terminal angle tangential method for which we have no original reference. It became apparent that this model results in appreciable errors for certain types of deviated holes. This is well illustrated, for example, in Refs. 3 and 4.

Five Models Based on Averaging

We now develop a class of models for directional survey calculations that includes some of the current models known to us but excludes the terminal angle tangential method, and for example, the circular arc method.[5]

The basic calculations for any model are to determine the values for increments of coordinates for each station interval from the incomplete data available, making use of the three basic equations given above. A characteristic feature of a model in the class being considered is that these incremental values for the ith station interval are computed in some way from the five items of available data, I_{i-1}, A_{i-1}, S_i, I_i, and A_i, using the earlier notation. A second characteristic is that some kind of averaging is carried out. In what follows we develop only the increment in the X-coordinate direction for the general station interval. Analogous expressions hold for increments in the Y and Z directions.

Before deriving the five models, we give below three general averaging relationships involving sin I to explain the notation and concepts.

$$\overline{\sin I} = \int_0^1 \sin\left[I_{i-1} + \alpha\,(I_i - I_{i-1})\right] d\alpha\,.$$

$$\overline{\overline{\sin I}} = \left[\frac{\sin I_{i-1} + \sin I_i}{2}\right].$$

$$\sin \bar{I} = \sin \bar{\bar{I}} = \sin\left[\frac{I_{i-1} + I_i}{2}\right].$$

The single bar symbol denotes the average value of the quantity beneath it with respect to I or A. The double bar symbol denotes the two-point average of the quantity beneath it.

Using this notation, we can summarize the expressions for X_i, the increments in the X coordinate direction, for five averaging models:

$$X_i = S_i \sin \bar{I} \sin \bar{A} \quad . \quad . \quad . \quad . \quad . \quad . \quad . \quad (1)$$

$$X_i = S_i \overline{\overline{\sin I \sin A}} \quad . \quad . \quad . \quad . \quad . \quad . \quad . \quad (2)$$

$$X_i = S_i \overline{\sin I}\;\overline{\sin A} \quad . \quad . \quad . \quad . \quad . \quad . \quad . \quad (3)$$

$$X_i = S_i \overline{\sin I \sin A} \quad . \quad . \quad . \quad . \quad . \quad . \quad . \quad (4)$$

$$X_i = S_i \overline{\overline{\sin I}}\;\overline{\overline{\sin A}} \quad . \quad . \quad . \quad . \quad . \quad . \quad . \quad (5)$$

Indeed it is possible to generate many other models using these averaging concepts, but the five above appear to be the only symmetrical ones.

We now develop each model at greater length.

Model 1 (Angle Averaging Method)

$$X_i = S_i \sin\left\{\int_0^1 \left[I_{i-1} + \alpha(I_i - I_{i-1})\right] d\alpha\right\} \cdot \sin\left\{\int_0^1 \left[A_{i-1} + \beta(A_i - A_{i-1})\right] d\beta\right\}$$

$$= S_i \sin\left(\frac{I_{i-1} + I_i}{2}\right) \sin\left(\frac{A_{i-1} + A_i}{2}\right). \quad . \quad . \quad . \quad . \quad . \quad . \quad . \quad . \quad . \quad (6)$$

$$X_i = S_i \sin \bar{I} \sin \bar{A} \quad . \quad . \quad . \quad . \quad . \quad . \quad . \quad (7)$$

Model 2 (Balanced Tangential Method)

$$X_i = S_i \int_0^1 \left[\sin I_{i-1} \sin A_{i-1} + \alpha(\sin I_i \sin A_i - \sin I_{i-1} \sin A_{i-1})\right] d\alpha$$

$$= S_i \left[\frac{\sin I_{i-1} \sin A_{i-1} + \sin I_i \sin A_i}{2}\right]. \quad . \quad . \quad . \quad . \quad . \quad . \quad . \quad . \quad . \quad (8)$$

$$X_i = S_i \overline{\overline{\sin I \sin A}} \quad . \quad . \quad . \quad . \quad . \quad . \quad . \quad (9)$$

Model 3 (Radius of Curvature Method)

$$X_i = S_i \int_0^1 \sin\left[I_{i-1} + \alpha(I_i - I_{i-1})\right] d\alpha \cdot \int_0^1 \sin\left[A_{i-1} + \beta(A_i - A_{i-1})\right] d\beta\,. \quad . \quad . \quad . \quad . \quad . \quad . \quad . \quad . \quad . \quad (10)$$

$$X_i = S_i \overline{\sin I}\;\overline{\sin A} \quad . \quad . \quad . \quad . \quad . \quad . \quad . \quad (11)$$

Model 4

$$X_i = S_i \int_0^1 \sin\left[I_{i-1} + \alpha(I_i - I_{i-1})\right] \cdot \sin\left[A_{i-1} + \alpha(A_i - A_{i-1})\right] d\alpha\,. \quad . \quad . \quad . \quad . \quad . \quad . \quad . \quad . \quad . \quad (12)$$

$$X_i = S_i \overline{\sin I \sin A}\,, \quad . \quad . \quad . \quad . \quad . \quad . \quad . \quad (13)$$

where $\overline{\sin I \sin A}$ denotes the average value of sin I sin A, where I and A vary together as linear functions of the single parameter α. As α varies from 0 to 1, I varies from I_{i-1} to I_i and A varies from A_{i-1} to A_i.

For completeness, the equations for X_i, Y_i, and Z_i are given in Appendix B.

Model 5

$$X_i = S_i \left\{\int_0^1 \left[\sin I_{i-1} + \alpha(\sin I_i - \sin I_{i-1})\right] d\alpha\right\} \cdot \left\{\int_0^1 \left[\sin A_{i-1} + \beta(\sin A_i - \sin A_{i-1})\right] d\beta\right\} \cdot$$

$$X_i = S_i \left[\frac{\sin I_i + \sin I_{i-1}}{2}\right] \left[\frac{\sin A_i + \sin A_{i-1}}{2}\right]. \quad . \quad . \quad . \quad . \quad . \quad . \quad . \quad . \quad . \quad (14)$$

$$X_i = S_i \overline{\overline{\sin I}}\;\overline{\overline{\sin A}} \quad . \quad . \quad . \quad . \quad . \quad . \quad . \quad (15)$$

The above five sets of equations describe five distinct models.

Further Remarks on the Five Models

Model 2, the Balanced Tangential Method, can be described in different ways. One point of view is summarized by the following three computational steps.

Step 1. Use the terminal angle tangential method and develop bottom-hole coordinates X, Y, and Z. As is well known, this procedure assumes that the

angles of inclination and azimuth measured at the bottom of a station interval hold throughout that interval.

Step 2. Repeat this process, but for each station interval use the inclination and azimuth angles measured at the top of the interval, and develop a new set of coordinates X', Y', and Z'.

Step 3. Compute the final solution for bottom-hole coordinates as:

$$X'' = (X + X')/2\,,$$
$$Y'' = (Y + Y')/2\,,$$
$$Z'' = (Z + Z')/2\,,$$

or, more explicitly,

$$X'' = \tfrac{1}{2} \sum_{i=1}^{n} S_i\,[\sin I_i \sin A_i + \sin I_{i-1} \sin A_{i-1}]\,,$$

$$Y'' = \tfrac{1}{2} \sum_{i=1}^{n} S_i\,[\sin I_i \cos A_i + \sin I_{i-1} \cos A_{i-1}]\,,$$

$$Z'' = \tfrac{1}{2} \sum_{i=1}^{n} S_i\,[\cos I_i + \cos I_{i-1}].$$

The bottom-hole coordinates are thus the means of the bottom-hole coordinates derived from two strictly linear-segment models.

This model can be reinterpreted as a single strictly linear-segment model with $n + 1$ linear segments in which the individual elements defined by triads I_i^*, A_i^*, S_i^* are constituted as follows:

$$\left.\begin{aligned} I_i^* &= I_i \\ A_i^* &= A_i \end{aligned}\right\} \quad i = 0, 1, 2, 3, \ldots n\,,$$

$$S_i^* = \tfrac{1}{2}\,(S_i + S_{i-1}) \quad i = 0, 1, 2, 3, \ldots n-1\,,$$

$$S_n^* = \tfrac{1}{2}\,S_n\,,$$

so that

$$\left.\begin{aligned} X'' &= \sum_{i=0}^{n} S_i^* \sin I_i^* \sin A_i^* \\ Y'' &= \sum_{i=0}^{n} S_i^* \sin I_i^* \cos A_i^* \\ Z'' &= \sum_{i=0}^{n} S_i^* \cos I_i^* \end{aligned}\right\} \quad \ldots \quad (16)$$

It is apparent that the balanced tangential method is a vector-averaging method, in which the contribution to the calculated well coordinates from each station interval is made up of the average of two vectors, one derived from readings at the top of the station interval and the other from readings at the bottom of the interval.

One form of Model 3, the Radius of Curvature Method, is given by

$$X_i = S_i \int_0^1 \sin\,[I_{i-1} + \alpha(I_i - I_{i-1})] \cdot \sin\left\{ A_{i-1} + (A_i - A_{i-1}) \cdot \frac{\cos I_{i-1} - \cos\,[I_{i-1} + \alpha(I_i - I_{i-1})]}{\cos I_{i-1} - \cos I_i} \right\} d\alpha \quad \ldots \quad (17)$$

This is essentially the form in which Wilson[3,4] developed his model and Rivero[1] enlarged on it. It represents a wellbore in which the angle of inclination from one station to the next varies linearly with L and the angle of azimuth varies linearly with distance along the projection of the wellbore axis in a horizontal plane. Although the Wilson and Rivero versions of the radius-of-curvature model are based on the same concept, under certain circumstances they will give different results. This is mainly because of the different ways the formulas are interpreted when the axis of the wellbore crosses either the east-west or the north-south directions. In fact, it is easy to construct a simple set of data for which the Wilson method gives a resultant southerly component and the Rivero method gives a resultant northerly component. Such an illustration is given by the following test case for which the results of the other models are included for completeness. We believe the Rivero interpretation is the correct one, and radius-of-curvature model results quoted elsewhere in this paper are based on that version.

Data for an Inclined Well

Measured Depth	Inclination	Azimuth
0	30°	N 70° E
100	32°	S 89° E

Computed Results

Model Number or Name	X	Y	Z
Tangential	53.0	−0.9	84.8
1	50.8	8.5	85.7
2	50.0	8.1	85.7
3 (Wilson)	50.5	−8.4	85.7
3 (Rivero)	50.5	8.4	85.7
4	50.5	8.4	85.7
5	49.9	8.4	85.7

Note: The angles in these numerical examples are measured in degrees.

It is perhaps interesting to note that in the form of Eq. 10 the integration over the I and A space is carried out independently, whereas in the form of Eq. 17 the two angles that play the role of an angle of inclination,

$$[I_{i-1} + \alpha(I_i - I_{i-1})]\,,$$

and an angle of azimuth,

$$\left\{ A_{i-1} + (A_i - A_{i-1}) \cdot \frac{\cos I_{i-1} - \cos\,[I_{i-1} + \alpha(I_i - I_{i-1})]}{\cos I_{i-1} - \cos I_i} \right\},$$

are constrained to vary together as a function of the variable of integration.

One point about the radius of curvature method is illustrated by the following survey data.

Measured Depth	Inclination	Azimuth
0	0°	N 75° E
100	1°	N 75° E
200	8°	S 76° E

The increment in the Y direction, corresponding to one station interval, is calculated in general from the following formula given in Ref. 1:

$$Y_i = S_i \frac{(\cos I_{i-1} - \cos I_i)(\sin A_i - \sin A_{i-1})}{(I_i - I_{i-1})(A_i - A_{i-1})} .$$

It is readily verified that the sign of the increment depends only on the two azimuth readings and not at all on the inclination values. The value of Y from the radius-of-curvature method is 0.29 ft. In comparison, the value from the balanced tangential method is -1.23 ft.

Models 3 and 4 have precise physical interpretations with the following properties:

1. The tangent at each station coincides with the tangent defined by the measured data.

2. The wellbore for each model varies smoothly between stations according to a well defined mathematical relationship. The two pertinent equations for Models 3 and 4 are Eqs. 17 and 12, respectively. In each, the upper limit of integration may be replaced by a variable, γ, indicating a general point on the wellbore ($0 \leq \gamma \leq 1$).

One consequence of the above is that we can generate calibration-type wellbores with known mathematical description for which one or more of the methods is exact.

It is apparent that for any given wellbore or part of a wellbore, one of the models may be more appropriate than the others. For example, Model 3 is appropriate when a wellbore has a steadily increasing inclination angle with respect to distance along the wellbore, L, and an azimuthal angle changing at a substantial acceleration rate with respect to L.

It is conceivable that a composite model could be developed that for any given station interval would select an appropriate model from these five models, depending on the local behavior of the station data. Such a model would, in general, be more accurate than any single model applied to the entire wellbore.

In this paper we have certainly not exhausted the model types that could be used. For example, we have not touched upon the type of model that performs some kind of local curve-fitting that might have the additional advantage over the methods mentioned in this paper of reducing some of the effect of data error. One drawback of using smoothing techniques is that one may not be readily able to distinguish between (1) the erratic reading due to data reading error that is preferably subjected to smoothing, and (2) that due to relatively abrupt changes in wellbore direction for whatever reason, which should not be smoothed away.

As a practical matter, whenever averaging takes place over the range of some azimuthal angle, that branch should always be chosen so that the range does not exceed 180°. Care must be exercised, particularly with regard to azimuths around the north. For example, with the data in Appendix A around measured depth 496 ft, the range of azimuthal angle considered should be the northerly one. This is pertinent to Models 1, 3, and 4.

Computational Results

We have a computer program package that includes an analysis for all the models mentioned in this paper.

First, we give some model comparisons based on results from simple contrived test data.

Large Azimuth Angle Difference At Adjacent Stations

It is interesting to note how the five models perform with the simple example described by the following data.

Measured Depth	Inclination	Azimuth
1	2°	S 90° W
100	2°	S 90° E
200	2°	S 90° W

One interpretation of the data is that it represents an S-shaped section of a wellbore lying completely in an east-west plane.

The results are shown in the following tabulation.

Model Number	Measured Depth = 100 ft		
	X	Y	Z
1	0	−3.49	99.9
2	0	0	99.9
3	0	−2.22	99.9
4	0	−2.22	99.9
5	0	0	99.9

Model Number	Measured Depth = 200 ft		
	X	Y	Z
1	0	−6.98	199.9
2	0	0	199.9
3	0	−4.44	199.9
4	0	−4.44	199.9
5	0	0	199.9

This example brings out two points that are perhaps worth mentioning. One is that conceptually an ambiguity occurs in the choice of A, cos A, or sin A when two adjacent station azimuthal readings are exactly 180° apart. This could occur, of course, only in the nearly vertical portions of the wellbore, thereby resulting in relatively small differences. This is pertinent to Models 1, 3, and 4.

The second point of interest is that when two adjacent station azimuthal readings are not exactly 180° apart and no ambiguity exists with Methods 1, 3, and 4 there might occur relatively large cumulative increments of horizontal departure that could be undesirable. A simple set of data illustrating this point, where the increments of horizontal departure are to the south, is as follows:

Measured Depth	Inclination	Azimuth
0	2°	S 89° W
100	2°	S 89° E
200	2°	S 89° W

Perhaps this example illustrates that I and A are not necessarily the best variables to work with directly in terms of smoothing.

Application of Models to Actual Well Data

Each model mentioned in this paper has been applied to directional survey data from several wells. In particular, each model has been applied to the data given in Appendix A, and the results are summarized in Table 1. The results using Models 1 through 5 are similar. Results from the terminal angle tangential method are different from the rest. We have found this to be typical with the examples used for comparison purposes. For this reason and others mentioned earlier, we conclude that this method is unreliable and we shall not discuss further the results of using it.

The results of applying Models 1 through 5 to ten other sets of survey data from real wells are shown in Table 2. These wells were selected to have a variety of deviation characteristics. For any individual well, these models give very similar results.

In what follows, we develop the concept we introduced earlier in this paper — that the error in calculated bottom-hole position is made up of two components.

Let us consider a particular well. There exists a true bottom-hole position for this well. Call it Point A. Suppose a set of survey data exists for this well obtained in the conventional manner using conventional equipment. Applying a model to this set of data provides an estimate of the bottom-hole position that we call Point C. Now let us imagine that we have an absolutely perfect directional survey tool that can be perfectly centered on the axis of the wellbore. Furthermore, assume that the axis of the wellbore is defined as the axis of the drillpipe. Suppose we have a set of data obtained by this perfect tool at ostensibly the same station points used for the data mentioned above. Applying the same model would give a third bottom-hole point estimate, B. The difference between Points A and B is the first component of error that we refer to as model error. The difference between Points B and C is the second component of error for the model used and is due to errors in the data.

The total error is, therefore, the sum of these two errors in the sense of vector addition:

$$\text{Total Error} = \overrightarrow{AC} = \overrightarrow{AB} + \overrightarrow{BC}.$$

In practice, of course one can never accurately measure model error. In what follows we attempt to derive an empirical relationship involving model error, average station interval, and degree of deviation of a well. We therefore require a measure of model error applicable to our five models and will use the variability in results from the five models for this purpose.

More specifically, for each of the 11 wells, we took the results as shown in Table 2 and calculated the mean point (centroid) from these bottom-hole positions. Since the five results for a well are based on the same set of survey data, the variability in the results can be taken to be due entirely to model errors. Of course the converse, that variability is the only result of model error, is not necessarily true.

Another way of looking at this is that we may conceive of this imperfect set of data as being a perfect set of data for some other (similar) well. From this viewpoint the bottom-hole points derived from each model are analogous to Points B in our earlier remarks, and we take the centroid of these points as our best estimate of Point A for this hypothetical well. One assumption that would make the centroid a best estimate for Point A is that the model errors for the five models are statistically unbiased. We take as the measure of average model error the average Euclidean distance from the centroid to each of the bottom-hole positions as determined by the five models. This average value is given in Table 3. It should be emphasized that this measure is somewhat arbitrary and that no adjustment has been made for bias due to using the sample centroid. In a companion paper to this (Ref. 7), a slightly different measure for model error has been used that relates more directly with expected absolute error.

Fig. 1 shows a plot of average station interval vs average model error in feet per 10,000 ft of measured depth.

TABLE 1—SUMMARY OF COMPUTATIONS FOR BOTTOM-HOLE RESULTS FOR AN ACTUAL WELL

	X	Y	Z	Closure	Azimuth Degrees	Min.	Sec.
Classic Tangential	−5074.93	3354.33	6925.22	6083.30	303	27	47
Angle Averaging (Model 1)	−5097.77	3367.44	6909.75	6109.57	303	26	51
Balanced Tangential (Model 2)	−5096.84	3367.07	6909.21	6108.60	303	26	58
Radius of Curvature (Model 3)	−5097.47	3367.22	6909.57	6109.20	303	26	50
Model 4	−5097.46	3367.30	6909.57	6109.24	303	26	53
Model 5	−5096.87	3366.78	6909.21	6108.46	303	26	49

Note: The horizontal ellipse of uncertainty (see Ref. 2) for this well has semi-axes of 2 ft × 14 ft for 50 percent probability. This corresponds to the data in Appendix A, which is Well 11 in Fig. 1 and Table 3.

With our original data, the average station interval ranges from 62 to 108 ft. To obtain results for data sets with larger average station intervals, we generated reduced data sets of approximately one-half, one-fourth, and one-eighth the number of stations from the original survey data and ran them with the five models.

In passing we mention that the four centroids that result from this procedure tend to fall on a curve, which would provide the basis for extrapolation to an estimated bottom-hole point that is generally more accurate than that obtained directly from the original data set. We plan to investigate this more fully.

Each well appears in Fig. 1 three times (No., No. A, No. B), corresponding to the original set of survey data, the data selected at odd-numbered stations only, and the data selected at even-numbered stations only. In all cases the terminal stations are included so that the total measured depth (TMD) is the same for the three cases. It may be observed from Fig. 1 that the average model errors using conventional surveying procedures are in no case greater than 1.22 ft per 10,000 ft of total measured depth.

Using this same measure for error, in the last column of Table 3 is shown the ratio of error in the horizontal direction to error in the vertical direction.

Another variable important in this study is the degree of deviation of a well. We have measured this in two ways as shown in Table 3. In Column 3 is shown the closure divided by Z, where closure is the projection in the horizontal plane of the Euclidean distance from the top of the hole to the bottom-hole point. In Column 4 is shown a measure of total well deviation arrived at by summing the elements of closure for all station intervals and dividing by total measured depth (TMD).

In general, as expected, the larger model errors occur with the more highly deviated wells and with large average station intervals. For wells with a measure of total deviation per foot within our sampled data, Fig. 1 can be used as a guide to obtain reasonable limits for the average model error in feet per

TABLE 2—RESULTS OF APPLYING MODELS TO REAL WELLS

		Model 1	Model 2	Model 3	Model 4	Model 5
Well 1						
	X	340.16	336.68	339.31	338.98	337.67
	Y	530.44	530.55	530.49	530.48	530.58
	Z	10799.25	10799.08	10799.08	10799.20	10799.08
Well 2						
	X	447.11	446.59	446.88	446.93	446.45
	Y	185.45	184.60	185.43	185.13	185.39
	Z	4850.23	4850.09	4850.18	4850.18	4850.09
Well 3						
	X	− 140.82	− 139.78	− 140.60	− 140.47	− 140.16
	Y	877.08	876.06	876.93	876.72	876.63
	Z	7529.11	7528.83	7529.02	7529.02	7528.83
Well 4						
	X	− 766.87	− 766.07	− 766.68	− 766.61	− 766.30
	Y	1594.35	1593.91	1594.16	1594.20	1593.80
	Z	7806.81	7806.39	7806.67	7806.67	7806.39
Well 5						
	X	− 2953.25	2952.23	− 2952.84	− 2952.91	− 2952.03
	Y	240.20	239.41	240.06	239.93	239.78
	Z	10996.24	10995.79	10996.09	10996.09	10995.79
Well 6						
	X	− 1686.78	− 1685.97	− 1686.43	− 1686.51	− 1685.74
	Y	1033.64	1032.20	1033.33	1033.13	1032.73
	Z	4736.49	4736.14	4736.37	4736.37	4736.14
Well 7						
	X	− 3774.96	− 3773.88	− 3774.65	− 3774.60	− 3774.03
	Y	2363.18	2362.97	2363.00	2363.11	2362.63
	Z	8338.76	8338.29	8338.60	8338.60	8338.29
Well 8						
	X	− 3295.15	3298.62	− 3299.01	− 3298.98	− 3298.73
	Y	3018.60	3018.25	3018.45	3018.48	3018.14
	Z	8342.80	8342.26	8342.62	8342.62	8342.26
Well 9						
	X	1859.19	1858.57	1858.81	1858.99	1858.04
	Y	− 1155.95	1155.08	1155.66	− 1155.66	− 1155.09
	Z	3975.15	3974.28	3974.86	3974.86	3974.28
Well 10						
	X	5326.22	5324.06	5325.64	− 5325.50	− 5324.48
	Y	3091.19	3090.17	3090.99	3090.83	3090.61
	Z	8125.30	8124.25	8124.95	8124.95	8124.25

10,000 ft in terms of average station interval. We feel that a stronger statement is not justified without further study.

As a matter of interest, the coefficient of variation for the station interval varies between 0.40 and 0.87 for the 11 survey data sets.

As a practical guide for an over-all error analysis of a directional survey calculation, in which one of these five models or some other model equivalent in general error characteristics is used, we offer the following general procedure.

Step 1. Carry out an analysis (Ref. 2) to obtain an appropriate probability distribution that represents statistically the uncertainties due to errors resulting from data inaccuracies.

Step 2. Compute a similar region of uncertainty, based on the ideas expressed here, that represents a distribution of model error.

Step 3. Add these two error variables together independently in a statistical sense to obtain a measure of total error (see Ref. 7).

Other Results

In addition to comparisons as described above, we have applied all models to several calibration-type wellbores for which the bottom-hole coordinates are known precisely from analytical considerations or very accurately from calculations applied to closely spaced data. Almost invariably, for deviated holes the terminal angle tangential method is subject to errors that can be appreciable, even in the vertical direction.

TABLE 3—ERROR FACTORS FOR REAL WELLS USING VARIOUS MODELS

Well Number	Total Measured Depth (ft)	Closure/Z	Measure of Total Deviation Per Foot	Average Total Model Error (ft)	Horizontal Error / Vertical Error
1	10,861	0.06	0.08	1.11	17.5
2	4,891	0.10	0.10	0.37	7.6
3	7,642	0.12	0.13	0.44	3.2
4	8,185	0.23	0.23	0.36	2.0
5	11,709	0.27	0.27	0.52	2.8
6	5,270	0.42	0.38	0.59	4.3
7	9,900	0.53	0.46	0.45	2.2
8	10,000	0.54	0.46	1.22	1.2
9	4,813	0.55	0.47	0.58	1.5
10	11,000	0.76	0.59	0.89	2.0
11	9,724	0.88	0.63	0.45	2.0

Conclusions

1. We conclude that the terminal angle tangential method should be abandoned because it is grossly susceptible to error.

2. Although the averaging-type Models 1 through 5 discussed in this paper have individual idiosyncrasies, there seems to be little to choose between them as far as accuracy is concerned. To our knowledge four of these models have not been described in previous literature. (However, in Refs. 6 and 8 it is mentioned that the "average angle" method of survey computation is used by THUMS Long Beach Co. for the East Wilmington Oil Field, Calif., and also by the Signal Oil and Gas Co. for their Hunting-

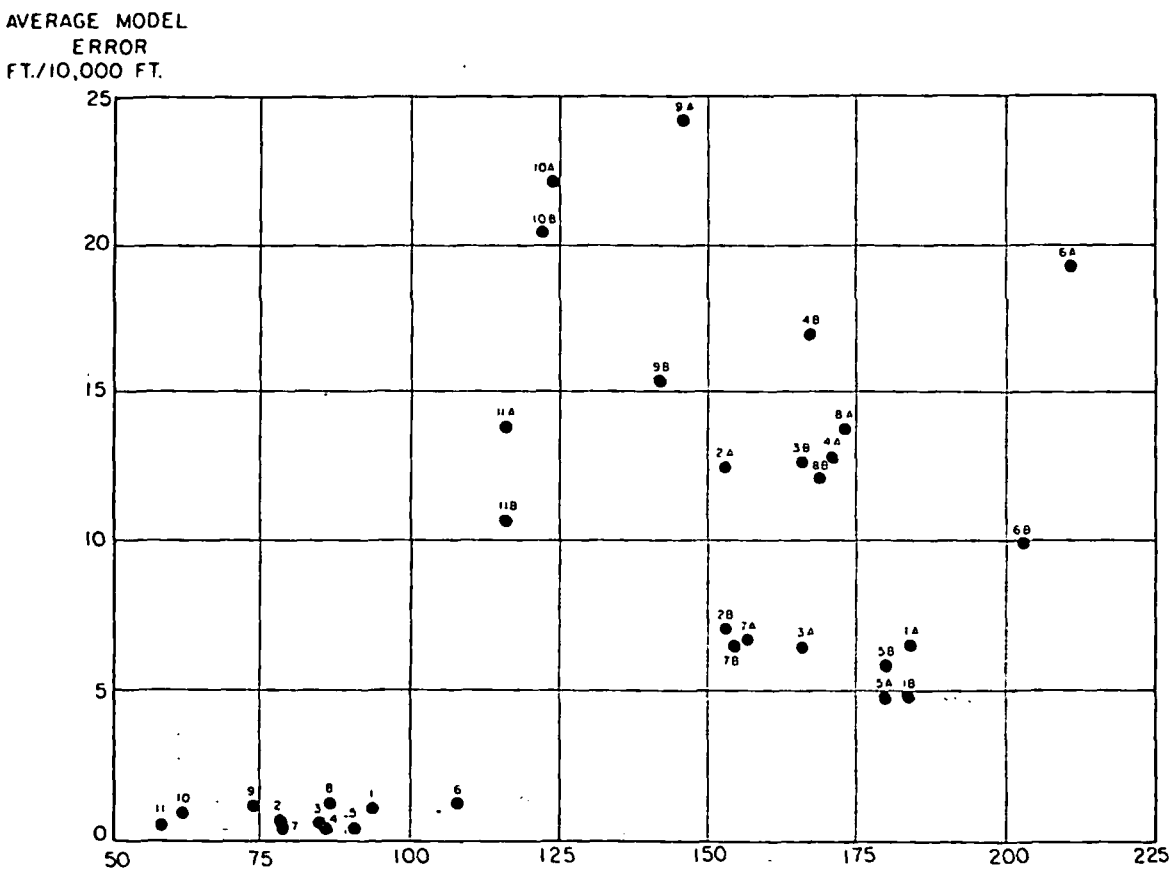

Fig. 1—Average station interval vs average model error.

ton Beach offshore operations.)

3. We have derived some data that can be used as a guide to provide reasonable limits on average model error in feet per 10,000 ft as a function of average station interval and well deviation when using one of the five models studied.

4. Our results from this and earlier papers indicate that most of the error in the calculated bottom-hole coordinates is generally due to random errors in the data readings rather than to errors inherent in the model, using current practices, equipment, and one of these five models.

5. We have found the balanced tangential method to be very efficient and have used it for more than 3 years. It lends itself very readily to a statistical analysis based on that given in Ref. 2.

Nomenclature

A_i = azimuthal angle at the ith station
$i = 0, 1, 2, 3, \ldots n$ = station number
$i = 0$, signifies top of the wellbore
I_i = inclination angle at ith station
L = distance along the axis of the wellbore from the top of the hole to a general point
L_i = distance from the top of the hole along the wellbore axis to the ith station
$S_i = L_i - L_{i-1}$ $(S_o = L_o = 0)$
X_i, X_i', X_i'' = increment in the X-coordinate direction from the ith station interval and similarly for $Y_i, Y_i', Y_i'', Z_i, Z_i', Z_i''$

Acknowledgment

We wish to acknowledge the support of the management of the Standard Oil Co. of California. In particular, we thank L. A. Swanson, W. W. Messick, and H. W. Crandall who have encouraged and supported this work.

References

1. Rivero, R. T.: "Use of the Curvature Method To Determine True Vertical Reservoir Thickness," *J. Pet. Tech.* (April, 1971) 491-496.
2. Walstrom, J. E., Brown, A. A. and Harvey, R. P.: "An Analysis of Uncertainty in Directional Surveying," *J. Pet. Tech.* (April, 1969) 515-523.
3. Wilson, G. J.: "Radius of Curvature Method for Computing Directional Surveys," *Proc.*, Ninth Annual SPWLA Logging Symposium, New Orleans, June 23-26, 1968.
4. Wilson, G. J.: "An Improved Method for Computing Directional Surveys," *J. Pet. Tech.* (Aug., 1968) 871-876.
5. Zaremba, W. A.: "Directional Survey by the Circular Arc Method," Standard Oil Co. of California Report, La Habra, Calif. (1970).
6. Truex, J. N.: "Directional Survey Problems, East Wilmington Oil Field, California," *Bull.*, AAPG (April, 1971)55, No. 4, 621-628.
7. Harvey, R. P., Walstrom, J. E. and Eddy, H. D.: "A Mathematical Analysis of Errors in Directional Survey Calculations," *J. Pet. Tech.* (Nov., 1971) 1368-1374.
8. Holbert, D. R., Thomas, G. B., Sweeney, M., von Tichl, R. D. and Ehring, T. W.: "A Computerized File for Directional Well Courses," *J. Pet. Tech.* (March, 1970) 267-276.

Original manuscript received in Society of Petroleum Engineers office April 11, 1971. Revised manuscript received March 6, 1972. Paper (SPE 3379) was presented at SPE 46th Annual Fall Meeting, held in New Orleans, Oct. 3-6, 1971.

APPENDIX A

0	0	0	N	0.	E	3353	53	0	N	54.	W
93	0	15	S	15.	W	3415	53	15	N	54.	W
124	0	15	N	55.	E	3477	53	45	N	54.	W
155	0	15	N	26.	E	3539	53	45	N	54.	W
186	0	15	N	12.	E	3601	53	30	N	55.	W
217	0	15	N	42.	E	3663	53	45	N	55.	W
248	0	30	N	37.	E	3725	53	30	N	55.	W
279	0	15	N	58.	E	3787	53	15	N	55.	W
310	0	30	N	78.	E	3849	53	45	N	55.	W
341	0	15	N	58.	E	3911	53	45	N	55.	W
372	0	0	N	0.	E	3973	53	30	N	55.	W
403	0	45	N	3.	W	4035	53	15	N	54.	W
434	1	0	N	5.	W	4097	53	15	N	54.	W
465	2	30	N	20.	W	4159	53	15	N	55.	W
496	3	30	N	15.	E	4221	53	15	N	55.	W
527	5	0	N	19.	W	4283	53	0	N	55.	W
558	5	30	N	41.	W	4345	52	45	N	54.	W
589	6	30	N	29.	W	4407	52	45	N	55.	W
620	8	0	N	24.	W	4469	52	45	N	54.	W
651	9	0	N	35.	W	4531	52	45	N	54.	W
682	9	30	N	50.	W	4593	52	45	N	53.	W
713	11	30	N	44.	W	4655	53	0	N	54.	W
744	13	0	N	41.	W	4717	53	15	N	54.	W
775	14	0	N	49.	W	4779	53	30	N	53.5	W
806	15	0	N	57.	W	4841	54	0	N	54.	W
837	16	0	N	61.	W	4903	53	45	N	54.5	W
868	17	0	N	53.	W	4965	54	0	N	54.5	W
899	19	0	N	56.5	W	5027	54	15	N	54.	W
930	20	45	N	57.	W	5089	54	15	N	53.5	W
961	22	0	N	55.	W	5151	54	0	N	53.5	W
993	23	15	N	58.	W	5213	54	0	N	54.	W
1024	25	0	N	59.	W	5275	53	45	N	53.5	W
1056	26	30	N	55.5	W	5337	53	15	N	54.	W
1088	27	0	N	59.	W	5399	53	0	N	54.5	W
1119	28	0	N	54.	W	5461	53	0	N	55.	W
1150	29	45	N	58.5	W	5523	53	0	N	56.5	W
1182	30	30	N	59.	W	5585	53	0	N	57.5	W
1214	32	0	N	58.	W	5647	52	45	N	58.5	W
1245	33	15	N	59.	W	5709	53	30	N	60.	W
1276	34	30	N	57.5	W	5771	53	45	N	60.	W
1307	35	15	N	56.5	W	5833	54	0	N	60.5	W
1338	37	0	N	55.5	W	5895	54	0	N	61.	W
1369	38	0	N	53.	W	5957	54	0	N	61.	W
1400	39	30	N	57.	W	6019	54	0	N	61.	W
1431	40	45	N	57.	W	6081	54	0	N	60.	W
1462	41	45	N	57.5	W	6143	54	0	N	61.	W
1493	43	0	N	56.	W	6205	54	0	N	61.	W
1524	44	30	N	55.5	W	6267	54	0	N	61.	W
1555	45	30	N	55.5	W	6329	54	0	N	61.	W
1586	47	0	N	55.	W	6391	54	0	N	61.	W
1617	48	15	N	54.	W	6453	54	0	N	61.	W
1648	50	0	N	54.	W	6515	54	0	N	60.	W
1679	50	45	N	54.	W	6546	53	45	N	61.	W
1710	51	30	N	54.	W	6569	53	45	N	61.	W
1741	52	15	N	54.	W	6743	52	45	N	61.	W
1772	53	0	N	54.	W	6929	52	15	N	61.	W
1803	53	30	N	53.5	W	7115	52	15	N	60.	W
1834	55	0	N	54.	W	7240	52	0	N	61.	W
1865	55	0	N	54.	W	7334	49	45	N	61.	W
1896	57	15	N	54.	W	7459	45	0	N	61.	W
1913	57	45	N	54.	W	7580	39	45	N	61.	W
1927	57	0	N	54.	W	7683	38	45	N	59.	W
1989	58	15	N	53.5	W	7776	38	30	N	58.	W
2051	58	0	N	53.5	W	7869	38	45	N	56.	W
2113	58	30	N	53.5	W	7960	38	0	N	55.	W
2175	59	0	N	53.5	W	8085	38	15	N	53.	W
2237	59	0	N	54.	W	8210	38	15	N	52.	W
2299	58	45	N	54.	W	8357	35	30	N	52.	W
2361	58	15	N	54.	W	8452	32	15	N	52.	W
2423	58	15	N	54.	W	8576	29	45	N	53.	W
2485	57	45	N	54.	W	8653	27	15	N	57.	W
2547	57	15	N	54.	W	8708	24	15	N	63.	W
2609	57	0	N	54.	W	8768	21	45	N	65.	W
2671	56	45	N	54.	W	8830	19	0	N	64.	W
2733	56	30	N	54.	W	8892	17	15	N	67.	W
2795	56	0	N	53.	W	8954	15	15	N	72.	W
2857	55	45	N	53.	W	9017	14	0	N	74.	W
2919	55	0	N	55.	W	9126	12	30	N	75.	W
2981	55	0	N	54.	W	9252	10	0	N	78.	W
3043	54	45	N	54.	W	9439	8	0	N	83.	W
3105	54	0	N	53.	W	9516	6	0	S	83.	W
3167	54	0	N	53.	W	9579	4	15	S	79.	W
3229	53	45	N	53.5	W	9640	3	45	S	78.	W
3291	53	30	N	53.5	W	9724	3	0	S	90.	W

APPENDIX I
Equations fc

$X_i = S$

$Y_i =$

$Z_i =$

In the even
be modifie
nearly equ

$Z_i =$

APPENDIX B

Equations for Coordinate Increments for Model 4

$$X_i = S_i \left[\frac{\cos\left(\frac{I_i - A_i + I_{i-1} - A_{i-1}}{2}\right) \sin\left(\frac{I_i - A_i - I_{i-1} + A_{i-1}}{2}\right)}{I_i - A_i - I_{i-1} + A_{i-1}} \right.$$

$$\left. \cdot - \frac{\cos\left(\frac{I_i + A_i + I_{i-1} + A_{i-1}}{2}\right) \sin\left(\frac{I_i + A_i - I_{i-1} - A_{i-1}}{2}\right)}{I_i + A_i - I_{i-1} - A_{i-1}} \right]$$

$$Y_i = S_i \left[\frac{\sin\left(\frac{I_i + A_i + I_{i-1} + A_{i-1}}{2}\right) \sin\left(\frac{I_i + A_i - I_{i-1} - A_{i-1}}{2}\right)}{I_i + A_i - I_{i-1} - A_{i-1}} \right.$$

$$\left. \cdot + \frac{\sin\left(\frac{I_i - A_i + I_{i-1} - A_{i-1}}{2}\right) \sin\left(\frac{I_i - A_i - I_{i-1} + A_{i-1}}{2}\right)}{I_i - A_i - I_{i-1} + A_{i-1}} \right]$$

$$Z_i = S_i \left(\frac{(\sin I_i - \sin I_{i-1})}{I_i - I_{i-1}} \right) .$$

In the event that one or more of the denominators are very small, the above expressions for X_i and Y_i should be modified by making use of the fact that sin f is approximately equal to f if f is small. Similarly, if I_i equals or nearly equals I_{i-1}, an alternative expression should be used for Z_i as follows:

$$Z_i = S_i \cos\left(\frac{I_i + I_{i-1}}{2}\right) .$$

JPT

SUBJ
GPHYS
Log
DMB

DIRECT MEASUREMENTS IN BOREHOLES OF PROPERTIES OF FAULT ZONES*

*Document provided by C. ~~Barry~~ Raleigh, Officer of Earthquake Studies, U. S. Geological Survey, March 1978

DIRECT MEASUREMENTS IN BOREHOLES OF PROPERTIES OF FAULT ZONES

A Program for Direct Measurement of the Relevant Physical and Chemical Parameters

Introduction

The strategy that has guided earthquake prediction research to this point is primarily a synoptic or data gathering strategy supplemented by some basic studies, and topical investigations. The logic of this strategy is very simple. We monitor the temporal and spatial variations of strain, seismicity, magnetic field and so on. Then, we correlate changes in these measurements with one another and attempt to determine the patterns of changes that may be useful for prediction. When distinctive patterns are observed we design a physical model that explains the observations and hopefully provides a basis for a reliable prediction system. Concurrently we fund a wide variety of topical studies as proposed by individuals in the research community in the hope that relevant basic research will lead to new insight and a "breakthrough".

This strategy has worked reasonably well, especially in the People's Republic of China where such empirical studies have led to successful predictions of major earthquakes. Measurements of seismicity, geodetic strain, tilt, creep on active faults, and magnetic field changes reveal systematic patterns of change that should eventually provide a basis for

an earthquake prediction system. The key to this strategy is the development of instruments, data handling, and interpretation systems necessary to produce the massive data base needed to reveal the "patterns" that can be identified as earthquake precursors.

One problem with this strategy is that there are not enough earthquakes of moderate size in any given area to provide an adequate data base in a reasonable period of time. The last significant earthquake in central California was in November 1974. This earthquake was associated with anomalies in tilt, magnetics, and possibly geodetic strain. But each of these measurements carries a high degree of uncertainty and it is not possible to resolve these uncertainties without more events large enough to produce significant anomalies. One solution to the time problem might be to instrument a large number of areas so that we would expect to capture at least one or two significant events every year, but realistic estimates of the cost of instrumenting many areas and maintaining high data quality over long periods of time suggest that this approach will require much more money than is available for earthquake prediction research.

The present strategy is directed toward building an empirical basis for prediction with fundamental studies in a secondary role directed primarily toward explaining the empirical observations. As an alternative, we propose, by a series of direct measurements in active fault zones, to determine which parameters are most significant and to develop a physical model for earthquakes that will predict in advance, the premonitory signals which should precede earthquakes. The empirical

data gathered by the monitoring networks, is needed to test these predictions, but testing a soundly based hypothesis will require only a relatively few events compared to the number of events required to develop a prediction capability primarily on an empirical basis.

An empirical scheme for predicting earthquakes will have some successes but it also seems certain to result in failures as well. For example, some earthquakes have foreshocks but others, equally large, do not. *Until the nature of the mechanical system which produces large earthquakes is well understood, earthquake prediction will be frustrating exercise, one which may self-destruct through society's intolerance of costly errors. We propose here a shift in the emphasis of our research program toward establishing a sound physical basis for earthquake prediction.*

RATIONALE

During the past decade, much has been learned about the processes that occur before, during and after earthquakes. However, the prediction or control of earthquakes requires a much greater understanding of the mechanisms of earthquakes than now exists.

The most damaging earthquakes are those in which large amounts of stored energy are released violently by some form of instability. Helpful methods of prediction, based mainly on premonitory phenomena, may be developed without a full understanding of the mechanisms involved. However, it seems more likely that real success in predicting earthquakes, and reductions in the uncertainties associated with such predictions, depend upon a much greater understanding of the mechanisms by which energy is stored and released than has been gained in studies to date. If this is true for prediction, it is probably even more true in respect of any potential there may be for the control of earthquakes.

In general terms, one can identify three principal components of earthquake phenomena:

i. The processes by which energy is accumulated, dissipated and released suddenly,

ii. The properties of the materials involved in these processes of energy accumulation, dissipation and release,

iii. The values of those conditions, such as stress and temperature, to which materials are subjected.

These components must be identified and measured on an appropriate geological scale, which poses formidable practical problems. It is largely for this reason that most of the data to date have been gathered by indirect methods of measurement. Unfortunately, indirect measurements are often neither as sensitive nor as unambiguous as now seems to be required to solve these problems. Likewise, it is unlikely that laboratory studies alone will provide all of the necessary information, because of the large disparity in, and important effects of, scale involved.

However, it does appear that a stage has been reached now in the understanding of earthquakes at which a number of direct measurements can be made, which have a very good chance of affecting a major advance in our understanding of the mechanisms of earthquakes and hence in the prospects for predicting and controlling them.

In very general terms, it seems certain that the source of the energy dissipated and released by earthquakes is the relative motion of lithospheric plates. To make use of this information for the prediction or control of earthquakes, a much more definitive model of the dynamics and kinematics of movements of the lithosphere and asthenosphere in the vicinity of active fault zones is needed. There are a number of ways by which this can be accomplished.

Comprehensive geodetic strain measurements in the area of interest on the scale ranging from a kilometer to a hundred kilometers can provide (and have provided partially) a description of recent displacements and

strains in the lithosphere. A large body of separately-derived evidence suggests that the relationship between strain and stress in the upper, seismically active part of the lithosphere (excluding those zones of discontinuity defined by faults) is near linear, in the range of times from periods of less than a second to a century. This fact is of the greatest importance on two counts. First, it provides a basis for compiling a comprehensive and coherent interpretation of the changes in strain throughout the region of concern from relevant geodetic measurements. Second, it implies that the absolute values of strain (which are not revealed by the geodetic measurements) can be found at a number of carefully chosen sites from appropriate stress measurements. These absolute values of strain can be used then to calibrate the absolute state of strain in the whole region of the lithosphere of concern.

The absolute values of strain and its spatial distribution appear to be fundamental to understanding the most important aspects of the mechanism of earthquakes. One of the most important features of big earthquakes is the large amount of energy (of which the seismic component is probably only a small fraction) suddenly released by them. The source of this energy is the accumulated elastic strain energy in the lithosphere. A knowledge of the state of strain in the lithosphere and its variation along potential earthquake faults would allow calculations to be made of the amounts of energy which could be released by

instabilities along portions of these faults.

Of equal importance, is the fact that instability itself arises from an imbalance between the amount of energy which can be dissipated in a stable manner by deformation of the material within the fault and the amount of energy which is available to be released from the adjacent lithosphere. Situations where large amounts of strain energy in the lithosphere can be released as a result of inelastic ("work-softening") movement along any portion of a fault zone, therefore, are likely to give rise to both instability and large earthquakes. Conversely, situations where the amounts of energy in the lithosphere are small are not likely to produce instabilities, and the release of energy is likely to be nearly stable, even if the inelastic movement along the relevant portion of the fault is "work-softening".

At this stage there would appear to be no other way of calibrating geodetic strain measurements so that they can be used as indicated above, except by suitable stress measurements. Such measurements of stress can be done only in boreholes of appropriate depth.

The dynamics of movements in the lithosphere and asthenosphere in the vicinity of earthquake faults are not well understood. However, using measured rates of deformation and plausible ranges of values for shear resistance, it has been shown that significantly different patterns of heat flow and temperature should exist for different, but otherwise reasonable modes of interaction. Measurements of heat flow and temperature have two distinct merits. First, they constitute an entirely

different approach to defining the dynamics. Second, because of the relatively long time constants involved in thermal diffusion, they provide one of the few methods for collecting data retrospectively.

Ultimately, an understanding of the mechanism of stable and unstable movement along faults depends upon a knowledge of the properties of the material in the fault. Until such time as this material can be studies and its properties measured, this knowledge will remain speculative, and probably, inadequate. The only economical and practical methods of examining and sampling this material from the relevant locations and depths, appears to be by drilling boreholes into it.

The importance of knowing the state of stress, pore pressures, temperature and permeability in, and in the vicinity of, earthquake fault zones is accepted widely. Attempts to measure of these quantities by indirect methods have generally not been successful. In any event, it is important to calibrate such measurements directly. Again, the only known way by which these quantities can be measured directly at the relevant locations and depths is by drilling appropriate boreholes.

PRINCIPAL MEASUREMENTS

1. CONDITIONS

In situ Stress

There is presently no direct or indirect estimation of the absolute state-of-stress on the San Andreas fault which meets with general acceptance. The laboratory measurements of the frictional strength of rock indicate that, with normal hydrostatic fluid pressure, shear stresses of one to two kilobars are required for shear failure on the San Andreas fault. However, from the absence of an anomaly in heat flow over the fault one may infer that the shear stress should be 100 to 200 bars, assuming predominantly conductive transfer of heat to the surface. If the shear stress is closer to the lower estimate, the fault zone must be pervaded by fluids at pressures very near the magnitude of the least principal stress, or the rocks in the fault must have abnormally low coefficients of static friction. These inferences, if correct, have profound implications for the nature of the instability that leads to great earthquakes. The size to which a rupture may grow will be related to the strain energy available which is related to the total shear stress; it also is a function of the distribution of the frictional strength along the fault. Furthermore, the magnitudes of the stresses both in the fault and with distance from the fault need to be measured to establish the boundary conditions for the loading of the lithospheric blocks which move during the earthquake.

Are parts of the fault creeping at low stresses or are those segments highly stressed, with the present seismicity being premonitory to a major earthquake? The differences between the sections characterized as creeping or locked are of fundamental importance to an understanding of the physical processes leading to earthquakes. Is the relative stability of the failure process in the creeping section due to the level of stress or to some intrinsic difference in mechanical properties or to pore pressure?

Indirectly estimated stresses might be derived from seismic velocity data, but only under the condition that seismic velocity anisotropy can be differentiated from lateral variations due to heterogeneities. Unfortunately, the fault zone is known, at least in central California, to have very rapid variations in velocity laterally, and it appears unlikely that anisotropy could be detected except, perhaps, in more uniform rocks away from the fault.

We propose making *in situ* stress measurements at depth in and near the fault using the hydraulic fracturing technique. Hydraulic fracturing measurements of the least principal compressive stress can be made routinely at depth and this will greatly constrain arguments such as those above. Over the past several years, we have gained considerable expertise both operationally and in interpretation of the data. Proper experimental technique should often yield estimates of the magnitude and orientation of the maximum principal stress and thereby provide detailed knowledge of the stress field near the fault.

There are several ways in which hydrofrac measurements can be used to provide information about stress on the fault. First, stress measurements can actually be made in the seismic region of the fault. Stresses have now been measured to 17,000 feet in hard rock; depths of 2 km near the San Andreas fault should thus be feasible. Secondly, a horizontal profile of stress measurements with distance from the fault can be used as a means of estimating the boundary conditions for loading as well as providing data for extrapolation should measurements in the fault zone proper prove to be exceptionally difficult.

In summary, boreholes to a depth of several km provide the possibility of measuring the absolute state-of-stress where earthquakes are presently occurring. The variability of the stresses, both the random part and the systematic change with depth and distance along and from the fault can be determined. The strategy for carrying out these measurements will be discussed in a later section.

Temperature and Heat Flow Measurements

Measurements of temperature and heat flow in the deeper boreholes envisioned here have several applications. Firstly, the thermal state of the fault zone is directly related to the ambient shear stress acting during creep or earthquakes. Thermal transients developed during earthquakes are proportional to the absolute shear stress. Secondly, the mechanical behavior of the fault zone rocks and fluids is strongly dependent on temperature. Thirdly, the influence of mass transport of heat laterally from the fault, a mechanism which has been invoked to

fer-

explained the absence of a distinct thermal anomaly over the fault, can be determined in deep boreholes slanted across the fault. Finally, the distribution of heat flow over the region of the plate boundary needs to be determined (in shallow holes) to characterize the thermal-mechanical machine that produces great earthquakes.

Surficial Site Investigations

As part of the logic behind drilling the fault zone, we aim toward the ultimate use of relatively inexpensive surface measurements to establish the areal distribution of some of the physical parameters governing fault behavior. Whether such a goal is even realistic can't be determined unless a careful attempt to calibrate the most promising surface measurements against direct measurements in boreholes. Consequently, the following preliminary site studies are called for before and after drilling the more expensive holes to depths of greater than 1 km.

Pre-drilling	Post drilling
Geologic mapping	Seismic reflection, refraction studies using down-hole sensors.
Electrical resistivity measurements	Heat flow in shallow holes distributed according to inferences about thermal regime gathered from deep hole.
Install creepmeters, strain and tiltmeters	

2. MATERIAL PROPERTIES

A thorough investigation of the structural state and mechanical properties of material in the fault zone seems necessary for an understanding of the nature and origin of earthquakes. Deep exploration may also, by providing a clearer understanding of actual physical properties, be helpful in development of techniques of earthquake prediction. There are at least two important reasons why this information can only be obtained through drilling in the fault zone.

In the first place, the materials and conditions near the source of earthquakes may be quite unique. They may be quite unlike either surface exposures of rocks or fault gouge, or the sheared material on ancient faults, exposed either at the surface or in mines or tunnels. On faults like the San Andreas large shear strain has been concentrated in a narrow zone of crushed rock. Based on microscopic study of highly sheared fault gouge produced in laboratory experiments, grain sizes ranges widely, but may go down to 100 Å or less. Fine grain size means rapid alteration, particularly at the higher temperatures prevalent in the deeper part of the seismic zone; it is hard to predict what the state of the fine-grained component will be. The natural gouge could be highly altered to clay minerals, contain glass, be completely unconsolidated, or be highly indurated. Obviously the mechanical properties of material in the fault zone will depend on these different unpredictable possibilities. What, for example, are the elastic moduli of this material, or its seismic velocity? Will the effective stress law hold, and what will be the deformational behavior under high stress? What are

the effects of temperature, both ambient and transient? Do the rocks have a cohesive strength. What are their rheological behaviors? It is impossible to resolve these questions without samples of the actual material.

Another reason why drilling appears essential is that rocks in the fault zone are highly fractured. This requires *in situ* measurement of many of the properties of interest. Important examples are fluid permeability and seismic velocity. At present there is no way of predicting these properties based on measured values for intact laboratory samples, when joints and other fractures are present. It is also possible that the fluid pressure in the fault zone is high, so that fractures will be particularly significant. The *in situ* measurements will have to be carried out at the natural level of pore pressure.

Many experimentalists are currently aware of the need to study the mechanical properties of fault gouge. However, since we have no clear idea of the state or condition of the actual material in the seismic zone, some present results may have little relevance. Actual samples from the focal region are needed to guide this work.

Permeability (and Pore Pressure)

If the ambient shear stress on seismically active faults proves to be low, high pore fluid pressures within the fault are required if the brittle or frictional material properties are normal. If the fluid pressures in the fault zone are high relative to those outside the zone, how are they maintained? Very low permeability in the fault zone is

implied, but permeability has been shown to increase exponentially as the pore fluid pressure approached the value of the least principal stress (Brace et al., 1968). Therefore the combination of high pore pressure and low permeability may be incompatible. Furthermore, as shear stresses approach the value required for failure, dilatant cracking may enhance the permeability.

Following the experiment in controlling earthquakes at Rangely, Raleigh, Healy and Bredehoeft (1976) proposed that earthquakes on the San Andreas fault might be controllable ultimately, given certain favorable conditions. To achieve the fluid pressure distribution required to limit the rupture length of earthquakes on the fault, the permeability cannot be too low. Further research on the feasibility of earthquake control is dependent on knowing the permeabilities of the fault zone materials.

Well Logging

Standard logging techniques provide information on the character of the rock and the pore fluids. In addition to these logs, use of borehole gravimeter to provide estimates of density with depth would be especially desirable. Borehole televiewer logging provides a detailed and complete view of the fracture pattern in the hole and is consequently the most important logging tool available.

Seismic Velocities

Healy and Peake (1975) have shown that the creeping part of the San Andreas fault zone has large lateral P-velocity gradients, with the central fault zone consisting of the lowest velocity material (Stierman,

1977). Recently, Bufe (personal comm.) has found the P-delays across the fault to be larger in the creeping segment than the currently quiescent segments to the north and south. Furthermore, there appears to be an unusually high V_p/V_S ratio of around 2 in this area. Attenuation of seismic waves in the fault zone is so severe as to make longitudinal seismic profiles to any distance difficult with acceptable-sized explosive charges. These observations indicate the presence of pervasive fracturing to considerable depth but detailed interpretations of seismic velocity structure in the fault zone itself currently seem beyond the reach of surface measurements. Interval velocity, surface to bottom hole velocity, and hole to hole velocity data would be of considerable value in clarifying our understanding of the nature of the elastic properties and seismic attenuation in the fault zone.

Taken together, down hole measurements of stress, pore fluid pressure, elastic and deformational behavior of the rocks, temperature and seismic velocity structure should provide the first set of adequate observations needed for the formulation of a realistic model of failure and instability in earthquakes.

CONTINUOUSLY MONITORING EXPERIMENTS

Seismic Observations

Once completed, a deep hole offers the possibility of measuring the interactions between the fault zone medium and changing conditions of loading with time at depths where earthquakes occur. There is some suggestion (McEvilly, pers. comm.) that seismic velocity may show a sensitivity to changes in stress of as much as 10^{-2} per bar. Given the relatively noise-free environment at the bottom of the a drill hole periodic monitoring of seismic velocity along a variety of ray paths could be undertaken relatively easily using non-destructive sources such as vibroseis.

Monitoring seismicity at depth and away from cultural and meteorological noise will greatly advance the limit of detectibility of small events. If very high frequency downhole seismometers are deployed in conjunction with a recording system capable of preserving data up to 100 Hz, very small earthquakes approaching magnitude 0 in size could be analyzed in hopes of identifying stuck patches on the fault (Wesson et al., 1973) or a variety of precursory signals. For example, changes in location, b slope, corner frequency, and stress drop could be sought with much smaller earthquakes than now used and this would add greatly to the resolution of such techniques.

Monitoring of Displacements, Tilts, Strains, Pore Pressure, etc.

There are a variety of measurements made near the surface for purposes of detecting precursors to earthquakes which suffer from serious environmental noise. Although the environment at the bottom of a deep

borehole is undoubtedly relatively noise-free, too few holes will be available from this program to warrant the cost of designing an all-purpose deep-hole instrument package for tilt and strain measurements for earthquake prediction purposes. Rather, an experiment designed to determine the optimum depth for holes drilled especially for such monitoring would be the best use of the deeper holes. If an instrument package is already available and relatively trouble-free, our judgment on this question might well be altered. Generally speaking, however, development of instrumentation for monitoring of strain, tilt, radon, etc. should not be an objective of this program.

If fluid from some level of the fault zone is allowed to rise in the well, monitoring of fluid pressure should be straightforward. Transients in pore fluid pressure related to earth tides or earthquakes will provide useful data on the intrinsic properties of the fault zone provided permeability is not too low.

POTENTIAL DRILLING SITES

Hollister-Parkfield

There are several reasons for attempting to drill somewhere in this area in the early stages of the program. Firstly, it is currently active seismically with earthquakes at some localities occurring at focal depths of 1 to 2 km (Figure 1). The shallower foci shown in the Figure 1 are located south of Bear Valley (Ellsworth, 1975). Just north of Stone Canyon, Bufe (pers. comm.) has also carefully located earthquakes M 3 with focal depths of 2 km or less.

Although uncertainties in focal depth in routinely processed data from the USGS seismic network in central California are fairly large, special studies conducted by these and other workers indicate that holes drilled to a depth of 1 to 2 km should be able to reach the hypocentral regions of small earthquakes. Moreover, the San Andreas fault in this area is creeping without accumulation of measurable elastic strain in the adjacent blocks (Savage and Burford, 1973). In the most rapidly creeping section near Slack Canyon the seismic activity is low relative to the other creeping segments of the fault, suggesting that stable sliding is occurring. Thus, the direct observations of stress, pore pressure, sampling of materials, afforded by boreholes could be used here to help characterize the nature of stable or near-stable fault motion.

The section of the San Andreas fault in central California is the most intensively studied anywhere. Its seismic velocity structure,

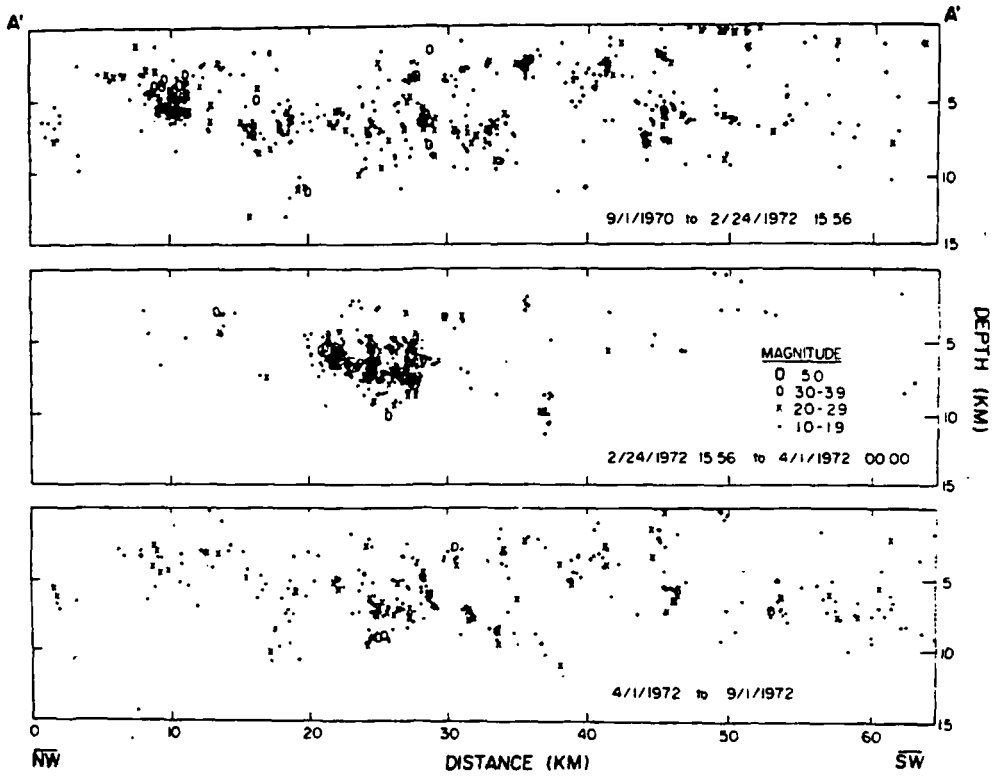

FIG. 7. Longitudinal projection of earthquake hypocenters, $M \geqq 1.0$, onto a vertical plane parallel to the San Andreas fault. *Upper section* shows the distribution of events recorded during 18 months preceding the M 5.0 earthquake of February 24, 1972. *Middle section* shows aftershocks of this earthquake occurring before April 1, 1972. *Lower section* shows continuing activity through August 1972.

Figure 1: After Ellsworth (1975).

electrical and magnetic properties, seismicity, strain and tilt are relatively well known, thus reducing the need for extensive site studies before drilling is begun.

Parkfield - Cholame Valley

Just south of the actively creeping section of the fault near Parkfield, the San Andreas has produced earthquakes near M = 6 in 1901, 1922, 1934 and 1966. The creep rate at Gold Hill, where surface rupturing occurred in 1966, is presently nil. To the north about 30 km, at Slack Canyon, the creep rate has been near 3 cm yr^{-1} so that since the earthquake in 1966, as much as 30 cm of potential displacement has accumulated to the north. The Parkfield - Cholame area seems a good candidate for another M = 6 earthquake in the next decade or so. Moreover, there is some indication that the 1857 Fort Tejon earthquake was preceded by a foreshock in this area. If great earthquakes on the southern to central section of the San Andreas are set off by a sort of keystone removal effect at Parkfield, it is an area which should be of great interest.

Seismic Gaps

Numerous earthquakes of magnitude 6 or greater have occurred along the San Jacinto branch of the San Andreas fault in this century with an average period of seven years. Two seismic gaps along the fault, about 50 km long, have been identified and are postulated to be potential sites for sizeable earthquakes in the future. From an earthquake prediction standpoint, intensive study of these areas hold great promise for capturing a sizeable earthquake in the least amount of time.

Locked Zones

The portions of the San Andreas fault north of about San Juan Bautista and roughly between the Carrizo Plain and Cajon Pass exhibit almost no seismicity and are usually referred to as "locked." Whether low ambient stress, fluid pressure, or high frictional strength, for example, account for this is unknown. Determining what distinguishes these regions from the active portion of the fault is of primary importance.

OBSERVATIONAL METHODS FOR *IN SITU* STRESS -- PORE PRESSURE, PERMEABILITY, STRESS AND MATERIALS PROPERTIES

The status of the current technology is such that all of these quantities can be measured with acceptable accuracy under favorable conditions. However, most researchers active in this area believe that the techniques can and should be improved. The methodology associated with each of the measurements will be discussed in order.

The drilling technique affects the ease with which subsurface data can be collected. Careful drilling with air usually provides more information on in-situ permeability, and pore fluids than drilling with either water or mud. In drilling with air one can keep track of the amount of fluid being produced from the hole. This information on fluid production identifies zones of higher permeability, and commonly, permeable fractures can be identified. Pore fluid samples uncontaminated by the drilling fluid can be collected during the drilling.

Drilling mud on the other hand is designed to coat the walls of the hole, sealing zones of higher permeability. Invasion of drillig mud into the rocks around a borehole can make permeability tests more difficult to interpret. The mud can also contaminate the pore fluid which also compilicates the collection of pore fluid for chemical purposes.

Pore Pressure

Pore pressure is one of the easier measurements which can be made in a borehole, assuming that the rock strata has at least modest permeability (greater than 1 millidarcy). Perhaps the simplest and most reliable pore pressure measurement is made by isolating an interval in

the drill hole and allowing the drill pipe to fill until the pressure in the fluid column balances the pore pressure. The rate at which fluid flows into the hole is dependent upon the hydraulic diffusivity (the ratio of the permeability to the compressibility of the rock plus the pore fluid) of the rock in the vicinity of the hole. The higher the permeability the more rapid the fluid exchange between the hole and the surrounding rock (the rate at which the hole fills is utilized to measure hydraulic diffusivity). Unfortunately, in rocks of low permeability the time necessary for fluid in the borehole to reach equilibrium may be long. If the rate of borehole filling can be observed, an extrapolation to static pore pressure can be made.

A number of techniques can be utilized to obtain the pore pressure. Measuring the fluid level is the oldest and perhaps simplest and most reliable method. It is necessary that one know the density of the fluid column in the hole for this method.

Pressure transducers are available which will measure fluid pressures to almost any desired sensitivity. The Hewlett-Packard device is the best of the available transducers. It can be lowered into the borehole to almost any depth; it has the same sensitivity over a very wide range of pressure. The device is expensive costing approximately $25,000.

Of the range of pressure transducers which cost from $100 to $3000, a number are available which can be used downhole. The sensitivity of these devices can be pushed electronically to almost any desired sensitivity. At high sensitivity, however, the range is limited. Our experience at Rangely where variable reluctance devices were used

continuously for several years, both downhole and at the surface, suggests that the devices drifted perhaps as much as one per cent over periods of several months. These are problems which can be eliminated with further research.

For long term measurements of pore pressure perhaps the most reliable and simplest device is mechanical float type recorder. These devices sense water-levels to a sensitivity of 0.3 cm over a wide dynamic range and are highly reliable.

Given a formation of modest permeability (1 millidarcy) the pore pressure can be sensed with a sensitivity of 10^{-2} psi and an accuracy of 10^{-2} psi for almost any period of time with current technology.

Permeability

Because of the heterogeneous nature of most media, permeability measured *in situ* commonly differs significantly from those measured in the laboratory. This discrepancy is especially true for fractured media. For a true porous media it is not uncommon to see discrepancies of two orders of magnitude variations between laboratory and in-situ measurements. Obviously, the inhomogeneities dominate the flow field for many of the media of interest in earthquake research. This necessitates *in-situ* measurements if the measurements are to be at all meaningful. Permeability can vary at least
10 orders of magnitude in common rock materials. Of all of the relevant variables, permeability has the widest range of possible variation.

Measuring permeability *in situ* requires 1) that an appropriate

interval be isolated, 2) that a flow rate be induced and measured, 3) that a head be measured during a period of flow, or during the period of recovery following a period of flow.

The drill stem test is widely utilized by the petroleum industry. (Comparable methods are widely utilized in hydrology). An interval of interest is isolated and allowed to flow into the drill string. Pressure is measured continuously at the base of the fluid column. The rate of flow is known from the rate at which the drill column fills. Results of the test yield the permeability and the hydraulic diffusivity.

There are a number of variations of hydraulic testing techniques which are utilized to measure permeability *in situ*. Many of these are simply variations on the drill-stem test techniques. Techniques are now under development to obtain *in situ* permeability measurements in rocks of very low permeability--less than 10^{-3} - 10^{-4} millidarcies.

The precision of the permeability measurement can be refined when a second hole can be utilized as an observation well.

Enough permeability measurements have been made under a wide variety of conditions to suggest that those media which behave even approximately as porous media--which includes a number of fractured media--yield good values of permeability. In fractured media the current status of the technology is less certain. For the single fracture the theory is well developed. For the case of multiple fractures the results are much less clear.

One can envision a technique which forces the flow field into a plane normal to the borehole within the interval of interest. This can be done by forcing a central flow interval between intervals of flow above and below. Such methods, while utilized for the *in situ* measurements of thermal properties, have not been tried for fluids. In sedimentary strata the bulk anisotropy of the layering operates causes the flow field to be planar, usually more or less normal to the borehole.

The technology to measure permeability *in situ* is available and well developed.

Stress

Of the present techniques hydraulic fracturing is the most reliable available method for measuring the in-situ state of stress. A number of investigators have demonstrated that under favorable conditions the method will yield:

1) the magnitude of the least principal stress, probably with an accuracy of 10 per cent;
2) the magnitude of the maximum principal stress (to an accuracy less than that of the least principal stress),
3) The orientation of stress tensor (assuming, of course, that it is orthogonal.)

Since the late 1940s, hydraulic fracturing has become a common technique for oil-well stimulation. The total number of wells hydraulically fractured is probably greater than 10^4, however, only a small handful have been made for the explicit purpose of determining the state of stress. This dearth is attributable, in part, to the cost involved. Until recently it was necessary either to obtain a

core of the interval to be fractured or to make a "trip" for each interval of interest to obtain a pre-hydrofracture impression in order to determine that the interval was fracture free. Once this had been established, fracturing was done utilizing conventional oil-field packers, which until recently required a trip into and out of the hole for each fracture. Finally, the orientation of the fractures was determined with in impression packer, which required another trip into the hole for each fracture. Thus the "conventional" method generally requires 1) either a carefully taken core of the intended fracture interval or a prefracture impression of each interval, 2) usually, a trip into and out of a hole to fracture each interval, and 3) a third trip for each fractured interval to obtain an orientation impression of the fracture--a time-consuming, expensive experiment.

In the interest of time, and possibly cost, we attempted to modernize the operation to facilitate a large number of tests on a regional scale. This was accomplished by 1) utilizing a borehole televiewer, an acoustic logging device, to detect pre-existing and induced fractures, 2) improving the packer design to permit repeated inflation and deflation without coming out of the hole to redress the tools, and 3) utilizing electronic pressure transducers to sense the pressure in the fractured interval as well as to detect leakage around the package.

Hydraulic fracturing is not without problems. It works well in brittle rocks, e.g., the Piceance Basin (Bredehoeft, et al, 1976). The current technique requires that the rock be unfractured in order to obtain the maximum principal stress and the orientation of horizontal components of the stress tensor. Further research may make it possible

to obtain these quantities in fractured sections.

The orientation of the hydraulically produced fracture must be measured in order to obtain the orientation of the stress tensor. Current methods which utilize either impression packers or the borehole televiewer, a sonic device, yield reliable orientations of the fracture in perhaps one out of two or three measurements. Further research should improve this reliability.

Strain

Borehole measurements can be utilized to measure the strain field. The two most promising methods which are well developed are observations of 1) pore pressure, and 2) borehole extensometers.

Earth tides are commonly observed in pore pressure measurements in deep holes. A double amplitude of 2 to 4 cm of fluid level fluctuation caused by the earth tides is not uncommon. The theory for this tidal fluctuation is reasonably well understood. The pore pressure fluctuation is produced by the tidal dilatation, the sum of the normal strains.

Since the tidal dilatation is of the order of 10^{-8}. one has a measure of the sensitivity of pore pressure measurements as strain indicators. Sensitivities of 1 part in 10^9 are readily achievable with old style mechanical water-level recorders which have been in use for 50 years. With good pressure transucers 1 part in 10^{10} should be achievable.

Unfortunately, pore pressure is also known to vary with other causes--barometric fluctuations, ground-water recharge and pumping. These effects must be separated from those caused by strain. Sophisticated digital filtering techniques have not been applied to this problem. The sensivitities are, however, such that measuring pore pressure in deep well should be promising as an indicator of dilatational strain.

Satellite Telemetry

Interest in pore pressure and strain data are normally for low frequency applications. Usually measurements at 15-minute intervals are sufficient. This type of information lends itself to telemetry. Data can be accumulated for period of several hours to a day at the well site. The station can then be interrogated and a relatively small block of data relayed to a central location.

The Water Resources Division of the USGS is currently operating several hundred sites from which water-level data is telemetered via satellite to a central location. The most promising of several of the systems which have been operated utilize a geosynchronous satellite. The ground station at the well is designed to operate on solar power batteries at remote locations. Such a system is ideally suited for long-term pore pressure or other borehole measurements. If the system were designed for one or two parameters, it could be built for several thousand dollars per installation.

Laboratory Measurements

Certain properties of cores should be determined routinely for comparison with *in situ* measurements: porosity, permeability, electrical conductivity, sound velocity (and derived dynamic elastic constants). All these measurements should be made under appropriately simulated effective confining pressure and temperature. Thermal conductivity cannot be measured *in situ*; it must be determined in the laboratory for use in associated heat-flow investigations.

Careful microscopic studies of samples taken from oriented, coherent cores will be necessary to acquire adequate understanding of the processes of failure in the fault zone. At relatively shallow depths to the order of 3 km, the principal mechanism of deformation is likely to be cataclasis which involves brittle fracture and Coulomb friction. The instability associated with the seismic stress drop may well be akin to the phenomenon of stick-slip observed in the laboratory. If so, the significant parameter is the stress drop which defines the difference between static and dynamic coefficients of friction. At greater depths, however, where the absolute temperatures approach about half that of melting, strain-rate dependent behavior is almost certainly significant, and the physical instability there may be due to such processes as water-weakening (or stress-corrosion) or partial thermodynamic melting. Evidence for all these potential failure processes should be gleanable from optical and electron-microscopic examinations of cores. They can be found in no other way.

At present there is no way to measure the strength of rock in a deep borehole. This property is critically important to our understanding of

failure processes. It can be determined only in the laboratory from triaxial compression testing, again under appropriately simulated effective confining pressures and temperatures.

Coring Techniques

Obtaining useful cores of fault-zone material may well require the development of new techniques. On faults like the San Andreas, high shear strain has apparently been concentrated in a narrow zone of crushed rock. The mechanical state of this fault zone is poorly understood, although its role may be as significant as that of the adjoining intact rock, both in the generation of seismic stress drops and as a source of varous precursory changes. The principal difficulty has been the sampling, even where relative unaltered material is available in surface excavations. Typical fresh fault zone material, or gouge, seems to resemble compact, heterogenous, poorly sorted soil. As such, mechanical properties are drastically altered if any remolding or restructuring of the material occurs during sampling or preparation for the laboratory. Sampling of fine-grained homogeneous soil is possible with well-established soil-mechanics procedures; sampling of typical fault gouge is another matter. Large fragments of rock may be present along with very fine-grained material down to clay sizes. The whole mixture has probably undergone average shear strains of 10 or more. Sampling should preserve the *in situ* structure of the fault-zone material as nearly as possible.

It should be emphasized that tools for such sampling are not now available, and that furthermore the expectably large range of "grain" sizes dictates the testing of the largest possible specimens if results

are to be statistically significant.

Coring Program

Because the San Andreas fault zone has never been sampled at depths, we can only guess what it might be like, but outcrop studies suggest the possibility of extreme heterogeneities of composition, texture and structure. Rational planning of a coring program before the fact is therefore virtually impossible. We should like to core the entire hole, but the cost would be prohibitive and perhaps ultimately unjustifiable. An irreducible minimum seems to be coring wherever drill-stem tests and hydraulic-fracturing measurements are to be done, perhaps every 200 meters or so. Beyond this requirement, the need for coring will have to be decided during the drilling operations as the variability of the material becomes evident from careful, continuous examination of cuttings and monitoring of penetration rates. Sidewall sampling using a wire-line can be carried out after drilling at selected intervals prior to casing the hole. The samples are not large but provide an adequate representation of the compositional and structure.

Continuous Monitoring Technology

A group of the stress-induced physical and chemical parameters which require downhole measurement conditions include but are certainly not limited to:

1. High-frequency acoustic emission to detect rock bursts before failure.
2. Airgun or vibroseis stacking experiment for high-gain, high-precision seismic velocity monitoring.
3. Downhole dilatometer installation.

4. Downhole tilt measurement to determine consistency or dependence of tilt on depth.
5. Vertical downhole strain measurement.
6. Self-potential (Piezoelectric) experiment.
7. Groundwater level measurement.
8. Deephole temperature/heatflow measurements.
9. Groundwater turbidity measurements.
10. Ground radon measurements of deep circulating fluids.
11. All water chemistry measurements of deep circulating fluids.

Not all these measurements are compatible in a single hole. Some need casing perforation, some don't, others can best be done without casing at all. Many of these instruments are under varying degrees of development. The enumeration of the above measurements reflects an order of data sampling rate which spans from almost 100 kHz for the high-frequency acoustic emission to less than one sample per day for water chemistry measurements. This has direct bearing on the strategy of data transmission and recording that is to be discussed below.

The deepwell monitoring program is likely to generate one to two dozen channels of information from each well site spanning a sampling bandwidth from 100 kHz to practically DC. Several data recording and transmission modes will have to be used to maximize the efficiency and reliability, and at the same time to achieve the continuous real time or nearly real time monitoring. Clearly, any data rate above 1 kHz cannot employ regular commercial telephone links, whereas it is uneconomical to transmit data of slow sampling rate (say 10^{-2} Hz) continuously through

a devoted data phone line. If radio links can be conveniently and reliably applied, substantial saving on data transmission cost can be realized. The final choice of the type of communication links will have to be decided on individual well site and the availability of commercial service. However, for all practical purposes, when a deepwell is fully monitored, the site itself will constitute a field observatory. A security enclosure with adequate heat (temperature) insulation will be built over the well-head. The structure is portable in the sense that it can be displaced when wire line service is necessary for instrument re-entry. The power consumption of on-site recording instruments and data telemetry devices is high enough that AC power is most likely needed. On-site standard time reference is required. We anticipate at least three data recording and transmission modes to be needed on each site:

a. Acoustic Emission Recorder:

It covers the information band from 100 kHz to 50 Hz. The present best approach is to record the signal on-site using a high quality professional tape recorder in combination with a digital delay and automatic triggering recording system.

b. Seismic Telemetry System:

It transmits seismic output in the information band of 10^{-1} to 50 Hz through the commerical or radio links using standard FM telemetry techniques.

c. Telemetry Interface Module:

For data of slow sampling rate, such as tilt, strain, self potential, groundwater level, temperature, radon, turbidity, and dilatometer output, we anticipate a sample per minute or every five to ten minutes. The best mode of recording and transmission makes use of on site-microprocessor as a temporary data storage, while the central recording laboratory will daily interrogate and acquire the stored data in the microprocessor through an interface mmodule. This mode does not tie up a telephone line, the period of interrogation and acquisition can be as short as a few minutes.

There remains a class of measurements such as water chemistry, hydrofracing, and borehole deformation; periodic field visits to the site will have to be necessary and no automatic recording nor transmission device can be employed. These visits also provide opportunity for calibration and adjustment of field recording instruments, changing tapes for the acoustic emission recorders.

The above recording modes a and b have been developed, and mode c should be complete at the end of 1977. No serious problems are anticipated in the program of deepwell continuous monitoring.